



Cardiff
Catalysis Institute
Sefydliad Catalysis
Caerdydd



Using supported metal nanoparticles for the conversion of biomass derived molecules

Thesis submitted in accordance with the requirements of Cardiff
University for the degree of Doctor of Philosophy

Daniel Robert Jones

2016

Summary

The energy demand of the world is increasing and the depletion of its reserves of fossil fuels are making energy production more expensive. The challenge therefore falls on researchers to develop novel ways of meeting this increased energy demand which are both cost-effective and environmentally friendly. Utilisation of biomass will be vital in achieving this goal because of its abundance and availability. In particular, levulinic acid has been identified as a valuable chemical feedstock. It can be easily converted into γ -valerolactone, which has vast potential applications in both the fuel and chemicals industries. The work presented in this thesis primarily focusses on the hydrogenation of levulinic acid into γ -valerolactone.

Hydrogenation of levulinic acid is well known, but catalysts that facilitate it usually incorporate expensive precious metals. In order for a process to become truly sustainable, the catalysts should also be sustainable. This requirement makes research into the use of cheap and abundant materials as catalysts desirable. The work presented in this thesis investigated the use of critical, precious metal catalysts compared with the cheaper, abundant, and non-critical base metals as potential replacements.

An investigation into lactic acid hydrogenation to 1,2-propanediol as a model reaction for levulinic acid hydrogenation was also carried out. Chapter 3 provides comparative data of a 5 wt.% Ru/C catalyst prepared by the sol immobilisation method and a commercial 5 wt.% Ru/C catalyst.

In Chapter 4, a variety of preparation parameters for the synthesis of 1 wt.% Ru/C catalysts were investigated, including the choice of Ru precursor, carbon support, and preparation method. 1 wt.% Ru/C from this chapter was set as the benchmark for base metals.

The second half of this thesis describes an investigation into the use of base metals as potential catalysts for levulinic acid hydrogenation. Chapter 5 shows that Cu-ZrO₂ catalysts were active for levulinic acid hydrogenation under much harsher reaction conditions compared with the benchmark (1 wt.% Ru/C). The synthesis of Cu-ZrO₂ was optimised through variation of the various preparation parameters and a detailed investigation was performed.

Chapter 6 shows that the incorporation of Ni into Cu-ZrO₂ improved the activity of Cu-ZrO₂, with a product yield of 100 % obtained after 90 minutes. This was attributed to an increased surface area and the formation of a Ni-Cu alloy. Modifying the preparation method further by adding a ball-milling step further increased the surface area of the catalyst and resulted in a product yield of 100 % after 30 minutes of reaction. It was found that there was more metal that required present in these catalysts, indicating a requirement of further work in order to produce catalysts with comparable catalytic activity.

*Dedicated to Mehryn Smith,
much loved, admired, and missed grandfather,
who showed me that a man is measured in how hard he works
and how much he gives.*

Acknowledgements

Completing a PhD is not an easy feat. It has been a rollercoaster of successes and failures, joys and frustrations, but also many fantastic opportunities, and it has been a fulfilling experience overall. However, completing a PhD is not something that one goes through alone, and here I offer my heartfelt gratitude to the people who have helped, guided, and supported me both academically and non-academically throughout my studies.

Foremost, I thank my academic supervisor Prof Graham Hutchings for giving me the opportunity to work as part of his vibrant research group, and for his help and guidance throughout my project.

I offer sincerest gratitude to my postdoctoral supervisor, Dr Sarwat Iqbal. It has been a great pleasure to work for and with her. I am incredibly grateful for our close working relationship, the opportunities she has provided, and for the help, encouragement, and confidence she had given me.

I would like to thank Dr David Willock, Dr Jonathan Bartley, and Dr Jennifer Edwards for the roles they played in supervising my project, their keen insight, and helpful guidance.

I would also like to thank the postdoctoral researchers in our group, Dr Simon Kondrat, Dr Ewa Nowicka, Dr Peter Miedziak, Dr Ourdia Akdim, Dr Gemma Brett, Dr Robert Armstrong, and Dr Mark Douthwaite for all of their help and support.

Working on NOVACAM has given me the opportunity to meet some of the most respected names in our field, and I must offer my gratitude to Prof Avelino Corma, Prof Emiel Hensen, and Prof Wataru Ueda for their discussions and encouragement. I would also like to thank Prof Satoshi Sato for collaborating with me.

I would like to thank the members of CCI's external advisory board, Dr Pelham Hawker, Dr Brian Harrison, Prof Jacob Moulijn, Prof Donald Bethell, Dr Mark Howard, and Dr Barry Murrer for providing their expertise and suggestions.

Some of the greatest experiences of a PhD come from the work you produce with your peers. Satoshi Ishikawa visited the CCI from Japan for the final year of his doctoral studies as part of the NOVACAM project. I had the great pleasure of working very closely with him while he was here and can say with complete sincerity that this was the most fulfilling experience of my PhD. Our close working relationship was absolutely pivotal to my development as a scientist. I would also like to thank my fellow NOVACAM colleagues Christian Reece and Liam Thomas for providing computational data to complement my experimental work, and for their friendship and support through a never-ending slew of NOVACAM meetings! I would like to thank Igor Orłowski who joined the group during the second year of my PhD for all the work he has done to complement my own and wish him the best for the rest of his PhD.

I must thank the multi-skilled Dr Greg Shaw, Chris Morgan, Steve Morris, Lee Wescombe, Julian Young, and Alun Davies for the work they do not only for me, but the entire group. Without them, we would cease to function. Their contributions cannot be understated.

My appreciation also goes to Prof Christopher Kiley of Lehigh University for his help in obtaining and interpreting the HAADF-STEM data presented in Chapter 3, and to Dr Stewart Parker at ISIS for his help in obtaining and interpreting the INS data presented in Chapter 4. I would also like to thank the staff at Warwick Analytical for the quick provision of the CHN data presented in Chapter 4.

My fellow PhD students at the CCI have always been helpful in a scientific capacity, but also in a personal one. I can't imagine completing my PhD without sharing the highs and lows with them. They have helped me learn that completing a PhD is about more than just the results and that it isn't the end of the world when things go wrong – which can be the hardest lesson to learn!

NOVACAM is a coordinated EU-Japan project and I gratefully acknowledge the financial support that was provided.

Finally, I would like to express my unending appreciation for my family and friends, who have always been loving, supportive and understanding – even if they aren't entirely sure sometimes what it is I've been doing! Throughout my life, they have motivated me to work hard and achieve, and I take great pleasure in making them proud.

Thank you.

Daniel R Jones

October 2016

Contents

List of tables	iv
List of figures	vi
List of abbreviations	x

Chapter 1: Introduction

1.1. Catalysis	1
1.2. Biomass valorisation	2
1.3. Platform molecules from cellulose	4
1.3.1. Conversion of cellulose into lactic acid	5
1.3.1.1. Lactic acid hydrogenation	7
1.3.2. Conversion of cellulose into levulinic acid	10
1.3.2.1. Levulinic acid hydrogenation	13
1.4. Aims and objectives	20
1.5. References	21

Chapter 2: Experimental

2.1. Materials	29
2.2. Catalyst preparation	30
2.2.1. Wet impregnation (WI)	30
2.2.2. Sol immobilisation (SI)	31
2.2.3. Co-precipitation (CP)	32
2.2.4. Oxalate gel precipitation (OG)	32
2.2.4.1. Ball milling (BM)	33
2.2.4.2. Physical mixing (PM)	33
2.3. Reaction data	34
2.3.1. Autoclave	34
2.3.1.1. Catalyst reuse studies	34
2.3.3. Reaction analysis	35
2.3.3.1. High performance liquid chromatography	34
2.3.3.2. Gas chromatography	36
2.3.3.3. Calculation of conversion and selectivity	38
2.3.3.4. Microwave plasma atomic emission spectroscopy	38
2.4. Characterisation	39

2.4.1. X-ray diffraction	39
2.4.2. Inelastic neutron scattering	40
2.4.3. Temperature programmed reduction	41
2.4.3.1. Temperature programmed reduction mass spectrometry	41
2.4.4. X-ray photoelectron spectroscopy	41
2.4.5. Transmission electron microscopy	42
2.4.6. Scanning electron microscopy	42
2.4.7. Energy dispersive X-ray spectroscopy	43
2.4.8. Brunauer-Emmett-Teller surface area analysis	43
2.4.9. N ₂ O adsorption for determination of metal surface area	44
2.4.10. Inductively coupled plasma atomic emission spectroscopy	44
2.4.11. CHN analysis	45
2.5. References	45

Chapter 3: Ru/C catalysts for the hydrogenation of lactic acid to 1,2-propanediol

3.1. Introduction	47
3.2. Results and discussion	48
3.2.1. Catalytic data	48
3.2.2. Characterisation	52
3.3. Conclusions	65
3.4. References	65

Chapter 4: Ru/C catalysts for the hydrogenation of levulinic acid

4.1. Introduction	67
4.2. Results and discussion	68
4.2.1. The effects of Ru precursor and carbon support	68
4.2.1.1. Characterisation	69
4.2.2. Characterisation of carbon supports	74
4.2.3. Investigation into SI preparation parameters	76
4.2.3.1. The effect of PVA variation	76
4.2.3.2. The effect of NaBH ₄ variation	81
4.2.4. Activity of SI catalysts over time	85
4.2.5. Catalyst re-use	86
4.2.6. Reaction kinetics	88
4.3. Conclusions	91

4.4. References	92
Chapter 5: Cu-ZrO₂ – an alternative to precious metal catalysts for the hydrogenation of levulinic acid	
5.1. Introduction	95
5.2. Results and discussion	96
5.2.1. Variation of Cu/Zr ratio	96
5.2.2. Variation of calcination temperature	103
5.2.3. Variation of precipitate ageing time	108
5.2.4. Catalyst reuse	112
5.3. Conclusions	114
5.4. References	115
Chapter 6: Cu-ZrO₂, Ni-ZrO₂, and Cu-Ni-ZrO₂ catalysts for the hydrogenation of levulinic acid	
6.1. Introduction	117
6.2. Results and discussion	118
6.2.1. The effect of Ni-Cu content in Ni-Cu-ZrO ₂	118
6.2.1.1. Catalytic data	118
6.2.1.2. Characterisation	121
6.2.2. Catalyst reuse and stability	131
6.2.3. Ball milling (BM) and physical mixing (PM)	134
6.2.4. Solvent Screening	138
6.3. Conclusions	140
6.4. References	141
Chapter 7: Conclusions	
7.1. Conclusions	143
7.2. Future Work	145

List of tables

Chapter 1: Introduction

Table 1.1. Equilibrium constants for hydrogenation reactions of lactic acid.	7
--	---

Chapter 2: Experimental

Table 2.1. A list of all materials used throughout this thesis and their suppliers.	29
---	----

Chapter 3: Ru/C catalysts for the hydrogenation of lactic acid to 1,2-propanediol

Table 3.1. A comparison of PDO yields for commercial catalyst with 5 wt.% Ru/C catalysts prepared by WI on different carbon supports.	48
Table 3.2. Turnover frequencies of catalysts prepared in this study compared to literature.	51
Table 3.3. The surface areas of the prepared 5 wt.%Ru/C catalysts and their supports.	53

Chapter 4: Ru/C catalysts for the hydrogenation of levulinic acid

Table 4.1. BET surface areas for 1 wt.% Ru/C catalysts supported on XC72R and G60.	72
Table 4.2. Ru(3d _{5/2}) and Ru(3p _{3/2}) binding energies and assignments for XC72R and G60 supported catalysts.	74
Table 4.3. CHN analysis of the carbon supports.	76
Table 4.4. BET surface areas of 1 wt.% Ru/C catalysts prepared with varying PVA/Ru ratios. NaBH ₄ /RuCl ₃ = 2.5.	79
Table 4.5. XPS analysis of a selection of catalysts with different PVA/Ru ratios.	80
Table 4.6. BET surface areas of 1 wt.% Ru/C catalysts prepared with varying NaBH ₄ /RuCl ₃ ratios.	83
Table 4.7. XPS analysis of a selection of catalysts with different NaBH ₄ /RuCl ₃ ratios.	85
Table 4.8. BET surface area of catalysts that underwent reuse tests.	87

Chapter 5: Cu-ZrO₂ – an alternative to precious metal catalysts for the hydrogenation of levulinic acid

Table 5.1. Theoretical and the measured Cu/Zr ratios in final catalysts.	96
Table 5.2. BET surface area for the catalysts prepared with different Cu/Zr ratios.	97
Table 5.3. Cu surface area of a selection of catalysts prepared with different Cu/Zr ratios.	98
Table 5.4. Particle sizes of catalysts prepared with different Cu/Zr ratio using the Scherrer equation.	99
Table 5.5. BET surface area for the catalysts calcined at different temperatures.	104
Table 5.6. Cu surface area of Cu-ZrO ₂ catalysts calcined at different temperatures.	104

Table 5.7. CuO particles sizes of catalysts calcined at different temperatures.	106
Table 5.8. XPS analysis for catalysts calcined at different temperatures.	106
Table 5.9. BET surface area for the catalysts prepared with different precipitate ageing times.	109
Table 5.10. Cu surface area for a selection of catalysts prepared with different precipitate ageing times.	109
Table 5.11. Particle sizes of CuO in the catalysts prepared with different precipitate ageing times.	111
 Chapter 6: Cu-ZrO₂, Ni-Cu-ZrO₂, and Ni-ZrO₂ catalysts for the hydrogenation of levulinic acid	
Table 6.1. The initial rates and TONs for Cu-ZrO ₂ , Ni-ZrO ₂ , and Ni-Cu-ZrO ₂ catalysts.	120
Table 6.2. Average particle sizes of the Cu-Ni alloy species calculated using the Scherrer equation at $2\theta = 42\text{--}46^\circ$.	123
Table 6.3. BET surface area and N ₂ O adsorption data of catalysts prepared with different Cu-Ni content.	123
Table 6.4. Surface metal ratios obtained by EDX analysis.	125
Table 6.5. Surface atomic concentrations of Ni, Cu, and Zr in all Ni-Cu-ZrO ₂ catalysts determined by XPS.	130
Table 6.6. Metal leaching from the catalyst in the post-reaction solution obtained by MP-AES.	132
Table 6.7. Metal leaching from 45Ni-5Cu-ZrO ₂ after reaction with model substrates.	133
Table 6.8. Particle sizes for BM and PM catalysts calculated by the Scherrer equation.	137
Table 6.9. BET surface areas of Cu-, Cu-Ni-, and Ni-ZrO ₂ catalysts related to their activity. BM: ball milled catalyst; PM: prepared by physical mixing.	138

List of figures

Chapter 1: Introduction

Figure 1.1. Example illustrating the effect of a catalyst on the reaction pathway.	2
Scheme 1.1. Schematic of cellulose conversion into lactic acid and levulinic acid.	5
Scheme 1.2. Schematic of the production of LA from lignocellulose.	10
Scheme 1.3. Mechanism of LA formation from HMF.	11
Scheme 1.4. Mechanistic pathways of LA hydrogenation to GVL.	13

Chapter 2: Experimental

Figure 2.1. Schematic of the autoclave used to obtain catalytic data.	34
Figure 2.2. Schematic of the HPLC apparatus used for reaction analysis.	36
Figure 2.3. Schematic of the GC apparatus used for reaction analysis.	37
Figure 2.4. Illustration of X-ray beams on a crystal from which Bragg's Law is derived.	39

Chapter 3: Ru/C catalysts for the hydrogenation of lactic acid to 1,2-propanediol

Figure 3.1. The activity of 5 wt.% Ru/XC72R-SI and the commercial Ru/C catalyst over extended time periods.	49
Figure 3.2. The activity of the SI and commercial catalysts up to 2.5 hours.	50
Figure 3.3. The activity of the SI and commercial catalysts on successive reuses.	51
Figure 3.4. Initial time-on-line profiles of the SI and commercial catalysts on initial use and reuse.	52
Figure 3.5. XRD patterns for the carbon supports only used for the preparation of catalysts by wet impregnation.	53
Figure 3.6. XRD patterns for 5 wt.% Ru/C catalysts supported on different carbons by WI.	54
Figure 3.7. TPR profiles for all 5 wt.% Ru/C catalysts prepared on different carbon supports.	55
Figure 3.8. Overlapping of Ru(3d) and C(1s) core-level signals in XPS (a) 5 wt.% Ru/C commercial; (b) 5 wt.% Ru/XC72R-SI.	56
Figure 3.9. Ru(3p) core-level spectra for successive reuse cycles. (a) 5 wt.% Ru/C commercial; (b) 5 wt.% Ru/XC72R-SI.	57
Figure 3.10. O(1s) core level spectra for the 5 wt.% Ru/C commercial after increasing reaction cycles.	58
Figure 3.11. O(1s) core level spectra for the 5 wt.% Ru/XC72R-SI after increasing reaction cycles.	59

- Figure 3.12.** Low magnification (a) BF-STEM and (b) HAADF-STEM images showing the typical particle size and shape distribution in the fresh 5 wt.% Ru/C commercial catalyst. (c) and (d) are higher magnification HAADF images showing greater structural detail in individual particles. 60
- Figure 3.13.** HAADF images showing structural detail in individual particles in 5 wt.% Ru/C commercial after 1 reaction. 61
- Figure 3.14.** (a) Low magnification HAADF-STEM image; (b) and (c) are higher magnification BF and HAADF images respectively for 5 wt.% Ru/C commercial. 61
- Figure 3.15.** (a) Low magnification HAADF-STEM image; (b) and (c) higher magnification HAADF images for unused 5 wt.% Ru/XC72R-SI catalyst. 62
- Figure 3.16.** (a) Low magnification HAADF-STEM image; (b) and (c) higher magnification HAADF images for 5 wt.% Ru/XC72R-SI catalyst after one reaction. 63
- Figure 3.17.** (a) Low magnification HAADF-STEM image; (b) and (c) higher magnification HAADF images for 5 wt.% Ru/XC72R-SI catalyst after 4 reaction cycles. 64
- Chapter 4: Ru/C catalysts for the hydrogenation of levulinic acid**
- Figure 4.1.** Activity of 1 wt.% Ru/C catalysts for LA hydrogenation. 68
- Figure 4.2.** XRD patterns of 1 wt.% Ru/C catalysts. (a) supported on XC72R; (b) supported on G60. 69
- Figure 4.3.** C and Ru EDX maps for G60 supported catalysts. (a) RuCl₃ used as precursor; (b) Ru(NO)(NO₃)₃ used as precursor. 70
- Figure 4.4.** C and Ru EDX maps for XC72R supported catalysts. (a) RuCl₃ used as precursor; (b) Ru(NO)(NO₃)₃ used as precursor. 71
- Figure 4.5.** TPR profiles of 1 wt.% Ru/C catalysts. (a) supported on XC72R; (b) supported on G60. 73
- Figure 4.6.** Mass spectroscopy signal of 1 wt.% Ru/XC72R prepared by sol immobilisation using RuCl₃ recorded during TPR. 73
- Figure 4.7.** INS spectra of XC72R and G60. 75
- Figure 4.8.** INS spectra of [XC72R–G60] compared with graphite. 75
- Figure 4.9.** The effect of PVA content on catalytic activity of 1% Ru/C. 77
- Figure 4.10.** XRD patterns of a selection of catalysts prepared with different PVA/Ru ratios. 78
- Figure 4.11.** TPR profiles for 1 wt.% Ru/C catalysts prepared varying PVA/Ru ratios. 80
- Figure 4.12.** The effect of NaBH₄ use on catalytic activity of 1 wt.% Ru/C. 82

Figure 4.13. XRD patterns of a selection of catalysts prepared with varying NaBH ₄ /RuCl ₂ ratios.	82
Figure 4.14. TPR profiles for 1 wt.% Ru/C catalysts prepared with varying NaBH ₄ /RuCl ₃ ratios (PVA/Ru = 0.1).	84
Figure 4.15. Time-on-line data for 1 wt.% Ru/C catalysts prepared with different PVA and NaBH ₄ contents.	86
Figure 4.16. Catalyst activity on successive reuse using 1 wt.% Ru/C catalysts.	87
Figure 4.17. TPR profiles of 1 wt.% Ru/C (PVA/Ru = 0.1, NaBH ₄ /RuCl ₃ = 2.5) catalyst before reaction and after 1 use.	88
Figure 4.18. Determination of the order of reaction with respect to LA.	89
Figure 4.19. Determination of the order of reaction with respect to H ₂ .	90
Figure 4.20. Arrhenius plot for the determination of reaction activation energy (using 1 wt.% Ru/C prepared by SI from RuCl ₃ supported on XC72R).	90
 Chapter 5: Cu-ZrO₂ – an alternative to precious metal catalysts for the hydrogenation of levulinic acid	
Figure 5.1. Effect of the variation of Cu/Zr ratio on GVL yield.	97
Figure 5.2. XRD patterns for catalysts prepared with varying Cu/Zr ratio.	98
Figure 5.3. (a) A typical XPS profile and (b) Auger peak of Cu-ZrO ₂ catalysts.	100
Figure 5.4. TPR profiles of the catalysts prepared with varying Cu/Zr ratio.	102
Figure 5.5. Effect of catalyst calcination temperature on GVL.	103
Figure 5.6. XRD patterns for catalysts calcined at different temperatures.	105
Figure 5.7. TPR profiles of catalysts calcined at different temperatures.	107
Figure 5.8. Effect of precipitate ageing time on GVL yield. (a) GVL yield; (b) GVL yield normalised by BET surface area.	108
Figure 5.9. XRD patterns for Cu-ZrO ₂ catalysts prepared with different precipitate ageing times.	110
Figure 5.10. TPR profiles of catalysts prepared with different ageing times.	112
Figure 5.11. Time-on-line profile for the most active Cu-ZrO ₂ catalyst.	113
Figure 5.12. The catalytic activity of Cu-ZrO ₂ with successive reuse.	114
Figure 5.13. XRD patterns of the most active Cu-ZrO ₂ catalyst before and after use.	114

Chapter 6: Cu-ZrO₂, Ni-Cu-ZrO₂, and Ni-ZrO₂ catalysts for the hydrogenation of levulinic acid

Figure 6.1. Catalytic activity of Ni-Cu-ZrO ₂ catalysts prepared with different Ni-Cu compositions and reduction temperatures.	118
Figure 6.2. Time-on-line data for Ni-Cu-ZrO ₂ prepared with different Ni-Cu compositions reduced at 400 °C.	119
Figure 6.3. Reaction order with respect to (a) LA, and (b) H ₂ .	120
Figure 6.4. XRD patterns of Cu-Ni-ZrO ₂ catalysts with increasing Cu-Ni contents, reduced at 400 °C.	122
Figure 6.5. TPR profiles of Cu-ZrO ₂ , Ni-Cu-ZrO ₂ , and Ni-ZrO ₂ catalysts.	125
Figure 6.6. SEM/EDX images of 5Ni-45Cu-ZrO ₂ .	126
Figure 6.7. SEM/EDX images of 15Ni-35Cu-ZrO ₂ .	127
Figure 6.8. SEM/EDX images of 35Ni-15Cu-ZrO ₂ .	127
Figure 6.9. SEM/EDX images of 45Ni-5Cu-ZrO ₂	128
Figure 6.10. SEM/EDX images of 35Ni-15Cu-ZrO ₂ .	128
Figure 6.11. XPS analysis of Ni-Cu-ZrO ₂ catalysts. (a) Cu(2p _{3/2}); (b) Ni(2p _{3/2}).	129
Figure 6.12. Activity of the 45Ni-5Cu-ZrO ₂ catalyst on successive reactions.	131
Figure 6.13. XRD patterns of 45Ni-5Cu-ZrO ₂ before and after reaction.	132
Figure 6.14. The effect of leached metal on GVL yield.	133
Figure 6.15. The effect of BM and PM methods on catalytic activity.	134
Figure 6.16. Time-on-line data for catalysts prepared with a BM step.	135
Figure 6.17. XRD patterns for Cu-ZrO ₂ catalysts prepared with varying methods.	136
Figure 6.18. XRD patterns of 45Ni-5Cu-ZrO ₂ catalysts prepared with varying methods.	136
Figure 6.19. XRD patterns of Ni-ZrO ₂ catalysts prepared with varying methods.	137
Figure 6.20. The effect of solvent on the catalytic activity of 50Cu-ZrO ₂ and 45Ni-5Cu-ZrO ₂ .	139
Figure 6.21. Activity of 50Cu-ZrO ₂ at increasing loadings of LA in MeOH and increasing reaction times.	140

List of abbreviations

BET	Brunaur, Emmett, Teller (surface area)
BM	Ball milling
CP	Co-precipitation
EDX	Energy dispersive X-ray (spectroscopy)
FID	Flame ionisation detector
GC	Gas chromatography
GVL	γ -valerolactone
HAADF	High-angle annular dark field (S/TEM)
HMF	Hydroxymethyl furfural
HPLC	High performance liquid chromatography
ICP-AES	Inductively coupled plasma atomic emission spectroscopy
INS	Inelastic neutron scattering
LA	Levulinic acid
ML	Methyl levulinate
MP- AES	Microwave plasma atomic emission spectroscopy
NCM	Non-critical metal
OG	Oxalate gel (co-precipitation)
PDO	1,2-propanediol
PM	Physical mixing
RID	Refractive index detector
SEM	Scanning electron microscopy
SI	Sol immobilisation
TCD	Thermal conductivity detector
TEM	Transmission electron microscopy
TOF	Turnover frequency
TON	Turnover number
TPD	Temperature programmed desorption
TPR	Temperature programmed reduction
WI	Wet impregnation
XPS	X-ray photoelectron spectroscopy
XRD	X-ray diffraction

Chapter 1

Introduction

1.1. Catalysts

A catalyst is a substance that provides an alternate pathway for a chemical reaction without being consumed during the process. Catalysts can generally be divided into three classes: homogeneous catalysts, where the catalyst is in the same state of matter as the reactants (organometallic compounds usually); biological catalysts, such as enzymes commonly found in living systems; and heterogeneous catalysts, where catalysts are of a different phase to the reactants – generally a solid material with liquid or gas reactants coming into contact with it. Typically, a much smaller amount of catalyst can convert a large quantity of reactants into the required products under milder reaction conditions than the stoichiometric reaction would require. Consider Figure 1.1, which shows the energy profile of reactants A and B forming product C. The activation energy, E_a , of the reaction is quite high. It might be that this barrier is so high that the reaction cannot proceed without significant energy input. However, when a catalyst is used, there is an alternative pathway available through which the reaction can proceed with an activation energy of E_a cat. Generally, there is a transitory state where the reactants are bound to the catalyst. Because E_a cat. $<$ E_a , the reaction can proceed with much lower energy input ¹.

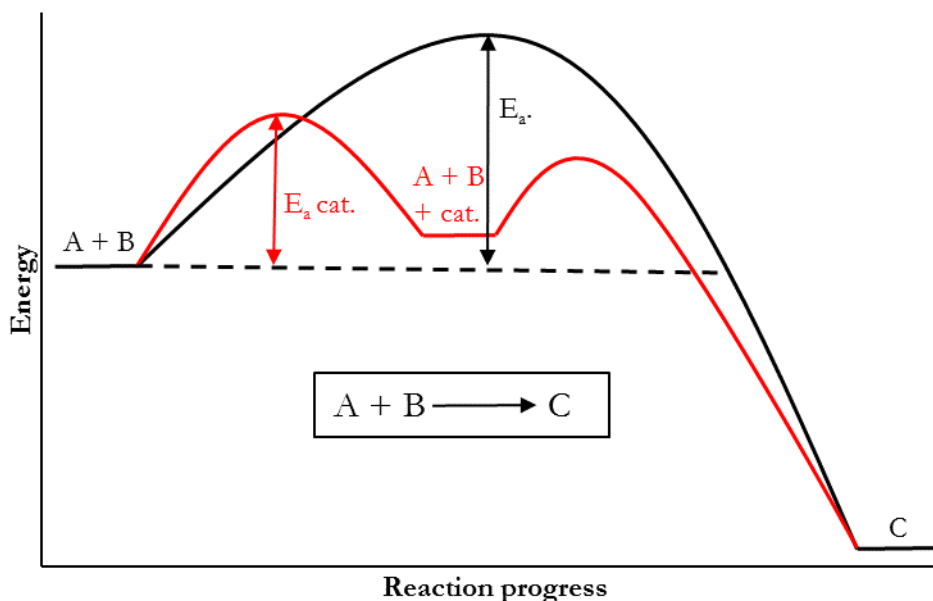


Figure 1.1. Example illustrating the effect of a catalyst on the reaction pathway. Black line: reaction without a catalyst; Red line: reaction with a catalyst (figure adapted from reference 1).

Catalysis is at the centre of modern day chemistry and chemical technology. Catalytic processes are utilised in energy processing, bulk and fine chemicals synthesis, and food production. It is estimated that over 90 % of commercially produced chemicals involve a catalytic step at some point in their synthesis. A catalytic step in a process can make it both cheaper and more environmentally conscious ².

1.2. Biomass valorisation

It is widely agreed that catalysis has to play a role in answering the world's challenging scientific questions. One of the major problems facing mankind at present is meeting an increasing energy demand. The growth of worldwide energy consumption has been stable for over 150 years and shows no signs of slowing down ³. In a world where traditional fossil fuel reserves are dwindling, costs are rising, and political and economic environments are unstable ⁴, development of efficient and renewable sources of energy to ensure self-sufficiency is of critical importance. One of the possible solutions in this regard is the utilization of biomass.

“Biomass” is the all-encompassing term for the organic material derived from plants, algae, trees, and crops. It includes land- and water-based plant material, and all organic waste streams. Fossil fuels are environmentally unsustainable due to their toxic emissions and contribution to the greenhouse effect through emission of excess CO_2 into the atmosphere ⁵. The burning of fossil fuels converts “old” biomass (plant matter transformed into coal or oil over the course of millions of years) into “new” CO_2 that is in excess of the cycle of photosynthesis and respiration. There is tremendous potential in biomass to

produce vast amounts of energy when converted into biofuels. Biofuels are classified into two types: first generation and second generation. First generation biofuels refer to fuels that have been produced from sources like starch, sugar, and vegetable oil, using established production routes⁶. Such biofuels generally compete with food sources. Second generation biofuels are distinguished from first generation biofuels in that they do not use food sources and aim to be net carbon neutral or even net carbon negative, meaning that the CO₂ emitted during the use of biofuel is less than the CO₂ removed from the atmosphere during cultivation of the plants that produce it⁷. Low value grasses, agricultural and forestry residues, and waste streams are the preferred biomass feedstocks from a techno- and socio-economic point of view, because these do not compete with food sources. Developing countries (where agriculture and crop growth are the primary industries) are ideally suited to site biomass plants, which would go a long way towards ensuring worldwide energy stability and security^{8,9}.

Biomass has three main components: cellulose, hemicellulose, and lignin. Cellulose, in contrast to hemicellulose and lignin, is crystalline in nature; the structures of hemicellulose and lignin vary by biomass type¹⁰. Cellulose is composed of hexoses (mainly glucose) and other heteropolymers, and is present in all plant cell walls along with hemicellulose¹¹. Cellulose and hemicellulose can be broken down into glucose and other saccharide molecules, both of which provide platform molecules for further upgradation¹². Hemicellulose is similar to cellulose in that it is comprised of several saccharide molecules, but unlike cellulose it has an amorphous structure and is the weakest of all biomass components because of its ability to degrade in acid, alkali, or even hot water¹³. Lignin is traditionally the most recalcitrant and difficult to deal with, producing a pyrolysis oil after treatment that is often resistant to any useful upgrading, though recent studies suggest that lignin can be utilised to greater effect if not subjected to technical processes such as the Kraft lignin process^{14,15}.

Utilisation of biomass has become a prominent research topic in modern chemistry. Conversion of biomass into useful products can be achieved by various methods. The choice of method is determined by the end application. The three main products derived from biomass are power/heat, transport fuels, and fine chemicals (or the precursors to fine chemicals).

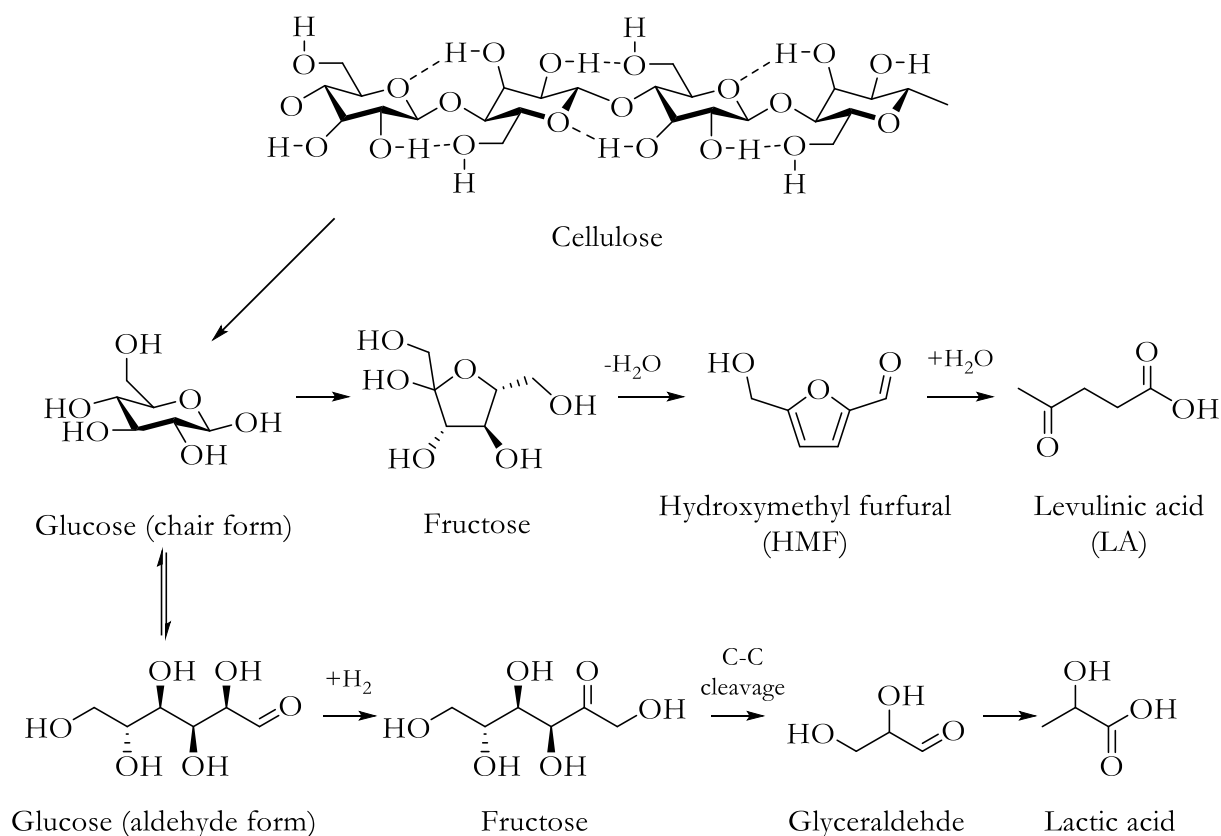
Pyrolysis of biomass to produce what is known as “bio-oil” or “bio-crude” is of increasing interest. This process involves the thermal decomposition of biomass in the absence of oxygen. In particular, moderate pyrolysis at *c.* 500 °C and short residence times has been shown to be optimal for the yield of up to 75 % liquid bio-oil that can be used in a variety of applications^{16,17}. Any form of biomass can be used for fast-pyrolysis, including trees and plants, agricultural waste, and forestry wastes.

1.3. Platform molecules from cellulose

The term “platform molecule” is generally agreed to refer to building block chemicals derived from biomass containing multiple functional groups that have the potential to be transformed into a number of useful molecules. Cellulose makes up 40–50 % of all lignocellulosic biomass, and is the most abundant non-edible biomass. Finding ways to effectively utilise it through conversion into useful chemicals is of vital importance. In addition to various other chemicals, lactic acid and levulinic acid are of primary importance and this thesis is devoted to the study of these two molecules.

Cellulose can be broken down into individual glucose molecules with a high yield using mineral acids such as H_2SO_4 or HCl as catalysts, but these are not ideal due to their corrosiveness, and the fact that they cannot be recycled^{18–20}. Mineral acids are inherently unselective and are able to catalyze the formation of subsequent products including polyols, alkyl glucosides, and organic acids^{18–20}. Hydroxymethyl furfural (HMF) can also be produced from cellulose degradation using mineral acids, which is an intermediate product in the synthesis of levulinic acid. Heterogeneous catalysts would be far more useful because they are reusable, can be tuned to be selective to the formation of particular products, and are more environmentally friendly than mineral acids. Cellulose breakdown has been reported by Fukuoka *et al.* using supported Pt and Ru catalysts under mild conditions in order to yield glucose and sugar alcohols, which are the precursors in the synthesis of lactic acid and levulinic acid^{21,22}.

The formation of both lactic acid and levulinic acid from cellulose requires that it be broken down into individual glucose molecules. The difference between the production of lactic acid and levulinic acid is that the aldehyde form of glucose is required for the production of lactic acid, whereas it is the chair form of glucose that is dehydrated into HMF which eventually forms levulinic acid. The two pathways are shown in Scheme 1.1.



Scheme 1.1. Schematic of cellulose conversion into lactic acid and levulinic acid (based on information presented in reference 23).

1.3.1. Conversion of cellulose into lactic acid

Lactic acid is one of the most ubiquitous hydroxycarboxylic acids in nature²⁴. It is found in most food products such as yoghurt, buttermilk, sourdough breads, and other fermented foods. Lactic acid is a vital metabolic intermediate in most living organisms, including humans. Advances in fermentation and separation technologies are increasingly making the fermentation of glucose more viable as a large scale lactic acid source. Though the main use of lactic acid is in the food industry (food additives and other food-related applications), there are other niche uses such as leather tanning, certain adhesives, textiles printing, and the development of commercial biopolymers such as polylactic acid (PLA). A wide variety of chemicals can also be produced from lactic acid, including acrylic acid, pyruvic acid, 2,3-pentanedione, 1,2-pentabediol, and lactate esters.

The conversion of cellulose into lactic acid involves the isomerisation of the aldehyde form of glucose into fructose followed by a C–C cleavage step in order to convert C₆ glucose into C₃ lactic acid. A homogeneous catalysis example of lactic acid production from cellulose used a lanthanide triflate catalyst that could be recycled and reused five times with no decline in catalytic activity²⁵. Wang *et al.* reported the use of a homogeneous Pb catalyst for the conversion of cellulose, glucose and fructose into

lactic acid²⁶. The Pb-based catalyst yielded an impressive 74 % lactic acid from cellulose, with fructose and HMF as minor by-products. Though the Pb could be recovered from solution, the large scale application of homogeneous Pb to water-based systems is undesirable from a health perspective.

The use of heterogeneous catalysts is preferred in industry due to the ease of separation. A Sn- β zeolite catalyst was first used for the conversion of cellulose into lactic acid by Holm *et al.*²⁷ They found that a 55 % yield of methyl lactate could be produced after a reaction of 16 h at 160 °C under 20 bar Ar. Dong *et al.*²⁸ revisited the Sn- β system and incorporated Zn into it, and found that a yield of 54 % lactic acid could be produced in 2 h – a much shorter time than Holm *et al.* under comparable conditions. Chambon *et al.* investigated the use of a variety of acid catalysts for the degradation of cellulose into lactic acid²⁹. Heteropoly acid (HPA) and HY-zeolite (which are predominantly Brønsted acidic) and tungstated ZrO₂ and tungstated Al₂O₃ (both Lewis acidic in nature) were applied as catalysts. The conversion of cellulose was similar for all catalysts tested (between 30–45 %, at 190 °C for 24 h), but the product distribution was reported to be different depending on the type of acid present – Brønsted acids were found to be more favourable for producing levulinic acid, whereas Lewis acids showed greater proportions of lactic acid.

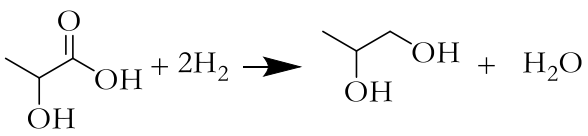
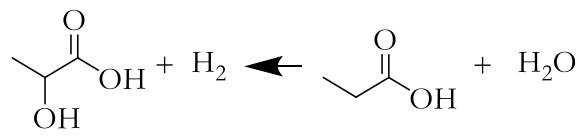
Lewis acids for the synthesis of lactic acid are well known in the literature, therefore recently the direction has turned to the investigation of redox catalysts. Perovskites are a good choice due to their superior thermochemical stability³⁰. Yang *et al.* have reported the use of LaCoO₃ perovskites for the catalytic conversion of cellulose³¹. A 24 % yield of lactic acid was produced from cellulose at 240 °C, while slightly higher yields of 40 % lactic acid were obtained when xylose and glucose were used as model substrates at 200 °C. The oxygen present in the catalyst was proposed to cause the oxidative decarboxylation of glucose units to eventually produce pyruvic acid, which was subsequently reduced to lactic acid. The catalyst was remarkably stable, with only a 5 % decline in lactic acid yield after 5 uses. The investigation of lactic acid production using perovskites is fledgling, but there is a lot of potential in this research area given that perovskites are largely unexplored for this purpose. There is a need for a larger body of research related with the conversion of cellulose into lactic acid using heterogeneous catalysts because the majority of the existing literature focusses on the optimisation of reaction conditions using mineral acids as catalysts.

1.3.1.1. Lactic acid hydrogenation to 1,2-propanediol

One of the most important products from the hydrogenation of lactic acid is 1,2-propanediol (PDO). PDO is an attractive commodity chemical used in de-icing fluids, antifreeze, cosmetics, and pharmaceuticals³². Traditionally, the production of PDO is achieved through the selective oxidation of propene³³. Propene oxide can be oxidised to propylene epoxide, followed by the opening of the three-membered ring of propylene epoxide to give PDO. The current synthetic processes of PDO are environmentally unfriendly due to the utilisation of fossil fuels, therefore, a greener alternative method is desirable.

Lactic acid and its esters are generally resistant to reactions with molecular hydrogen³⁴⁻³⁷. To produce PDO, the carbonyl group of lactic acid must be hydrogenated without removing the α -hydroxyl group. This can be difficult given that hydrogenation of the α -hydroxyl group to form propanoic acid is favoured thermodynamically³⁸. The equilibrium constants for the vapour-phase hydrogenation of lactic acid at 1 bar H₂ are provided in Table 1.1 (adapted from references 38 and 39). The values indicate that PDO formation would be favoured by lower temperatures, and it is suggested by Dumesic and co-workers that lower concentrations of lactic acid and higher H₂ pressure would also shift the equilibrium towards the production of PDO³⁹.

Table 1.1. Equilibrium constants for hydrogenation reactions of lactic acid^{38,39}.

Reactions	Equilibrium constant / K _p		
	150 °C	200 °C	250 °C
	5.00 × 10 ⁰	1.26 × 10 ⁰	4.00 × 10 ⁻¹
	1.01 × 10 ¹⁰	1.30 × 10 ¹⁰	1.61 × 10 ⁸

Broadbent *et al.* first demonstrated the hydrogenation of lactic acid to PDO in 1959 using a supported Re-black catalyst⁴⁰. An 80 % yield of PDO was obtained at 150 °C and 270 bar of H₂ pressure. Further, a perovskite supported Pt catalyst (Pt-BaZrO₂) combined with a homogenous co-catalyst (CeCl₂) was found to be active for the production of ethylene and propylene glycol from cellulose, which are products of lactic acid hydrogenation, with combined yields of 40 % achieved⁴¹. There were low yields of lactic acid and it is likely that the Pt catalyst caused the hydrogenation of some of the lactic acid formed. In current literature, Ru has been identified as the most active metal catalyst for lactic acid hydrogenation and has been dealt with in many recent studies⁴²⁻⁴⁸. Ru supported on carbon, Al₂O₃, and TiO₂ all exhibit

greater activity than non-noble metals such as Cu/Cr and Ni/Al₂O₃^{42,49}. Jang *et al.* reported that Ru/SiO₂ was more active for lactic acid hydrogenation compared with other metals such as Ni and Pt, producing a yield of 35 % PDO after 7 h at 120 °C and 80 bar H₂ compared with 30 % and 20 % conversion for Ni and Pt catalysts respectively⁵⁰. The same group also investigated Ru supported on different types of carbon supports⁵¹. The highest yield of PDO produced was above 90 % after 4 h, at 130 °C and 80 bar H₂. The data showed that higher support surface areas resulted in the formation of small Ru nanoparticles, higher dispersions, and consequently a greater catalytic activity. These data are in agreement with Primo *et al.* who confirmed that higher Ru dispersions on TiO₂ result in higher catalytic activity⁴⁹. Ru/TiO₂ was found to be bifunctional in terms of catalytic activity, with Ru dissociating the molecular hydrogen and the TiO₂ adsorbing the acid and activating the carbonyl group at the periphery of the nanoparticles at 150 °C⁴⁹. Yang *et al.* used a novel method of preparing Ru supported on carbon spheres (previously developed by Sun *et al.*⁵²) for ethyl lactate hydrogenation⁴⁷. They achieved a 95 % selectivity to PDO at 94 % conversion, and the catalyst was very stable, with conversion and selectivity decreasing to only 90 % after 6 reaction cycles. The surface groups of the carbon spheres were reported to prevent agglomeration of the Ru nanoparticles, and the minimal loss in catalytic activity was attributed to leaching of the Ru into the aqueous solution.

Promoters have been added to Ru catalysts in an attempt to further improve their catalytic activity. Luo *et al.* showed that the addition of 7 mol.% Sn to a Ru-B catalyst increased the conversion of ethyl lactate from 79 % to 91 %, with above 90 % selectivity to PDO⁴⁵. It is generally agreed that B and Sn are useful for activating carbonyl groups⁵³. Highly selective Ru-MoO_x catalysts supported on carbon and SiO₂ showed superior activity compared with Ru-only catalysts⁵⁴. A 54 % conversion of lactic acid and 95 % selectivity to PDO was obtained after 2 hours at 120 °C and 80 bar H₂ for Ru-MoO_x/C compared to 13 % conversion of lactic acid with the same selectivity to PDO for Ru/C on its own. In addition, Ru-MoO_x/C was more active than Ru-MoO_x/SiO₂, which converted 31 % lactic acid with 92 % selectivity to PDO. Based on previous studies⁵⁵, the role of MoO_x as a promoter was reported to produce a highly active hydride species from H₂, resulting in an enhanced rate of reaction. The benefits of adding MoO_x do not only extend to Ru-based catalysts. Li and co-workers have reported a Ir-MoO_x/SiO₂ (0.26 % MoO_x) catalyst that showed superior activity to its monometallic variant in lactic acid hydrogenation⁵⁶. A lactic acid conversion of 63 % and PDO selectivity of 44 % was obtained at 100 °C at 60 bar H₂.

Though Ru has been identified as being the best metal catalyst, base metal alternatives have also been investigated, which have the benefits of being cheaper and more abundant in nature. PDO yields have been reported to be as high as 80 % when Raney® Ni catalysts were used at a temperature of 250 °C under 20–30 bar of H₂⁵⁷. A Cu-SiO₂ catalyst gave a high conversion of lactic acid with a reasonable

selectivity towards PDO in the gas phase at atmospheric pressure³⁹. A study by Huang *et al.* investigated several non-precious metals supported on SiO₂ for ethyl lactate hydrogenation⁴⁸. Cu and Co catalysts were found to be highly active, both yielding over 97 % PDO, but Ni/SiO₂ achieved only 3.3 % conversion of ethyl lactate at 180 °C and 50 bar H₂. The activity of Co/SiO₂ was reported to be dependent on the percentage of bulk Co₃O₄ present, not Co dispersion. However, a later study suggests that preparation of these catalysts using different solvents can have an effect on the Co₃O₄ particle size and dispersion and shows that smaller particle sizes and increased dispersions translate into an improved activity for ethyl lactate hydrogenation⁵⁸. A Cu-hydroxysilicate catalyst has been shown to be active for lactic acid hydrogenation, giving 95 % conversion of lactic acid, with 65 % selectivity of PDO⁵⁹. The downside of this process was the relatively poor selectivity to PDO compared with other studies, and while the reaction was carried out at only 1 bar H₂, a high temperature of 200 °C was needed compared with the temperatures up to a maximum of 150 °C used in the examples discussed above. Recently, there has been an interesting development reported by Xiao *et al.* using CuO and Zn metal powder as a catalyst system for lactic acid hydrogenation using water as a hydrogen source⁶⁰. A 93 % yield of PDO was obtained after 2 h at 250 °C and autogenous pressure. The use of gaseous hydrogen under the same reaction conditions produced a 43 % yield of PDO. It was proposed that Zn produced *in situ* H₂ which was more efficient than externally added H₂. This is so far the only reported instance of *in situ* generated H₂ being used for lactic acid hydrogenation, however the hydrogenolysis of glycerol using *in situ* generated H₂ has been reported by Roy *et al.*⁶¹ The combination of a 5 wt.% Pt/Al₂O₃ as a glycerol reforming catalyst and a 5 wt.% Ru/C catalyst as a hydrogenolysis catalyst showed higher selectivity to PDO when H₂ was generated *in situ* vs. externally added H₂. It was suggested that external H₂ in excess was available to shift the reaction equilibrium to other pathways.

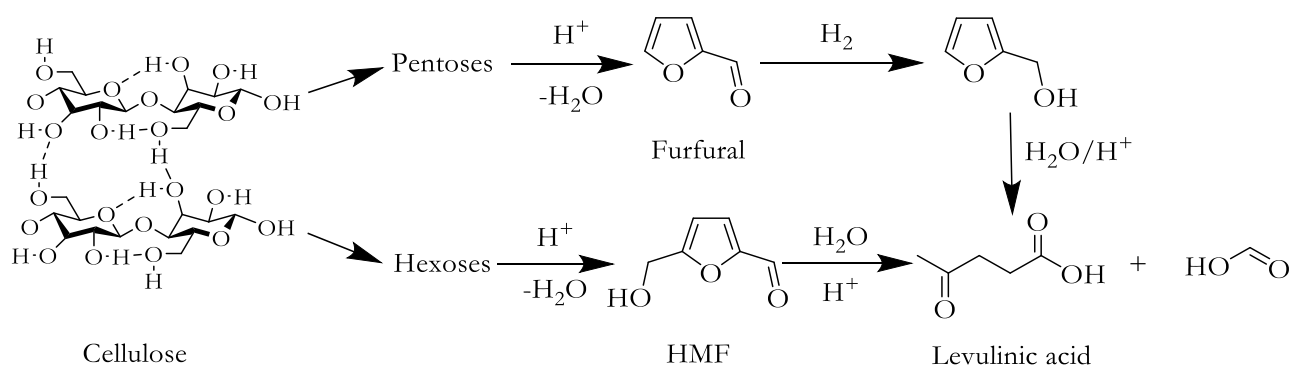
The reaction conditions usually employed for lactic acid hydrogenation – especially the high pressures required in cases where Ru is used – could be seen as prohibitive if upscaling to an industrial level. The literature focuses heavily on modification of the catalyst to activate lactic acid/lactate ester, and highlights the importance of a higher Ru dispersion and smaller particle size. What is lacking in the literature are novel preparation methods in order to achieve high Ru dispersion, and better characterisation of the role of the support, especially where carbon is used. Ru catalysts also tend to use at least 5 wt.% loadings of Ru; and while there have been reports of 1 wt.% Ru/C catalysts being employed for lactic acid hydrogenation⁶², more comparative data on the effect of lowering the metal content is required.

Alternative metal catalysts including Cu and Co are emerging as cheaper alternatives to Ru in lactic acid hydrogenation catalysts. However, use of base metal catalysts come with compromises. While in some of the cases discussed above, atmospheric H₂ pressure could be used (which is a considerable

reduction in pressure from Ru systems that require at least 30 bar H_2) in all cases, the reaction temperature had to be increased to at least 200 °C. While the use of NCM catalysts is attractive from a materials cost point of view, it may not necessarily offset the operating costs of higher heat input if such a catalyst was to be used on an industrial scale *vs.* a Ru catalyst. The challenge in using NCM catalysts lies in activating them so that they are active at lower temperatures. The idea of replacing Ru with cheaper and more abundant materials is fairly recent, therefore there have been no studies reported thus far on modifying the preparation of NCM catalysts to make them active for lactic acid hydrogenation. In Chapter 3, the hydrogenation of lactic acid using Ru/C has been studied, with a particular emphasis on catalyst preparation and reusability.

1.3.2. Conversion of cellulose into levulinic acid

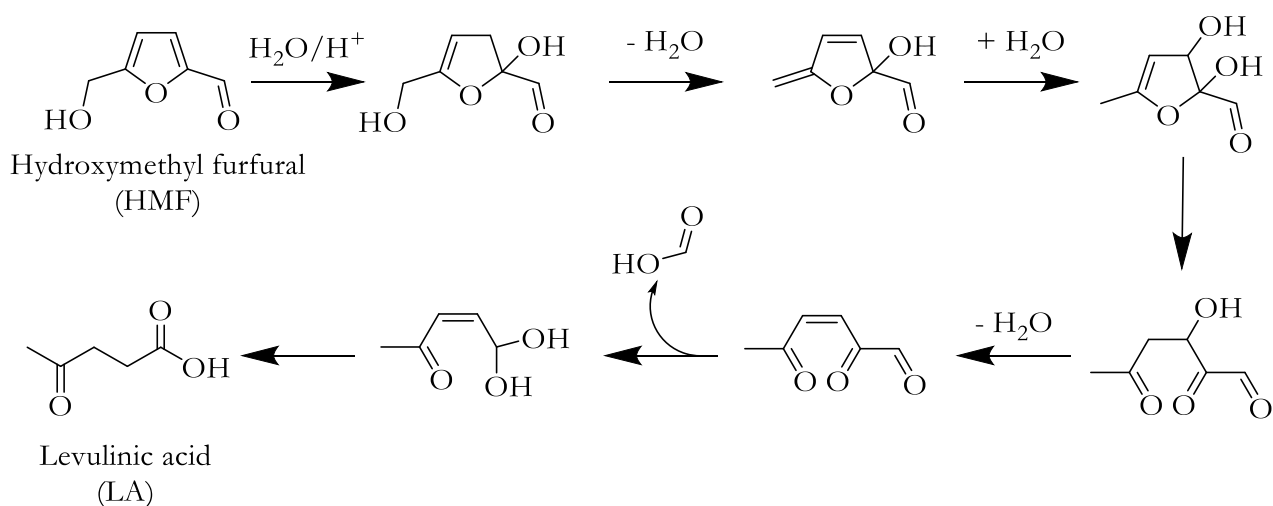
Levulinic acid (LA), also known as 4-oxopentanoic acid, is a low molecular weight carboxylic acid containing a carbonyl group. LA is considered one of the most important platform molecules for producing chemicals and fuels⁶³ and is the main substrate investigated throughout this thesis. While LA itself finds uses as a solvent, in food, in the fragrance industry, and in the textiles industry to name but a few examples, the research community has become increasingly interested in it due to its potential to be upgraded^{32,64} into levulinic esters⁶⁵⁻⁶⁹, angelica lactone³², and γ -valerolactone (GVL)^{32,64}. LA is usually obtained from cellulose *via* furfural or hydroxymethyl furfural (HMF) as shown in Scheme 1.2.



Scheme 1.2. Schematic of the production of LA from lignocellulose.

The very first reported incidence of LA production was in 1840 by Mulder, who used mineral acids as catalysts to produce LA from glucose at high temperatures⁷⁰. Mineral acids as homogeneous catalysts are a popular choice for LA production owing to the high yields of LA that can be produced in relatively shorter timeframes. Mascal *et al.* reported a yield of 90 % LA from sucrose, utilising HCl as a catalyst in the presence of dimethyl chloride⁷¹. Dimethyl chloride was used in order to produce (chloromethyl)furfural during the process, which is desirable because it is hydrophobic and easily isolated from the reaction solution in high yields^{72,73}. While this was indeed a positive result the use of chlorinated

solvents is not desirable from an environmental perspective. Takeuchi *et al.* reported a 55 % yield of LA from the dehydration of glucose using HCl at pH 1.5 in just 5 minutes⁷⁴. They also showed the dependence of acid strength on the formation of LA from HMF, with the yield increasing in step with increasing acidic strength at an order of $\text{H}_3\text{PO}_4 < \text{H}_2\text{SO}_4 < \text{HCl}$. Industrially, a multistep process requiring strong acids such as H_2SO_4 or HCl at 100 °C is employed³². Acid treatment causes the hydrolysis of polysaccharides such as cellulose and hemicellulose into monosaccharides. The resulting acidic solution is boiled for 20–48 h. Hexose sugars produced from cellulose are dehydrated to produce HMF, which is subsequently hydrated along the C₂–C₃ bond of the furan ring to cause ring opening and produce LA and one equivalent of formic acid, according to the mechanism reported by Horvat *et al.*⁷⁵ (Scheme 1.3). Acid treatments are the most widely employed processes in open literature, with most of the studies focussing on the optimisation of reaction conditions.



Scheme 1.3. Mechanism of LA formation from HMF (adapted from Horvat *et al.*⁷⁵).

BioMetics Inc. patented the Biorefine Process for the production of LA specifically from waste streams and agricultural residues at industrial scale^{76,77}. This is a continuous process where the carbohydrate containing material is fed into a reactor to undergo hydrolysis at 175 °C under 31 bar pressure in the presence of 2–5 wt.% H_2SO_4 . The HMF is continuously removed and transferred to a second reactor where it undergoes heat treatment at 193 °C under 15 bar pressure. Around 70–80 % of the theoretical yield of LA can be obtained, corresponding to 50 % mass yield on the basis of C₆-sugars. The rest of the mass balance is made up of the formic acid by-product (20 %) and water-insoluble polymers known as humins (30 %)⁶⁴.

Ionic liquids are gaining traction as efficient systems for cellulose decomposition into HMF and LA. It has been demonstrated that Brønsted acid ionic liquids can be used for the decomposition of cellulose into glucose units at low temperature (70 °C)⁷⁸. Brandt *et al.* have shown that the concentration of acid in ionic liquids is important for the production of HMF and LA⁷⁹. Ren *et al.* recently reported the

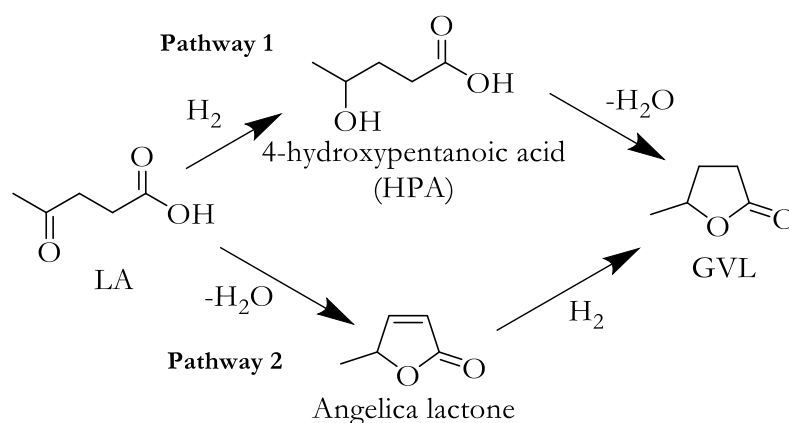
use of ionic liquids for cellulose decomposition with up to 86 % yield of LA in 5 h at 170 °C⁸⁰. Though ionic liquids are considered to be environmentally friendly, there are significant technological and environmental challenges associated with the use of ionic liquids on large scales at present, thus more research is required in this area^{81,82}.

Heterogeneous catalysts for LA production would be preferable from an environmental standpoint and to mitigate the risks of dealing with strong, concentrated mineral acids at an industrial scale. Schraufnagel *et al.* reported the use of ion-exchange resins for the production of HMF and LA⁸³. This catalyst had several advantages, including shape selectivity and good reusability, and the process could take place at a moderate temperature (100 °C), but the reaction rate was low, thus long reaction times were required to produce moderate yields of LA. It is no surprise that zeolites, with their acidic properties^{84–86}, and other solid acid catalysts are beginning to supplant ion exchange resins as catalysts for LA production from biomass. Huber and co-workers proposed a two-step process for the conversion of cellulose to LA⁸⁷. Cellulose was first decomposed into glucose at high temperatures (190–270 °C), then converted into HMF/LA using a solid catalyst (zirconium phosphate) under milder conditions (160 °C) and resulted in a 28 % yield of LA. Though the yield was not particularly high, the advantage of the process was that unreacted cellulose could be recycled, and the production of water insoluble humins was low. Ramli *et al.* have recently reported the use of a 10 wt.% Fe/HY-zeolite catalyst yielding 62 % LA from glucose at 180 °C in 180 minutes⁸⁸. The modification of the HY-zeolite with Fe was found to increase the total number of acid sites and increased the ratio of Lewis/Brønsted acid sites, indicating that Lewis acidity is an important consideration for this reaction. HMF dehydration was reported to take place in the zeolite pores, thus increasing the porosity was a requirement for better catalytic activity. The catalyst was remarkably stable, showing only a 15 % decline in LA yield over five successive reuse cycles⁸⁹. Dumesic and co-workers showed that H-ZSM-5 was active for producing LA from furfuryl alcohol, with yields >70 % at 120 °C⁹⁰. The pore dimensions of the zeolite were found to be optimal for the reaction to take place. There were issues with stability however, with the catalytic activity halving after one reaction due to build-up of a polymer species. The advantage of zeolites is that they have high thermal stability, so a calcination step regenerated the catalyst resulting in the catalytic activity seen originally, though a further reaction showed the same trend of catalytic deactivation. Guzmán *et al.* confirmed the importance of acidity and porosity in their recent work, which showed a ZSM-5 zeolite active for producing a 77 % yield of LA from furfuryl alcohol at 140 °C under 20 bar H₂⁹¹. The high yield was attributed to the use of 2-butanone as a solvent and the use of gaseous H₂ suppressing the formation of furanic resins (i.e. humins). Though catalyst reuse was not investigated in this study, the suppression of polymers formed should go some way to addressing the stability issue observed by Dumesic and co-workers without needing to regenerate the catalyst by calcination after a single use.

Research into the use of heterogeneous catalysts for cellulose conversion into LA is promising, but still in its infancy. Zeolites have been identified as being active due to their acidic properties and optimal pore sizes, but more research is needed in order to achieve higher yields of LA (>80 %), address issues with catalytic stability, and suppress reactions that compete with LA production – especially formation of humins.

1.3.2.1. Levulinic acid hydrogenation to γ -valerolactone

Hydrogenation of LA to γ -valerolactone (GVL) is an increasingly active area of research at present due to the potential of GVL to be used as a biofuel, and for the subsequent transformation of GVL into hydrocarbon fuels^{92,93} and other useful compounds such as 2-MTHF^{94–96}. The mechanism of LA hydrogenation to GVL has been proposed to take one of the two pathways presented in Scheme 1.4. Pathway 1 shows the hydrogenation of the ketone group of LA to form 4-hydroxypentanoic acid (HPA), which undergoes rapid intramolecular ring closure (esterification) to form GVL, which is the thermodynamically favoured pathway. The alternative, pathway 2, is the dehydration of LA to angelica lactone, followed by the rapid addition of H₂ across the double bond to make GVL. There has been debate in the literature about the dominance of pathway 1 or 2, and there has been no concrete evidence presented as to the relative contribution of each pathway, but Bond and co-workers have suggested that pathway 1 *via* HPA appears to dominate kinetically at lower temperatures⁹⁷. H¹-NMR also appears to suggest the pathway proceeds through HPA⁹⁸. A recent study by Piskun *et al.*⁹⁹ shows the presence of HPA during the hydrogenation reaction and not angelica lactone, which would also suggest the dominance of pathway 1. However, there is no absolute consensus, with recent studies claiming that the reaction proceeds *via* pathway 2^{100,101}.



Scheme 1.4. Mechanistic pathways of LA hydrogenation to GVL. (1) hydrogenation followed by dehydration; (2) dehydration followed by hydrogenation.

The hydrogenation of LA to GVL has been reported using both homogeneous and heterogeneous catalysts. Ru^{94,102,103} and Ir^{104,105} complexes are the generally employed homogeneous catalysts¹⁰⁶, but any of Re, Ru, Pd, and Pt have been the generally explored precious metal heterogeneous catalysts. Re catalysts did not show satisfactory GVL yields even at high temperatures and pressures¹⁰⁷, and while Pt and Pd tend to be highly active for LA conversion, GVL yields were low, instead favouring up to 70 % of by-product α -angelica lactone^{108,109}. Au-Pt random alloy catalysts supported on TiO₂ prepared by a modified impregnation method were found to be active species for GVL production from LA, with almost 100 % yield of GVL produced after 5 h¹¹⁰. Li *et al.* reported the use of a Rh/SiO₂ catalyst for LA hydrogenation which yielded 77 % GVL at only 80 °C¹¹¹. They also showed that modifying the Rh/SiO₂ catalyst with MoO_x increased the hydrogenation activity of the catalyst by promoting the hydrogenation of the carbonyl group of GVL thereby producing 1,4-pentanediol at the same temperature.

Ru based systems have repeatedly been demonstrated to be superior metal catalysts for LA hydrogenation. Colloidal Ru nanoparticles alone are able to catalyse the transformation, either using an external hydrogen source or formic acid (transfer hydrogenation)¹¹². However, owing to the difficulties in separation and reusability of colloids, heterogeneous systems are generally preferred.

Luo *et al.* showed that 1 wt.% Ru/TiO₂ catalysts were highly active for LA hydrogenation, producing a 97.5 % yield of GVL from LA at 200 °C and 40 bar H₂ after a reaction time of 10 h¹¹³. The work of Al-Shaal *et al.*¹¹⁴ showed that the type of TiO₂ support was important, with Ru supported on TiO₂(P25) resulting in superior activity (81 % conversion of LA, 88 % selectivity to GVL) to a pure rutile phase TiO₂, which was completely inactive for LA conversion. The activity of Ru supported on TiO₂(P25) was attributed to facile adsorption of LA compared with rutile TiO₂. Ruppert *et al.* carried out a more in-depth study of the effect of TiO₂ phase¹¹⁵. Ru supported on TiO₂(R20) comprised of 20 % rutile phase and 80 % anatase phase was found to be the most active catalyst, giving LA conversion of 99 % with GVL selectivity of 95 %. Ru supported on pure anatase TiO₂ was completely inactive for the reaction. These results were linked to the electronic properties of the support and a high Ru dispersion on Ru/TiO₂(R20). Recently, it has been shown by Ftouni *et al.* that ZrO₂ is a superior catalyst support for Ru compared with TiO₂ in terms of catalyst stability for LA hydrogenation¹¹⁶. The GVL yield from the TiO₂ supported Ru decreased from 96 % to 65 % after 5 reaction cycles due to a decrease in BET surface area and pore size of the support but ZrO₂ supported Ru retained a GVL yield of 98 % for 4 reaction cycles, with a decrease to 89 % observed after the fifth reaction cycle.

The literature listed above shows that Ru catalysts are popular. Carbon is an attractive support because of its high surface area and tuneable porosity¹¹⁷⁻¹²⁰. Up to 90 % conversion, with complete selectivity to GVL has been achieved in aqueous solution at 130 °C and 12 bar H₂ using a 5 wt.% Ru/C

catalyst¹²¹. Addition of solid acids to the reaction has also been shown to enhance the catalytic activity under mild reaction conditions. A system comprising a 5 wt.% Ru/C catalyst and Amberlyst 70 achieved 98 % GVL yield at 70 °C and 5 bar H₂ after 3 hours of reaction¹²². Piskun *et al.* carried out a study using millimetre sized Ru/C pellets preferred by industry to use to avoid excessive pressure drop in continuous flow systems⁹⁹. Due to the size of catalyst particles, they found the activity was strongly affected by mass transport, but they obtained high yields of GVL up to 95 %. A decrease in catalytic activity was observed after longer reaction times (90 % LA conversion after 0.5 h compared with 80 % after 6 h at 150 °C and 45 bar H₂), which was attributed to a decrease in surface area (probably due to coking) and Ru particle sintering. Ru leaching was reported to be minimal and of little consequence. Ruppert *et al.* used a Ru/C catalyst for the hydrogenation of LA using H₂ produced *in situ* from the decomposition of formic acid¹²³. A GVL yield of 57 % at LA conversion of 81 % was obtained after 5 h of reaction at 190 °C. A reaction using 25 bar H₂ yielded 82 % GVL after just 30 minutes at 190 °C, but the use of formic acid as a H₂ source is desirable because it obviates the need for high external H₂ pressures.

Bimetallic catalysts incorporating Ru are also known. Weckhuysen and co-workers showed that the addition of Pd to Ru catalysts diluted and isolated the active sites, resulting in a high yield of GVL and good catalyst stability on reuse related with the prevention of sintering¹¹⁰. The catalyst stability on reuse had also been reported with a bimetallic RuSn/C catalyst by Wettstein *et al.*¹²⁴ which is more cost effective compared with Pd/Ru catalyst system. Luqueb and co-workers studied monometallic Ru and bimetallic Ni-Ru catalysts supported on ZrO₂ and Al₂O₃ for the solvent-free hydrogenation of LA to GVL using formic acid as a H₂ source¹²⁵. Ru/Al₂O₃ was found to be superior to Ru/ZrO₂ (GVL yield of 50 % *vs.* 30 % respectively) because of the higher acidity, specific surface area, and pore volume of the support. However, Ru/Al₂O₃ activity decreased drastically on reuse due to pore blocking, whereas the activity of Ru/ZrO₂ was consistent after 4 uses. Ni-Ru/Al₂O₃ gave a higher yield of GVL compared with Ru/Al₂O₃ (71 % *vs.* 30 % respectively) due to a larger amount of Ru(0) species present on the surface as determined by XPS.

While optimisation of reaction conditions has been covered in the open literature utilising commercially available Ru/C catalysts^{97,99,108,122}, the optimisation of catalyst preparation and design of catalysts on a per system basis appears to be in its infancy. Pérez-Ramírez and co-workers have recently reported the preparation of hydroxymethyl-dimethyl ammonium dihydrogen phosphate (HHDMA) stabilised Ru nanoparticles supported on TiSi₂O₆ that are highly active for LA hydrogenation¹²⁶. At reaction conditions of 130 °C and 10 bar H₂, the HHDMA catalyst was 4 times more active than a state of the art commercial Ru/C catalyst and active after 15 h on stream. Density functional theory revealed that the reason for this increase in activity was due to an increase in the local pH at the metal/stabiliser/water interface. This increase in local pH also disallowed the formation of RuO_x, thereby

mitigating deactivation. Wu *et al.* have used Ru supported on graphene for the hydrogenation of LA, with activity achieved at room temperature, and full conversion of LA into GVL at 80 °C¹²⁷. Li and co-workers showed that Ru supported on reduced graphene oxide (Ru/RGO) was a highly active catalyst for LA hydrogenation, fully converting LA into GVL at just 40 °C in 2 h at 40 bar H₂¹²⁸. Stability tests showed that the catalyst did not lose activity after 4 uses. 100 % yield of GVL was also obtained after 5 h at 30 °C and after 8 h at 20 °C. Most impressively, the catalyst achieved a yield of 70.6 % GVL after a reaction time of 12 h at -10 °C, which is the highest yield of GVL reported at sub-zero temperatures. This incredible activity was ascribed to the transfer of electrons from RGO to Ru, thereby activating it for the hydrogenation of C=O bonds. Xiao *et al.* have reported 2 wt.% Ru supported on few layer graphene (FLG) as an active and stable catalyst¹²⁹. Full conversion of LA and 100 % selectivity for GVL was achieved after 8 h at room temperature (20 °C) and 4 bar H₂, and was maintained for 5 reaction cycles. Upare *et al.* have also reported graphene oxide supported Ru giving a 92 % yield of GVL from LA at 265 °C and 25 bar H₂⁹⁶. A recent study from the group of Ren and co-workers¹³⁰ has revealed a unique and novel synthesis of extremely high surface area Ru supported on carbon nanofibers (>1000 m² g⁻¹). These catalysts were found to be 18 times more active (in terms of turnover frequency) than the leading commercial Ru/C catalyst for LA hydrogenation. These works suggest that the need for new novel syntheses has been recognised.

For a process to become truly sustainable, the substrates must be renewable and the catalyst(s) must be inexpensive and abundant in nature. Cu is one of the most abundant elements that is active for hydrogenation reactions making it a desirable replacement for Ru-based catalysts. Cu-based catalysts such as CuO/ZnO, Cu/ZnO/ZrO₂, and CuO/ZnO/Al₂O₃ are prevalent in the literature as catalysts for the MeOH synthesis reaction^{131–134}. These catalysts have a track record of activation of hydrogen for hydrogenation reactions, therefore, it is no surprise that they have started to find increasing use in the hydrogenation reactions dealing with biomass valorisation. There have been reports of Cu being used as an alternative to Ru for LA hydrogenation^{100,135}. Zhu *et al.* have suggested that Cu-based catalysts are preferred over other cheaper metals (such as Ni) due to their preference for C–O bond cleavage as opposed to C–C bond cleavage in organic molecules¹³⁶. An early example of Cu for LA hydrogenation was reported by Christian *et al.* who produced >70 % 1,4-pentanediol from LA at 273 °C and 100 bar H₂¹³⁷. Cu-Cr catalysts have been reported by Yan *et al.* for LA hydrogenation, alongside a Cr-free Cu-Fe catalyst^{138,139}. Though these catalysts have been shown to be active, the use of Cr is not desirable from health or environmental perspectives, and alternative metal catalysts need to be investigated.

ZrO₂ is commonly used as a catalyst support due to its mechanical strength and high thermal stability^{131–133,140,141}. ZrO₂ itself is known to be a hydrogenation catalyst on its own^{142–144}. Chia and Dumesic have shown that ZrO₂ can catalyse LA and its esters to GVL with a hydrogen donating alcohol

solvent through the Meerwein-Ponndorf-Verley (MPV) reaction¹⁴⁴. Enumula *et al.* have also demonstrated that SBA-15 supported ZrO₂ is an active catalyst for catalytic transfer hydrogenation (CTH)¹⁴⁵. However, there are no reports of ZrO₂ alone catalysing the reaction using external gaseous H₂ and for this reaction generally ZrO₂ supported metal catalysts are used.

It is also well established that ZrO₂ undergoes modification during co-precipitation with another metal such as Cu, due to the generally large amount of metal used during the co-precipitation procedure^{146–148}. The result is that Cu is incorporated into the ZrO₂ matrix and also dispersed across the surface of ZrO₂. Samson *et al.* reported that Cu incorporated into ZrO₂ increased the Lewis and Brønsted acidity of the material¹⁴⁸. It was determined by XPS analysis that Cu was present not only as Cu(0) but also as Cu(I) and as a hydroxide. The metallic Cu clusters and Cu(I) stabilised in the oxygen vacancy of ZrO₂ gave rise to the Lewis acidity, while the OH groups associated with the Cu(I) were responsible for the Brønsted acidity. The concentration of Lewis acid sites was several times higher than the concentration of Brønsted acid sites and the activity of the catalyst for MeOH synthesis from CO₂ was attributed to the Lewis acidity of the catalyst.

Cu-ZrO₂ catalysts prepared by oxalate gel precipitation have been reported by Fan and co-workers^{149–152}. Hengne and Rode have reported Cu-ZrO₂ and Cu-Al₂O₃ composite catalysts that were active for liquid phase LA hydrogenation and CTH of methyl levulinate to GVL using both water and methanol as solvents¹⁴⁶. Complete conversion of LA was achieved with >90 % selectivity to GVL in 5 hours at 200 °C using 35 bar H₂. Characterisation of these catalysts was not particularly forthcoming, and insufficient to derive the reason for the catalytic activity. A report by Yuan *et al.* showed Cu-ZrO₂ catalysts prepared by oxalate gel precipitation, which utilises oxalic acid as a precipitant¹⁴⁷. They demonstrated that a 20 wt.% Cu/ZrO₂ prepared by this method could be used to catalyse the hydrogenation of LA to GVL using formic acid as a source of hydrogen, with a 100 % yield of GVL achieved after 6 hours of reaction. This preparation method has since been widely applied for Cu based catalysts, both in low temperature MeOH–steam reforming¹⁵², and in LA hydrogenation to GVL¹⁵³ (using an external hydrogen source in contrast to the previous referenced work by Yuan *et al.*¹⁴⁷), and GVL conversion to value added products such as 1,4-pentanediol and 2-MTHF¹⁵⁴. The advantages of using oxalate gel over conventional co-precipitation method is that catalysts are generally prepared with higher metal dispersions and BET surface areas, and larger pore sizes, which tends to translate into higher activity¹⁵¹. Oxalate gel precipitation, while simple, can be sensitive to factors such as the solvent used. Deng and co-workers showed that the choice of solvent used during oxalate gel precipitation can influence on the catalyst activity¹⁵⁰. It was found that the solvent with a low surface tension and high viscosity caused the formation of an amorphous precursor structure that produced ultra-fine Cu/ZnO/ZrO₂ catalysts upon calcination that were highly active for MeOH synthesis. Recently there has been a report from Balla *et al.*

who found that 5 wt.% Cu/ZrO₂ is an active catalyst in the vapour phase hydrogenation of LA, with a conversion of 81 % LA and 83 % selectivity of GVL¹⁰⁰, with angelica lactone and pentanoic acid produced as the major by-products. These catalysts were stable for a period of 24 h, after which the conversion declined drastically, with only 25 % LA conversion achieved after 50 h. The decline was attributed to coking of the catalyst surface and a decrease in active sites due to sintering. The same study also investigated other supports including SiO₂, TiO₂, and Al₂O₃. All of these catalysts except Cu/Al₂O₃ performed worse than Cu/ZrO₂. Cu/Al₂O₃ was found to achieve 98 % LA conversion and 87 % selectivity of GVL *vs.* Cu/ZrO₂ (68 % LA conversion, 69 % GVL selectivity) due to the superior BET and Cu metal surface area of Cu/Al₂O₃. Though it would seem Al₂O₃ is the best support, a study by Hengne and Rode indicated that leaching of Cu was a problem when supported on Al₂O₃, which was a problem for catalyst reusability¹⁴⁶.

Ni is considered as the next metal in the series of cheap and abundant metal catalyst systems known to catalyse the formation of GVL from LA. Ni supported on γ -Al₂O₃ has been shown by Hengst *et al.* to produce GVL with 100 % selectivity in aqueous conditions¹⁵⁵. The same work also showed high yields of GVL under solvent free conditions. However, the catalyst stability was found to be an issue in this study. Characterisation of the spent catalyst did not reveal any changes to the catalyst structure that could explain the decrease in activity, and ICP-OES (optical emission spectroscopy) analysis showed there was no leaching of Ni from the catalyst. Washing of the catalyst and re-calcination and reduction caused the catalyst to regain a small measure of its activity, which indicates coking might have been the cause of deactivation. Rao and co-workers reported 30 wt.% Ni/SiO₂ as an active catalyst that showed full conversion of LA with 85–90 % selectivity to GVL and was stable over a period of 25 h¹⁵⁶. Further SiO₂ was compared with other supports including Al₂O₃, ZrO₂, TiO₂, ZnO, and MgO. Ni/Al₂O₃ showed comparable conversions of LA, whereas Ni/TiO₂, Ni/ZnO, and Ni/MgO performed poorly due to lower Ni dispersion on the surface and low acidity. The Ni-ZrO₂ catalyst also performed poorly. Although the Ni-ZrO₂ catalyst was shown to have high acidity (important for the dehydration step of the mechanism), the catalytic activity was hindered by a large Ni particle size and low Ni dispersion. Mohan *et al.* showed a 30 wt.% Ni/H-ZSM-5 catalyst that produced high yields of GVL (90 %) ¹⁰¹. The activity was attributed to its high acidity and high dispersion of Ni (the same characteristics present in the active Ni/SiO₂ catalyst reported by Rao and co-workers above¹⁵⁶). Stability was an issue in this case, with GVL yield decreasing to 65 % after just 5 h, possibly as a result of water generated during the reaction. Varkolu *et al.* reported Ni supported on Al₂O₃, MgO, and hydrotalcite that exhibited the same deactivation because of the water generated during the reaction¹⁵⁷. MgO and hydrotalcite supports showed a drastic decline in activity due to phase changes caused by interaction with water. Al₂O₃ was also affected by the water, though to a lesser extent. Shimizu *et al.* showed that Ni can be modified with MoO_x for an improvement

in hydrogenation activity¹⁵⁸. The authors claim that the TON of the Ni-MoO_x/C catalyst is comparable to a state of the art Ru based catalyst, however a high temperature of 250 °C is required and there is no mention of stability. This is common theme in the literature regarding Ni-based catalysts. There needs to be more research dedicated to the long term stability of the catalysts, especially in the presence of water, and to making them active at lower temperatures.

It may be possible to combine Cu and Ni in the same catalyst to improve activity. Ni can be added to a Cu-SiO₂ system to alleviate the stability problems suffered by the Cu-SiO₂, as reported by Upare *et al* where a 96 % yield of GVL was achieved at 265 °C and 25 bar of H₂¹⁵⁹. This catalyst was also used to hydrogenate LA using formic acid as a H₂ source, and was stable after 100 h on stream¹⁶⁰. Arias and co-workers investigated the effect of Ni-Cu catalysts supported on Al₂O₃ for LA hydrogenation to 2-MTHF, which occurs *via* GVL as an intermediate¹⁶¹. Ni-Al₂O₃ was found to be the most active catalyst, and Cu-Al₂O₃ was the most selective to MTHF. An optimum combination of the two metals resulted in a yield of 56 % 2-MTHF in 5 h at 250 °C, which is the highest yield achieved by a non-noble metal catalyst so far. The authors concluded that there was a synergistic effect between mixed Ni-Cu particles that was responsible for the improved yield of 2-MTHF.

Although there are few examples as yet of these catalysts being used for LA hydrogenation, the combination of Ni and Cu is well documented for other reactions. Miranda *et al.* have reported the use of Ni-Cu/ γ -Al₂O₃ catalysts for glycerol hydrogenation¹⁶². The characterisation of the materials revealed that there were both electronic and geometric interactions between the two metals. Addition of Cu to Ni caused a decrease in the reduction temperature of NiO (a phenomenon also observed by Arias and co-workers¹⁶¹) suggesting an electronic interaction, which was confirmed by XANES results. XPS suggested an enrichment of Cu at the surface where the Cu-content of the catalyst was found to be high. This led to a geometric effect observed by CO adsorption FTIR, which showed that CO bridged between adjacent Ni atoms decreased with increasing content of Cu. In cases where Ni acted as the primary active site, the Cu enrichment was detrimental to catalytic activity. The interaction between Ni and Cu was investigated in more detail by Naghash *et al.* who found that the solid solutions formed between the two metals is highly sensitive to both the Cu content and the reduction temperature used during catalyst synthesis¹⁶³. The effect has been reported for Ni-Cu nanoparticles supported on graphene for dimethyl carbonate synthesis from MeOH and CO₂¹⁶⁴; Ni-Cu/C and Ni-Cu/Al₂O₃ catalysts for the reverse water-gas-shift reaction¹⁶⁵; and CO hydrogenation to methanol¹⁶⁶. In each case it has been reported that while only a fraction of the metals deposited are present as part of an alloy/solid solution, the presence of those alloys/solid solutions has had a beneficial effect on the catalytic activity. There needs to be more research devoted to the use of these types of catalyst for LA hydrogenation to GVL, as well as investigations into their stability.

One common feature of the non-noble metal catalysts discussed above (Cu, Ni, and Cu-Ni) is their dependence on their metal surface area and total surface area. It is therefore important to consider synthesis techniques that maximise surface area. Because a high surface area support can lead to highly dispersed metal on the surface, there is a particular need for studies regarding the support. Popular supports like ZrO₂ discussed previously generally have a low surface area (<60 m² g⁻¹). Chuah *et al.* have reported the use of ion addition (Na⁺, K⁺, and NH₄⁺) to increase the surface area of ZrO₂¹⁴⁰, which was particularly effective when Na⁺ ions was used. Addition of the ions caused a small distortion of the lattice resulting in a higher degree of atomic ordering, thus producing a material with high surface areas of 214–263 m² g⁻¹. Águila *et al.*¹⁶⁷ and Rezaei *et al.*¹⁴¹ have both reported reflux syntheses that use ammonia to form high surface area ZrO₂. This approach is said to decrease the crystalline character of the ZrO₂, producing amorphous forms of ZrO₂ that tend to have higher surface areas than the more crystalline tetragonal-(t)- and monoclinic-(m)-ZrO₂ polymorphs¹³¹. These types of approaches now need to find their way into the synthesis of the catalyst used for LA hydrogenation.

The potential of LA as a platform chemical cannot be overstated. There has been an exponential increase into the number of research publications centred on LA in the hopes of making useful chemicals and fuel additives. LA hydrogenation to GVL has been extensively researched. Ru-based catalysts have been found to be the most active for LA hydrogenation, but mostly efforts have focussed on the optimisation of reaction conditions. What is required now is a greater emphasis on catalyst synthesis tailored to maximise the features that result in an improved catalytic activity, and making these catalysts suitable for industrial deployment. Non-noble metals (predominantly Cu- and Ni-based catalysts) have been shown to be active for LA to GVL, but in all instances their use requires high temperatures and pressures. Stability has also been shown to be an issue. There should now be emphasis on finding ways to make these non-noble metals more active under mild conditions so that they are a viable competitor to expensive Ru catalysts. The issues with stability also need to be addressed in order to make them industrially viable. Once again, this will involve catalyst design specific to the reaction, rather than fitting the reaction to known catalysts.

1.4. Aims and objectives

The work presented in this thesis is part of a larger project called NOVACAM (Novel and Cheap Abundant Materials)¹⁶⁸. The aim of the project is to harness the underutilised potential of lignocellulosic biomass by designing catalysts that incorporate cheap and abundant materials, thus lowering the cost of biomass conversion. One of the main themes of the project is the valorisation of cellulose to produce GVL. Cellulose conversion is a long, complicated reaction and requires optimization of the intermediates. LA is one of the most important intermediates synthesized from HMF dehydration, which itself is

generated from dehydration of sugar molecules. Conversion of LA to GVL was the main focus of the current study. The aims and objectives of the thesis are as follows:

- Investigate the use of Ru/C catalysts for the hydrogenation of lactic acid – a model compound for levulinic acid.
- Investigate the use of Ru/C catalysts for the hydrogenation of LA to GVL as a benchmark system for the development of cheap and abundant catalysts.
- Develop catalysts to replace Ru for the hydrogenation of LA to GVL.

Chapter 1 has given a brief insight into catalysis and its application in the valorisation of biomass. Brief overviews on biomass and the challenges in its upgrading are provided and an in-depth discussion of important platform molecules obtained from biomass treatment of interest in this thesis (lactic acid and levulinic acid) is presented. Chapter 2 will give all the experimental details for the catalyst preparation techniques, characterisation techniques, reaction procedures, and the data analysis used throughout this thesis. Detailed studies on lactic acid conversion using Ru/C catalyst are described in Chapter 3. Chapter 4 reports LA conversion into GVL with Ru/C catalysts, and a detailed investigation into the catalyst preparation and characterisation is presented. Chapters 5 and 6 are based on the same reaction using ZrO₂ supported Cu and Cu-Ni catalysts. A detailed investigation into reaction parameters, catalyst preparation and their stability is also reported. As indicated above this thesis initially investigates the use of Ru catalysts, then moves to the use of Cu- and Ni-based catalysts for hydrogenation reactions in order to determine whether cheap abundant metals can be viable alternatives to previously established precious metal catalysts. The future avenues of research for catalysts dealing with each process will be considered.

1.5. References

- 1 I. Chorkendorff and J. W. Niemantsverdriet, *Concepts of Modern Catalysis and Kinetics*, Wiley, 2006.
- 2 H. Bönemann, *Appl. Organomet. Chem.*, 2008, **22**, 412.
- 3 A. J. Jarvis, D. T. Leedal and C. N. Hewitt, *Nat. Clim. Chang.*, 2012, **2**, 668–671.
- 4 K. S. Deffeyes, *Beyond Oil: The View from Hubbert's Peak*, Farrar, Straus and Giroux, 2005.
- 5 Y. Yu, X. Lou and H. Wu, *Energy & Fuels*, 2007, **22**, 46–60.
- 6 S. N. Naik, V. V Goud, P. K. Rout and A. K. Dalai, *Renew. Sustain. Energy Rev.*, 2010, **14**, 578–597.
- 7 B. Antizar-Ladislao and J. L. Turrion-Gomez, *Biofuels, Bioprod. Biorefining*, 2008, **2**, 455–469.
- 8 D. O. Hall, J. L. Scrase and F. Rosillo-Calle, *Asp. Appl. Biol.*, 1997, **49**, 1–10.
- 9 G. Berndes, M. Hoogwijk and R. van den Broek, *Biomass and Bioenergy*, 2003, **25**, 1–28.
- 10 J. X. Sun, X. F. Sun, H. Zhao and R. C. Sun, *Polym. Degrad. Stab.*, 2004, **84**, 331–339.
- 11 H. V. Scheller and P. Ulvskov, *Annu. Rev. Plant Biol.*, 2010, **61**, 263–289.
- 12 R. D.W. and D. W.O., *Biofuels, Bioprod. Biorefining*, 2011, **5**, 198–214.

- 13 Z. C. Zhang, *Wiley Interdiscip. Rev. Energy Environ.*, 2013, **2**, 655–672.
- 14 P. Ferrini and R. Rinaldi, *Angew. Chemie Int. Ed.*, 2014, **53**, 8634–8639.
- 15 X. Wang and R. Rinaldi, *Energy Environ. Sci.*, 2012, **5**, 8244–8260.
- 16 A. V. Bridgwater, *Biomass and Bioenergy*, 2012, **38**, 68–94.
- 17 S. Czernik and A. V. Bridgwater, *Energy & Fuels*, 2004, **18**, 590–598.
- 18 S. de Vyver, J. Geboers, P. A. Jacobs and B. F. Sels, *ChemCatChem*, 2011, **3**, 82–94.
- 19 M. Yabushita, H. Kobayashi and A. Fukuoka, *Appl. Catal. B Environ.*, 2014, **145**, 1–9.
- 20 C.-H. Zhou, X. Xia, C.-X. Lin, D.-S. Tong and J. Beltramini, *Chem. Soc. Rev.*, 2011, **40**, 5588–5617.
- 21 A. Fukuoka and P. L. Dhepe, *Angew. Chemie Int. Ed.*, 2006, **45**, 5161–5163.
- 22 P. L. Dhepe and A. Fukuoka, *ChemSusChem*, 2008, **1**, 969–975.
- 23 W. Deng, Q. Zhang and Y. Wang, *Sci. China Chem.*, 2015, **58**, 29–46.
- 24 R. Datta and M. Henry, *J. Chem. Technol. Biotechnol.*, 2006, **81**, 1119–1129.
- 25 F.-F. Wang, C.-L. Liu and W.-S. Dong, *Green Chem.*, 2013, **15**, 2091–2095.
- 26 Y. Wang, W. Deng, B. Wang, Q. Zhang, X. Wan, Z. Tang, Y. Wang, C. Zhu, Z. Cao, G. Wang and H. Wan, *Nat. Commun.*, 2013, **4**, 2141.
- 27 M. S. Holm, Y. J. Pagan-Torres, S. Saravanamurugan, A. Riisager, J. A. Dumesic and E. Taarning, *Green Chem.*, 2012, **14**, 702–706.
- 28 W. Dong, Z. Shen, B. Peng, M. Gu, X. Zhou, B. Xiang and Y. Zhang, *Sci. Rep.*, 2016, **6**, 26713.
- 29 F. Chambon, F. Rataboul, C. Pinel, A. Cabiac, E. Guillon and N. Essayem, *Appl. Catal. B Environ.*, 2011, **105**, 171–181.
- 30 M. A. Peña and J. L. G. Fierro, *Chem. Rev.*, 2001, **101**, 1981–2018.
- 31 X. Yang, L. Yang, W. Fan and H. Lin, *Catal. Today*, 2016, **269**, 56–64.
- 32 A. Corma, S. Iborra and A. Velty, *Chem. Rev.*, 2007, **107**, 2411–2502.
- 33 A. Chauvel and G. Lefebvre, *Petrochemical Processes*, Editions OPHRYS.
- 34 M. A. Dasari, P.-P. Kiatsimkul, W. R. Sutterlin and G. J. Suppes, *Appl. Catal. A Gen.*, 2005, **281**, 225–231.
- 35 E. P. Maris and R. J. Davis, *J. Catal.*, 2007, **249**, 328–337.
- 36 T. Miyazawa, Y. Kusunoki, K. Kunimori and K. Tomishige, *J. Catal.*, 2006, **240**, 213–221.
- 37 T. Miyazawa, S. Koso, K. Kunimori and K. Tomishige, *Appl. Catal. A Gen.*, 2007, **329**, 30–35.
- 38 P. Mäki-Arvela, I. L. Simakova, T. Salmi and D. Y. Murzin, *Chem. Rev.*, 2014, **114**, 1909–1971.
- 39 R. D. Cortright, M. Sanchez-Castillo and J. A. Dumesic, *Appl. Catal. B Environ.*, 2002, **39**, 353–359.
- 40 H. S. Broadbent, G. C. Campbell, W. J. Bartley and J. H. Johnson, *J. Org. Chem.*, 1959, **24**, 1847–

1854.

- 41 E. Girard, D. Delcroix and A. Cabiacc, *Catal. Sci. Technol.*, 2016, **6**, 5534–5542.
- 42 Z. Zhang, J. E. Jackson and D. J. Miller, *Appl. Catal. A Gen.*, 2001, **219**, 89–98.
- 43 Y. Chen, D. J. Miller and J. E. Jackson, *Ind. Eng. Chem. Res.*, 2007, **46**, 3334–3340.
- 44 J. N. Chheda, G. W. Huber and J. A. Dumesic, *Angew. Chemie Int. Ed.*, 2007, **46**, 7164–7183.
- 45 G. Luo, S. Yan, M. Qiao, J. Zhuang and K. Fan, *Appl. Catal. A Gen.*, 2004, **275**, 95–102.
- 46 B.-W. Mao, Z.-Z. Cai, M.-Y. Huang and Y.-Y. Jiang, *Polym. Adv. Technol.*, 2003, **14**, 278–281.
- 47 Q. Yang, J. Zhang, L. Zhang, H. Fu, X. Zheng, M. Yuan, H. Chen and R. Li, *Catal. Commun.*, 2013, **40**, 37–41.
- 48 L. Huang, Y. Zhu, H. Zheng, M. Du and Y. Li, *Appl. Catal. A Gen.*, 2008, **349**, 204–211.
- 49 A. Primo, P. Concepcion and A. Corma, *Chem. Commun.*, 2011, **47**, 3613–3615.
- 50 T. Y. Jang, K. B. Chung, H. R. Eom, D. K. Noh, I. K. Song, J. Yi and S.-H. Baeck, *Res. Chem. Intermed.*, 2011, **37**, 1275–1282.
- 51 H. Jang, S.-H. Kim, D. Lee, S. E. Shim, S.-H. Baeck, B. S. Kim and T. S. Chang, *J. Mol. Catal. A Chem.*, 2013, **380**, 57–60.
- 52 X. Sun and Y. Li, *Angew. Chemie Int. Ed.*, 2004, **43**, 597–601.
- 53 V. M. Deshpande, K. Ramnarayan and C. S. Narasimhan, *J. Catal.*, 1990, **121**, 174–182.
- 54 Y. Takeda, T. Shoji, H. Watanabe, M. Tamura, Y. Nakagawa, K. Okumura and K. Tomishige, *ChemSusChem*, 2015, **8**, 1170–1178.
- 55 K. Chen, K. Mori, H. Watanabe, Y. Nakagawa and K. Tomishige, *J. Catal.*, 2012, **294**, 171–183.
- 56 Z. Wang, G. Li, X. Liu, Y. Huang, A. Wang, W. Chu, X. Wang and N. Li, *Catal. Commun.*, 2014, **43**, 38–41.
- 57 H. Adkins and H. R. Billica, *J. Am. Chem. Soc.*, 1948, **70**, 3121–3125.
- 58 S.-B. Qiu, Y.-J. Weng, Q.-Y. Liu, L.-L. Ma, Q. Zhang and T.-J. Wang, *Wuli Huaxue Xuebao/ Acta Phys. - Chim. Sin.*, 2016, **32**, 1511–1518.
- 59 M. N. Simonov, I. L. Simakova and V. N. Parmon, *React. Kinet. Catal. Lett.*, 2009, **97**, 157–162.
- 60 J. Xiao, Z. Huo, D. Ren, S. Zhang, J. Luo, G. Yao and F. Jin, *Process Biochem.*, 2015, **50**, 793–798.
- 61 D. Roy, B. Subramaniam and R. V Chaudhari, *Catal. Today*, 2010, **156**, 31–37.
- 62 D. R. Jones, S. Iqbal, S. A. Kondrat, G. M. Lari, P. J. Miedziak, D. J. Morgan, S. F. Parker and G. J. Hutchings, *Phys. Chem. Chem. Phys.*, 2016, **18**, 17259–17264.
- 63 J. J. Bozell and G. R. Petersen, .
- 64 K. Yan, C. Jarvis, J. Gu and Y. Yan, *Renew. Sustain. Energy Rev.*, 2015, **51**, 986–997.
- 65 J. Lilja, D. Y. Murzin, T. Salmi, J. Aumo, P. Mäki-Arvela and M. Sundell, *J. Mol. Catal. A Chem.*,

- 2002, **182–183**, 555–563.
- 66 K. Yan, G. Wu, J. Wen and A. Chen, *Catal. Commun.*, 2013, **34**, 58–63.
- 67 S. Saravanamurugan and A. Riisager, *Catal. Commun.*, 2012, **17**, 71–75.
- 68 D. R. Fernandes, A. S. Rocha, E. F. Mai, C. J. A. Mota and V. T. da Silva, *Appl. Catal. A Gen.*, 2012, **425–426**, 199–204.
- 69 W. Ciptonugroho, M. G. Al-Shaal, J. B. Mensah and R. Palkovits, *J. Catal.*, 2016, **340**, 17–29.
- 70 B. Girisuta, *Levulinic acid from lignocellulosic biomass*, University Library Groningen, 2007.
- 71 M. Mascal and E. B. Nikitin, *Green Chem.*, 2010, **12**, 370–373.
- 72 M. Mascal and E. B. Nikitin, *Angew. Chemie*, 2008, **120**, 8042–8044.
- 73 M. Mascal and E. B. Nikitin, *ChemSusChem*, 2009, **2**, 859–861.
- 74 Y. Takeuchi, F. Jin, K. Tohji and H. Enomoto, *J. Mater. Sci.*, 2008, **43**, 2472–2475.
- 75 J. Horvat, B. Klaić, B. Metelko and V. Šunjić, *Tetrahedron Lett.*, 1985, **26**, 2111–2114.
- 76 S. W. Fitzpatrick, WO Patent 010362, 1989.
- 77 S. W. Fitzpatrick, WO Patent 040609, 1996.
- 78 A. S. Amarasekara and O. S. Owereh, *Ind. Eng. Chem. Res.*, 2009, **48**, 10152–10155.
- 79 A. Brandt, M. J. Ray, T. Q. To, D. J. Leak, R. J. Murphy and T. Welton, *Green Chem.*, 2011, **13**, 2489–2499.
- 80 H. Ren, B. Girisuta, Y. Zhou and L. Liu, *Carbohydr. Polym.*, 2015, **117**, 569–576.
- 81 S. Peleteiro, S. Rivas, J. L. Alonso, V. Santos and J. C. Parajó, *Bioresour. Technol.*, 2016, **202**, 181–191.
- 82 A. M. da Costa Lopes and R. Bogel-Lukasik, *ChemSusChem*, 2015, **8**, 947–965.
- 83 R. A. Schraufnagel and H. F. Rase, *Prod. Res. D*, 1975, **14**, 40–44.
- 84 A. Corma, *J. Catal.*, 2003, **216**, 298–312.
- 85 A. Corma, *Chem. Rev.*, 1997, **97**, 2373–2420.
- 86 A. Corma, *Chem. Rev.*, 1995, **95**, 559–614.
- 87 R. Weingarten, W. C. Conner and G. W. Huber, *Energy Environ. Sci.*, 2012, **5**, 7559–7574.
- 88 N. A. S. Ramli and N. A. S. Amin, *Appl. Catal. B Environ.*, 2015, **163**, 487–498.
- 89 N. A. S. Ramli and N. A. S. Amin, *Energy Convers. Manag.*, 2015, **95**, 10–19.
- 90 M. A. Mellmer, J. M. R. Gallo, D. M. Alonso and J. A. Dumesic, *ACS Catal.*, 2015, **5**, 3354–3359.
- 91 I. Guzmán, A. Heras, M. B. Güemez, A. Iriondo, J. F. Cambra and J. Requies, *Ind. Eng. Chem. Res.*, 2016, **55**, 5139–5144.
- 92 I. T. Horvath, H. Mehdi, V. Fabos, L. Boda and L. T. Mika, *Green Chem.*, 2008, **10**, 238–242.
- 93 M. G. Al-Shaal, A. Dzierbinski and R. Palkovits, *Green Chem.*, 2014, **16**, 1358–1364.
- 94 F. M. A. Geilen, B. Engendahl, A. Harwardt, W. Marquardt, J. Klankermayer and W. Leitner,

- Angew. Chemie Int. Ed.*, 2010, **49**, 5510–5514.
- 95 J. J. Bozell, L. Moens, D. C. Elliott, Y. Wang, G. G. Neuenschwander, S. W. Fitzpatrick, R. J. Bilski and J. L. Jarnefeld, *Resour. Conserv. Recycl.*, 2000, **28**, 227–239.
- 96 P. P. Upare, M. Lee, S.-K. Lee, J. W. Yoon, J. Bae, D. W. Hwang, U.-H. Lee, J.-S. Chang and Y. K. Hwang, *Catal. Today*, 2016, **265**, 174–183.
- 97 O. A. Abdelrahman, A. Heyden and J. Q. Bond, *ACS Catal.*, 2014, **4**, 1171–1181.
- 98 S. Hirose, E. G. R. Putra, M. Chalid, H. J. Heeres and A. A. Broekhuis, *Procedia Chem.*, 2012, **4**, 260–267.
- 99 A. S. Piskun, J. E. de Haan, E. Wilbers, H. H. van de Bovenkamp, Z. Tang and H. J. Heeres, *ACS Sustain. Chem. Eng.*, 2016, **4**, 2939–2950.
- 100 P. Balla, V. Perupogu, P. K. Vanama and V. R. C. Komandur, *J. Chem. Technol. Biotechnol.*, 2016, **91**, 769–776.
- 101 V. Mohan, C. Raghavendra, C. V. Pramod, B. D. Raju and K. S. Rama Rao, *RSC Adv.*, 2014, **4**, 9660–9668.
- 102 K. Osakada, T. Ikariya and S. Yoshikawa, *J. Organomet. Chem.*, 1982, **231**, 79–90.
- 103 H. Mehdi, V. Fábos, R. Tuba, A. Bodor, L. T. Mika and I. T. Horváth, *Top. Catal.*, 2008, **48**, 49–54.
- 104 W. Li, J.-H. Xie, H. Lin and Q.-L. Zhou, *Green Chem.*, 2012, **14**, 2388–2390.
- 105 J. Deng, Y. Wang, T. Pan, Q. Xu, Q.-X. Guo and Y. Fu, *ChemSusChem*, 2013, **6**, 1163–1167.
- 106 P. J. Deuss, K. Barta and J. G. de Vries, *Catal. Sci. Technol.*, 2014, **4**, 1174–1196.
- 107 H. S. Broadbent and C. W. Whittle, *J. Am. Chem. Soc.*, 1959, **81**, 3587–3589.
- 108 P. P. Upare, J.-M. Lee, D. W. Hwang, S. B. Halligudi, Y. K. Hwang and J.-S. Chang, *J. Ind. Eng. Chem.*, 2011, **17**, 287–292.
- 109 M. L. E., *Appl. Catal., A*, 2004, **272**, 249.
- 110 W. Luo, M. Sankar, A. M. Beale, Q. He, C. J. Kiely, P. C. A. Bruijninx and B. M. Weckhuysen, *Nat Commun.*, 2015, **6**.
- 111 M. Li, G. Li, N. Li, A. Wang, W. Dong, X. Wang and Y. Cong, *Chem. Commun.*, 2014, **50**, 1414–1416.
- 112 C. Ortiz-Cervantes and J. J. García, *Inorganica Chim. Acta*, 2013, **397**, 124–128.
- 113 W. Luo, U. Deka, A. M. Beale, E. R. H. van Eck, P. C. A. Bruijninx and B. M. Weckhuysen, *J. Catal.*, 2013, **301**, 175–186.
- 114 M. G. Al-Shaal, W. R. H. Wright and R. Palkovits, *Green Chem.*, 2012, **14**, 1260–1263.
- 115 A. M. Ruppert, J. Grams, J. M., J. Matras-Michalska, N. Keller, K. Ostojaska and P. Sautet,

- ChemSusChem*, 2015, **8**, 1538–1547.
- 116 J. Ftouni, A. M. Murillo, A. E. Goryachev, J. P. Hofmann, E. J. M. Hensen, L. Lu, C. J. Kiely, P. C. A. Bruijninx and B. M. Weckhuysen, *ACS Catal.*, **0**, null.
- 117 H. Zhang, W. Chu, C. Zou, Z. Huang, Z. Ye and L. Zhu, *Catal. Letters*, 2011, **141**, 438–444.
- 118 S. Zhang, L. Chen, S. Zhou, D. Zhao and L. Wu, *Chem. Mater.*, 2010, **22**, 3433–3440.
- 119 A. Tavasoli, K. Sadagiani, F. Khorashe, A. A. Seifkordi, A. A. Rohani and A. Nakhaeipour, *Fuel Process. Technol.*, 2008, **89**, 491–498.
- 120 A. Tavasoli, M. Trépanier, A. K. Dalai and N. Abatzoglou, *J. Chem. Eng. Data*, 2010, **55**, 2757–2763.
- 121 Z. Yan, L. Lin and S. Liu, *Energy & Fuels*, 2009, **23**, 3853–3858.
- 122 A. M. R. Galletti, C. Antonetti, V. De Luise and M. Martinelli, *Green Chem.*, 2012, **14**, 688–694.
- 123 A. M. Ruppert, M. Jedrzejczyk, O. Sneká-Platek, N. Keller, A. S. Dumon, C. Michel, P. Sautet and J. Grams, *Green Chem.*, 2016, **18**, 2014–2028.
- 124 S. G. Wettstein, J. Q. Bond, D. M. Alonso, H. N. Pham, A. K. Datye and J. A. Dumesic, *Appl. Catal. B Environ.*, 2012, **117–118**, 321–329.
- 125 M. Al-Naji, A. Yopez, A. M. Balu, A. A. Romero, Z. Chen, N. Wilde, H. Li, K. Shih, R. Gläser and R. Luqueb, *J. Mol. Catal. A Chem.*, 2016, **417**, 145–152.
- 126 D. Albani, Q. Li, G. Vile, S. Mitchell, N. Almora-Barrios, P. Witte, N. Lopez and J. Perez-Ramirez, *Green Chem.*, 2016.
- 127 L. Wu, J. Song, B. Zhou, T. Wu, T. Jiang and B. Han, *Chem. – An Asian J.*, 2016, **11**, 2792–2796.
- 128 J. Tan, J. Cui, X. Cui, T. Deng, X. Li, Y. Zhu and Y. Li, .
- 129 C. Xiao, T.-W. Goh, Z. Qi, S. Goes, K. Brashler, C. Perez and W. Huang, .
- 130 Y. Yang, C.-J. Sun, D. E. Brown, L. Zhang, F. Yang, H. Zhao, Y. Wang, X. Ma, X. Zhang and Y. Ren, *Green Chem.*, 2016, **18**, 3558–3566.
- 131 T. Witoon, J. Chalorngtham, P. Dumrongbunditkul, M. Chareonpanich and J. Limtrakul, *Chem. Eng. J.*, 2016, **293**, 327–336.
- 132 K. T. Jung and A. T. Bell, *Catal. Letters*, 2002, **80**, 63–68.
- 133 M. D. Rhodes and A. T. Bell, *J. Catal.*, 2005, **233**, 198–209.
- 134 Q. Sun, Y.-L. Zhang, H.-Y. Chen, J.-F. Deng, D. Wu and S.-Y. Chen, *J. Catal.*, 1997, **167**, 92–105.
- 135 S. Y. Fu, Y. Z. Li, W. Chu, C. Li and D. G. Tong, *Catal. Sci. Technol.*, 2015, **5**, 1638–1649.
- 136 S. Zhu, X. Gao, Y. Zhu, Y. Zhu, H. Zheng and Y. Li, *J. Catal.*, 2013, **303**, 70–79.
- 137 R. V. C. Jr., H. D. Brown and R. M. Hixon, *J. Am. Chem. Soc.*, 1947, **69**, 1961–1963.
- 138 K. Yan, J. Liao, X. Wu and X. Xie, *RSC Adv.*, 2013, **3**, 3853–3856.
- 139 K. Yan and A. Chen, *Energy*, 2013, **58**, 357–363.

- 140 G. K. Chuah, *Catal. Today*, 1999, **49**, 131–139.
- 141 M. Rezaei, S. M. Alavi, S. Sahebdehfar and Z.-F. Yan, *Powder Technol.*, 2006, **168**, 59–63.
- 142 J. Kondo, Y. Sakata, K. Domen, K. Maruya and T. Onishi, *J. Chem. Soc. { } Faraday Trans.*, 1990, **86**, 397–401.
- 143 J. Wang, S. Jaenicke and G.-K. Chuah, *RSC Adv.*, 2014, **4**, 13481–13489.
- 144 M. Chia and J. A. Dumesic, *Chem. Commun.*, 2011, **47**, 12233–12235.
- 145 S. S. Enumula, V. R. B. Gurram, M. Kondeboina, D. R. Burri and S. R. R. Kamaraju, *RSC Adv.*, 2016, **6**, 20230–20239.
- 146 A. M. Hengne and C. V Rode, *Green Chem.*, 2012, **14**, 1064–1072.
- 147 J. Yuan, S.-S. Li, L. Yu, Y.-M. Liu, Y. Cao, H.-Y. He and K.-N. Fan, *Energy Environ. Sci.*, 2013, **6**, 3308–3313.
- 148 K. Samson, M. Śliwa, R. P. Socha, K. Góra-Marek, D. Mucha, D. Rutkowska-Zbik, J.-F. Paul, M. Ruggiero-Mikolajczyk, R. Grabowski and J. Słoczyński, *ACS Catal.*, 2014, **4**, 3730–3741.
- 149 Lu-Cun Wang, Qian Liu, Miao Chen, Yong-Mei Liu, Yong Cao, He-Yong He and Kang-Nian Fan, *J. Phys. Chem. C*, 2007, **111**, 16549–16557.
- 150 Y. Ma, Q. Sun, D. Wu, W.-H. Fan, Y.-L. Zhang and J.-F. Deng, *Appl. Catal. A Gen.*, 1998, **171**, 45–55.
- 151 X.-R. Zhang, L.-C. Wang, C.-Z. Yao, Y. Cao, W.-L. Dai, H.-Y. He and K.-N. Fan, *Catal. Letters*, 2005, **102**, 183–190.
- 152 C.-Z. Yao, L.-C. Wang, Y.-M. Liu, G.-S. Wu, Y. Cao, W.-L. Dai, H.-Y. He and K.-N. Fan, *Appl. Catal. A Gen.*, 2006, **297**, 151–158.
- 153 D. R. Jones, S. Iqbal, S. Ishikawa, C. Reece, L. M. Thomas, P. J. Miedziak, D. J. Morgan, J. K. Edwards, J. K. Bartley, D. J. Willock and G. J. Hutchings, *Catal. Sci. Technol.*, 2016, **6**, 6022–6030.
- 154 X.-L. Du, Q.-Y. Bi, Y.-M. Liu, Y. Cao, H.-Y. He and K.-N. Fan, *Green Chem.*, 2012, **14**, 935–939.
- 155 K. Hengst, M. Schubert, H. W. P. Carvalho, C. Lu, W. Kleist and J.-D. Grunwaldt, *Appl. Catal. A Gen.*, 2015, **502**, 18–26.
- 156 V. Mohan, V. Venkateshwarlu, C. V. Pramod, B. D. Raju and K. S. R. Rao, *Catal. Sci. Technol.*, 2014, **4**, 1253–1259.
- 157 M. Varkolu, V. Velpula, D. R. Burri and S. R. R. Kamaraju, *New J. Chem.*, 2016, **40**, 3261–3267.
- 158 K. Shimizu, S. Kanno and K. Kon, *Green Chem.*, 2014, **16**, 3899–3903.
- 159 P. P. Upare, Y. K. Hwang, J.-M. Lee, D. W. Hwang and J.-S. Chang, *ChemSusChem*, 2015, **8**, 2345–2357.
- 160 P. P. Upare, M.-G. Jeong, Y. K. Hwang, D. H. Kim, Y. D. Kim, D. W. Hwang, U.-H. Lee and J.-

- S. Chang, *Appl. Catal. A Gen.*, 2015, **491**, 127–135.
- 161 I. Obregón, I. Gandarias, N. Miletić, A. Ocio and P. L. Arias, *ChemSusChem*, 2015, **8**, 3483–3488.
- 162 B. C. Miranda, R. J. Chimentão, J. Szanyi, A. H. Braga, J. B. O. Santos, F. Gispert-Guirado, J. Llorca and F. Medina, *Appl. Catal. B Environ.*, 2015, **166–167**, 166–180.
- 163 A. R. Naghash, T. H. Etsell and S. Xu, *Chem. Mater.*, 2006, **18**, 2480–2488.
- 164 J. Bian, M. Xiao, S. Wang, X. Wang, Y. Lu and Y. Meng, *Chem. Eng. J.*, 2009, **147**, 287–296.
- 165 M. Lortie, R. Isaifan, Y. Liu and S. Mommers, *Int. J. Chem. Eng.*, 2015.
- 166 F. Studt, F. Abild-Pedersen, Q. Wu, A. D. Jensen, B. Temel, J.-D. Grunwaldt and J. K. Nørskov, *J. Catal.*, 2012, **293**, 51–60.
- 167 G. Águila, J. Jiménez, S. Guerrero, F. Gracia, B. Chornik, S. Quinteros and P. Araya, *Appl. Catal. A Gen.*, 2009, **360**, 98–105.
- 168 <http://www.novacam.eu/>

Chapter 2

Experimental

2.1. Materials

Table 2.1. A list of all materials used throughout this thesis and their suppliers.

Materials for catalyst preparation	
Material	Supplier
Ru(NO)(NO ₃) ₃ (1.5 wt.% Ru in HNO ₃)	Sigma Aldrich UK
RuCl ₃ .xH ₂ O (45–55 wt.% Ru)	Sigma Aldrich UK
Darco G60	Cabot Corporation
Cabot Vulcan XC72R	Cabot Corporation
Norit GCN3070	Cabot Corporation
Norit ROX 0.8 (pellets)	Cabot Corporation
Graphene oxide	Sigma Aldrich UK
5 wt.% Ru/C	Sigma Aldrich UK
Polyvinylalcohol (PVA)	Sigma Aldrich UK
NaBH ₄	Sigma Aldrich UK
Cu(NO ₃) ₂ .3H ₂ O	Sigma Aldrich UK
Ni(NO ₃) ₂ .6H ₂ O	Sigma Aldrich UK
ZrO(NO ₃) ₂ .6H ₂ O	Acros Organics UK
Oxalic acid	Sigma Aldrich UK
K ₂ CO ₃	Sigma Aldrich UK

Reactants and products

Material	Supplier
Lactic acid	Sigma Aldrich UK
1,2-propanediol (PDO)	Sigma Aldrich UK
Propanoic acid	Sigma Aldrich UK
Methanol	Sigma Aldrich UK
Ethanol	Sigma Aldrich UK
1-propanol	Sigma Aldrich UK
2-propanol	Sigma Aldrich UK
Levulinic acid (LA)	Sigma Aldrich UK
γ -valerolactone (GVL)	Sigma Aldrich UK
Methyl levulinate	Sigma Aldrich UK
1,4-pentanediol	Sigma Aldrich UK
2-methyltetrahydrofuran (2-MTHF)	Sigma Aldrich UK
α -angelica lactone	Sigma Aldrich UK
Pentanoic acid	Sigma Aldrich UK
Pentanoic esters	Sigma Aldrich UK
2-butanol	Sigma Aldrich UK
Methane	BOC
Ethane	BOC
Propane	BOC

Note: all products purchased for HPLC/GC calibration were of analytical purity $\geq 98\%$.

Notes on the natures of the carbon supports used in this thesis (obtained from their suppliers):

- Darco G60: A high purity, steam activated carbon with excellent adsorptive capacity, making it ideal for the treatment of fine chemicals and pharmaceuticals.
- Cabot Vulcan XC72R: A highly conductive carbon with low sulphur content and low ionic contamination.
- Norit GCN 3070: A coconut shell-based granular activated carbon.
- Norit ROX 0.8: An acid washed high purity extruded carbon prepared by steam activation.

2.2. Catalyst preparation

2.2.1. Wet impregnation (WI)

Wet impregnation (WI) is the simplest method for catalyst preparation. In this method, a solution of the metal salt precursor is added to the support material and mixed so that the metal is distributed throughout the pores of the support¹. The material is then dried in order to remove the solvent, but care must be taken that the drying is carried out in a way that the metal component does not migrate to the

surface from the pores. After drying, calcination or elevated heat treatment may be carried out to decompose metal salt precursors or prepare the catalytic sites. Reduction treatment may also be employed. Incipient wetness impregnation is a variation of WI where the volume of the metal salt solution is equal to or smaller than the pore volume of the support.

This process is simple, quick, reproducible, and ensures that all the metal is directly deposited onto the surface thereby reducing waste, which is especially important when expensive precious metals are used. Industries frequently use WI for the preparation of heterogeneous metal catalysts for these reasons.

WI was used in Chapters 3 and 4 as a preparation technique. The appropriate amount of Ru precursor – either $\text{Ru}(\text{NO})(\text{NO}_3)_3$ or $\text{RuCl}_3 \cdot x\text{H}_2\text{O}$ – to produce 5 wt.% (Chapter 3) or 1 wt.% (Chapter 4) Ru based on 2 g of catalyst was dissolved in deionised water required. This aqueous metal solution was added to the carbon support. If required, more deionised water was added so that the mixture achieved a “toothpaste” like consistency. Where carbon ROX 0.8 was used as a support, the pellets were ground into a powder using a pestle and mortar beforehand. This slurry was stirred for 15 minutes then transferred to a drying oven at 110 °C for 16 h. The resulting material was then heat treated at 300 °C under a flow of N_2 for 3 h (10 °C min^{-1} heating rate).

2.2.2. Sol immobilisation (SI)

Sol immobilisation (SI) involves the preparation of metal nanoparticles in solution followed by their subsequent immobilisation on a support ^{2,3}. A metal salt is dissolved in a large excess of deionised water and a stabilising agent – usually a polymer – is added to generate a sol. A reducing agent is then used to generate metallic nanoparticles, the growth of which is determined by Turkevich’s methodology ⁴. Once nanoparticles are generated, the support is added and the nanoparticles are immobilized onto the surface by altering the charge of the support through addition of an acid. The electrochemical double layer surrounding the metal nanoparticles causes them to be attracted to the support. Because metallic nanoparticles are laid onto the support surface, there is seldom need for subsequent reduction treatment when SI is used for catalyst preparation. The advantage of SI is that it is applicable to any type of support. The use of the stabilising agent also allows control over the metal particle size, and usually results in the production of a highly dispersed metal catalyst. The stabilising agent can have a positive effect on the long term stability of the catalyst, but it has been shown that stabilising agents can be easily removed by thermal decomposition or solvent washing ⁵. This method can also generate a lot of waste solvent, and deposition of all the metal onto the support cannot always be guaranteed.

The SI method was utilised in Chapters 3 and 4. The appropriate amount of Ru precursor – either $\text{Ru}(\text{NO})(\text{NO}_3)_3$ or $\text{RuCl}_3 \cdot x\text{H}_2\text{O}$ – to produce 5 wt.% (Chapter 3) or 1 wt.% (Chapter 4) Ru based on 2 g of catalyst was dissolved in 800 mL of deionised water. The desired amount of PVA was added to the

solution (PVA/Ru = 0.65 in Chapter 3; and a varied ratio of PVA/Ru in Chapter 4) to generate the sol and the solution was stirred for 15 minutes. The desired amount of NaBH₄ was then added (NaBH₄/RuCl₃ = 3.3 in Chapter 3; and a varied ratio of NaBH₄/RuCl₃ in Chapter 4) to generate metallic Ru and the solution was further stirred. After 15 minutes, the carbon support was added to the solution and acidified to pH 1 using H₂SO₄ and stirred for 2 h at room temperature. The resulting materials were filtered, washed with 1000 mL of deionised water to remove any trace of H₂SO₄, and dried in an oven at 110 °C for 16 h. In contrast to the catalyst prepared by WI, the catalysts prepared by SI *did not* undergo a heat treatment step after drying.

2.2.3. Co-precipitation (CP)

Co-precipitation (CP) is a common catalyst preparation technique that involves the simultaneous precipitation of two or more metal components using a precipitant under a constant or a varied pH. There are many factors to consider in the synthesis of catalysts by CP including temperature, pH, flow rate of precipitating agent, ageing time, and washing. All of the preparation parameters must be controlled carefully in order to ensure that the catalysts are prepared reproducibly.

Because catalysts can be prepared reproducibly by CP, this method has been applied for large scale production of heterogeneous catalysts ⁶. The main drawback of this technique is that there can be large mass loss during the derivation of the final product. Calcination is often required to decompose the material to the active catalyst.

The Cu-ZrO₂ catalysts presented in Chapter 5 were synthesized by CP. 0.005 mol of Cu(NO₃)₂·3H₂O and 0.005 mol of ZrO(NO₃)₂·6H₂O were dissolved in 200 mL water in order to obtain the desired Cu/Zr ratio. K₂CO₃ solution (0.2 mol dm⁻³) was added dropwise to the solution to raise the pH from 3 to 9. The precipitate was aged in solution for the desired amount of time at room temperature. The precipitate was filtered under vacuum followed by washing with 1000 mL of deionised water. The precipitate was dried in an oven at 110 °C for 16 h and calcined at the desired temperature between 300–800 °C (heating rate 20 °C min⁻¹) in static air for 4 h.

2.2.4. Oxalate gel precipitation (OG)

Oxalate gel precipitation (OG) is a variation of the CP procedure discussed in Section 2.2.3, so called because it uses oxalic acid as the precipitating agent, resulting in a sol-gel being formed in solution. The conditions of OG must be carefully controlled in the same way as CP method.

The Cu-, Ni-Cu-, and Ni-ZrO₂ catalysts investigated in Chapter 6 were prepared by the OG method. Cu(NO₃)₂·3H₂O and Ni(NO₃)₂·6H₂O (Cu + Ni = 0.01 mol) and ZrO(NO₃)₂·6H₂O (0.01 mol) were dissolved in 200 mL of ethanol. Solid oxalic acid (0.024 mol) was added into the metal solution, and the resulting precipitate was aged in solution at room temperature for 2 h. The precipitate was then

filtered without a washing step. The material was dried in an oven at 110 °C for 16 h, calcined at 550 °C (heating rate 10 °C min⁻¹) in static air for 2 h, then treated at the desired temperature in a flow of 5 % H₂/Ar (heating rate 10 °C min⁻¹) for 2 h. The catalysts were denoted xNi-yCu-ZrO₂ (where x + y = 50 mol.%)

2.2.4.1. Ball milling (BM)

Catalysts presented in Chapter 6 that have undergone physical grinding were prepared using the OG method described in Section 2.2.3.1. After the calcination stage, the material was ball milled at 400 rpm for 1 h. The resulting material was then reduced at the desired temperature (heating rate 10 °C min⁻¹) in a flow of 5 % H₂/Ar. Catalysts were denoted xNi-yCu-ZrO₂-BM (where x + y = 50 mol.%).

2.2.4.2. Physical mixing (PM)

Catalysts by physical mixing (PM) presented in Chapter 6 were prepared using a variation of the method described in Section 2.2.3. Cu(NO₃)₂·3H₂O and Ni(NO₃)₂·6H₂O (Cu + Ni = 0.01 mol) were dissolved in 100 mL of ethanol. Solid oxalic acid (0.012) was added and the resulting precipitate was aged for 2 h. The precipitate was then filtered without a washing step. The material was dried in an oven at 110 °C for 16 h, calcined at 550 °C (heating rate 10 °C min⁻¹) in static air for 2 h. Separately, the same procedure was carried out using ZrO(NO₃)₂·6H₂O (0.01 mol). The two calcined materials were ball milled together at 400 rpm for 1 h. The resulting material was then reduced at the desired temperature (heating rate 10 °C min⁻¹) in a flow of 5 % H₂/Ar as described previously. Catalysts were denoted xNi-yCu-ZrO₂-PM (where x + y = 50 mol.%).

2.3. Reaction data

2.3.1. Autoclave

All reaction data presented throughout this thesis were obtained using an autoclave reactor. Autoclave reactors are used to carry out batch reactions at high temperatures and pressures. Figure 2.1 shows a schematic of the autoclave reactor used.

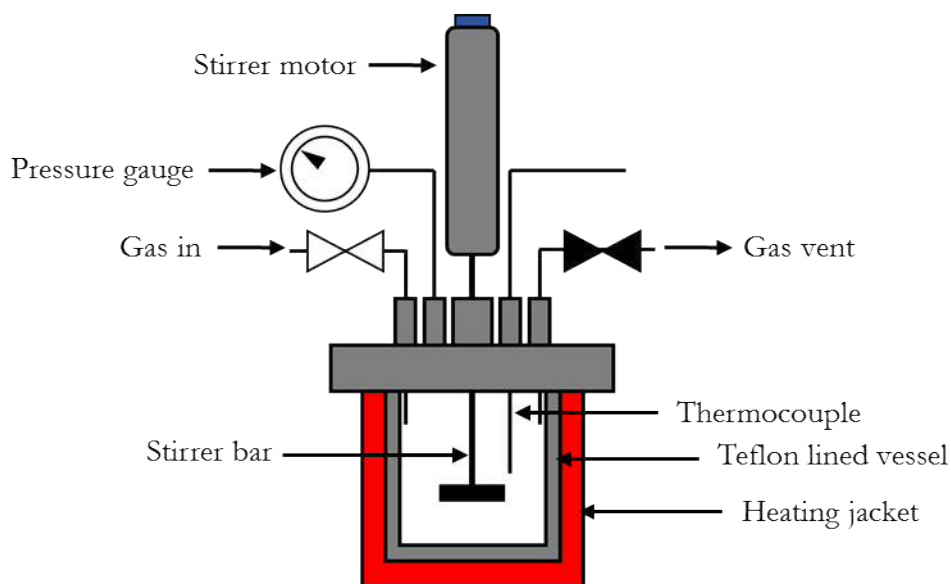


Figure 2.1. Schematic of the autoclave used to obtain catalytic data.

Reactions were carried out using a 50 mL, Parr Instruments, Model 5500HP stainless steel stirred autoclave equipped with a Teflon liner. The liner was charged with the desired amounts of catalyst and substrate(s) and sealed inside the autoclave. The sealed autoclave was purged three times with N_2 in order to remove residual air, and three times with H_2 to remove residual N_2 before being pressurised to the desired pressure with H_2 . The autoclave was heated to the desired temperature. The stirring rate was increased to 2000 rpm when the desired reaction temperature was reached, which was considered to be T_0 for the reaction. When the reaction was completed, the autoclave was rapidly cooled in an ice bath in order to quench the reaction. The gasses were vented when the temperature was <10 °C, and the autoclave was opened. The catalyst was filtered using filter paper and the reaction solution was analysed using offline HPLC or GC.

2.3.1.1. Catalyst reuse studies

The following procedure was carried out to investigate whether a catalyst was reusable. An excess of catalyst (between 0.1–0.5 g) was subjected to a reaction as described in 2.3.1. When the reaction was complete, the catalyst was filtered, washed with deionised water and acetone (10 mL of each) and dried in an oven at 110 °C for 16 h (1 use). From this batch of catalyst, the requisite amount for a regular

reaction was taken in order to determine its activity. The used batch was subjected to another reaction, dried and filtered as before, and the requisite amount for a regular reaction taken in order to determine its activity (2 uses). This was repeated to determine the activity of the catalyst for the desired number of uses.

2.3.2. Reaction analysis

2.3.2.1. High performance liquid chromatography

High performance liquid chromatography (HPLC) is an analytical technique that separates liquid mixtures into their individual components. The sample is injected into the head of a chromatographic column and transported through it by the flow of a liquid mobile phase. The retention time of the various compounds is affected by the interaction of the compounds with the stationary column. The components of an HPLC (shown in Figure 2.2) are as follows:

- **Pump:** the role of the pump is to keep the liquid mobile phase flowing through the apparatus at a specific flow rate.
- **Injector:** the role of the injector is to introduce the sample into the flow of the mobile phase
- **Column:** The column is the most important part of the HPLC, where the compounds of the mixture are separated based on various physical and chemical parameters of the column and the substrate.
- **Detector:** The detector detects the individual compounds that elute from the column. A *refractive index detector* (RID) was used in the study reported in Chapter 3. RID measures the change in refractive index of the eluting compound relative to the mobile phase. The advantage of using a RID is that it is considered a universal detector, because it can detect anything with a different refractive index from the solvent. However, RIDs are known for their low sensitivity meaning that very small concentrations of substrate cannot always be detected.
- **Data acquisition:** A computer is used to operate the HPLC and to process the raw chromatographic data.

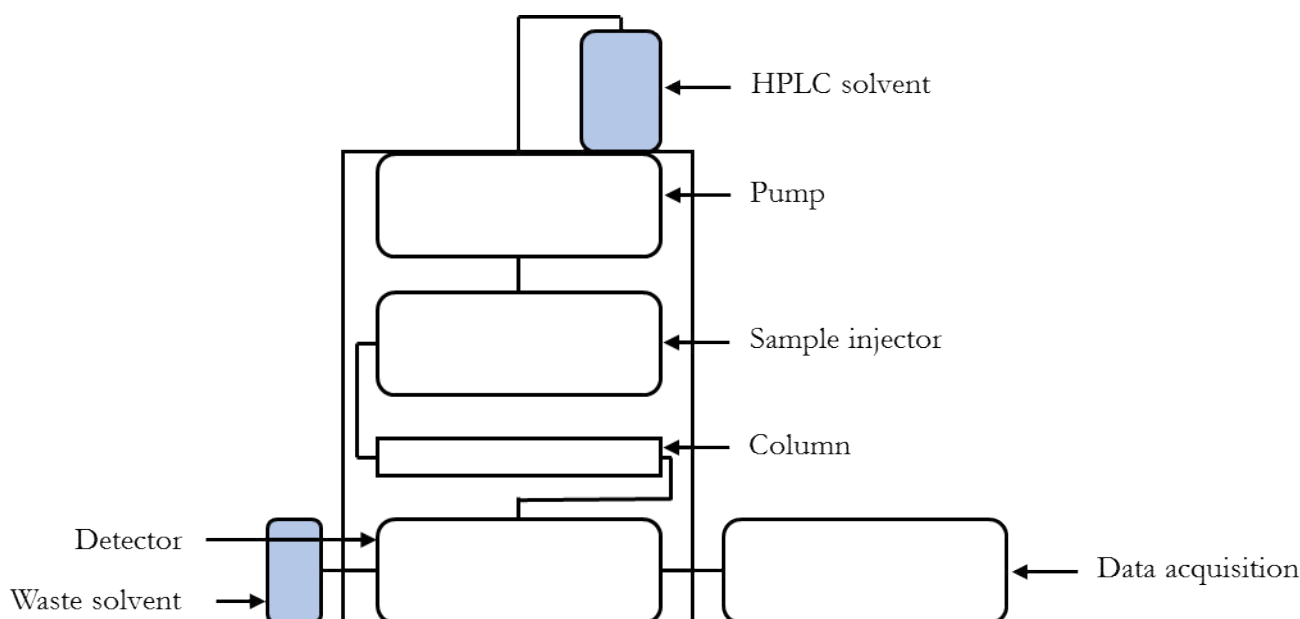


Figure 2.2. Schematic of the HPLC apparatus used for reaction analysis.

The data reported in Chapter 3 was prepared by analysing the reaction solutions through an Agilent Technologies 1260 Infinity HPLC equipped with an auto-sampler, Varian MetaCarb 67H capillary column (0.65 x 30 cm), and a RID. 0.1 % H_3PO_4 in H_2O was used as the mobile phase.

2.3.2.2. Gas chromatography

Gas chromatography (GC) is conceptually identical to HPLC described in Section 2.3.2.1. The difference between GC and HPLC is that GC samples are vaporised prior to injection at the head of a chromatographic column. The sample is then carried through the column by an inert carrier gas. Components of a GC (schematic given in Figure 2.3) are as follows:

- **Carrier gas:** The carrier gas is used to carry the sample through the column at a constant flow rate. It must be an inert gas, usually He, N_2 , or Ar.
- **Sample injector:** The sample injector is the spot at the head of the column where the sample is injected. Sample injector is kept at a high temperature in order to vaporise the liquid samples so that they are in the vapour when flowing through the column.
- **Column:** The column in GC serves the same purpose as it does in HPLC, to separate the various compounds present in the reaction mixture based on the physical and chemical interactions between the column and the substrate. The column is kept in an oven in order to ensure that the samples are kept in the vapour phase; condensation of samples in the column can lead to errors in the chromatographic data obtained.
- **Detector:** A *flame ionisation detector* (FID) was used to analyse the products eluting from the GC. The carrier gas carries the sample into a hydrogen flame at the top of an FID. There is a metal collector

plate located close to the flame that attracts compounds ionised by the flame. The current generated translates into a detector signal. The greater the amount of analyte, the greater the response of the FID. FIDs are low cost and easy to maintain, but they are best suited to analyse hydrocarbon molecules that are not highly functionalised. FIDs are not considered universal detectors.

- **Data acquisition:** As with HPLC, a computer is used to operate the GC and to process the raw chromatographic data.

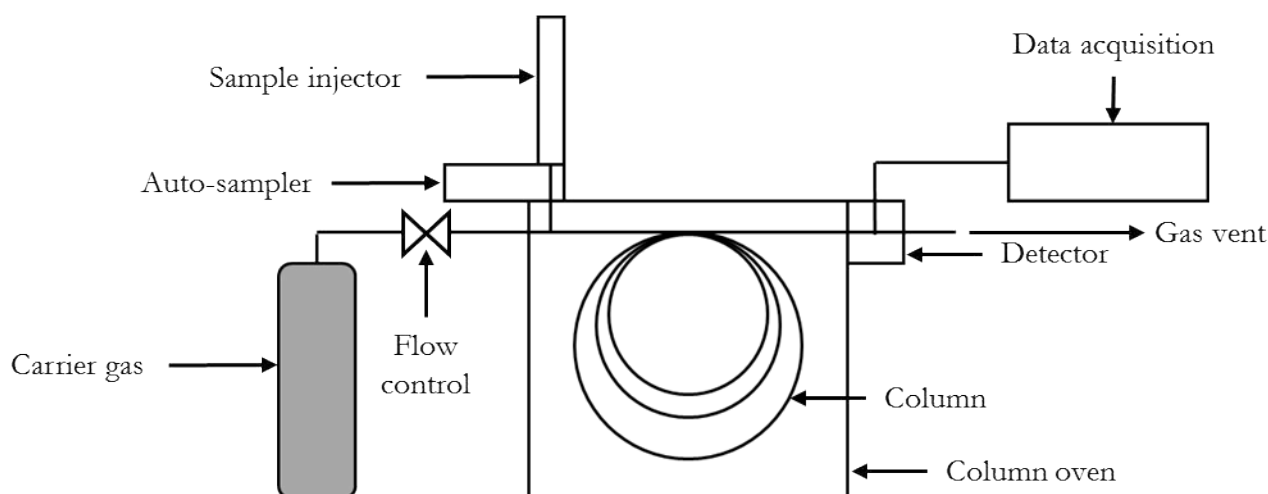


Figure 2.3. Schematic of the GC apparatus used for reaction analysis.

In Chapters 4–6, liquid products were analysed using a GC equipped with CP-Sil 5CB (50 m, 0.32 mm, 5 μ m) column which separates compounds based on their boiling point, and detected by a FID detector. He was used as the carrier gas. 0.1 mL of acetonitrile was added to 0.9 mL of the reaction solution as an external standard, which was used to offset any errors in injection volume.

2.3.2.3. Calculation of conversion and selectivity

Both HPLC and GC were calibrated to obtain response factors both for reactants and products. Typically, concentrations between 1–5 wt.% substrate in solution were used for calibration. Response factors were obtained by taking the gradient of the line resulting from plotting the peak area *vs.* the concentration ($R^2 \geq 0.998$).

Conversion, selectivity, and yield were calculated using Equations 2.1–2.3. Carbon balance was calculated using Equation 2.4.

Equation 2.1.

$$\text{Conversion of R (\%)} = \frac{[R]_0 - [R]_1}{[R]_0} \times 100$$

where R = reactant; $[R]_0$ = initial concentration of reactant; $[R]_1$ = final concentration of reactant determined by HPLC/GC analysis.

Equation 2.2.

$$\text{Selectivity to } P_i \text{ (\%)} = \frac{[P_i]}{[P_0]} \times 100$$

where P_i = product *i*; $[P_i]$ = concentration of P_i determined by HPLC/GC analysis; $[P_0]$ = total concentration of all products determined by HPLC/GC.

Equation 2.3.

$$\text{Yield of } P_i \text{ \%} = \text{Conversion of R \%} \times \text{Selectivity of } P_i \text{ \%}$$

Equation 2.4.

$$\text{Carbon balance \%} = \frac{[C]_1}{[C]_0} \times 100$$

where $[C]_0$ = carbon concentration of reactants; $[C]_1$ = carbon concentration of residual reactant and products determined by HPLC/GC analysis.

2.3.2.4. Microwave plasma atomic emission spectroscopy

Microwave plasma atomic emission spectroscopy (MP-AES) uses the light from a plasma flame in order to analyse the elemental composition of a solution. Photons become discharged from the compounds as they transition from a high energy state to a low energy state after interaction with the plasma. The photons are of a characteristic wavelength for each element or substance. The technique is both qualitative, determining whether an element is present, and quantitative, with the photon count being proportional to the amount of element present⁷.

MP-AES was performed using an Agilent 4100 MP-AES. The samples were introduced to the nitrogen plasma using a single pass spray chamber at a pressure of 120 kPa without air injection. The instrument was calibrated with 1, 2, 4, 7, 10 ppm standard solutions in 10 % HCl. The samples were tested in triplicate and the average result was used. A lactic acid (Chapter 3) or levulinic acid (Chapter 5 and 6) rinse solution (5 wt.%) was introduced between samples for 15 s to ensure there was no sample contamination. Ru content (Chapter 3) was analysed using two emission lines with wavelengths of 349.894 nm and 371.803 nm. Cu content was analysed with two emission lines with wavelengths of 324.754 nm and 327.395 nm (Chapter 5 and 6), and Ni content was analysed with two emission lines with wavelengths of 341.476 nm and 352.454 nm (Chapter 6).

2.4. Characterisation

2.4.1. X-ray diffraction

X-ray diffraction (XRD) is a non-destructive technique that can give information about the crystallographic structure of a material. It can give information on the dimensions of the unit cell, crystallite size, and the phase composition. Diffraction occurs when X-rays interact with materials with crystal lattice of dimensions similar to the X-ray wavelength. XRD is a bulk techniques and does not provide surface information.

A simple illustration of XRD is given in Figure 2.4. X-ray beams of wavelength λ are reflected from the sample and produce constructive interference that satisfies Bragg's Law (Equation 2.5). This phenomenon can be applied to both single crystals or powders with large number of randomly oriented crystalline planes, which diffract X-rays at an angle of 2θ .

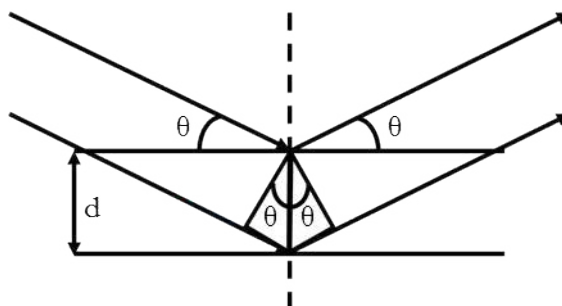


Figure 2.4. Illustration of X-ray beams on a crystal from which Bragg's Law is derived.

Equation 2.5.

$$2d \sin \theta = n\lambda$$

where d = inter-planar spacing; θ = diffraction angle; n = integer; λ = X-ray wavelength.

The average crystallite size of the material can be determined using Scherrer's equation (Equation 2.6). Scherrer's equation is only applicable to particles smaller than 100 nm. XRD reflections must be well defined as the full-width half-maximum (FWHM) is a parameter in the equation meaning that poorly defined reflections indicating small particles sizes cannot always be used to determine the particle size using Scherrer's equation.

Equation 2.6.

$$\tau = \frac{K\lambda}{\beta \cos \theta}$$

where τ = mean crystallite size; K = shape factor; λ = X-ray wavelength; β = FWHM; θ = Bragg angle.

Powder XRD was performed using a PANalytical X'Pert Pro fitted with an X'Celerator detector and a CuK α X-ray source operated at 40 kV and 40 mA, $2\theta = 10$ – 80° . Each sample was scanned from $2\theta = 10^\circ$ to 80° for 30 minutes. The catalysts were ground into fine powder before the analysis. The results obtained were compared with the information in SPDF library for each catalyst.

2.4.2. Inelastic neutron scattering

Inelastic Neutron scattering (INS) is the scattering of free neutrons by matter. Conceptually, they are similar to X-ray scattering techniques such as XRD. Neutrons interact with the nucleus of an atom, contrasting with X-rays that interact with the charge cloud surrounding the atom. Though the technique is highly penetrating, it is non-destructive. It is a bulk technique however, and can only give information averaged across the entire sample. INS is used to study atomic vibrations and other energy transitions. The energy of the incident neutron beam is either lost or increased through its interaction with the sample. The advantages of INS are that all vibrational modes can be accessed (and in theory analysed) and it is a quantitative technique. Hydrogen, in particular, has the highest neutron scattering cross section, making INS an excellent technique for studying hydrogen containing materials such as the carbon supports used in Chapter 4.

INS spectra were recorded with the TOSCA^{8,9} spectrometer at ISIS¹⁰. TOSCA provides high resolution in the region of 24–2000 cm^{-1} . The dried carbon samples (approximately 20 g), were loaded into aluminium cans and then into a closed cycle cryostat, cooled to <30 K and the spectra recorded for approximately 20 h.

2.4.3. Temperature programmed reduction

Temperature programmed reduction (TPR) is used in order to obtain information on the oxidation state of a material and its reducibility. H_2 is passed over the material at a constant flow rate and heating rate. The uptake of H_2 by the sample is detected by thermal conductivity detector (TCD) and is represented as a peak at the corresponding temperature. The area of the peak can be used to quantify the uptake of H_2 .

TPR was carried out using a Thermo 1100 series TPDRO under 75 ml min^{-1} 5 % H_2/Ar , $10 \text{ }^\circ\text{C min}^{-1}$ ramp rate. Samples (0.1 g) sandwiched between quartz wool were pre-treated at $110 \text{ }^\circ\text{C}$ (heating rate = $20 \text{ }^\circ\text{C min}^{-1}$) under Ar for 1 hour prior to reduction in order to clean the surface. After cooling to ambient temperature, analysis was performed under 10 % H_2/Ar (25 ml min^{-1}) between $30\text{--}800 \text{ }^\circ\text{C}$ (heating rate $10 \text{ }^\circ\text{C min}^{-1}$).

2.4.3.1. Temperature programmed reduction mass spectrometry

Mass spectrometry (MS) is used to characterise chemical species by their masses. Samples are ionised and separated based on their mass to charge ratio. In Chapter 4, MS was used in conjunction with TPR (Section 4.3.2) in order to analyse the vent gasses and determine the products of reduction from a carbon support.

A Quantachrome ChemBET was used to carry out TPR analysis on the carbon support. Samples (0.1 g) sandwiched between quartz wool were pre-treated at $110 \text{ }^\circ\text{C}$ (heating rate = $20 \text{ }^\circ\text{C min}^{-1}$) under Ar for 1 hour prior to reduction in order to clean the surface. After cooling to ambient temperature, analysis was performed under 10 % H_2/Ar (25 ml min^{-1}) between $30\text{--}800 \text{ }^\circ\text{C}$ (heating rate $10 \text{ }^\circ\text{C min}^{-1}$). A Hiden Instruments QGA bench-top MS was attached to the apparatus at the vent line in order to analyse mass ranges up to 200 AMU.

2.4.4. X-ray photoelectron spectroscopy

X-ray photoelectron spectroscopy (XPS) is a commonly used surface technique in catalysis research for the analysis of elemental composition, elemental oxidation state, and metal dispersion. The photoelectron effect is the basis of XPS. An atom absorbs a photon of energy ($h\nu$) and ejects a photoelectron with kinetic energy defined by Equation 2.7. The kinetic energy measured by XPS is used to determine the binding energy of the photoelectron, which is characteristic for each element. Because the binding energy is not only characteristic of the element, but affected by the chemical state of the atom, chemical information can be obtained by XPS. XPS is considered surface sensitive, but X-rays can penetrate a sample to a depth of approximately 10 nm.

Equation 2.7.

$$E_k = h\nu - E_b - \phi$$

where E_k = kinetic energy of the ejected photoelectron; $h\nu$ = energy of the X-ray photon; E_b = binding energy of the photoelectron with respect to the fermi level; ϕ = work function of the spectrometer.

XPS was performed using a Kratos Axis Ultra-DLD photoelectron spectrometer, using monochromatic Al $K\alpha$ radiation, operating at 144 W power. High resolution and survey scans were performed at pass energies of 40 and 160 eV respectively. Spectra were calibrated to the C (1s) signal at 284.8 eV and quantified using Casa XPS v2.3.17, using modified Wagner sensitivity factors supplied by the manufacturer.

2.4.5. Transmission electron microscopy

Transmission electron microscopy (TEM) involves the scanning of high energy electrons across a sample surface. Electrons are produced using a tungsten filament, which are then focussed using electromagnetic fields and lenses through a vertical vacuum chamber to the sample. The interaction of the electron beam with the sample results in the emission of secondary electrons and electromagnetic radiation (e.g. X-rays), which are detected and processed to produce an image.

Catalysts investigated by TEM in Chapter 3 were prepared by dispersing the dry catalyst powder onto a holey carbon film supported by a 300 mesh copper TEM grid. Samples were then subjected to bright field (BF) and high angle annular dark field (HAADF) imaging using an aberration corrected JEOL ARM 200CF microscope operating at 200kV.

Catalysts investigated by TEM in Chapter 4 were prepared by dispersing the powder catalyst in ethanol and dropping the suspension onto a lacey carbon film over a 300 mesh copper grid. TEM was carried out using a JEOL 2100 with a LaB6 filament operating at 200 kV.

2.4.6. Scanning electron microscopy

Scanning electron microscopy (SEM) is very similar to TEM. The main differences between TEM and SEM are: TEM uses a broad static beam as opposed to the focussed fine point that scans in a rectangular raster pattern in SEM; the accelerating voltages used for SEM are much lower than used for TEM; and the samples do not need to be thin for SEM, simplifying sample preparation. SEM cannot obtain the same high resolution images that TEM can obtain.

Catalysts investigated by SEM presented in Chapter 6 were prepared by dispersing the powder catalyst onto a carbon adhesive. Images were obtained using a Hitachi TM3030 Tabletop Microscope operating at 15 kV.

2.4.7. Energy dispersive X-ray spectroscopy

Energy dispersive X-ray spectroscopy is a technique generally used in conjunction with TEM or SEM for determination of the surface elemental composition of a sample. An incident electron beam is fired at the sample surface, resulting in the ejection of an electron from a core electron energy level and the formation of a “core-hole”. In order to fill the core-hole, an electron from an outer electron energy shell occupies the vacancy and excess energy is released in the form of an X-ray. EDX detectors measure the number of X-rays produced against their energy, which is characteristic of the element they are emitted from. This technique can be used to create elemental “maps” of the surface of a sample, as demonstrated in Chapters 4 and 6. EDX analysis was carried out in conjunction with the TEM and SEM analyses and uses the same apparatus as described in Sections 2.4.5 and 2.4.6.

2.4.8. Brunauer-Emmett-Teller surface area analysis

Surface area analysis is an important consideration in catalysis research and has been shown to affect the activity of catalysts. It is therefore important to determine it accurately. The Brunauer-Emmett-Teller (BET) method is the most widely used technique for surface area determination. This method is an extension of the Langmuir model of monolayer adsorption to cover multilayer adsorption. The method makes three key assumptions:

1. Gas molecules can adsorb on a solid in infinite layers
2. There is no interaction between each layer
3. The Langmuir model can be applied to each model

The determination of BET surface area is given by the BET equations show in Equations 2.8–2.10.

Equation 2.8.

$$\frac{p}{V(p_0 - p)} = \frac{1}{V_m C} + \frac{C - 1}{V_m C} \cdot \frac{p}{p_0}$$

where p = equilibrium pressure of the adsorbate at the adsorption temperature; p_0 = saturation pressure of the adsorbate at the adsorption temperature; V = volume of gas adsorbed at pressure p ; V_m = volume of gas required to form a monolayer; C = BET constant, which is related to the heat of adsorption.

Equation 2.9.

$$S_{\text{total}} = \frac{V_m N_A \sigma}{22414}$$

where S_{total} = total surface area; N_A = Avogadro's constant; σ = the adsorption cross section of the adsorbing species; 22414 L mol⁻¹ is the molar volume of a gas.

Equation 2.10.

$$S_{\text{BET}} = \frac{S_{\text{total}}}{m}$$

where S_{BET} = BET surface area; m = mass of the solid sample.

Surface areas were determined by multi-point N₂ adsorption at 77 K on a Micromeritics Gemini 2360 according to the Brauner Emmet Teller (BET) method. Prior to the analysis, samples were degassed at 120 °C for 1 h under N₂ flow.

2.4.9. N₂O titration determination of metal surface area

N₂O titration is used for the determination of metal surface area. N₂O can oxidise surface metal particles while itself being reduced to N₂ as shown in Scheme 2.1 below.

Scheme 2.1.

The volume of N₂ is obtained, and the number of molecules of Cu is calculated using Avagadro's constant. A total of 1.46×10¹⁹ Cu atom m⁻² and a stoichiometry of 2Cu/N₂ were used to calculate Cu surface area^{11,12}.

N₂O titration was performed on a Quantachrome ChemBet equipped with a zeolite trap. Prior to the analysis, the catalysts were reduced *in-situ* under 30 ml min⁻¹ of 10% H₂/Ar flow at 180 °C. Then the temperature was reduced to 65 °C with He purging in order to remove H₂ adsorbed on the catalyst surface. N₂O was pulsed until no signals due to N₂ formation were detected using a TCD detector. After titration, a known amount of N₂ was fed for calibration.

2.4.10. Inductively coupled plasma atomic emission spectroscopy

Inductively coupled plasma atomic emission spectroscopy (ICP-AES) is identical to MP-AES (described in Section 2.3.2.4) except it uses inductively coupled plasma (ICP) rather than microwave plasma (MP) to excite atoms and ions. The ICP-AES data presented in Chapter 5 were obtained using a Shimadzu ICPE-9000 instrument. 25 mg of catalyst was dissolved in 0.5 mL of HF, diluted with 3 mL of HNO₃ and left at 80 °C overnight. After dissolution of the catalyst the solution was diluted to 50 mL with deionised water. 1 mL of this solution was further diluted to 50 mL with deionised water, which was

used for the analysis. The instrument was calibrated using Cu and Zr solutions of 0, 0.1, 0.5, 1.0, 2.0, and 5.0 ppm (diluted from a solution of 1000 ppm). The Cu and Zr wavelengths used for the analysis were 213.60 nm and 339.20 nm respectively.

2.4.11. CHN analysis

CHN analysis is a type of combustion analysis used to determine the amounts of carbon, hydrogen, and nitrogen in an organic sample. During the combustion process, carbon is converted to CO₂; H₂ is converted to H₂O; and N₂ is evolved as a gas or converted to an oxide of N₂. The combustion products are then passed over high purity Cu by an inert gas (usually He) in order to remove any oxygen not consumed in during the initial combustion process and to convert any oxides of N₂ to N₂ gas. The gasses are then quantified using a TCD.

CHN analysis is presented in Chapter 4 for the characterisation of carbon supports. CHN analysis was carried out by Warwick Analytical Services, University of Warwick Science Park, The Venture Centre, Sir William Lyons Road, Coventry, CV4 7EZ, UK using a CE440 Elemental Analyser equipped with a TCD¹³.

2.5. References

- 1 M. V. Twigg, *Catalyst Handbook*, Manson Pub., 1996.
- 2 L. Prati and A. Villa, *Catalysts*, 2012, **2**, 24.
- 3 L. Prati and G. Martra, *Gold Bull.*, 1999, **32**, 96–101.
- 4 J. Turkevich, *Gold Bull.*, 1985, **18**, 86–91.
- 5 J. A. Lopez-Sanchez, N. Dimitratos, C. Hammond, G. L. Brett, L. Kesavan, S. White, P. Miedziak, R. Tiruvalam, R. L. Jenkins, A. F. Carley, D. Knight, C. J. Kiely and G. J. Hutchings, *Nat Chem*, 2011, **3**, 551–556.
- 6 P. N. Dyer and R. Pierantozzi, US 4605639 A, 1986.
- 7 K. W. Jackson and T. M. Mahmood, *Anal. Chem.*, 1994, **66**, 252R–279R.
- 8 P. C. H. Mitchell, *Vibrational Spectroscopy with Neutrons: With Applications in Chemistry, Biology, Materials Science and Catalysis*, World Scientific, 2005.
- 9 D. Colognesi, M. Celli, F. Cilloco, R. J. Newport, S. F. Parker, V. Rossi-Albertini, F. Sacchetti, J. Tomkinson and M. Zoppi, *Appl. Phys. A*, 2002, **74**, s64–s66.
- 10 <https://www.isis.stfc.ac.uk/>

- 11 X.-R. Zhang, L.-C. Wang, C.-Z. Yao, Y. Cao, W.-L. Dai, H.-Y. He and K.-N. Fan, *Catal. Letters*, 2005, **102**, 183–190.
- 12 C.-Z. Yao, L.-C. Wang, Y.-M. Liu, G.-S. Wu, Y. Cao, W.-L. Dai, H.-Y. He and K.-N. Fan, *Appl. Catal. A Gen.*, 2006, **297**, 151–158.
- 13 <https://www.exeteranalytical.co.uk/>

Chapter 3

Ruthenium supported on carbon for the hydrogenation of lactic acid to 1,2-propanediol

3.1. Introduction

The production of 1,2-propanediol (PDO), discussed in Chapter 1, section 1.3.1.1, is a very interesting and useful topic in green chemistry. Though it would seem that the selective synthesis of PDO has been achieved, it has mostly been investigated using commercially available Ru/C materials. Studies in the open literature are mostly focussed on the optimisation of reaction parameters^{1,2} or the use of promoters^{3,4}. It has been noted that the dispersion of Ru is a key factor in the catalytic activity of Ru-based catalysts², and that a high surface area support can encourage a good dispersion of Ru⁵. Though novel preparations of Ru-based catalysts, such as one proposed by Yang *et al.*⁶, have been reported, there are currently few examples. Work on the optimisation of the catalysts' preparation is largely absent from the literature.

The work presented here is similar to the work presented by Jang *et al.*⁵. A selection of carbon black supports was investigated for the hydrogenation of lactic acid using Ru. They found that the Ru particle size was strongly influenced by the surface area of the carbon support. A Ketjen black-supported Ru catalyst had the highest surface area, pore size, smallest Ru particle size, and consequently activity toward lactic acid hydrogenation. This work goes slightly further than investigating carbon supports, and investigates the use of an alternative catalyst preparation method (sol immobilisation) and the use of milder reaction conditions. The carbons in this study were not treated with acids, unlike those presented in the study by Jang *et al.*

The following work in this chapter investigates the choice of carbon support used and its effect on the catalytic activity. An alternative preparation method – sol immobilisation – is also studied and compared with a commercially obtained catalyst.

3.2. Results and discussion

3.2.1. Catalytic data

A series of 5 wt.% Ru/C catalysts were prepared on a range of different carbon supports by wet impregnation (WI) as described in Chapter 2, section 2.2.1. The catalysts were tested for the activity to lactic acid hydrogenation and compared with a commercial 5 wt.% Ru/C catalyst, which was used as a benchmark. The results are shown in Table 3.1.

The only product observed by HPLC analysis was PDO, therefore the selectivity to PDO was considered to be 100 %. When compared with literature, this observation is unusual. For example, Dumesic and co-workers have reported by-products such as propanol and propanoic acid when using a Cu/SiO₂ catalyst⁷, and Zhang *et al.* reported lower hydrocarbon production using a Ru/C catalyst under much harsher conditions (higher temperature and H₂ pressure)⁸. The high selectivity to PDO in this case can be attributed to the different preparation methods used, the varying types of carbon support and comparatively milder reaction conditions employed.

Table 3.1. A comparison of PDO yields for commercial catalyst with 5 wt.% Ru/C catalysts prepared by WI on different carbon supports. **Reaction conditions:** 5 wt.% lactic acid, 120 °C, 35 bar H₂, 2.5 h.

Type of carbon support	PDO yield / %
Commercial 5 wt.% Ru/C catalyst	19
ROX 0.8	13
GCN3070	10
G60	9
Graphene oxide	2
XC72R	15

All the catalysts prepared by WI on different carbon types showed some activity, but all were less active than the commercial catalyst. Graphene oxide showed the lowest activity with a conversion of only 2 %. This is in agreement with the work of Jang *et al.*⁵ who showed that graphitic carbon had a low surface area, which in turn resulted in a large Ru particle size and a low activity towards lactic acid hydrogenation. Of the prepared catalysts, XC72R was the most active showing 15 % conversion (*vs.* 19 % for the commercial catalyst). Because XC72R was the most active carbon support, it was chosen as the support to investigate an alternative method of metal deposition.

A 5 wt.% Ru/C catalyst was prepared by SI (designated 5 wt.% Ru/XC72R-SI) and compared once again with the commercial catalyst. Under the same reaction conditions presented in Table 3.1, 5 wt.% Ru/XC72R-SI performed better than commercial catalyst and achieved a 1,2-propanediol yield of 23 % compared to 19 % for the commercial catalyst. 5 wt.% Ru/XC72R-SI also performed better than the Ru/XC72R catalyst prepared by WI (23 % *vs.* 15 %), which shows that the deposition method of the Ru onto the support is as important a factor as the choice of support itself.

Considering the result obtained with 5 wt.% Ru/XC72R-SI, it and the commercial catalyst were investigated in greater detail. Figure 3.2 shows the activity of the catalyst over an extended time period up to and including 32 hours. Even at longer reaction times, the only product observed by both HPLC and GC analysis was PDO for both catalysts. There are three important features in Figure 3.1. The first observation is that both catalysts showed an induction period of approximately 15 minutes. Secondly, the catalyst prepared by SI was initially more active than the commercial catalyst. Finally, the SI catalyst ceased to be active after 5 hours, but the commercial catalyst continued to be active for much longer and achieved a conversion of 75 % after 32 hours.

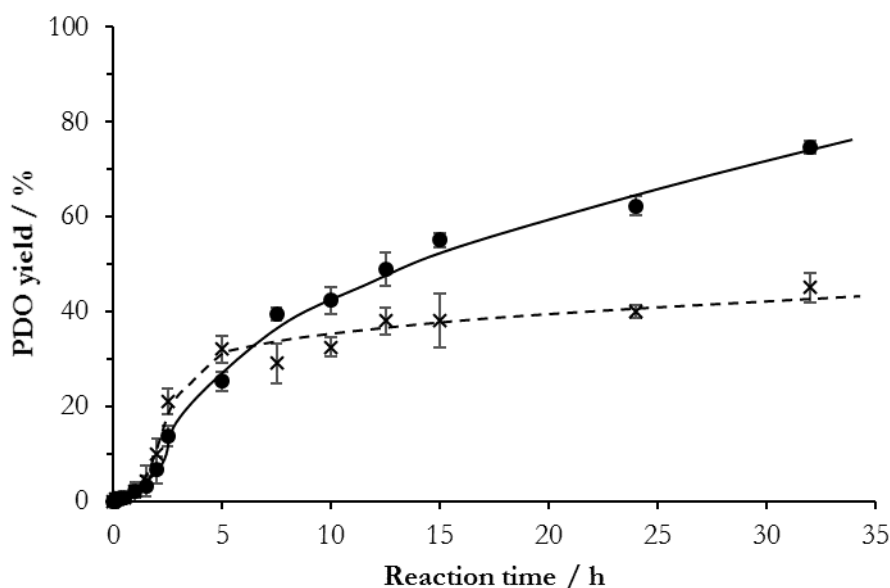


Figure 3.1. The activity of 5 wt.% Ru/XC72R-SI and the commercial Ru/C catalyst over extended time periods. ×: 5 wt.% Ru/XC72R-SI; •: 5 wt.% Ru/C commercial. **Reaction conditions:** 5 wt.% lactic acid in H₂O, 120 °C, 35 bar H₂.

Addressing the first observation made in the previous paragraph, there are several reasons why an induction period may be observed. Figure 3.2 shows the induction period more clearly. One possible cause is the leaching of Ru from the carbon support prior to a reaction taking place catalysed by the leached Ru in solution. The reaction solution was subjected to MP-AES analysis and it was found that

no Ru was present after the reaction. The hydrogenation of lactic acid is therefore a heterogeneous process and the induction period cannot be attributed to metal leaching. Another possible cause is the reduction of surface Ru particles *in situ*. To investigate if this was the cause, both catalysts (5 wt.% Ru/XC72R-SI and 5 wt.% Ru/C commercial) were reduced *ex-situ* prior to the reaction. Both of these catalysts were less active than the non-reduced catalysts. After 2.5 hours 5 wt.% Ru/XC72R-SI showed 23 % conversion versus 18 % conversion for the non-reduced and reduced catalysts respectively, while the 5 wt.% Ru/C commercial catalyst showed 19 % conversion versus 13 % conversion for non-reduced and reduced catalysts respectively. However, the ease with which Ru oxidises is a well-known phenomenon⁹⁻¹¹, so the apparent decrease in activity on pre-reduction could well be due to an extended heat treatment rather than reduction of the metal. However, it is also possible that the hydrophobic nature of the carbon supports plays a role in keeping the water off the surface of the catalyst, preparing it for the adsorption of the organic acid. The induction period therefore probably involves the preparation of the active catalyst surface, which includes both lactic acid, H₂ and H₂O.

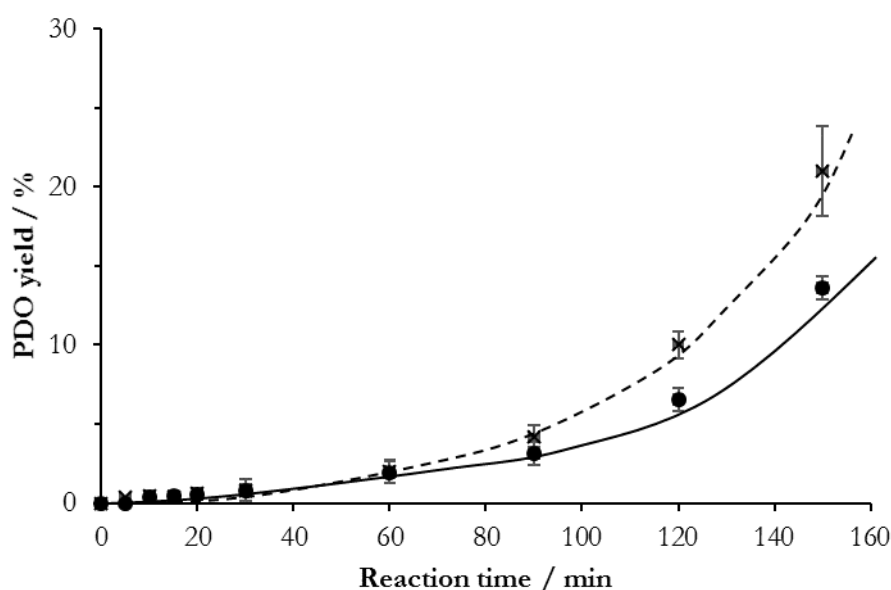


Figure 3.2. The activity of the SI and commercial catalysts up to 2.5 hours. ×: 5 wt.% Ru/XC72R-SI; ●: 5 wt.% Ru/C commercial. **Reaction conditions:** 5 wt.% lactic acid in H₂O, 120 °C, 35 bar H₂.

Between 15 and 160 minutes (following the induction period), the reaction was determined to be first order in lactic acid, and the first order rate constants measured to be $4.5 \times 10^{-4} \text{ s}^{-1}$ and $3.7 \times 10^{-4} \text{ s}^{-1}$ for 5 wt.% Ru/XC72R-SI and 5 wt.% Ru/C commercial catalysts respectively. Table 3.2 shows the turnover frequencies (TOF) of the catalysts compared to TOFs calculated from data provided in the literature as a comparison. Jang *et al.* (Table 3.2, final entry) also used a 5 wt.% Ru/C catalyst, and under

much harsher conditions than this work (150 °C and 50 bar H₂), This highlights the importance of catalyst preparation in the activity of the final catalyst.

Table 3.2. Turnover frequencies of catalysts prepared in this study compared to literature.

Catalyst	Productivity / mol LA g _{catalyst} ⁻¹ h ⁻¹	TOF / h ⁻¹	Reference
5 wt.% Ru/XC72R-SI	1.84	4116	This work
5 wt.% Ru/C commercial	1.1	2312	This work
Ru/C	0.2	405	Miller <i>et al.</i> ¹
Ru/C	0.71	1435	Jang <i>et al.</i> ⁵

Both the SI and commercial catalysts were both tested for their activities on successive reuses as described in Section 2.3.1. The results of these experiments are shown in Figure 3.3.

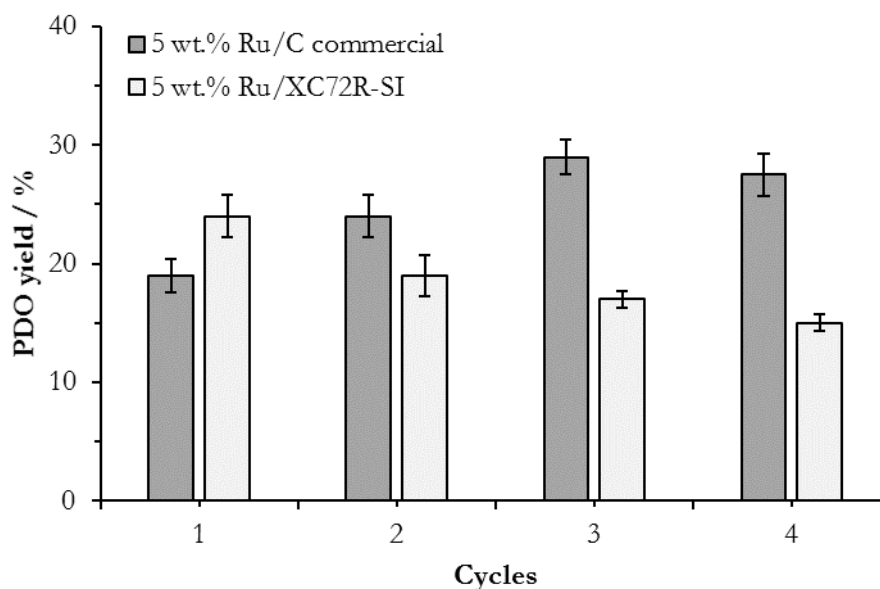


Figure 3.3. The activity of the SI and commercial catalysts on successive reuses.

Reaction conditions: 5 wt.% lactic acid in H₂O, 120 °C, 35 bar H₂, 2.5 h.

Both catalysts show significantly different behaviour on reuse studies. In both cases the only product observed was, once again, PDO. 5 wt.% Ru/XC72R-SI showed a steady decrease in activity on successive reuse, but the 5 wt.% Ru/C commercial catalyst showed a steady increase in activity. These trends can be directly compared to the time-on-line profiles in Figure 3.1. The four reuse cycles are simulated well by the first 10-hour period of the reaction. During the first 10-hour period the activity of the 5 wt.% Ru/C commercial catalyst steadily increased, whereas the SI catalyst activity effectively ceased after 5 hours. The catalyst time-on-line data was recorded for the initial period of the reaction after reuse

and compared to the initial time-on-line data in Figure 3.4. Comparing the used catalyst to the fresh catalyst reveals two interesting features. Both catalysts showed an induction period even on reuse, which would suggest that the preparation of the active surface suggested as the explanation previously needed to happen again after the catalysts drying step. 5 wt.% Ru/C commercial catalyst showed an increase in activity after 30 minutes, but 5 wt.% Ru/XC72R-SI showed a slight decrease. In order to understand the described data above, the catalysts were characterised.

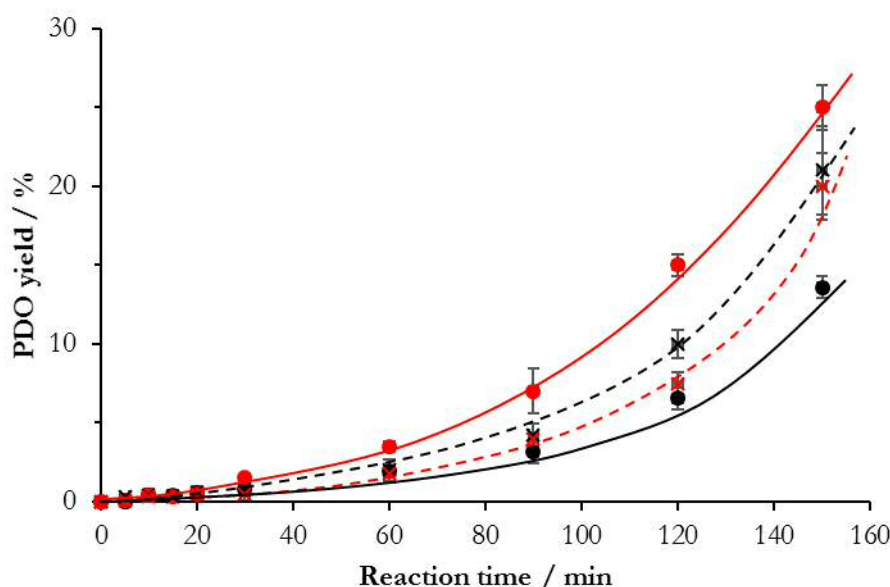


Figure 3.4. Initial time-on-line profiles of the SI and commercial catalysts on initial use and reuse. ×: 5 wt.% Ru/XC72R-SI fresh; ●: 5 wt.% Ru/C commercial fresh; ×: 5 wt.% Ru/XC72R-SI after 1 use; ●: 5 wt.% Ru/C commercial after 1 use. **Reaction conditions:** 5 wt.% lactic acid in H₂O, 120 °C, 35 bar H₂.

3.2.2. Characterisation

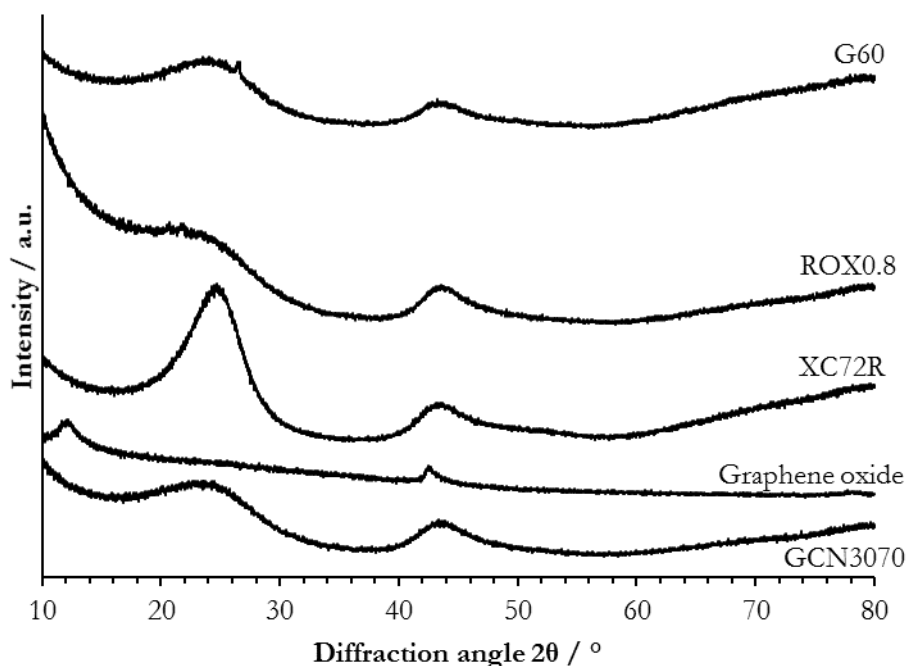
The BET surface area of both the catalysts and the carbon supports were determined and are shown in Table 3.3. The addition of Ru to the carbon did not have a significant effect on the overall surface area for any of the carbon supports. Furthermore, the BET surface area did not show any correlation with the activity data. Though 5 wt.% Ru/C commercial showed both the highest activity and the highest BET surface area of the catalysts prepared by wet impregnation, the catalyst prepared using G60 had the next largest surface area, but exhibited poor activity. By contrast, 5 wt.% Ru/XC72R-SI showed high initial activity compared to 5 wt.% Ru/C commercial but had a significantly lower surface area (835 and 200 m² g⁻¹) respectively. It also shows that the surface area of the overall catalyst in this case wasn't affected by the deposition method of the Ru, with 5 wt.% Ru/XC72R-WI and -SI showing similar surface areas.

Table 3.3. The surface areas of the prepared 5 wt.% Ru/C catalysts and their supports.

Carbon support	Surface area / $\text{m}^2 \text{g}^{-1}$		
	Carbon only ^a	5 wt.% Ru/C ^a	Ru surface area ^b
Commercial	n/a	835	3.0
ROX 0.8	495	489	n/d
GCN3070	586	580	n/d
G60	635	650	n/d
XC72R (WI)	213	204	n/d
XC72R (SI)	213	200	3.1

n/d = not determined; ^a BET total surface area; ^b Metal surface area determined by CO chemisorption.

XRD patterns for the carbons and the 5 wt.% Ru/C catalysts prepared by wet impregnation (Figures 3.5 and 3.6 respectively) showed that there were no differences after deposition of Ru as there were no reflections that can be assigned to Ru, indicating either a homogeneous metal dispersion or that the metal particles sizes are below 3-4 nm. However, CO chemisorption on 5 wt.% Ru/XC72R and the commercial 5 wt.% Ru/C catalyst showed that there is Ru present on the surface and that the metal surface areas were similar at $3 \text{ m}^2 \text{g}^{-1}$.

**Figure 3.5.** XRD patterns for the carbon supports only used for the preparation of catalysts by WI.

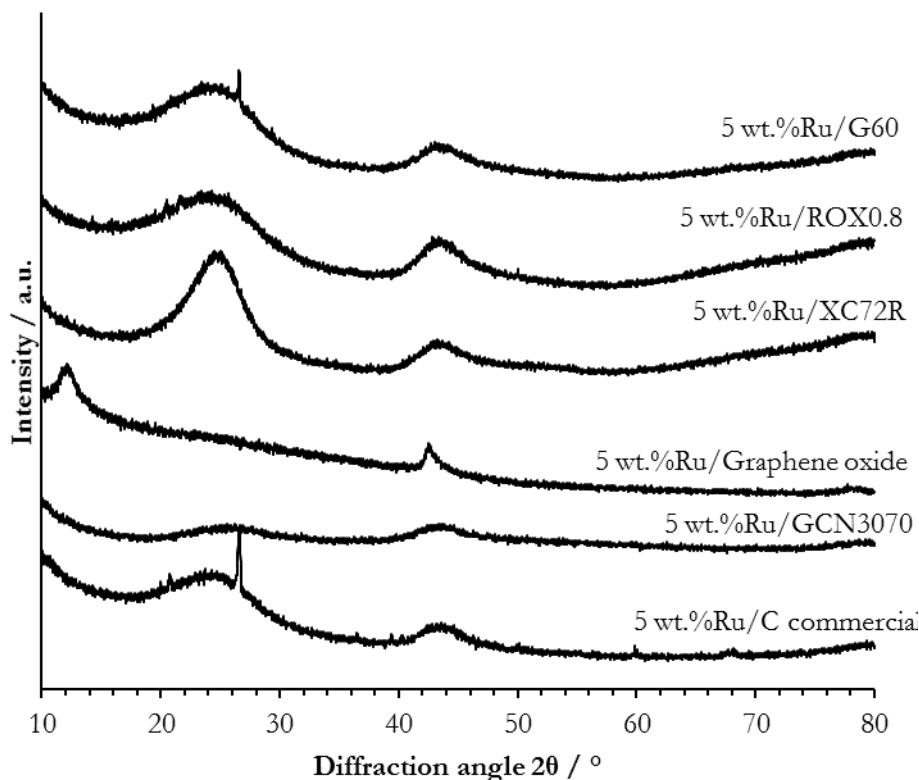


Figure 3.6. XRD patterns for 5 wt.%Ru/C catalysts supported on different carbons by WI.

All catalysts were subject to TPR analysis (Figure 3.7). The TPR profiles are quite different depending on the type of carbon support used. 5 wt.% Ru/C commercial and the catalyst supported on GCN3070 showed two distinctive reduction signals at just below 100 °C and above 200 °C. GCN 3070 is an acid activated carbon and the presence of the higher reduction peaks may be due to the reduction of surface functional groups. 5 wt.% Ru/XC72R showed two reduction signals below 100 °C and another, much broader reduction signal at 140 °C. The first two lower temperature signals can be assigned to the reduction of Ru(III) to Ru(II) and the second (higher temperature) reduction signal to the sequential reduction of Ru(II) to Ru(I), but there is a possibility of total reduction from Ru(II) to metallic Ru(0)^{11,12}. The catalysts prepared using G60 and ROX0.8 show reduction peaks around 100 °C, but the catalysts are far less active. 5 wt.% Ru/graphene oxide was observed to reduce at a higher temperature than the others, with a single high intensity reduction signal at 150 °C. None of the catalysts were reduced prior to the reaction, but it is expected that all catalysts, with the exception of 5 wt.% Ru/graphene oxide, were reduced under reaction conditions (120 °C, 35 bar H₂) and were active. The inactivity of the catalyst supported on graphene oxide can therefore be attributed to the lack of metallic Ru on the catalyst during reaction. The reduction of the catalysts is expected to have occurred in situ during the 15-minute induction period observed in Figures 3.2 and 3.4. The relative sharpness of the TPR peak for the catalyst supported on XC72R compared with the commercial catalyst is indicative of a faster and more facile

reduction process, which helps to explain why the induction period observed is shorter than the commercial catalyst – the surface reduction of Ru occurs faster and is available more quickly for reaction. It could be considered that this is due to the nature of the carbon support. XC72R is a highly conductive support and reduction is a process of electron gain; the rate of the Ru reduction may be enhanced by this compared with the less conductive commercial catalyst.

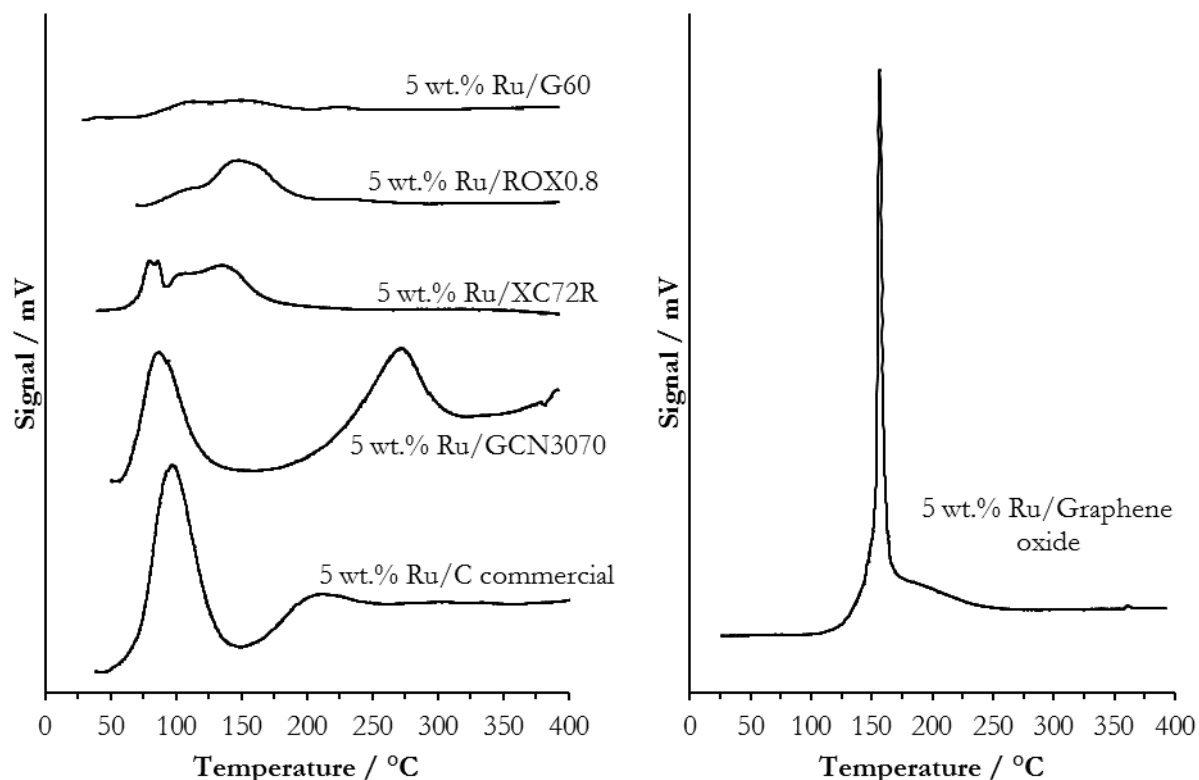


Figure 3.7. TPR profiles for all 5 wt.% Ru/C catalysts prepared on different carbon supports. Note: 5 wt.% Ru/graphene oxide is on a separate axis due to the much higher intensity of the reduction signal compared to the other TPR traces.

Because the two most active catalysts – 5 wt.% Ru/XC72R-SI and 5 wt.% Ru/C commercial – showed two completely different reaction profiles with both continuous use (Figure 3.1) and successive reuse (Figures 3.3), therefore both were characterised in greater detail. There was no change in BET surface area on extended use or successive reuse, suggesting there was no coking or pore blocking restricting the reactants' access to the Ru metal sites. MP-AES analysis revealed that there was no leaching of the Ru during the reaction causing the deactivation of the catalyst, or contributing to the activity in the case of 5 wt.% Ru/C commercial catalyst.

XPS analysis was performed on the fresh and used catalyst samples and the data for both 5 wt.% Ru/C commercial and 5 wt.% Ru/XC72R-SI is presented in Figures 3.8 and 3.9 respectively. Because there was an overlap of the C(1s) and Ru(3d_{5/2}) core energy levels, XPS analysis of Ru/C systems can be

difficult. Looking at the lesser-studied Ru(3p_{3/2}) energy levels in combination with the Ru(3d_{5/2}) can still yield useful chemical state information however. There was a clear shift in the binding energies for Ru(3p_{3/2}) and Ru(3d_{5/2}) towards lower binding energies for both catalysts on successive reuse cycles. The binding energies of the Ru(3p_{3/2}) levels in 5 wt.% Ru/C commercial and 5 wt.% Ru/XC72R-SI were 463.0 and 463.5 eV respectively, which is consistent with RuO₂. The 0.5 eV difference between both values can be attributed to different levels of hydration, which is consistent with analysis of bulk hydrated and bulk anhydrous RuO_x species^{13,14}. Note that there are on 3 use cycles analysed for 5 wt.% Ru/XC72R-SI compared with 4 for 5 wt.% Ru/C commercial due to limited amount of material.

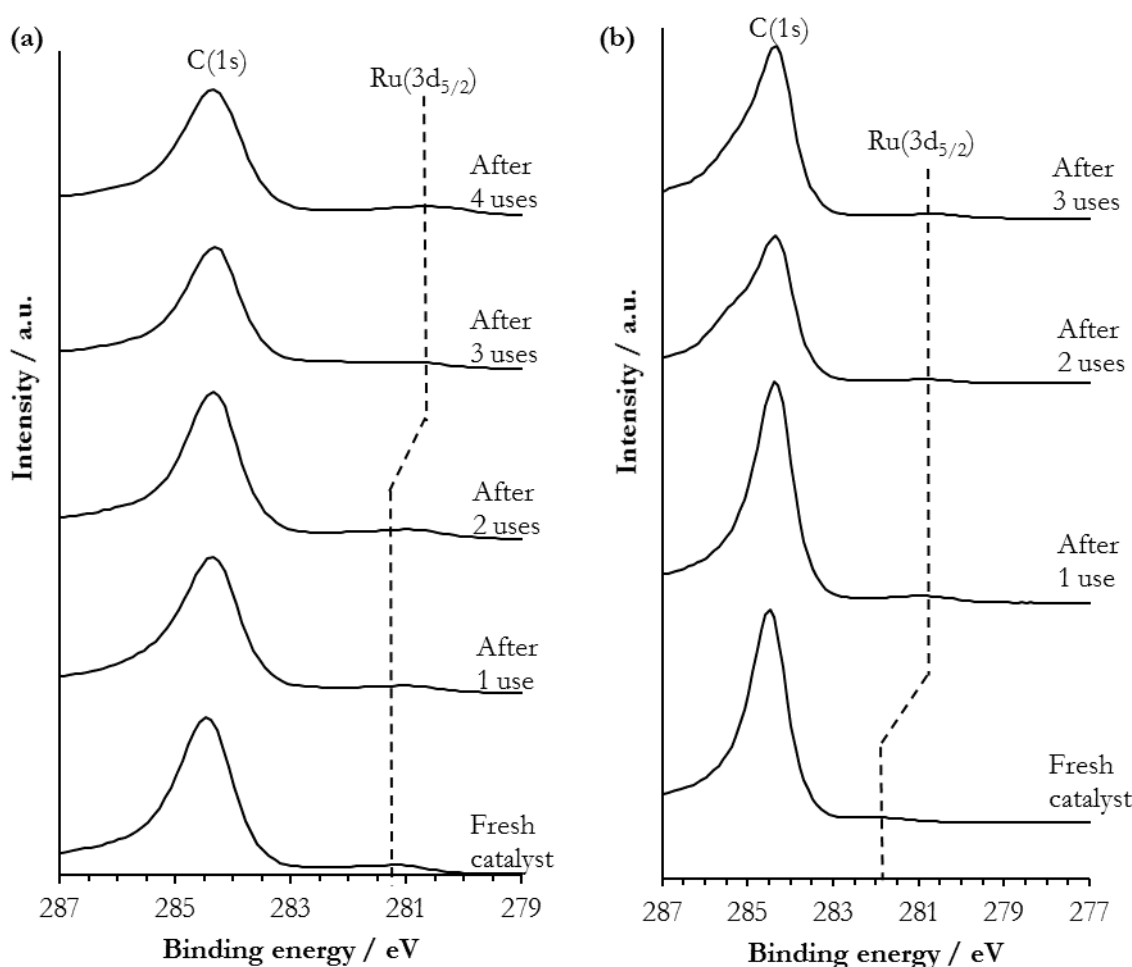


Figure 3.8. Overlapping of Ru(3d_{5/2}) and C(1s) core-level signals in XPS (a) 5 wt.% Ru/C commercial; (b) 5 wt.% Ru/XC72R-SI.

There was a downward shift in binding energy in both the Ru(3p) and Ru(3d) levels by approximately 1 eV on successive reuse of both catalysts. The final binding energies after 4 reaction cycles for the Ru(3p_{3/2}) and Ru(3d_{5/2}) energy levels were 462.2 and 280.3 eV respectively, which is consistent with presence of metallic Ru. The downward shift was most pronounced after the fourth reaction in the commercial 5 wt.% Ru/C catalyst, but observed after just one reaction in 5 wt.% Ru/XC72R-SI. The

shift occurred after each catalyst showed their greatest activity, further confirming that metallic Ru is essential for the catalyst activity. The XPS data show that Ru remained reduced to an extent after each reaction despite the earlier mention of difficulty in keeping Ru in a reduced state. This observation would suggest that re-oxidation of the Ru on exposure to ambient conditions was not a deep oxidation, but the formation of a surface oxide layer.

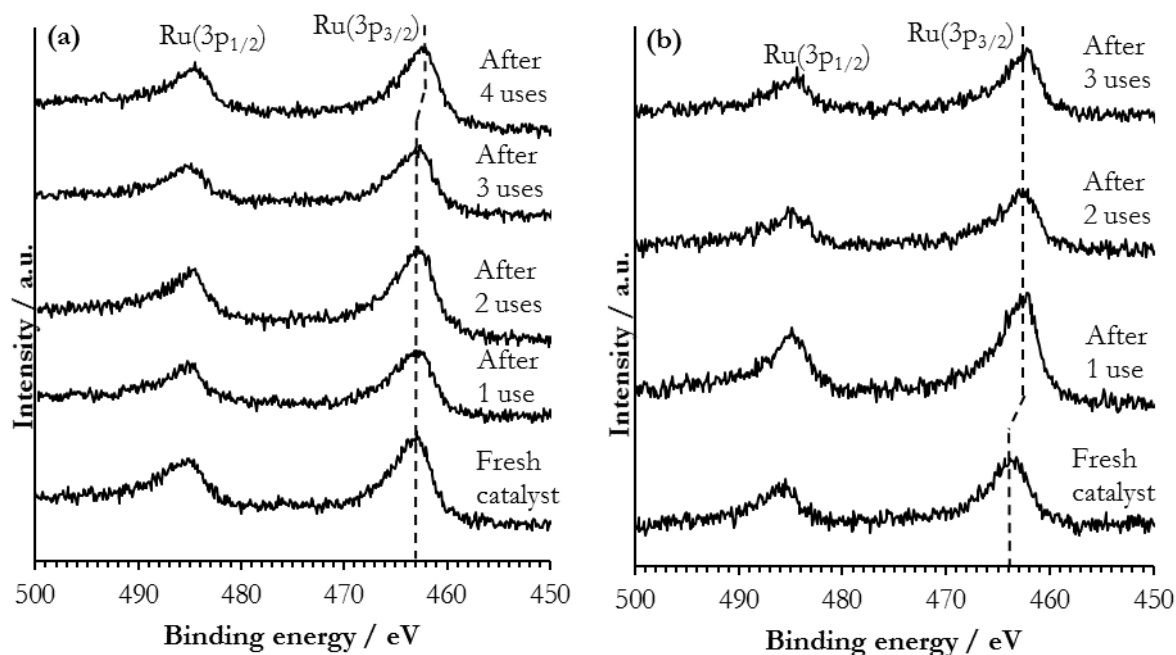


Figure 3.9. Ru($3p_{3/2}$) core-level spectra for successive reuse cycles. (a) 5 wt.% Ru/C commercial; (b) 5 wt.% Ru/XC72R-SI.

The change in Ru energy levels was consistent between the two catalysts, but there was a marked difference in C(1s) and O(1s) signals between 5 wt.% Ru/C commercial and 5 wt.% Ru/XC72R-SI. On successive reuse of the 5 wt.% Ru/XC72R-SI catalyst there were new features observed in both C(1s) (at 286.7 and 289.2 eV) and O(1s) (at 532.5 and 533.6 eV) that can be seen in Figures 3.9b and 3.11 respectively. The values are indicative of $-C-O$ containing species such as either of hydroxyl groups, and $-C=O$ groups, including ketones, carboxylic acid, anhydride and lactone groups¹⁵. This could suggest the retention of lactic acid or the formation of poly- or cyclic-lactide species on the surface of the catalyst¹⁶. Retention of lactide species on the Ru active sites could inhibit further reactivity and be responsible for the catalyst deactivation. These features were not observed on 5 wt.% Ru/C commercial, which explains why the catalyst did not deactivate on successive reuse cycles, but it still needs to be explained *why* these features are not observed. The PVA stabilising ligand used in 5 wt.% Ru/XC72R-SI may be responsible for these effects. PVA can be washed from a catalyst prepared by SI by washing at elevated temperatures with water¹⁷. Partial removal is achieved but enough to allow the reactants to access the

active sites. It is possible that, under reaction conditions, the residual PVA can react with lactic acid and form a surface layer that would deactivate the catalyst. This effect was absent from the commercial catalyst due to the absence of PVA. Partial removal of the PVA from 5 wt.% Ru/XC72R-SI would also contribute to the induction period observed in both the unused and used catalyst in Figures 3.2 and 3.4 respectively.

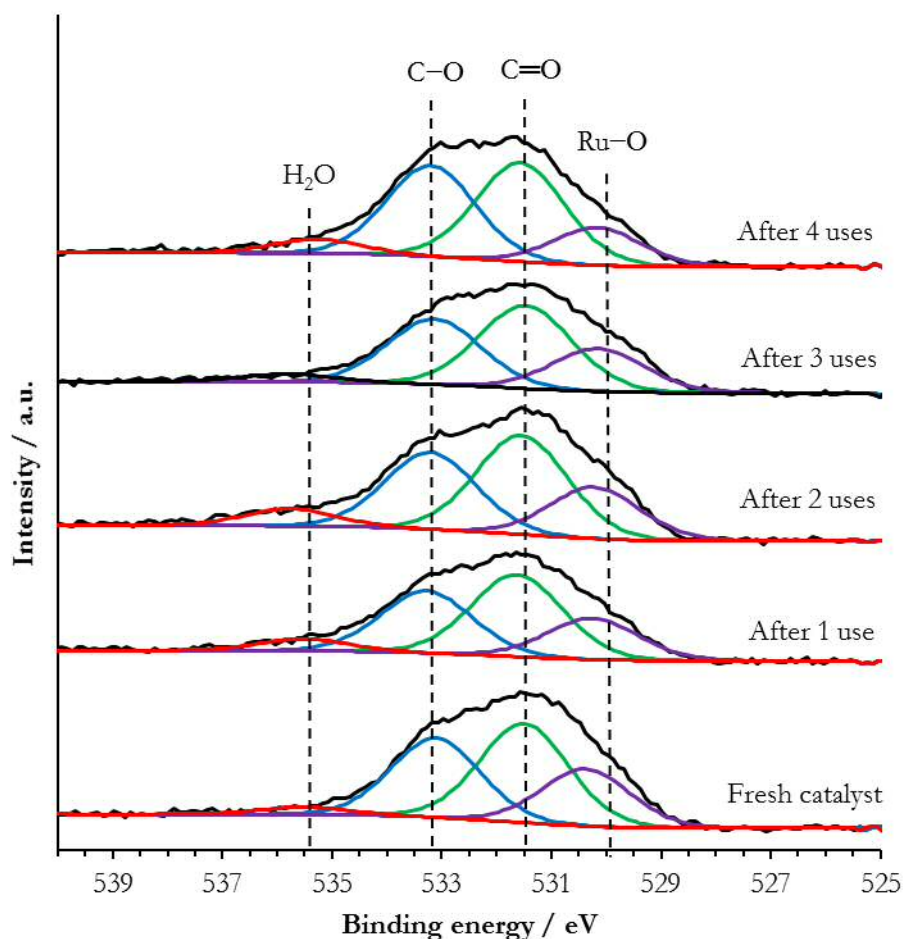


Figure 3.10. O(1s) core level spectra for the 5 wt.% Ru/C commercial after increasing reaction cycles.

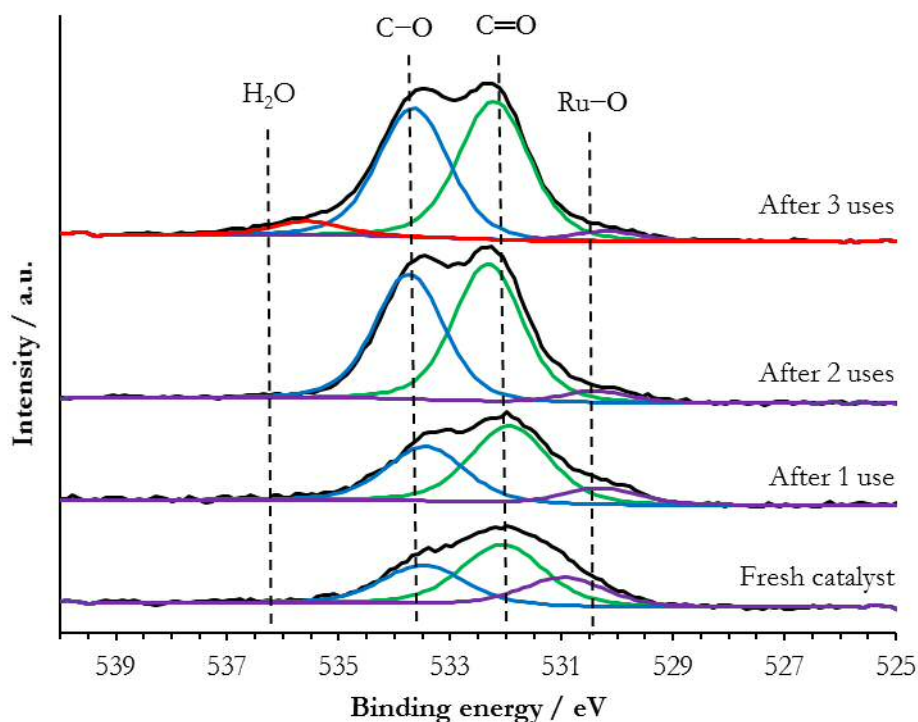


Figure 3.11. O(1s) core level spectra for the 5 wt.% Ru/XC72R-SI after increasing reaction cycles.

There was a further O(1s) species observed at approximately 530 eV that decreased in intensity on successive reuse for both 5 wt.% Ru/C commercial and 5 wt.% Ru/C XC72R-SI (Figures 3.10 and 3.11). Signals around this energy are generally assigned to metal oxides, which would appear to be reducing to metallic Ru. This could be attributed to RuO_x/Ru as samples are air handled prior to analysis in the spectrometer. The signal at 535.5 eV is characteristic of chemisorbed water¹⁸. 5 wt.% Ru/C commercial showed a very similar oxygen profile but the overall concentrations of oxygen and the carbon functionalities were far less than those present in 5 wt.% Ru/XC72R-SI, as evidenced by the lack of a signal at 289 eV in the C(1s)/Ru(3d_{5/2}) spectra.

High-angle annular dark field scanning transmission electron microscopy (HAADF-STEM) analysis was carried out on fresh catalysts as well as at different stages of their reuse cycles. In the fresh 5 wt.% Ru/C commercial catalyst (Figure 3.12) there were discrete particles present with a size of approximately 2 nm, but also present were longer lines of more amorphous particles that were 1–1.5 nm in width and up to 10 nm in length that also contain Ru. The discrete nanoparticles were semi-crystalline, but the longer lines more disordered and lacking in any arrangement could be assigned to Ru metal. These disordered structures may be indicative of only partially converted Ru precursor material or hydrated RuO_x . After the first cycle of catalytic testing, the structure of these particles started to change (Figure 3.13). The discrete nanoparticles with an approximate size of 2 nm were still present, but the disordered structures started to break down to form discrete particles themselves with an approximate size of 1 nm.

The newly formed particles were still semi-crystalline however, thereby suggesting they were still RuO_x species, rather than metallic Ru. The average particle size was 1.4 nm. After 4 reaction cycles, the surface of the catalyst changed significantly (Figure 3.14). The mean particle size increased to 2.2 nm, the size distribution increased, and the particles were more crystalline in nature in a way that was more consistent with metallic Ru. This observation correlates well with the XPS data presented earlier, which suggested showed a shift in binding energy towards Ru(0) after the 4th reaction cycle, suggesting Ru with increasing metallic character is formed. These observations suggest that exposure to reaction conditions resulted in the formation of crystalline Ru nanoparticles on the catalyst surface, which correlates to a continued increase in activity on extended use and increased activity on successive reuse cycles.

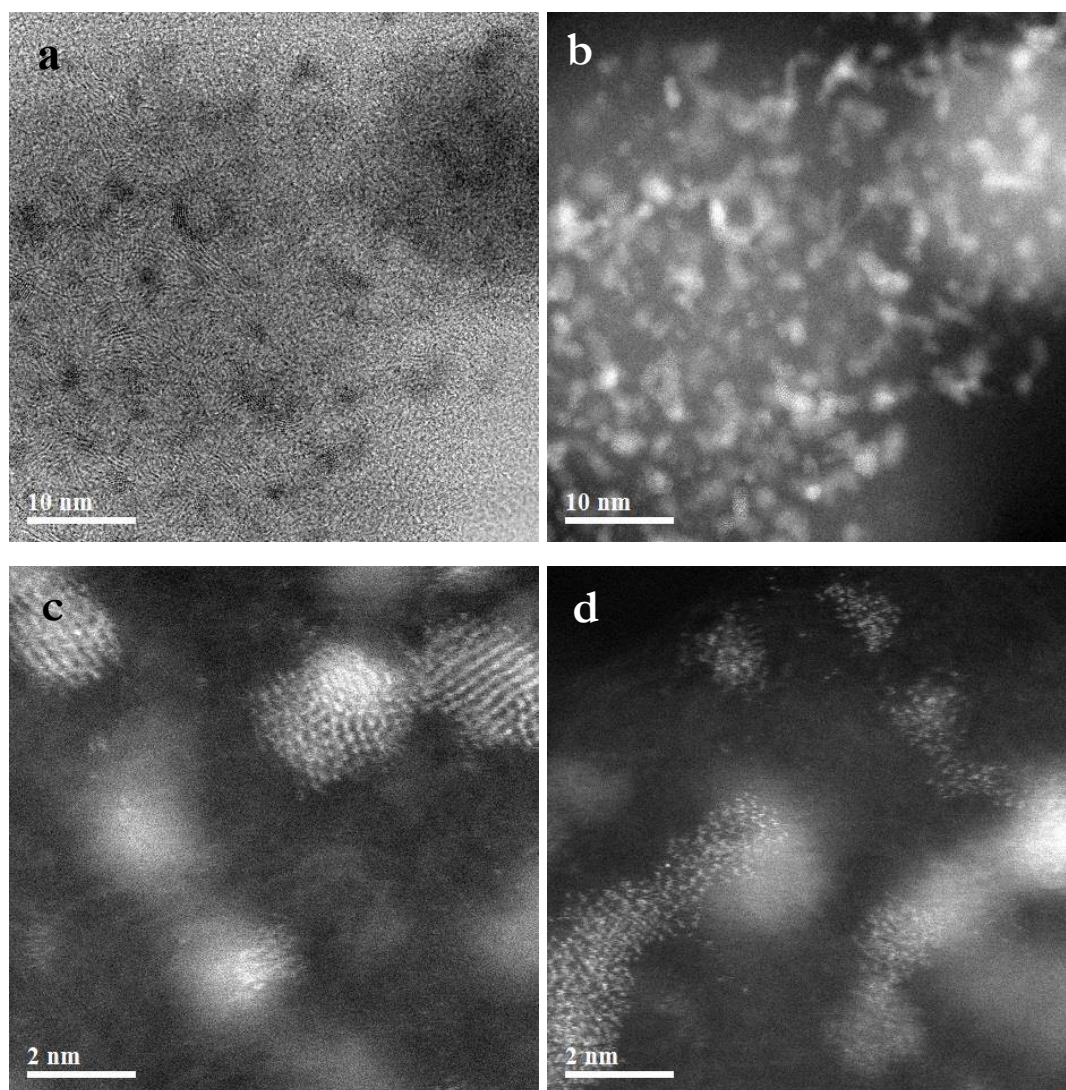


Figure 3.12. Low magnification (a) BF-STEM and (b) HAADF-STEM images showing the typical particle size and shape distribution in the fresh 5 wt.% Ru/C commercial catalyst. (c) and (d) are higher magnification HAADF images showing greater structural detail in individual particles.

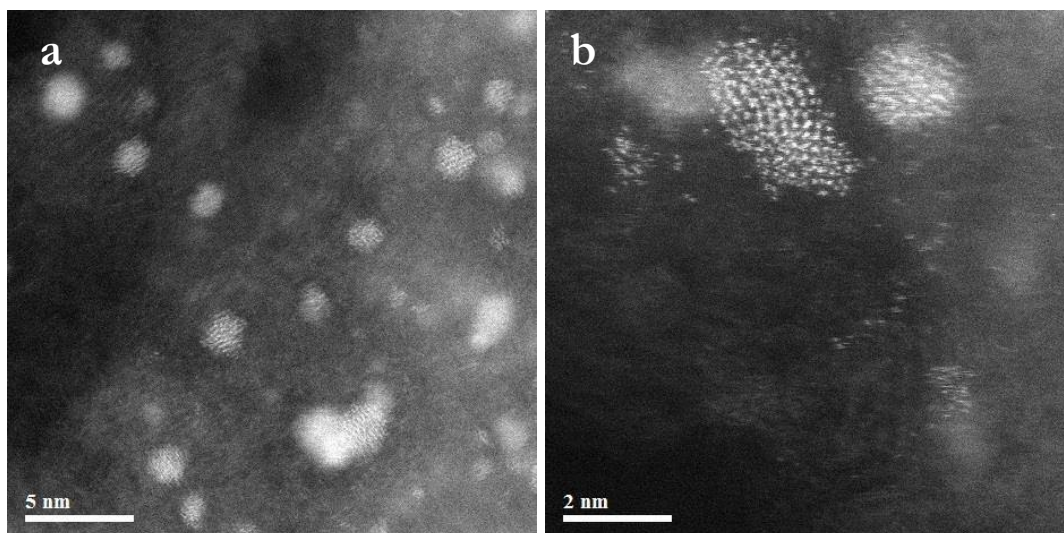


Figure 3.13. HAADF images showing structural detail in individual particles in 5 wt.% Ru/C commercial after 1 reaction.

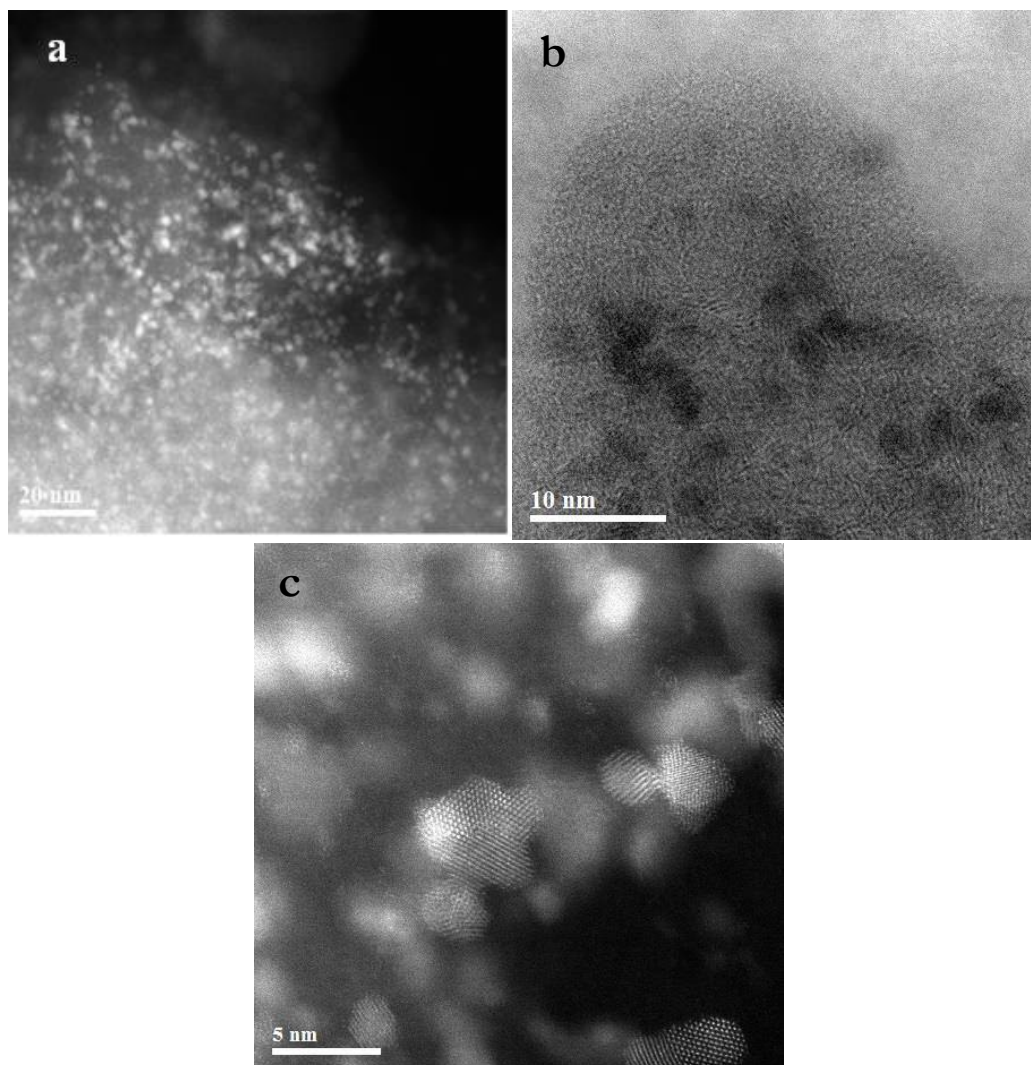


Figure 3.14. (a) Low magnification HAADF-STEM image; (b) and (c) are higher magnification BF and HAADF images respectively for 5 wt.% Ru/C commercial.

There were significant differences in 5 wt.% Ru/XC72R-SI when compared to 5 wt.% Ru/C commercial. HAADF-STEM imaging of the fresh catalyst prepared by SI revealed homogeneously dispersed crystalline Ru nanoparticles with a narrow size distribution and a mean particle size of 1.25 nm (Figure 3.15). Imaging of the catalyst after 1 reaction cycle caused some minimal sintering of the nanoparticles to a mean particle size of approximately 1.5 nm (Figure 3.16), but crystallinity was largely maintained. The larger particles were made up of crystalline Ru, whereas the smaller ones were slightly more disordered and made up of RuO_x as observed in 5 wt.% Ru/C commercial. After 4 catalyst use cycles it could be seen that the gradual sintering had continued to a mean particle size of 1.8 nm though the particle crystallinity was largely maintained (Figure 3.18).

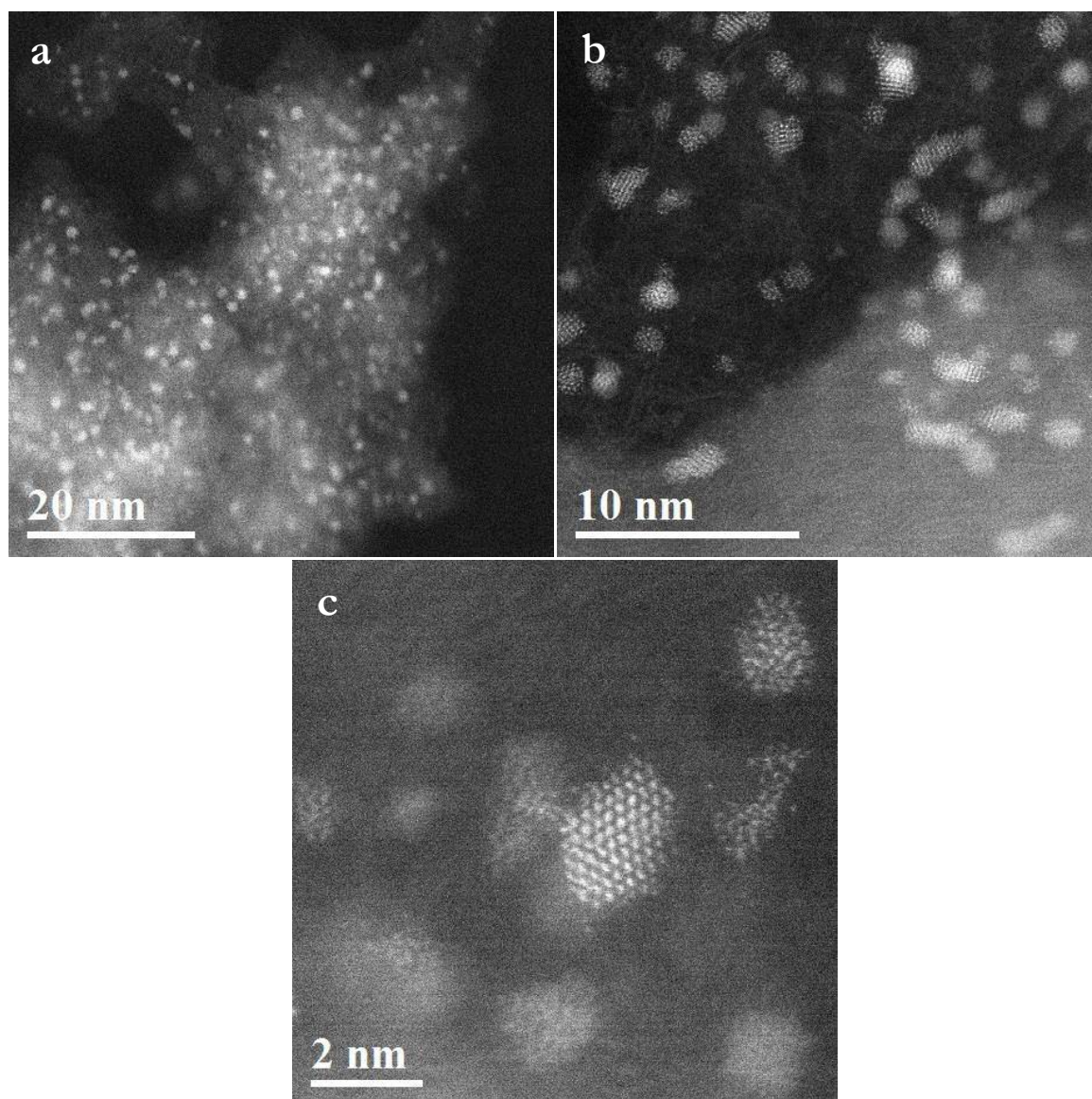


Figure 3.15. (a) Low magnification HAADF-STEM image; (b) and (c) higher magnification HAADF images for unused 5 wt.% Ru/XC72R-SI catalyst.

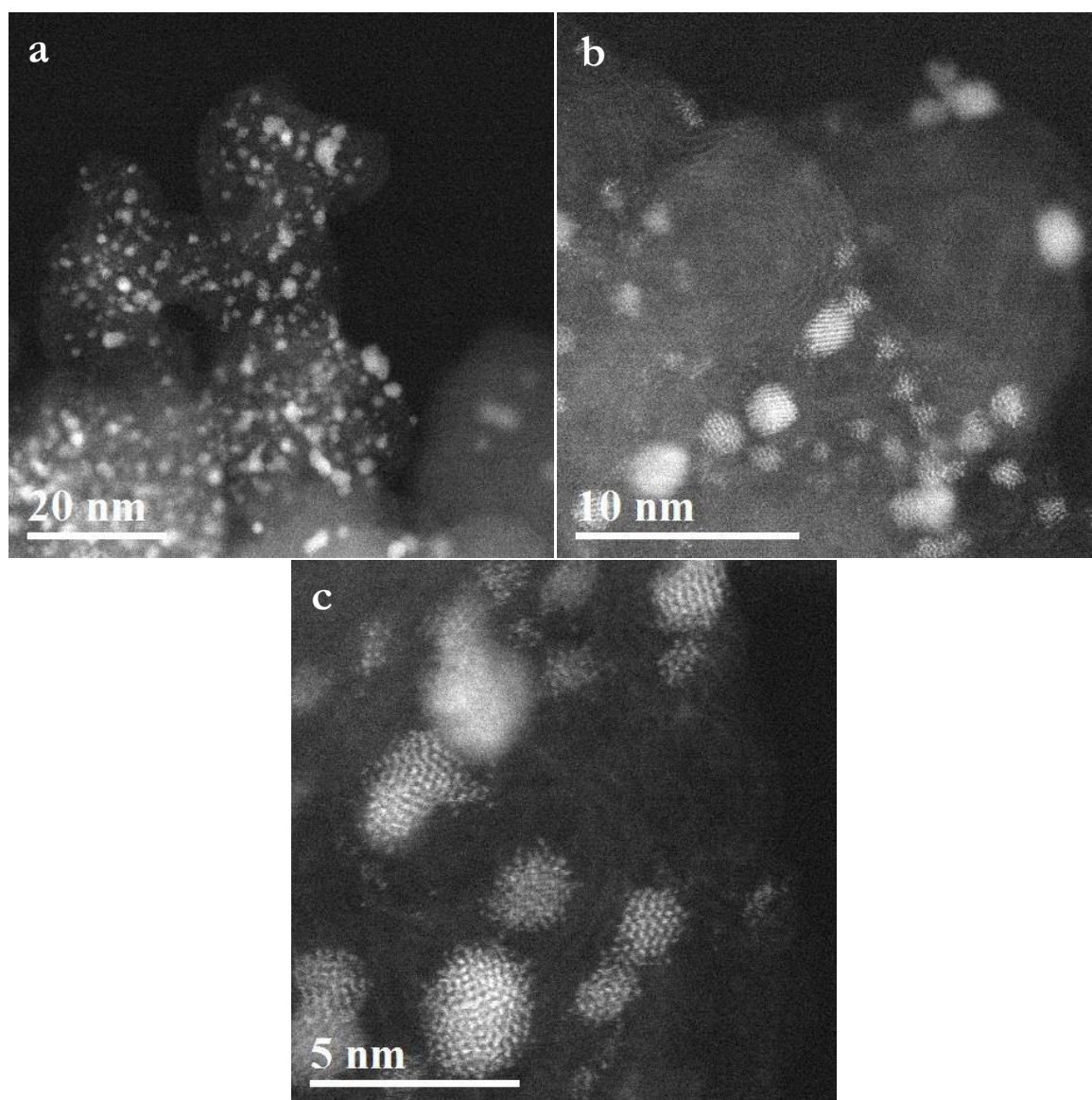


Figure 3.16. (a) Low magnification HAADF-STEM image; (b) and (c) higher magnification HAADF images for 5 wt.% Ru/XC72R-SI catalyst after one reaction.

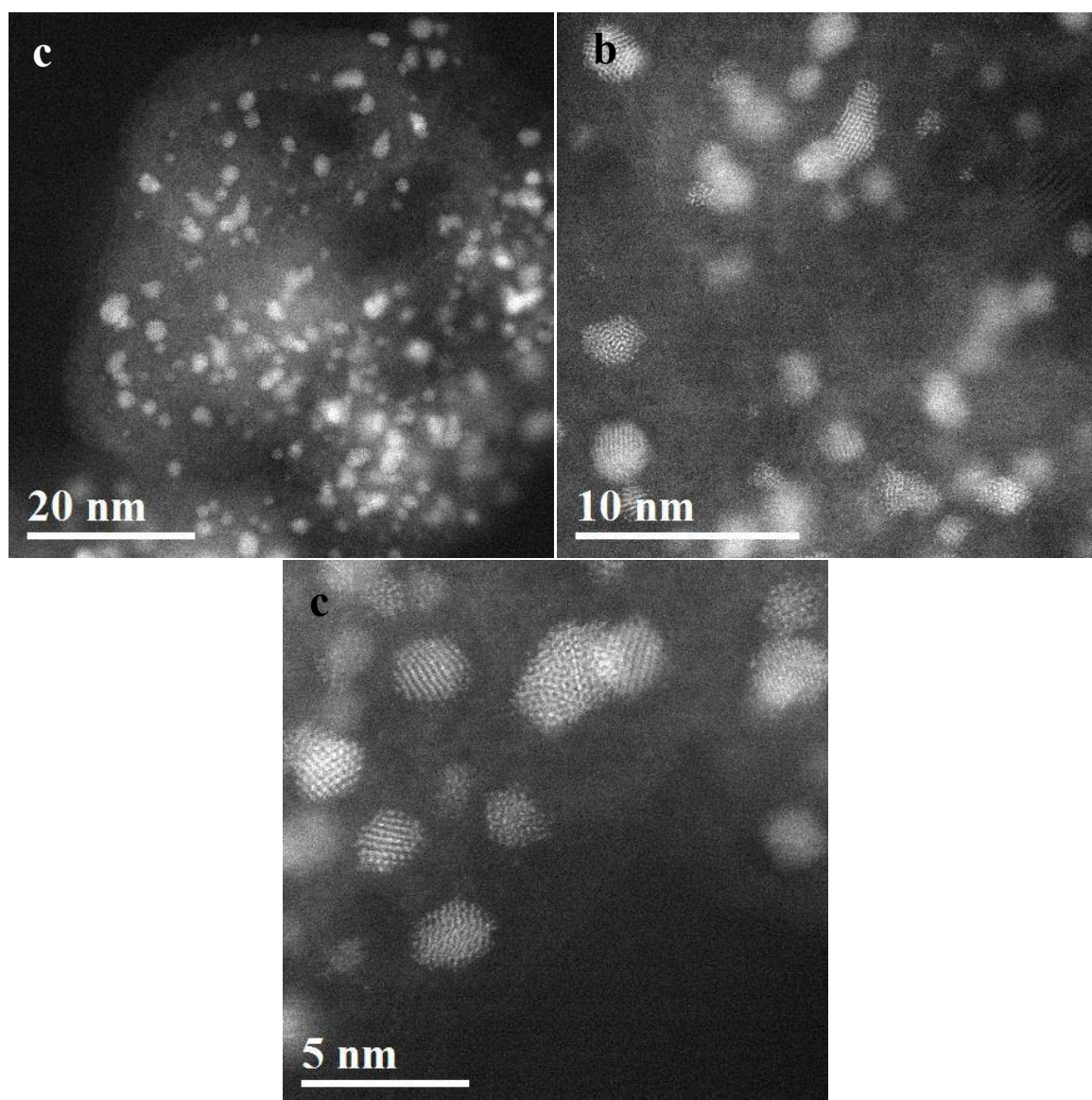


Figure 3.17. (a) Low magnification HAADF-STEM image; (b) and (c) higher magnification HAADF images for 5 wt.% Ru/XC72R-SI catalyst after 4 reaction cycles.

The differences observed by the HAADF-STEM analysis of these catalysts can be related back to their activities. Both 5 wt.% Ru/C commercial and 5 wt.% Ru/XC72R-SI had discrete nanoparticle morphologies on their surfaces at the points when they were most active (Figures 3.10 and 3.11 respectively). In the case of the 5 wt.% Ru/XC72R-SI, this was prior to its first use, but in the case of 5 wt.% Ru/C commercial, it was after 2 uses in reaction. From the HAADF-STEM analysis it can be concluded that 5 wt.% Ru/XC72R was initially more active than 5 wt.% Ru/C commercial because it already had the discrete nanoparticle morphology required for the activity. 5 wt.% Ru/C became progressively more active on extended use and successive reuse because it formed the required morphology over time under reaction conditions. Though the HAADF-STEM analysis can explain why the SI catalyst was initially more active than the commercial catalyst, it cannot explain the deactivation.

Though some minimal sintering was observed after reuse for the SI catalyst, the Ru particle size after 4 uses was similar for both catalysts, yet the commercial catalyst was far more active after reuse. This suggests that particle size is not the only determining factor in the catalysts activity, and that sintering is not the sole cause of deactivation.

3.3. Conclusions

This work has shown that the key features of Ru/C catalysts responsible for activity are, (i) the Ru present in its reduced, metallic state, and (ii) a discrete nanoparticle morphology. A highly active 5 wt.% Ru/C can be produced by a SI method. This is the first time such a method has been employed for the synthesis of Ru/C catalysts¹⁹. This catalyst was compared with a commercial Ru/C catalyst and was found to be much more active initially, but showed marked deactivation on reuse and at long reaction times. XPS analysis revealed that the reason for the SI deactivation was the accumulation of lactide species over the active sites through interaction with unremoved PVA. This was not observed with the commercial catalyst, which was not as initially active, but became progressively more active on reuse.

Detailed characterisation revealed that the SI catalyst already had the desirable characteristics of an active catalyst prior to use, whereas the commercial catalyst only achieved the appropriate morphology and metallic state after being subjected to reaction conditions. The results presented here are in slight contrast to the conclusions drawn by Jang *et al.* While they showed the surface area of the carbon is important for the formation of small Ru nanoparticles, the present study does not necessarily show that this is the case. While small nanoparticles are undoubtedly required for an active catalyst – and this was achieved as shown by HAADF-STEM analysis – the morphology of the particles are also of great importance. A combination of these factors is likely required for active catalyst synthesis. It could be hypothesized that a catalyst prepared by SI using the Ketjen black support found to be the best by Jang *et al.*⁵ would be highly active.

This work has shown that the catalyst preparation method is of great importance and can affect the reaction behaviour of the final catalyst. Further work on this system should focus on the stabilising the SI catalysts so that the initial high activity can be maintained.

3.4. References

- 1 Z. Zhang, J. E. Jackson and D. J. Miller, *Appl. Catal. A Gen.*, 2001, **219**, 89–98.
- 2 A. Primo, P. Concepcion and A. Corma, *Chem. Commun.*, 2011, **47**, 3613–3615.
- 3 G. Luo, S. Yan, M. Qiao, J. Zhuang and K. Fan, *Appl. Catal. A Gen.*, 2004, **275**, 95–102.
- 4 Y. Takeda, T. Shoji, H. Watanabe, M. Tamura, Y. Nakagawa, K. Okumura and K. Tomishige, *ChemSusChem*, 2015, **8**, 1170–1178.

- 5 H. Jang, S.-H. Kim, D. Lee, S. E. Shim, S.-H. Baeck, B. S. Kim and T. S. Chang, *J. Mol. Catal. A Chem.*, 2013, **380**, 57–60.
- 6 Q. Yang, J. Zhang, L. Zhang, H. Fu, X. Zheng, M. Yuan, H. Chen and R. Li, *Catal. Commun.*, 2013, **40**, 37–41.
- 7 R. D. Cortright, M. Sanchez-Castillo and J. A. Dumesic, *Appl. Catal. B Environ.*, 2002, **39**, 353–359.
- 8 Z. Zhang, J. E. Jackson and D. J. Miller, *Ind. Eng. Chem. Res.*, 2002, **41**, 691–696.
- 9 P. G. J. Koopman, A. P. G. Kieboom and H. van Bekkum, *J. Catal.*, 1981, **69**, 172–179.
- 10 T. Komanoya, H. Kobayashi, K. Hara, W.-J. Chun and A. Fukuoka, *Appl. Catal. A Gen.*, 2011, **407**, 188–194.
- 11 A. M. Hengne, N. S. Biradar and C. V Rode, *Catal. Letters*, 2012, **142**, 779–787.
- 12 K. Aika, T. Takano and S. Murata, *J. Catal.*, 1992, **136**, 126–140.
- 13 H. Y. H. Chan, C. G. Takoudis and M. J. Weaver, *J. Catal.*, 1997, **172**, 336–345.
- 14 H. Over, *Chem. Rev.*, 2012, **112**, 3356–3426.
- 15 J. P. Chen and S. Wu, *Langmuir*, 2004, **20**, 2233–2242.
- 16 J. F. Watts, *Surf. Interface Anal.*, 1993, **20**, 267.
- 17 J. A. Lopez-Sanchez, N. Dimitratos, C. Hammond, G. L. Brett, L. Kesavan, S. White, P. Miedziak, R. Tiruvalam, R. L. Jenkins, A. F. Carley, D. Knight, C. J. Kiely and G. J. Hutchings, *Nat Chem*, 2011, **3**, 551–556.
- 18 A. Laheäär, S. Delpeux-Ouldriane, E. Lust and F. Béguin, *J. Electrochem. Soc.*, 2014, **161**, A568–A575.
- 19 S. Iqbal, S. A. Kondrat, D. R. Jones, D. C. Schoenmakers, J. K. Edwards, L. Lu, B. R. Yeo, P. P. Wells, E. K. Gibson, D. J. Morgan, C. J. Kiely and G. J. Hutchings, *ACS Catal.*, 2015, **5**, 5047–5059.

Chapter 4

Ru/C catalysts for the hydrogenation of levulinic acid

4.1. Introduction

Levulinic acid (LA) is widely regarded as being an important platform molecule for the production of second generation biofuels¹. GVL in particular has been identified as being a potential additive for fuels, making its production an attractive target²⁻⁴ as is detailed in Chapter 1.

The effect of carbon support has already been touched upon in Chapter 3, and it was demonstrated that the type of carbon had an effect on the catalytic activity for hydrogenation reactions⁵. Carbons play an important role as both catalyst^{6,7} and catalyst support^{5,8-10} in chemical and enzymatic reactions dealing with biomass owing mostly to their high specific surface areas and tuneable porosity¹¹⁻¹⁴. A study by Aksoylu *et al.* has shown that the choice of carbon support is important as each have different textural and chemical properties¹⁵. It is widely agreed that carbon is a superior support in catalysts used for biomass transformations and will become increasingly important because it can also be prepared from residual biomass, thus becoming a direct part of the carbohydrate economy that is an aim of the future^{16,17}.

There was a discussion in Chapter 1 about the use of Ru-based catalysts for LA hydrogenation. Generally, optimisation of reaction conditions using commercial catalysts has been predominant in the open literature^{8,9,18,19}. It has been recognised that the dispersion of Ru across the surface is an important factor affects the catalytic activity: highly dispersed Ru results in very active catalysts²⁰⁻²².

This chapter will investigate the influence of preparation method and the choice of carbon support for 1 wt.% Ru/C catalysts. This will be the first instance where a low-metal content Ru-based catalyst prepared by SI is proposed as an efficient catalyst for LA hydrogenation to GVL. This catalyst is more active and efficient than the higher metal content ones outlined in the literature review (Chapter 1)

and consequently cheaper due to the use of less Ru metal. Catalytic performance and characterisation data obtained by TPR, XRD, XPS, N₂ adsorption, and TEM are reported herein in order to understand the origins of the catalytic activity and inform the development of even more highly active catalysts.

4.2. Results and discussion

4.2.1. The effects of Ru precursor and carbon support

1 wt.% Ru/C catalysts were prepared on two types of carbon; G60 and XC72R using the chloride and nitrosyl nitrate precursors of Ru following the preparation methods (SI and WI) detailed in Chapter 2, section 2. All the catalysts were tested for LA hydrogenation under identical reaction conditions and the resulting GVL yield is presented in Figure 4.1. Given that the carbon supports and Ru precursors are being compared at this point, trends in the catalytic data are more important than the raw conversion values. In each case, the selectivity to GVL was 100 %. The most active catalyst for LA hydrogenation was Ru supported on XC72R and prepared by SI, yielding 92 % GVL. The catalyst prepared by WI using Ru(NO)(NO₃)₃ gave moderate yields of GVL (55 % and 75 % GVL yield for the catalysts supported on G60 and XC72R respectively), whereas the catalysts prepared by WI using RuCl₃ and SI using Ru(NO)(NO₃)₃ gave a maximum GVL yield of 30 %. For all precursors, the performance of the catalysts supported on XC72R was superior to those supported on G60.

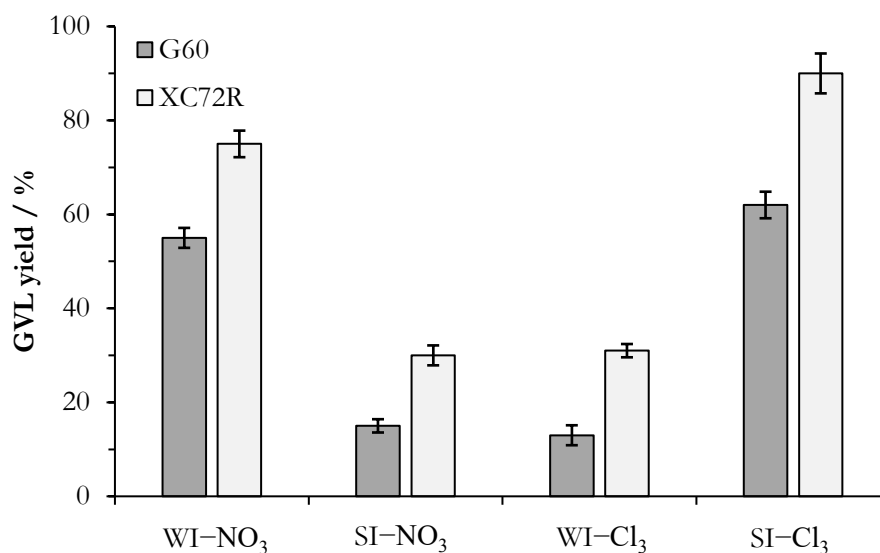


Figure 4.1. Activity of 1 wt.% Ru/C catalysts for LA hydrogenation. NO₃: Ru(NO)(NO₃)₃ precursor; Cl₃: RuCl₃ precursor. **Reaction conditions:** 100 °C, 5 bar H₂, 5 wt.% LA/H₂O, 0.025 g of catalyst.

A discussion of the mechanism of LA hydrogenation was given in Chapter 1, section 1.3.2.1. Neither 4-hydroxypentanoic acid (HPA) nor angelica lactone were observed with either of the Ru/C catalysts. A control experiment was carried out using α -angelica lactone as a substrate under the same

reaction conditions using the catalyst prepared by SI from RuCl_3 supported on XC72R. Only trace conversion into GVL was observed. Given the mildness of the reaction conditions used, it is likely that the mechanism proceeds by the HPA pathway, as suggested by Bond and co-workers¹⁹.

4.2.2.1. Characterization

XRD patterns were obtained in order to gain information on phase composition and the data are shown in Figure 4.2. Except for the catalysts prepared using RuCl_3 on XC72R, the XRD patterns of the catalysts were indistinguishable from the XRD patterns of the carbon supports. Reflections at $2\theta = 34^\circ$ and 54° corresponding to RuO_2 were observed where RuCl_3 was used with XC72R. The presence of these reflections implies that Ru was not as well dispersed in these catalysts as in others, and indicates that Ru was present in its oxide form and not as metallic $\text{Ru}(0)$. However, the low intensity and broadness of these reflections meant that the Scherrer equation could not be used to determine the particles size with any accuracy.

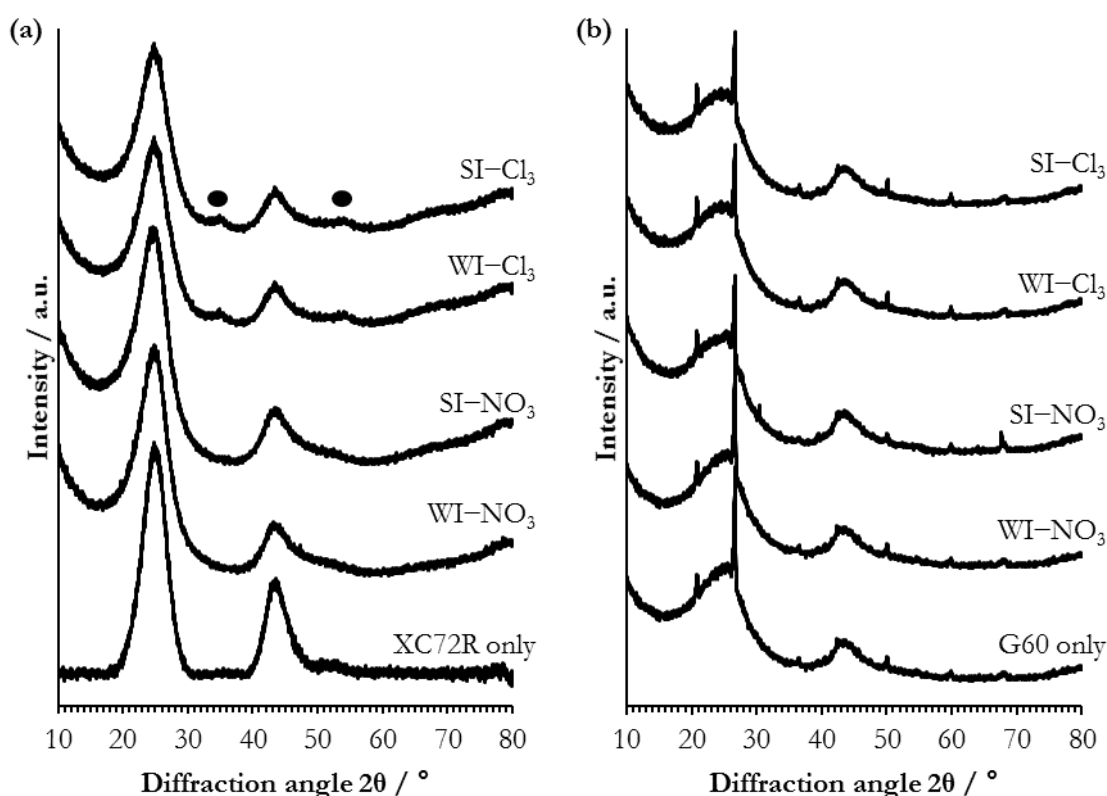


Figure 4.2. XRD patterns of 1 wt.% Ru/C catalysts. (a) supported on XC72R; (b) supported on G60. NO_3 : $\text{Ru}(\text{NO})(\text{NO}_3)_3$ used as precursor; Cl_3 : RuCl_3 used as precursor. ●: RuO_2 .

TEM analysis was attempted on the 1 wt.% Ru/C catalysts, but there were significant difficulties in observing metal particles. This could simply be due to the amorphous nature of the carbon supports,

but it is likely that the particles were below the detection limit of the conventional TEM. The previous work discussed in Chapter 3 employed an aberration corrected TEM, showing Ru particles well below the detection limit of conventional TEM confirms that this is the case⁵. This apparatus was not available for use for this particular study. EDX analysis (Figures 4.3 and 4.4) confirmed that Ru was present on the surface of the catalysts however, and was well dispersed across the carbon support regardless of the precursor used.

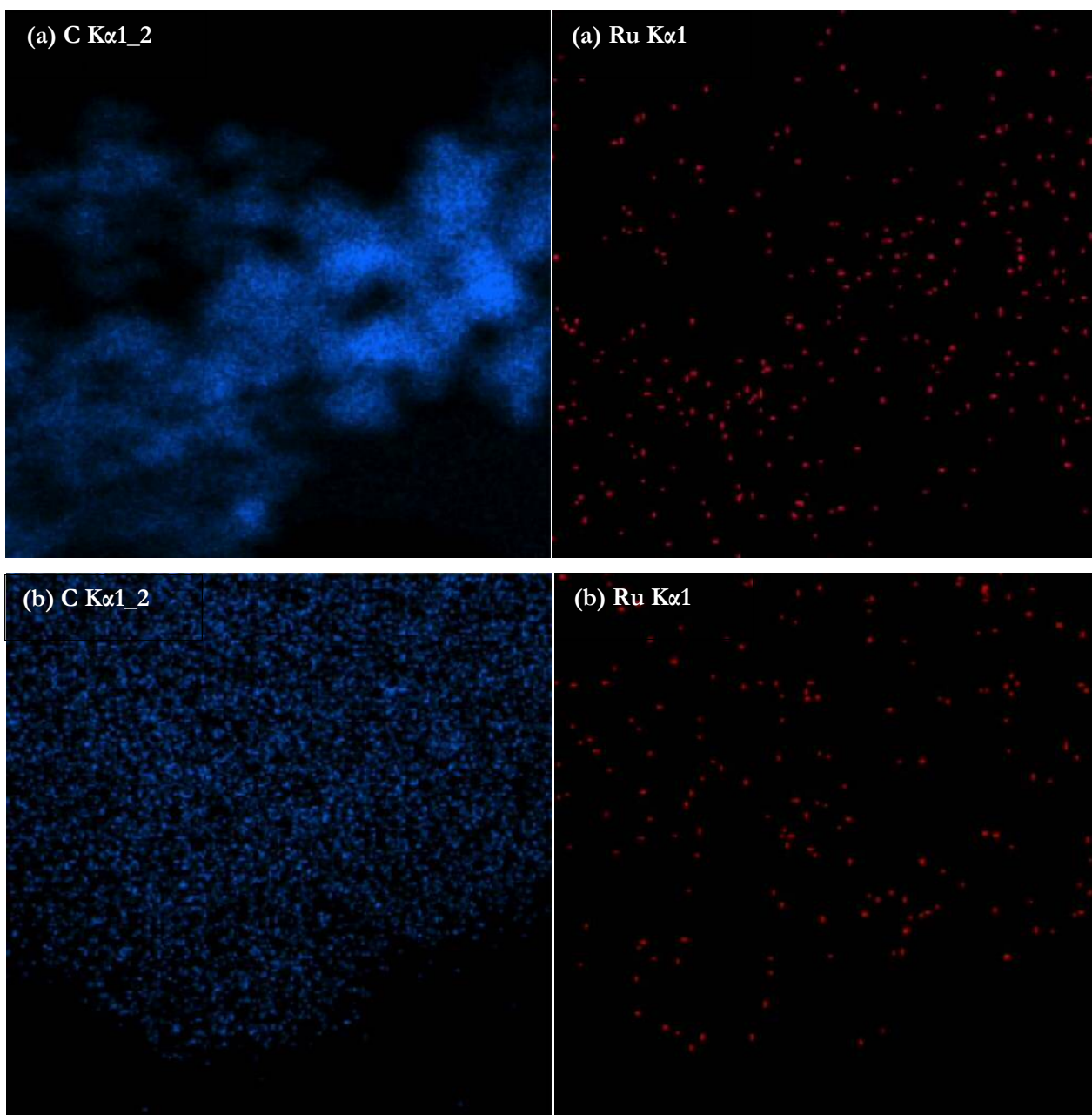


Figure 4.3. C and Ru EDX maps for G60 supported catalysts. (a) RuCl₃ used as precursor; (b) Ru(NO)(NO₃)₃ used as precursor.

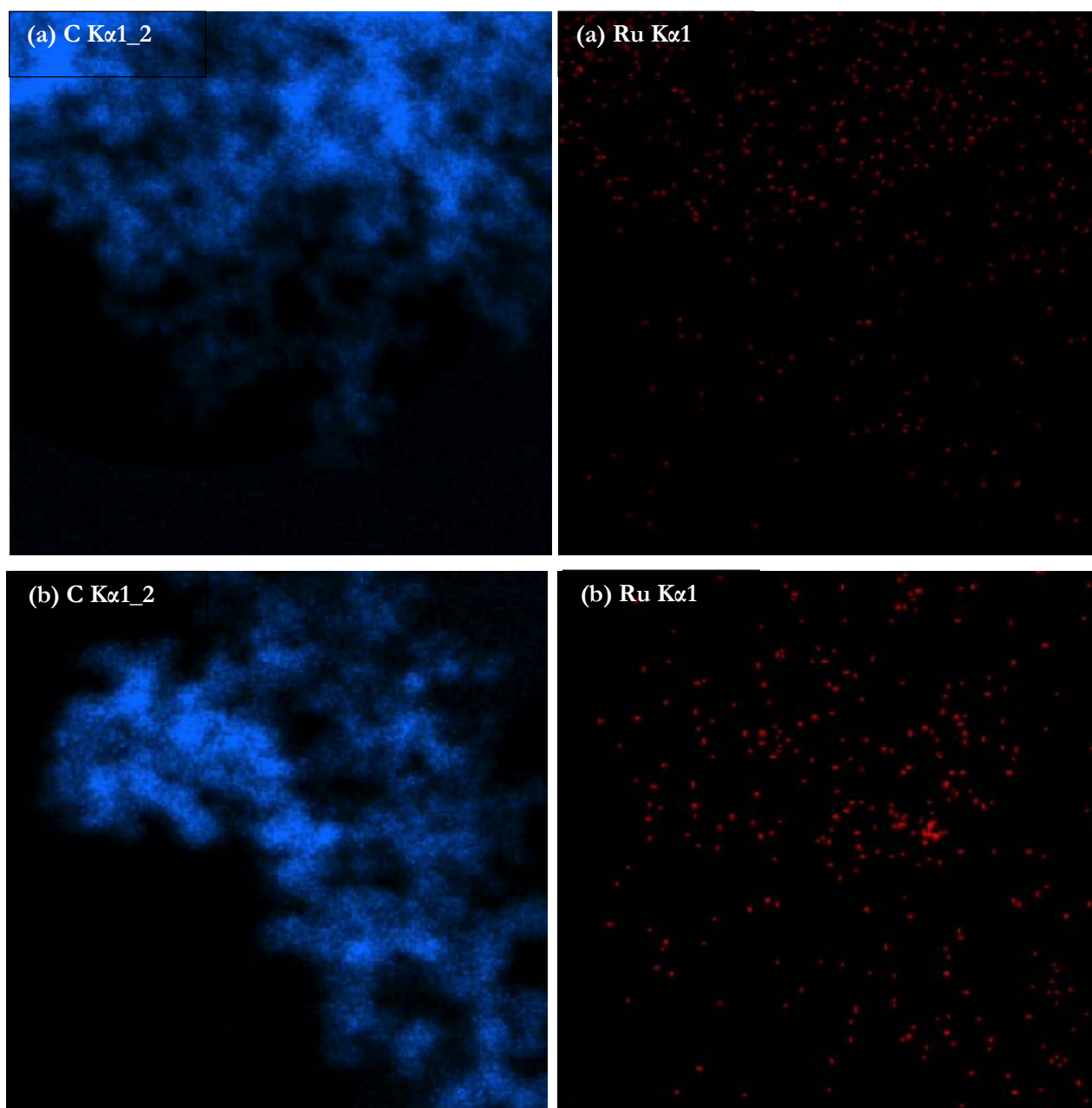


Figure 4.4. C and Ru EDX maps for XC72R supported catalysts. (a) RuCl₃ used as precursor; (b) Ru(NO)(NO₃)₃ used as precursor.

BET surface area analysis presented in Table 4.1 shows there was a large difference between the surface areas of pure XC72R and G60 which had values of 220 m² g⁻¹ and 680 m² g⁻¹ respectively. The surface area was not largely affected by the presence of Ru regardless of the precursor or preparation method used. Ru has already been shown to be well dispersed across the surface regardless of which precursor was used, and the higher surface area of G60 did not translate into significantly higher catalytic activity. This would suggest that total surface area is not a significant factor in the catalytic activity of these catalysts. This contrasts with previous reports which suggested a higher carbon surface area results in catalysts with superior activity²³. Instead, surface speciation should be considered.

Table 4.1. BET surface areas for 1 wt.% Ru/C catalysts supported on XC72R and G60.

Carbon	Ru precursor	Preparation method	BET surface area / $\text{m}^2 \text{g}^{-1}$
G60	Ru(NO)(NO ₃) ₃	WI	650
		SI	630
	RuCl ₃	WI	670
		SI	610
XC72R	Ru(NO)(NO ₃) ₃	WI	220
		SI	200
	RuCl ₃	WI	210
		SI	200

TPR analysis was conducted (Figure 4.5) that showed that there were generally three principal reduction signals observed in most of the catalysts. The lower temperature signals have been proposed to be due to the reduction RuO_x species to Ru(0), or the reduction of Ru(IV)/Ru(III) to Ru(II), while the signals between 200–400 °C are reported to be due to the reduction of Ru(II) to Ru(0)^{24,25}. Higher temperature peaks (above 500 °C) were due to the reduction of species attached to the carbon supports, or methanation of the carbon support. Mass spectrometry carried out during the TPR experiments (Figure 4.6 – showing 1 wt.% Ru/XC72R, SI, Cl₃ only but representative of all catalysts) showed an evolution of methane, carbon monoxide, and water which is indicative of high temperature support degradation and removal of oxygen containing species (pre-treatment had already removed adsorbed atmospheric water). These high temperature signals were more prominent for G60 supported catalysts than XC72R supported catalysts. A sharp reduction signal was observed around 100 °C when RuCl₃ was used for SI on both XC72R and G60. This was the lowest observed reduction temperature, and implies that the catalysts were easily reducible when prepared by this method. The generally superior activity of these catalysts (Figure 4.1) suggests that reducibility of the catalyst is an important consideration. The sharpness of the peak indicates that reduction occurred quickly, suggesting the active surface was prepared much faster for this catalyst than others, resulting in greater overall activity. The catalysts that showed reduction signals between 250–300 °C on either of the carbon supports, e.g. SI using Ru(NO)(NO₃)₃, were generally less active. These results imply that the reduced forms of Ru are important for these reactions to proceed. Catalysts that had reduction signals predominately above the range of reaction temperatures used (100–120 °C), may have had a lower proportion of reduced/metallic Ru species compared to the catalysts that did not have reduction signals in that range and were generally less active, as exemplified by RuCl₃ by SI and Ru(NO)(NO₃)₃ by SI respectively.

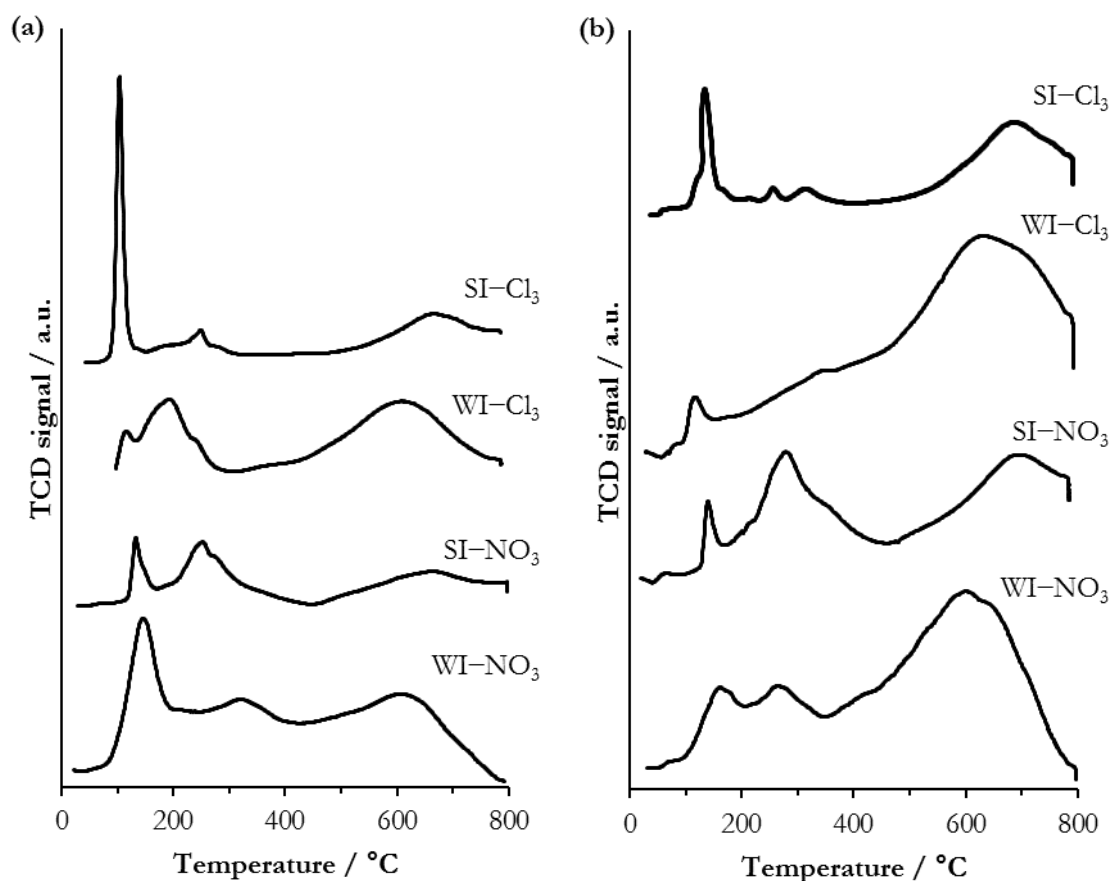


Figure 4.5. TPR profiles of 1 wt.% Ru/C catalysts. (a) supported on XC72R; (b) supported on G60. NO_3 : $\text{Ru}(\text{NO})(\text{NO}_3)_3$ used as precursor; Cl_3 : RuCl_3 used as precursor.

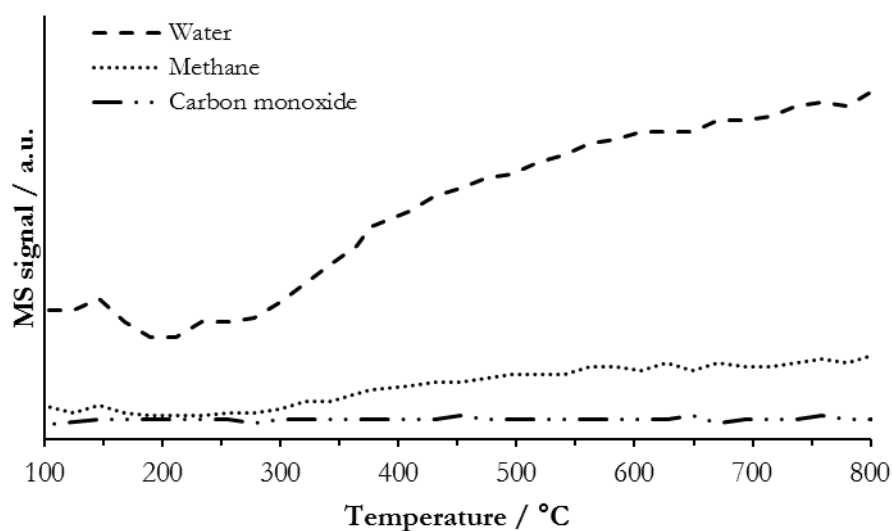


Figure 4.6. Mass spectroscopy signal of 1 wt.% Ru/XC72R prepared by SI using RuCl_3 recorded during TPR.

XPS was utilised to gain a deeper understanding of the surface species present on the catalyst surface and the data are presented in Table 4.2. Ru supported on G60 is generally present as both Ru(0) and RuO₂, however RuO₂ alone is present when SI method is adopted with RuCl₃ to prepare the catalyst. Ru was always present only as RuO₂ in catalysts prepared using XC72R. The small shifts of both the Ru(0) and RuO₂ binding energies by approximately 0.3 eV (Table 4.2) can be attributed to either, or a combination of, particle size effects or hydration of RuO₂, which have both been demonstrated in the literature to affect peak width and binding energy^{26,27}. The presence of RuO₂ on the catalyst surface could be taken to mean that it is the catalytically active species, but this would contradict the TPR data that seems to suggest that Ru(0) metal is the active species. It can therefore be suggested that RuO₂ is a precursor of the catalytically active species, but it is very difficult to conclusively determine whether it is the pure form of RuO₂ or the hydrated form, because RuO₂ has a high affinity for water, even in ultra-high vacuum conditions²⁸.

Table 4.2. Ru(3d_{5/2}) and Ru(3p_{3/2}) binding energies and assignments for XC72R and G60 supported catalysts.

Carbon	Ru precursor	Preparation method	Ru(3d _{5/2}) / eV	Ru(3p _{3/2}) / eV	Ru species ^b	
XC72R	Ru(NO)(NO ₃) ₃	WI	281.2	463.5	RuO ₂ ·(xH ₂ O)	
		SI	n/d ^a	464.2	RuO ₂ ·(xH ₂ O)	
	RuCl ₃	WI	281.3	463.7	RuO ₂ ·(xH ₂ O)	
		SI	281.5	463.6	RuO ₂ ·(xH ₂ O)	
G60	Ru(NO)(NO ₃) ₃	WI	280.4 (21 %)	462.8	Ru(0)	
			281.2 (79 %)	462.5	RuO ₂ ·(xH ₂ O)	
	SI		280.4 (22 %)	463.7	Ru(0)	
			281.3 (78 %)	462.0	RuO ₂ ·(xH ₂ O)	
	RuCl ₃	WI		280.1 (45 %)	462.2	Ru(0)
				281.0 (46 %)	464.0	RuO ₂ ·(xH ₂ O)
SI			281.4	463.7	RuO ₂ ·(xH ₂ O)	

^a n/d = not determined as concentration too low; ^b Assignments made against binding energies determined from bulk references.

4.2.2. Characterisation of the carbon supports

Both types of the carbons (XC72R and G60) were analysed by INS. Figure 4.7 shows the INS spectra of the carbons normalised to 1 g of sample. The spectrum of XC72R is ×2 scaled with respect to the G60. This indicates that both carbons had different hydrogen contents (G60 > XC72R). Previous research indicates that there is approximately 10 times as much hydrogen in G60 than in XC72R and that

XC72R is very similar to pure graphite. $[\text{XC72R}-\text{G60}]$ was calculated in order to remove the hydrogen features and compared with graphite (Figure 4.8). The similarity between the two spectra is clear. The features at around 1150 and 850 cm^{-1} were assigned to in-plane and out-of-plane bending modes of C-H bonds that terminate the graphene planes, as previously suggested by Albers *et al.*²⁹ The same work also suggests that the local environment can be determined by the position and number of the out of plane bending modes. The hydrogen present in XC72R was mostly isolated, whereas there were two or more adjacent C-H groups are present in G60.

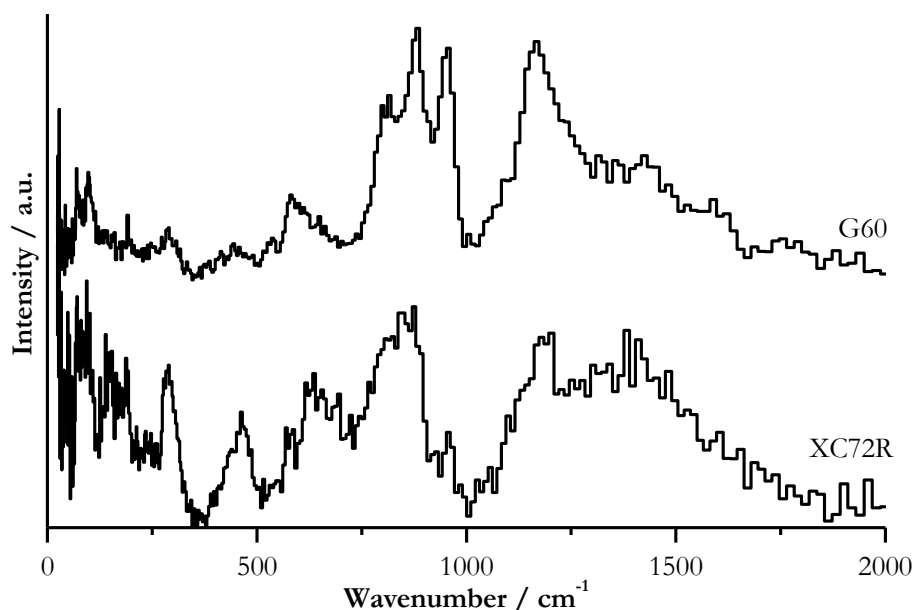


Figure 4.7. INS spectra of XC72R and G60. Note that XC72R is $\times 2$ scaled relative to G60.

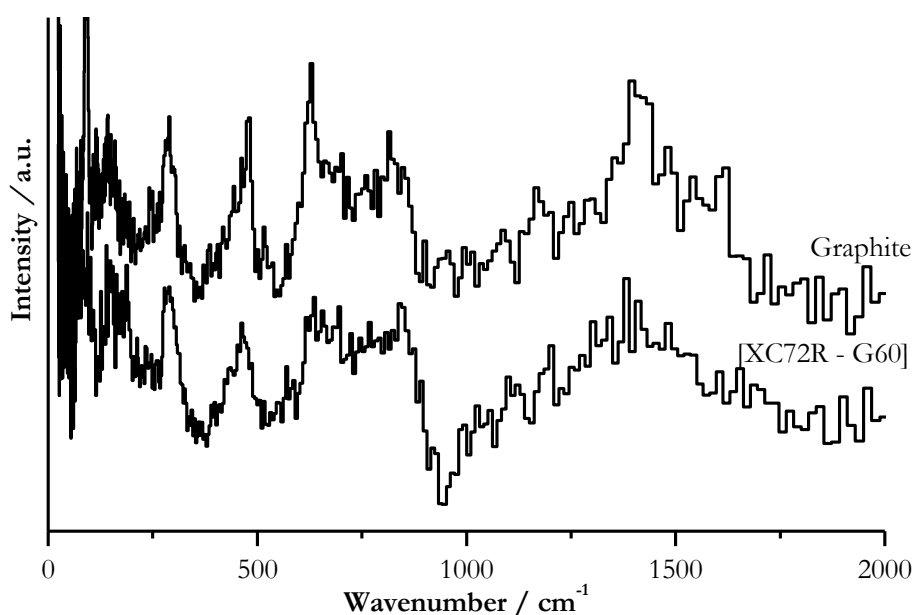


Figure 4.8. INS spectra of $[\text{XC72R}-\text{G60}]$ compared with graphite.

CHN analysis of XC72R and G60 shown in Table 4.3 confirmed the suggestion that there was approximately 10 times more hydrogen present in G60 than in XC72R – 1.15 % vs. 0.14 % respectively.

Table 4.3. CHN analysis of the carbon supports.

Support	Elemental composition (wt.%)		
	Carbon	Hydrogen	Nitrogen
G60	86.76	1.15	0.26
XC72R	98.64	0.14	0.46

When the INS data is taken into account, it would appear that the greater hydrogen content of the G60 support compared with the XC72R support resulted in more easily reducible Ru on the surface on the catalyst – indeed, XPS showed that there was metallic Ru present on the surface of G60 supported catalysts, whereas XC72R supported catalysts had Ru present in only its oxide form. However, XC72R supported catalysts showed overall greater catalytic activity than G60 supported catalysts for LA hydrogenation. This suggests that factors other than the oxidation state of Ru is the determining factor in the catalytic activity of Ru/C catalysts for LA hydrogenation. For example, Vlachos and co-workers showed that a synergistic effect between Ru(0) and RuO₂ is responsible for the catalytic activity in furfural hydrogenation³⁰, or else the carbon–substrate interaction is a major contributing factor, with different functional groups present in different carbons affecting the substrate differently.

4.2.3. Investigation into SI preparation parameters

The activity data (Figure 4.1) showed that 1 wt.% Ru/C prepared by SI on XC72R was the most active catalyst for LA hydrogenation. Catalyst preparation by the SI method involves the use of a stabilising agent in order to encapsulate the Ru nanoparticles and gain greater control over the particle size³¹, and the use of a reducing agent to produce metal nanoparticles in solution and negate the need for reduction treatment under a high temperature flow of H₂ at a later stage³². It is therefore important to study and optimize the effects of both.

4.2.3.1. The effect of PVA variation

Various catalysts were prepared by varying the ratio of PVA to Ru by the SI method detailed in Chapter 2, section 2.2.2, and the results of LA hydrogenation test using these catalysts are provided in Figure 4.9. It is clear that increasing the PVA content in the catalyst resulted in a gradual decrease in GVL yield. During the preparation, a Ru colloid is formed, which is subsequently immobilised onto the carbon support. While it is known that the use of enough PVA can result in nanoparticles with a uniform distribution of small particles, overuse of PVA can result in blocking of the active sites³². Blocking of

the active sites by an excess of PVA explains low the conversion of LA when the highest PVA/Ru ratio (of 3) was used³³. It was discussed in Chapter 3 that PVA caused the accumulation of lactide species in lactic acid hydrogenation⁵; therefore, a similar theory can be postulated here. It is important to note that the use of a small amount of PVA (PVA/Ru = 0.1) was significant in order to provide increased catalytic activity. A 1 wt.% Ru/C catalyst prepared without PVA gave an average GVL yield of 50 %. The use of PVA results in steric size control of the nanoparticles³⁴. Without PVA there can be no size control of the particles, but conversely, the use of excess PVA can have a detrimental effect on the catalytic activity³³.

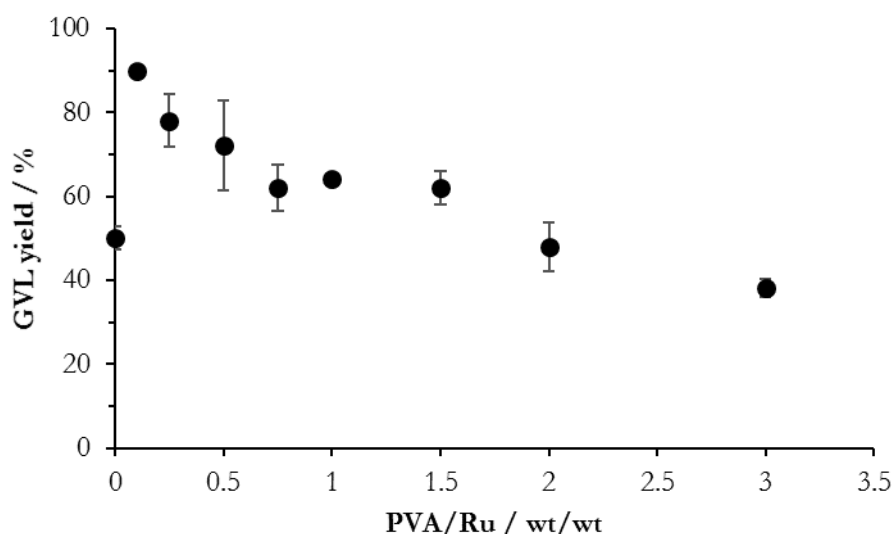


Figure 4.9. The effect of PVA content on catalytic activity of 1% Ru/C. *Reaction conditions:* 100 °C, 5 bar H₂, 1 hour, 5 wt.% LA/H₂O, 0.025 g catalyst.

XRD analyses on catalysts prepared with a variation in PVA/Ru content are shown in Figure 4.10. There were no observable reflections corresponding to Ru containing species. This suggests, as discussed before in Figure 4.2(a), that the Ru was very well dispersed across the surface of the carbon support (XC72R) and had a crystallite size smaller than 5 nm.

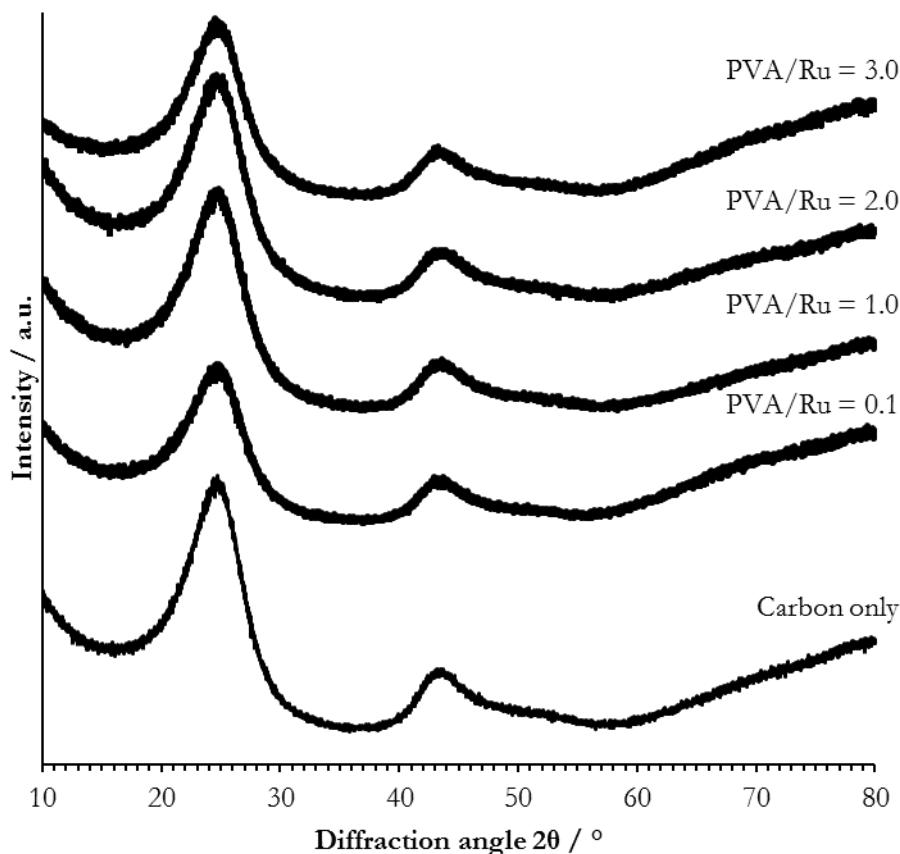


Figure 4.10. XRD patterns of a selection of catalysts prepared with different PVA/Ru ratios.

BET surface areas for this series of catalysts are presented in Table 4.4. When a low PVA content was used (0.1 and 0.25), the BET surface area was higher than that of the support at $250 \text{ m}^2 \text{ g}^{-1}$ and $240 \text{ m}^2 \text{ g}^{-1}$ vs. $220 \text{ m}^2 \text{ g}^{-1}$. From the TEM previously shown in Figure 4.4(a), it is known that Ru from the RuCl_3 precursor became highly dispersed on the XC72R support when prepared by SI. As the PVA/Ru ratio was increased above 0.25, a steady decline in surface area was observed. It is known that the use of excess stabilising polymers can have a detrimental effect of blocking active metal sites (as discussed in Chapter 3). When the catalytic activity is considered, a larger amount of PVA resulted in a steady decline in the GVL yield. Though it has been noted already that surface area is not a particularly discriminating factor in the catalyst activity between two types of carbon, the change in surface area can in this case be used to understand the cause of the decline in activity (Figure 4.10) with a larger amount of PVA used³³. The GVL yield normalised by BET surface area (Table 4.4) shows a decline with an increasing PVA/Ru ratio, which mirrors the trend between GVL yield and PVA/Ru ratio. If the decline in activity was due solely to the decrease in surface area, the normalised GVL yield would have remained a constant value. This data indicates that a decline in surface area cannot be the sole factor causing a decrease in GVL yield.

Table 4.4. BET surface areas of 1 wt.% Ru/C catalysts prepared with varying PVA/Ru ratios. ($\text{NaBH}_4/\text{RuCl}_3 = 2.5$).

PVA/Ru / wt/wt	BET surface area / $\text{m}^2 \text{g}^{-1}$	GVL yield normalised by BET surface area / $\% (\text{m}^2 \text{g}^{-1})^{-1}$
0.1	250	0.36
0.25	240	0.325
0.5	220	0.327
0.75	200	0.31
1.0	200	0.32
1.5	200	0.24
3.0	200	0.19

TPR analyses of a selection of SI catalysts prepared with varying amounts of PVA are presented in Figure 4.11. Many of the same features already discussed previously (Figure 4.5) are present in the TPR traces: intense reduction signals at approximately 100–150 °C corresponding to Ru reduction, and a broader feature above 400 °C assigned to carbon degradation through methanation or reduction of surface functional groups. It is entirely possible that the PVA used during the preparation was removed at higher temperatures and contributed to the reduction signal above 450 °C, but quantification of the loss of PVA from a carbon support is difficult. The catalyst prepared with a PVA/Ru ratio of 0.1 was the most active for LA hydrogenation. The TPR trace shows that this catalyst had the most intense low temperature reduction signals, and considerably less signal in the region of 150–200 °C, which suggests a greater proportion of the reduced Ru species was present under reaction conditions (100 °C, 5 bar H_2) for PVA/Ru = 0.1 compared with the catalysts prepared with a larger PVA content. Because of the presence of prominent TPR signals at temperatures > 150 °C in catalysts with PVA/Ru = 0.75, 1.5, and 3.0, it could be suggested that the use of large amounts of PVA decreased the reducibility of the catalyst by blocking the access of H_2 to the Ru species.

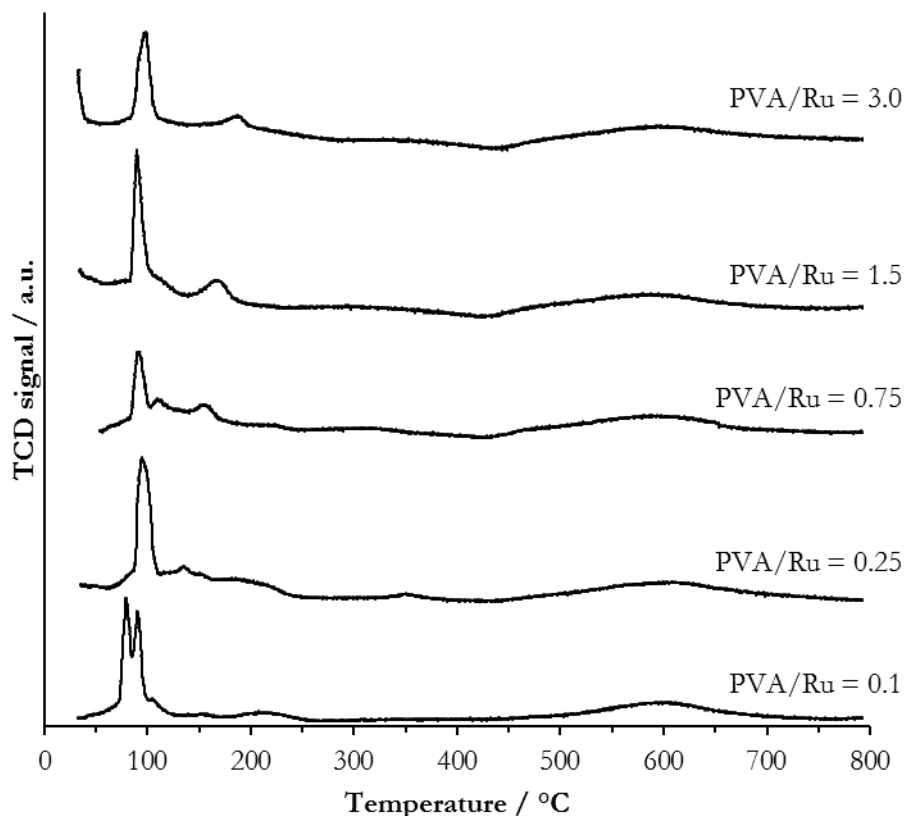


Figure 4.11. TPR profiles for 1 wt.% Ru/C catalysts prepared with different PVA/Ru ratios.

XPS analysis was performed on the catalysts prepared with varying ratio of PVA to Ru and the data are presented in Table 4.5. Both Ru(3p_{3/2}) and Ru(3d_{5/2}) binding energies were in the same range as those reported previously in Table 4.2, suggesting RuO₂·(xH₂O) on the surface to some extent. However, at higher PVA usage a binding energy closely corresponding to that of RuCl₃ was observed in the Ru(3p_{3/2}) signal. RuCl₃ may be present due to an excess of PVA preventing the formation of RuO₂. These catalysts also produced lower yields of GVL (Figure 4.9). It could be that PVA blocked the active sites, as previously suggested, or that the use of PVA prevents the formation of RuO₂, which is suggested as the precursor to the catalytically active Ru species⁵. The Ru(3d_{5/2}) signal did not suggest the presence of Ru(III), but it is likely that it was incorporated into the signal that appeared at 281.2 eV.

Table 4.5. XPS analysis of a selection of catalysts with different PVA/Ru ratios.

PVA/Ru / wt/wt	Ru(3d _{5/2}) / eV	Ru(3p _{3/2}) / eV	Ru species ^a
0.1	281.2	462.6	RuO ₂ ·(xH ₂ O)
1.0	281.1	463.0	RuO ₂ ·(xH ₂ O)/RuCl ₃
3.0	281.3	463.6	RuCl ₃

^a Assignments made against binding energies determined from bulk references.

4.2.3.2. The effect of NaBH₄ variation

With the knowledge that a PVA/Ru ratio of 0.1 resulted in the most active catalyst, 1 wt.% Ru/C catalysts were prepared with an increasing amount of NaBH₄ and were tested for LA hydrogenation in order to investigate the effect of reduction during the preparation. The activity data for LA conversion is shown in Figure 4.12. Aside from the observation that a NaBH₄/RuCl₃ ratio of 2.5 was found to be optimal, there are two main features of the activity data. An initial increase in activity with an increase in NaBH₄ use up to NaBH₄/RuCl₃ ≤ 2.5, and a gradual decline in catalytic activity up to the maximum amount of NaBH₄ used (NaBH₄/RuCl₃ = 15). An incomplete reduction of the Ru during the preparation of the sol would be expected when an amount of NaBH₄ lower than the stoichiometric value required for reduction of Ru is used. It is known that unreduced RuCl₃ particles can be very large³⁵, which are known not to be optimal for an enhanced catalytic activity^{21,22}. As the amount of NaBH₄ used increases, there would be more reduced Ru prepared and supported on the catalyst. The increase in activity up to NaBH₄/RuCl₃ ≤ 2.5 can be attributed to increasingly available metallic Ru. The decrease and subsequent stabilisation of the activity when NaBH₄/RuCl₃ > 2.5 were used can be related to the kinetics of nanoparticle formation. Turkovic gave insight into the kinetics of nanoparticle formation using a gold citrate sol and showed that an increased rate of nanoparticles formation generally results in larger nanoparticles³⁶. In accordance with this, work by Prati and co-workers showed that using an excess of NaBH₄ in an SI procedure for gold catalysts decreased their activity for glycerol oxidation due to the presence of particles that were too large to achieve high activity^{31,32}. The catalytic data obtained in Figure 4.12 is in agreement with both of these previous findings. It has been shown in this work and in previous works^{5,20–22} that small, well dispersed Ru particles are required for high catalytic activity. An increase in NaBH₄/RuCl₃ can form large Ru nanoparticles that are not as active for LA hydrogenation. The consistency of the activity at NaBH₄/RuCl₃ > 5 suggests that an excessive amount of NaBH₄ does not increase the rate any further i.e. there comes a point at which the reduction of RuCl₃ becomes zero order. Colloids can be investigated by UV spectroscopy. It would be interesting to investigate the change in oxidation state of Ru during the reduction process and at varying amounts of NaBH₄ in order to determine the nature of the Ru species immobilised onto the carbon support.

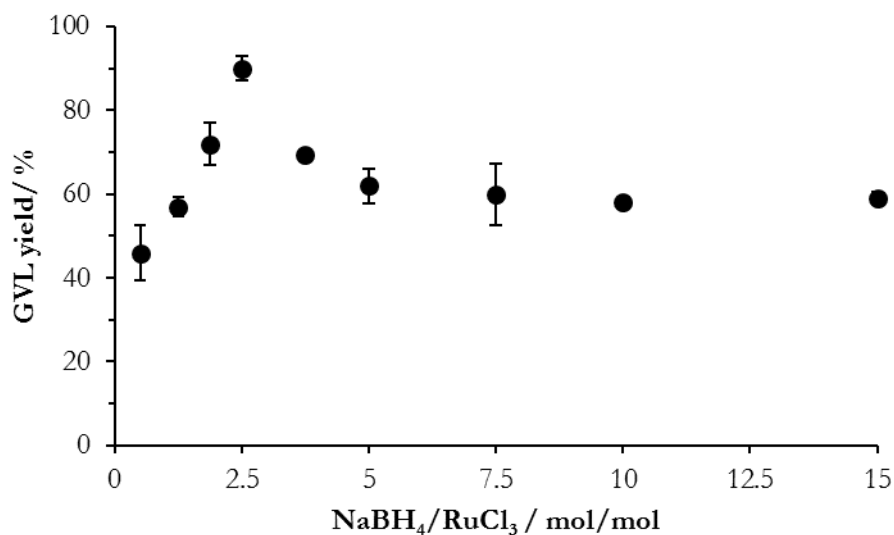


Figure 4.12. The effect of NaBH₄ use on the catalytic activity of 1 wt.% Ru/C. *Reaction conditions:* 100 °C, 5 bar H₂, 1 hour, 5 wt.% LA/H₂O, 0.025 g catalyst.

XRD analysis was carried out on this series of catalyst and is presented in Figure 4.13. Once again, as observed with variation of PVA/Ru, there were no significant features to be observed in the XRD patterns, indicating small, well dispersed Ru particles were present on the support surface.

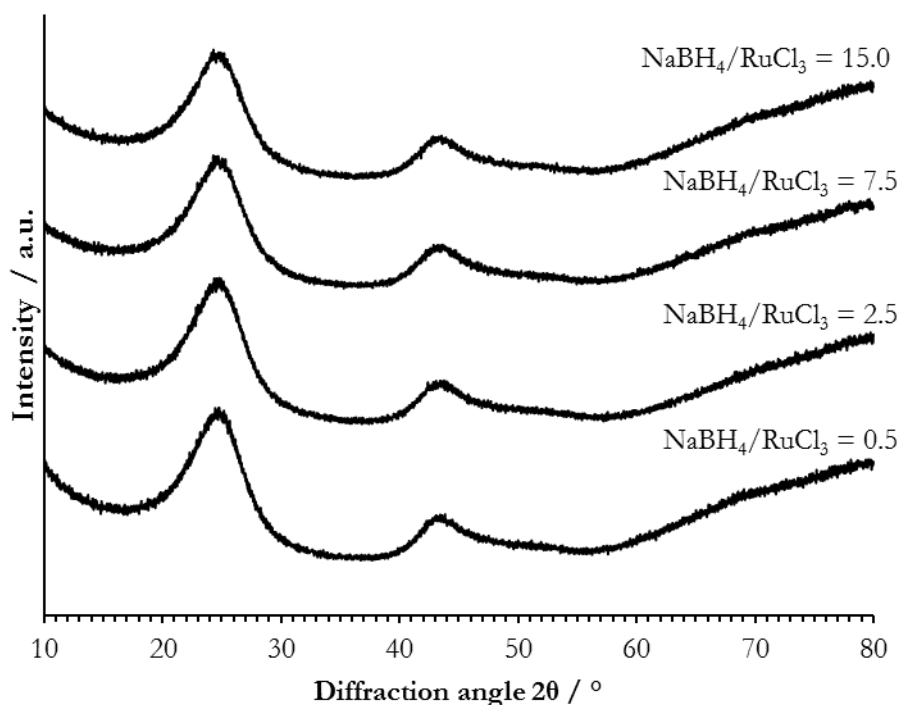


Figure 4.13. XRD patterns of a selection of catalysts prepared with varying NaBH₄/RuCl₂ ratio.

The BET surface area (Table 4.6) was shown to decrease in line with increasing NaBH₄/RuCl₃ ratio. The BET surface area was approximately 250 m² g⁻¹ for catalysts prepared with NaBH₄/RuCl₃ ≤ 2.5, but started to decrease for the catalysts prepared with larger amounts of NaBH₄. Larger amounts of NaBH₄ were used, with the intention of forming stabilised highly dispersed Ru nanoparticles^{35,37}. The peak in activity was observed at NaBH₄/RuCl₃ = 2.5, which could be due to both the required Ru surface species and particle sizes which may have resulted in an optimal activity. At higher NaBH₄/RuCl₃ ratios, the kinetics of nanoparticle formation can play more of a role as discussed previously in relation to the catalytic data (Figure 4.12). Large Ru particles would have a smaller surface area than small Ru nanoparticles, which would explain the overall decrease in the catalyst surface area. The activity data shows a decrease in activity after NaBH₄/RuCl₃ > 2.5. The larger particle size postulated to be caused by the increased reduction may well be the cause of this^{31,32}. The GVL yield normalised by BET surface area showed the same trend with the change in NaBH₄/RuCl₃ ratio as was observed in the catalytic activity data (Figure 4.12), suggesting that the change in catalytic activity was not solely due to the change in BET surface area similar to what we have seen with the variation of PVA/Ru ratios (Table 4.4).

Table 4.6. BET surface areas of 1 wt.% Ru/C catalysts prepared with varying NaBH₄/RuCl₃ ratios. PVA/Ru = 0.1.

NaBH ₄ /RuCl ₃ / mol/mol	BET surface area / m ² g ⁻¹	GVL yield normalised by BET surface area / % (m ² g ⁻¹) ⁻¹
0.25	255	0.18
0.5	250	0.22
1.25	255	0.36
2.5	250	0.27
5.0	230	0.28
7.5	215	0.31
10	190	0.18

TPR analyses were performed on the catalysts prepared by varying the ratio of NaBH₄/Ru and the data are presented in Figure 4.14. The reduction signals were found to be comparable with those observed with the varying ratio of PVA/Ru (Figure 4.11). The most notable observation from this data is the evolution of two reduction signals below 100 °C which showed a higher intensity with an increased amount of NaBH₄. The catalyst prepared with NaBH₄/RuCl₃ = 2.5 showed almost same intensity of both signals compared with the catalysts prepared with the higher ratios (i.e. NaBH₄/RuCl₃ = 5 and 7.5). The lower temperature reduction signals correspond to the facile reduction of Ru(OH)₃, which arise due

to the affinity of Ru with water^{24,38}. Each of the catalysts in this series were easily reducible under reaction conditions.

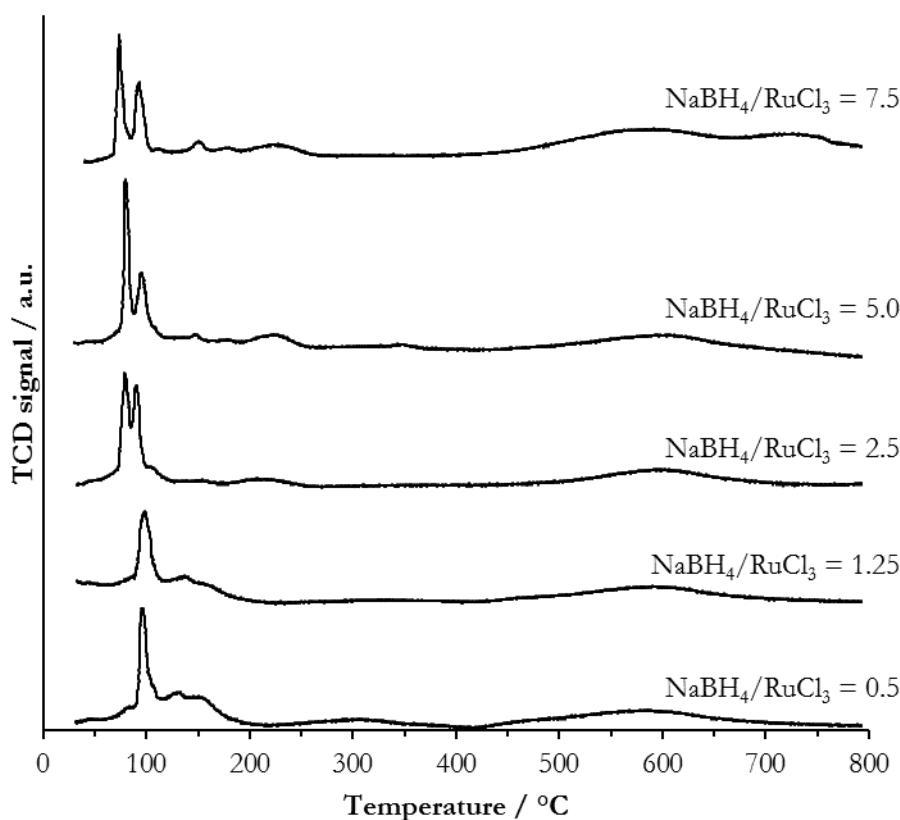


Figure 4.14. TPR profiles for 1 wt.% Ru/C catalysts prepared with varying NaBH₄/RuCl₃ ratios (PVA/Ru = 0.1).

XPS analysis of the catalyst prepared with varying amounts of NaBH₄ are presented in Table 4.7. Features at 280.4 eV (Ru(3d_{5/2})) and 462.5 eV (Ru(3p_{3/2})) were observed with increased amounts of NaBH₄. This was again an indication of the presence of RuO₂ species. However, there was a peak shift towards binding energies of Ru metal. This could suggest that with an increased amount of NaBH₄, the catalyst contained a greater proportion of metallic Ru – though metallic Ru was not observed by XPS. However, given that less GVL was produced when larger amounts of NaBH₄ were used during the catalyst preparation, it cannot be the presence of an increased amount of metallic Ru that is responsible for the activity. The XPS data, when considered in its entirety, suggests that RuO₂ must be present as the precursor to the active species under reaction conditions. Though the use of excess NaBH₂ resulted in Ru species more like metallic Ru, these particles were likely too large due to the high rate of reduction to be particularly active. Given that the reduction of Ru *in situ* is likely a facile process – as discussed in Chapter 3 – the use of an optimum amount of NaBH₄ to produce smaller particles is preferable.

Table 4.7. XPS analysis of a selection of catalysts with different NaBH₄/RuCl₃ ratios.

NaBH ₄ /RuCl ₃ / mol/mol	Ru(3d _{5/2}) / eV	Ru(3p _{3/2}) / eV	Ru species ^a
0.5	281.0	463.4	RuO ₂ ·(xH ₂ O)/RuCl ₃
2.5	280.4	462.5	RuO ₂ ·(xH ₂ O)
5.0	280.3	462.3	RuO ₂ ·(xH ₂ O)
7.5	279.9	461.8	RuO ₂ ·(xH ₂ O)/Ru ⁰

^aAssignments made against binding energies determined from bulk references.

4.2.4. Activity of SI catalysts over time

The activity of a selection of catalysts, with varying compositions of the highest and the lowest PVA and NaBH₄ contents were tested for their activity over time and the time-on-line data are shown in Figure 4.15. The most active catalyst (PVA/Ru = 0.1; NaBH₄/RuCl₃ = 2.5) produced a GVL yield of 90 % after 1 hour, whereas the catalyst prepared with PVA/Ru = 3.0 and NaBH₄/RuCl₃ = 2.5 produced a GVL yield of approximately 35 % after the same reaction time. The catalyst with the optimal content of PVA (PVA/Ru = 0.1) and low NaBH₄ content (NaBH₄/RuCl₃ = 0.5) was less active than the catalyst prepared with a large excess of NaBH₄ used, in agreement with the trend previously discussed indicating that there is a minimum amount of NaBH₄ required in order to fully reduce the Ru in solution.

The key feature of all the time-on-line profiles is that there appeared to be an induction period. This is similar to the induction period discussed in relation to 5 wt.% Ru/C catalysts for lactic acid hydrogenation discussed in Chapter 3, It is likely that the induction period was due to the pre-reduction of surface RuO_x to metallic Ru (i.e. preparation of the active surface), or due to removal of PVA, which is known to be facile and achievable under the reaction conditions ³⁹. Alternatively, the induction period could be due to the rejection of water from the hydrophobic surface allowing the adsorption of the more hydrophilic levulinic acid prior to the reaction taking place.

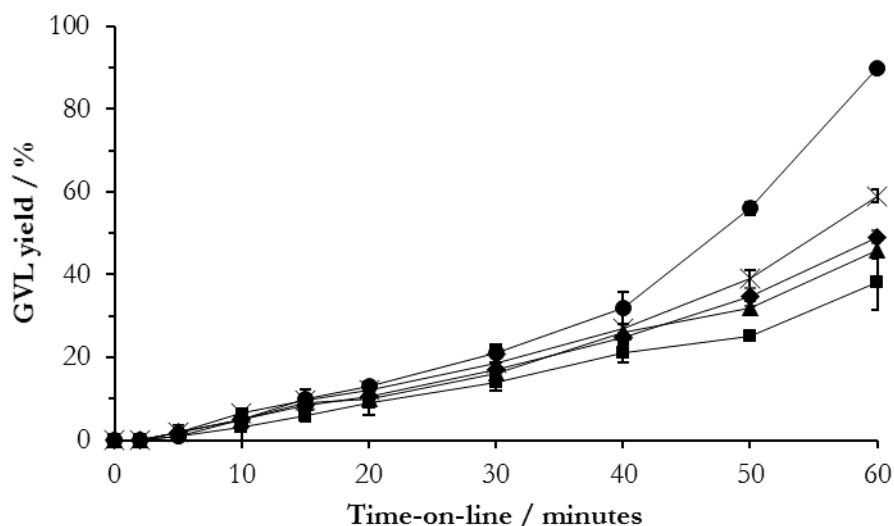


Figure 4.15. Time-on-line data for 1 wt.% Ru/C catalysts prepared with different PVA and NaBH₄ contents. ● PVA/Ru = 0.1, NaBH₄/RuCl₃ = 2.5; ■ PVA/Ru = 3.0, NaBH₄/RuCl₃ = 2.5; ▲ PVA/Ru = 0.1, NaBH₄/RuCl₃ = 0.5; × PVA/Ru = 0.1, NaBH₄/RuCl₃ = 15; ◆ PVA/Ru = 0, NaBH₄/RuCl₃ = 2.5. **Reaction conditions:** 100 °C, 5 bar H₂, 5 wt.% LA/H₂O, 0.025 g catalyst.

4.2.5. Catalyst re-use

Reuse tests were carried out using 1 wt.% Ru/C catalysts prepared by using NaBH₄/RuCl₃ = 2.5 and varying amounts of PVA (PVA/Ru = 0.1, 1.0, and 3.0 – Figure 4.16). Each of these catalysts achieved very different yields of GVL on initial use (as already discussed in Figure 4.15). With each subsequent reuse, the catalysts produced lower yields of GVL compared with the fresh catalysts (indicated by cycle 1 in Figure 4.16). This mirrors the downward trend in activity with successive reuse as was seen in Chapter 3 using 5 wt.% Ru/XC72R-SI for lactic acid hydrogenation. The extent of deactivation between the different catalysts shown in Figure 4.16 is very different. The catalyst prepared with PVA/Ru = 0.1 was initially the most active (90 % yield of GVL), but resulted in a yield of only 40 % on second use (cycle 2, Figure 4.16). The catalyst prepared with PVA/Ru = 3.0 initially showed a lower activity, with a yield of only 35 % GVL, but did not deactivate in the same way catalysts PVA/Ru = 0.1 and PVA/Ru = 1.0 did. By the third use, the three catalysts produced comparable amounts of GVL, and by the fourth use all produced approximately 10 % GVL. Overall, this data suggests that the catalysts are not reusable regardless of the PVA/Ru used during the preparation.

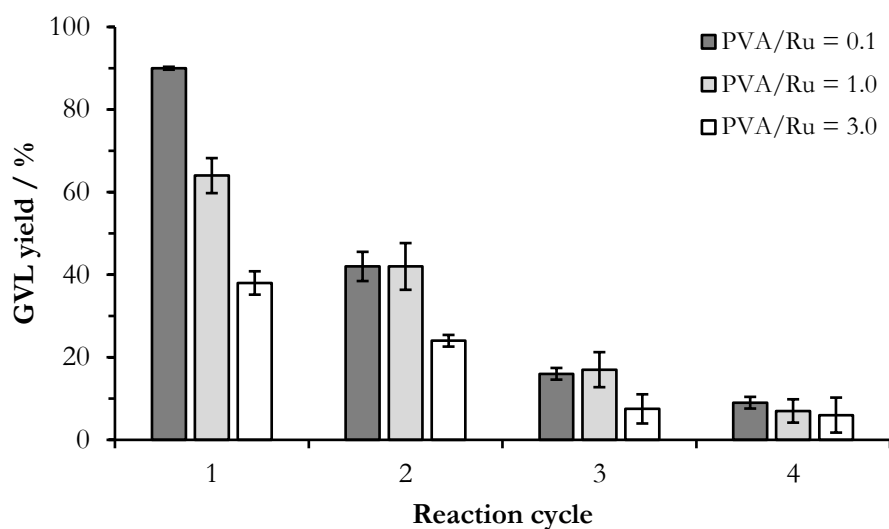


Figure 4.16. Catalyst activity on successive reuse using 1 wt.% Ru/C catalysts. *Reaction conditions:* 100 °C, 5 bar H₂, 1 hour, 5 wt.% LA/H₂O, 0.015 g catalyst.

BET surface analysis of the catalyst subjected to reuse study was carried out and the data are reported in Table 4.8. The surface area of all of the catalysts gradually decreased after each reaction cycle. The decrease in surface area correspond with a decrease in GVL yield after each reaction cycle. Though it was established above in Table 4.1 that the surface area of the carbon support did not ultimately determine the activity, the severity of the change in the surface area of the catalyst after each reaction cycle is indicative of a surface change that may have influenced the catalytic activity. Inhibition of the surface active sites by products or intermediates, coking, or metal sintering are likely the deactivation mechanisms. Ru catalysts have been shown to be susceptible to coking, and sintering as is proposed as a deactivation mechanism¹⁸. Decrease in surface area has also been reported as a possible reason for deactivation for Ru catalysts¹⁸. Though Ru/C catalysts by SI have never been reported, AuPd catalysts prepared by SI have been reported by Hutchings and co-workers to be more sensitive to sintering when supported on carbon than on other supports such as TiO₂⁴⁰.

Table 4.8. BET surface area of catalysts that underwent reuse tests.

Reaction cycle	BET surface area / m ² g ⁻¹		
	PVA/Ru = 0.1	PVA/Ru = 1.0	PVA/Ru = 3.0
1	250	200	200
2	180	160	150
3	140	130	125
4	70	60	60

TPR analysis on the used catalyst (the most active catalyst: PVA/Ru = 0.1, NaBH₄/RuCl₃ = 2.5) was carried out and is shown in Figure 4.17. There was a reduction signal observed between 100–150 °C, which is at a slightly higher temperature than observed before reaction. This signal is much broader and less intense. The lack of intensity suggests that less Ru is undergoing reduction during the second TPR cycle. When considered alongside the observations made by XPS in Chapter 3, in which Ru remained in a metallic state after a number of reaction cycles, it can be suggested that only a surface oxide layer is undergoing reduction. An increase in reduction temperature above reaction conditions correlates with a decrease in catalytic activity on reuse, suggesting that there was not enough metallic Ru present on the catalyst surface in reaction cycle 2 onwards (Figure 4.16). It cannot be ruled out that LA/levulinate species may have collected on the surface in much the same way as lactate species did (already discussed in Chapter 3 section 3.2.2).

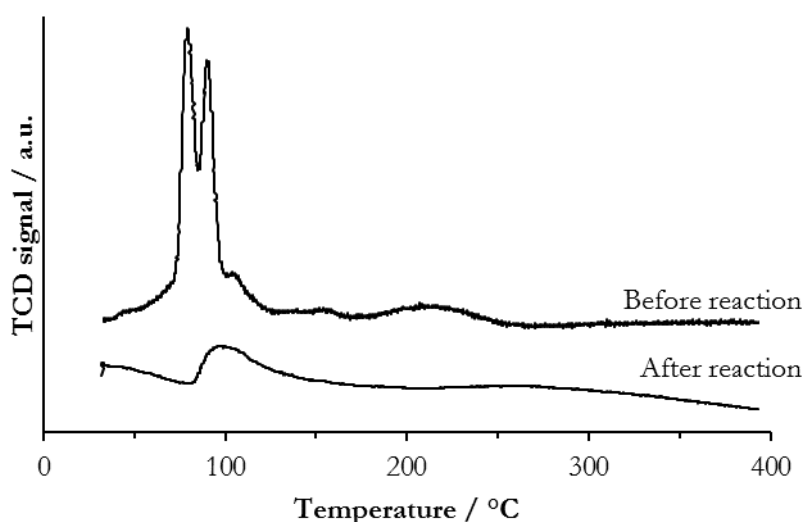


Figure 4.17. TPR profiles of 1 wt.% Ru/C (PVA/Ru = 0.1, NaBH₄/RuCl₃ = 2.5) catalyst before reaction and after 1 use.

There were no differences in the XPS signals after the reaction, though shifts to Ru(0) binding energies might be expected given the exposure to 5 bar H₂ pressure. As seen in Chapter 3 once again, Ru did not remain in a reduced state on exposure to ambient conditions. This is in line with the TPR data observed in Figure 4.17, which showed TPR on a used catalyst still showed a reduction signal.

4.2.6. Reaction kinetics

Kinetic measurements were carried out using the most active catalyst in this study – 1 wt.% Ru/C prepared by SI from RuCl₃ supported on XC72R, with a PVA/Ru ratio of 0.1 and NaBH₄/RuCl₃ ratio of 2.5. From Figures 4.18 and 4.19 it can be determined that the reaction was zero order with respect to LA, and a fractal order of 1.25 with respect to H₂ was observed. Zero order dependency of organic species

are documented in the literature and is attributed to a facile adsorption of the substrate on the surface, resulting in a saturation of the species on active sites prior to the hydrogenation step⁴¹. The fractal order of 1.25 was twice as large as the order reported by Bond and co-workers for a 5 wt.% Ru/C catalyst¹⁹, though a direct comparison cannot be made as there are key differences between the two systems. The reaction studied by Bond and co-workers used a 5 wt.% Ru/C catalyst and was carried out in the gas phase. The reaction presented here used a 1 wt.% Ru/C catalyst in the liquid phase. Diffusion of H₂ through water is a consideration in the rate of reaction in the case of this work *v.s.* Bond and co-workers. The same kinetics measurements were carried out using one of the less active catalysts for LA hydrogenation i.e. 1 wt.% Ru/C prepared by WI from Ru(NO)(NO₃)₃ on XC72R, and the values obtained were in good agreement with the values obtained for the catalyst prepared by SI: -0.0912 order with respect to LA, and 0.978 with respect to H₂. The differences in the catalysts brought about by the different preparation methods did not affect the order of the reaction. Therefore, it is reasonable to suggest that the rate equation for the reaction is well represented by Equation 4.1.

Equation 4.1.

$$\text{Rate} = k \cdot p_{\text{H}_2}^{1.25}$$

Because the order of reaction was found to be 0 in LA, the Arrhenius plot shown in Figure 4.20 can be taken as an estimate of the barrier to H₂ dissociation, which was calculated to be 37.85 KJ mol⁻¹.

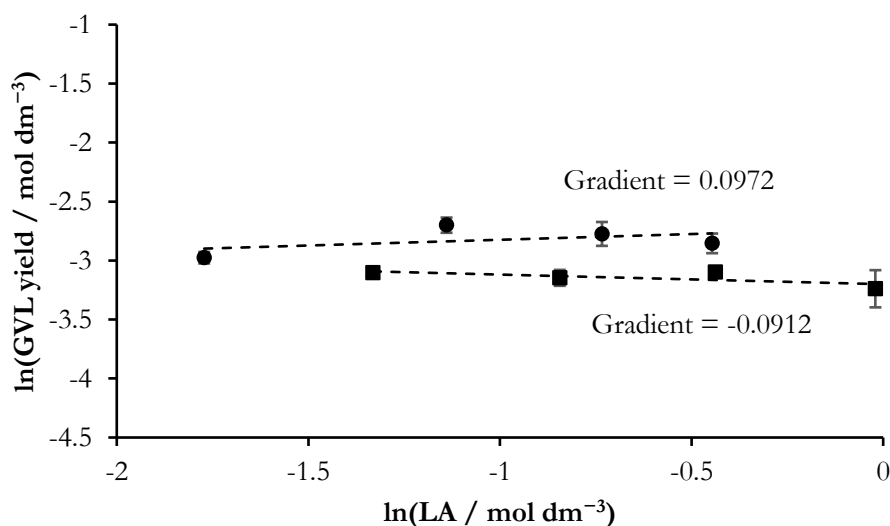


Figure 4.18. Determination of the order of reaction with respect to LA. ●: 1 wt.% Ru/C prepared by SI from RuCl₃ on XC72R; ■: 1 wt.% prepared by WI from Ru(NO)(NO₃)₃ on XC72R.

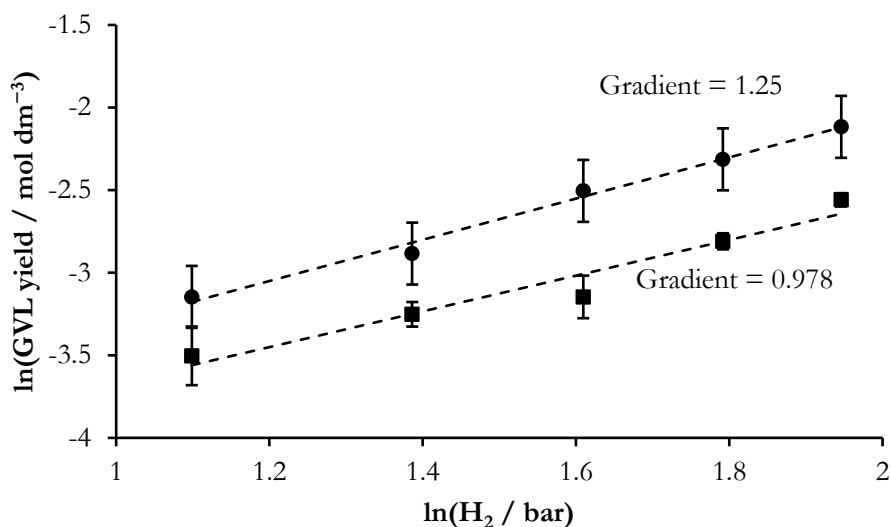


Figure 4.19. Determination of the order of reaction with respect to H_2 . ●: 1 wt.% Ru/C prepared by SI from $RuCl_3$ on XC72R; ■: 1 wt.% prepared by WI from $Ru(NO)(NO_3)_3$ on XC72R.

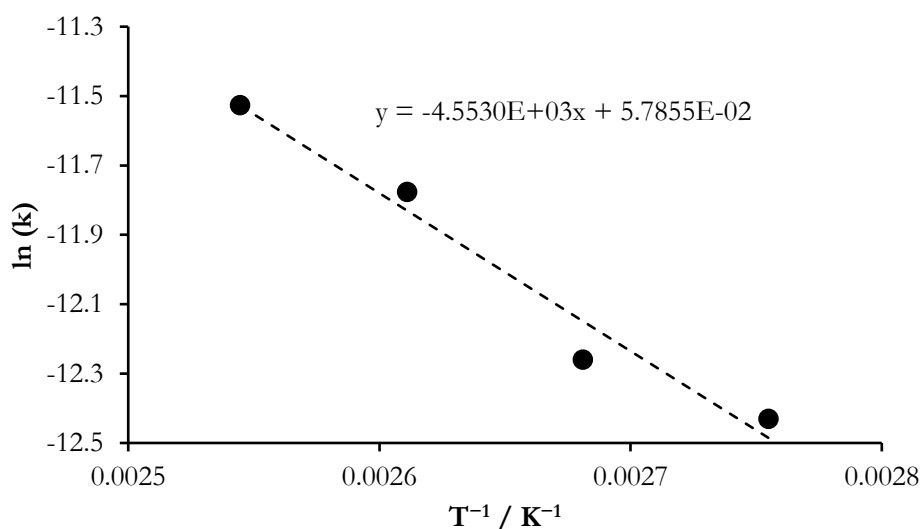


Figure 4.20. Arrhenius plot for the determination of reaction activation energy (using 1 wt.% Ru/C prepared by SI from $RuCl_3$ supported on XC72R).

The kinetic data support the notion that the reaction mechanism proceeded *via* a hydrogenation followed by ring closing mechanism. The activation energy of the process was the value expected for a hydrogenation process. Moreover, the hydrogenation was found to be the rate limiting step. Because α -angelica lactone was not observed by GC analysis, even at short reaction times, the hydrogenation process must have occurred first. There was no observation of the 4-hydroxypentanoic acid intermediate that arises from the mechanism, but given the ease of the intramolecular aldol reaction to close the ring, this is not surprising.

4.3. Conclusions

This chapter has investigated the use of 1 wt.% Ru/C catalysts for the hydrogenation of LA to GVL. The choice of carbon support (XC72R and G60) was investigated. INS showed that the hydrogen content of the G60 carbon was approximately 10 times that of XC72R. XC72R supported catalysts were more active for LA hydrogenation than G60 supported catalysts.

The effects of the preparation method and Ru precursor were investigated on both types of carbon. All of the three variables were found to have a significant effect on the catalytic activity for both reactions. For the first time it has been demonstrated that a low-metal content Ru/C (1 wt.% Ru) catalyst prepared by SI can produce up to 90 % yield of GVL under mild reaction conditions.

Following this, an optimisation of the catalyst preparation by SI was investigated by varying the use of PVA as a stabiliser and NaBH₄ as a reducing agent. During this procedure, a Ru colloid was formed. It was found that the use of PVA was important because the catalytic activity was seen to increase *vs.* a catalyst prepared without using PVA, but the use of an excessive amount of PVA was ultimately detrimental to catalytic activity. This was attributed to the blocking of active sites on the surface. As the use of NaBH₄ during the preparation was increased, a volcano-like plot was observed, with NaBH₄/RuCl₃ = 2.5 being optimum. XPS and TPR analysis showed that even when a large excess of NaBH₄ was used, the final catalyst was comprised of mostly RuO₂ on the surface. Whereas NaBH₄ is used in the preparation of Au/TiO₂ for the reduction of Au, its role in the case of Ru is to only dictate the rate of nanoparticle formation and therefore the particle size. UV studies on the colloid are recommended to better understand the nature of the Ru species formed during the reduction process.

XPS analysis suggested that RuO₂ (which may or may not be hydrated to some extent) is, or is the precursor to, the active Ru species during hydrogenation, as it is so ubiquitously present across the catalyst surface. The instances where Ru(III) was observed as RuCl₃ correlated with low GVL yields suggesting either that the presence of chloride had a poisoning effect or prevented the reduction of Ru under reaction conditions.

Kinetic data presented also provided some insight into the mechanism of the reaction. A hydrogenation process (as opposed to a dehydration) was shown to be the rate limiting step of the reaction. There was no evidence of α -angelica lactone being formed during the reaction, indicating that the hydrogenation step had to have happened before the dehydration step. Therefore, the reaction proceeds *via* pathway 1, as discussed earlier in Chapter 1 (section 1.3.2.1)¹⁹.

Investigations into optimising catalyst synthesis to a particular reaction are increasingly valuable as catalytic science shifts into a paradigm of designing for specific reactions. The more data that can be obtained about catalysts prepared with various changes, large or small, to the synthesis procedure, the better informed catalyst design can be. This investigation is a small contribution towards that ideal.

4.4. References

- 1 J.-P. Lange, *Biofuels, Bioprod. Biorefining*, 2007, **1**, 39–48.
- 2 T. Werpy and G. Petersen, *Top Value Added Chemicals from Biomass: Volume I -- Results of Screening for Potential Candidates from Sugars and Synthesis Gas*, 2004.
- 3 I. T. Horvath, H. Mehdi, V. Fabos, L. Boda and L. T. Mika, *Green Chem.*, 2008, **10**, 238–242.
- 4 E. L. Kunke, D. A. Simonetti, R. M. West, J. C. Serrano-Ruiz, C. A. Gärtner and J. A. Dumesic, *Science*, 2008, **322**, 417–421.
- 5 S. Iqbal, S. A. Kondrat, D. R. Jones, D. C. Schoenmakers, J. K. Edwards, L. Lu, B. R. Yeo, P. P. Wells, E. K. Gibson, D. J. Morgan, C. J. Kiely and G. J. Hutchings, *ACS Catal.*, 2015, **5**, 5047–5059.
- 6 E. C. Larsen and J. H. Walton, *J. Phys. Chem.*, 1940, **44**, 70–85.
- 7 H. Jüntgen, *Fuel*, 1986, **65**, 1436–1446.
- 8 P. P. Upare, J.-M. Lee, D. W. Hwang, S. B. Halligudi, Y. K. Hwang and J.-S. Chang, *J. Ind. Eng. Chem.*, 2011, **17**, 287–292.
- 9 A. M. R. Galletti, C. Antonetti, V. De Luise and M. Martinelli, *Green Chem.*, 2012, **14**, 688–694.
- 10 J. M. Planeix, N. Coustel, B. Coq, V. Brotons, P. S. Kumbhar, R. Dutartre, P. Geneste, P. Bernier and P. M. Ajayan, *J. Am. Chem. Soc.*, 1994, **116**, 7935–7936.
- 11 S. Zhang, L. Chen, S. Zhou, D. Zhao and L. Wu, *Chem. Mater.*, 2010, **22**, 3433–3440.
- 12 H. Zhang, W. Chu, C. Zou, Z. Huang, Z. Ye and L. Zhu, *Catal. Letters*, 2011, **141**, 438–444.
- 13 A. Tavasoli, K. Sadagiani, F. Khorashe, A. A. Seifkordi, A. A. Rohani and A. Nakhaeipour, *Fuel Process. Technol.*, 2008, **89**, 491–498.
- 14 A. Tavasoli, M. Trépanier, A. K. Dalai and N. Abatzoglou, *J. Chem. Eng. Data*, 2010, **55**, 2757–2763.
- 15 A. E. Aksoylu, M. Madalena, A. Freitas, M. F. R. Pereira and J. L. Figueiredo, *Carbon N. Y.*, 2001, **39**, 175–185.
- 16 Y. Yang, K. Chiang and N. Burke, *Catal. Today*, 2011, **178**, 197–205.
- 17 E. Lam and J. H. T. Luong, *ACS Catal.*, 2014, **4**, 3393–3410.

- 18 A. S. Piskun, J. E. de Haan, E. Wilbers, H. H. van de Bovenkamp, Z. Tang and H. J. Heeres, *ACS Sustain. Chem. Eng.*, 2016, **4**, 2939–2950.
- 19 O. A. Abdelrahman, A. Heyden and J. Q. Bond, *ACS Catal.*, 2014, **4**, 1171–1181.
- 20 W. Luo, M. Sankar, A. M. Beale, Q. He, C. J. Kiely, P. C. A. Bruijninx and B. M. Weckhuysen, *Nat Commun.*, 2015, **6**.
- 21 S. G. Wettstein, J. Q. Bond, D. M. Alonso, H. N. Pham, A. K. Datye and J. A. Dumesic, *Appl. Catal. B Environ.*, 2012, **117–118**, 321–329.
- 22 Y. Yang, C.-J. Sun, D. E. Brown, L. Zhang, F. Yang, H. Zhao, Y. Wang, X. Ma, X. Zhang and Y. Ren, *Green Chem.*, 2016, **18**, 3558–3566.
- 23 H. Jang, S.-H. Kim, D. Lee, S. E. Shim, S.-H. Baeck, B. S. Kim and T. S. Chang, *J. Mol. Catal. A Chem.*, 2013, **380**, 57–60.
- 24 I. Rossetti, N. Pernicone and L. Forni, *Appl. Catal. A Gen.*, 2003, **248**, 97–103.
- 25 A. M. Hengne, N. S. Biradar and C. V Rode, *Catal. Letters*, 2012, **142**, 779–787.
- 26 M. Baron, O. Bondarchuk, D. Stacchiola, S. Shaikhutdinov and H.-J. Freund, *J. Phys. Chem. C*, 2009, **113**, 6042–6049.
- 27 D. J. Morgan, *Surf. Interface Anal.*, 2015, **47**, 1072–1079.
- 28 A. Foelske, O. Barbieri, M. Hahn and R. Kötz, *Electrochem. Solid-State Lett.*, 2006, **9**, A268–A272.
- 29 P. Albers, K. Seibold, G. Prescher, B. Freund, S. F. Parker, J. Tomkinson, D. K. Ross and F. Fillaux, *Carbon N. Y.*, 1999, **37**, 437–444.
- 30 P. Panagiotopoulou, N. Martin and D. G. Vlachos, *J. Mol. Catal. A Chem.*, 2014, **392**, 223–228.
- 31 L. Prati and A. Villa, *Catalysts*, 2012, **2**, 24.
- 32 L. Prati and G. Martra, *Gold Bull.*, 1999, **32**, 96–101.
- 33 A. Villa, N. Dimitratos, C. E. Chan-Thaw, C. Hammond, G. M. Veith, D. Wang, M. Manzoli, L. Prati and G. J. Hutchings, *Chem. Soc. Rev.*, 2016.
- 34 N. Dimitratos, C. Hammond, C. J. Kiely and G. J. Hutchings, *Appl. Petrochemical Res.*, 2014, **4**, 85–94.
- 35 R. G. Patharkar, S. U. Nandanwar and M. Chakraborty, *J. Chem.*, 2013, **2013**, 5 pages.

-
- 36 J. Turkevich, *Gold Bull.*, 1985, **18**, 86–91.
- 37 M. Zahmakıran and S. Özkar, *J. Mol. Catal. A Chem.*, 2006, **258**, 95–103.
- 38 A. M. Hengne, N. S. Biradar and C. V Rode, *Catal. Letters*, 2012, **142**, 779–787.
- 39 J. A. Lopez-Sanchez, N. Dimitratos, C. Hammond, G. L. Brett, L. Kesavan, S. White, P. Miedziak, R. Tiruvalam, R. L. Jenkins, A. F. Carley, D. Knight, C. J. Kiely and G. J. Hutchings, *Nat Chem*, 2011, **3**, 551–556.
- 40 N. Dimitratos, J. A. Lopez-Sanchez, D. Morgan, A. F. Carley, R. Tiruvalam, C. J. Kiely, D. Bethell and G. J. Hutchings, *Phys. Chem. Chem. Phys.*, 2009, **11**, 5142–5153.
- 41 M. Boudart and G. Djega-Mariadassou, *Kinetics of Heterogeneous Catalytic Reactions*, Princeton University Press, 2014.

Chapter 5

Cu-ZrO₂ – an alternative to precious metal catalysts for the hydrogenation of levulinic acid

5.1. Introduction

As discussed in Chapter 1, the production of GVL is desirable, be it for its own properties or further conversion to value added products such as 2-MTHF, pentanoic acid or esters, or liquid fuel products. It was also highlighted in Chapter 1 that Cu is an emerging base metal alternative to Ru for the conversion of LA into GVL. If the price of catalyst production can be decreased, it is likely that the overall cost of biomass utilisation will also be decreased, making it much more economically viable. Fan and co-workers have demonstrated Cu-ZrO₂ catalysts are highly active for LA to GVL in the liquid phase¹⁻⁵. Balla *et al.* demonstrated that Cu can also be utilised effectively in the vapour phase hydrogenation of LA⁶. Hengne and Rode showed that Cu-ZrO₂ catalysts prepared by aqueous co-precipitation can convert 100 % of LA into GVL in 5 h⁷. Although Cu-based catalysts are cheaper, they require much harsher reaction conditions than Ru in order to achieve comparable activity. Deactivation of the catalyst after long reaction times is also an issue, with sintering and catalyst coking being cited as principle mechanisms of deactivation⁶.

This chapter focusses on the optimisation of Cu-ZrO₂ catalysts prepared by co-precipitation (CP) following from the work of Hengne and Rode⁷. The aim of the experiments herein was to determine the origins of the catalyst activity by varying the preparation parameters, including Cu/Zr ratio, calcination temperature, and precipitate ageing time. Characterisation was carried out aimed at elucidating the active component of these catalysts.

5.2. Results and discussion

5.2.1. Variation of Cu/Zr ratio

Cu-ZrO₂ catalysts were prepared by varying the Cu/Zr ratio during CP. ICP-AES analysis was carried out on the final catalysts in order to determine the actual amounts of metals in prepared catalysts. The data for LA conversion are shown in Table 5.1. The actual Cu/Zr ratios calculated by ICP-AES were in good agreement with the intended Cu/Zr ratios calculated for the synthesis. These values indicate that all metals were precipitated successfully and any loss during filtration or washing step was minimal. The theoretically calculated values of Cu/Zr will be quoted throughout this chapter.

Table 5.1. Theoretical and the measured Cu/Zr ratios in final catalysts.

Theoretical Cu/Zr / mol/mol	Actual Cu/Zr determined by ICP-AES/ mol/mol
0.25	0.27
0.50	0.50
0.75	0.80
1.00	0.99
1.25	1.25
1.50	1.53
2.00	2.04

All of the catalysts prepared by variation of Cu/Zr ratio were tested for the hydrogenation of LA and the resulting GVL yields are presented in Figure 5.1. The catalyst prepared with a Cu/Zr = 1 showed the highest GVL yield. Catalysts with Cu/Zr ratios above and below 1 produced significantly less GVL. Figure 5.1 also shows the GVL yield normalised by BET surface area (Table 5.2). The largest surface area was observed for the catalyst prepared with Cu/Zr = 1. A steady decline was observed in surface area for the catalysts prepared with Cu/Zr ratio above unity. The activity data normalised to BET surface area showed a constant trend that started to decrease after Cu/Zr = 1.25. These data suggest that the catalytic activity was dependent on the BET surface area at Cu/Zr ≤ 1.25 and the normalised GVL yield remained largely constant (approximately 0.5 % (m² g⁻¹)⁻¹) as the amount of Cu was increased. This observation is notable because it suggests that most of the copper present at higher copper loadings is not part of a catalytically active site. The BET total surface area of the Cu-ZrO₂ catalysts was found to be much higher than that of ZrO₂ on its own (7 m² g⁻¹). It is commonly observed that ZrO₂ supports have low surface areas⁸. The addition of Cu generally increases the surface area by distortion of the material lattice⁹, though there can be a limit to the amount of copper added^{8,10,11}.

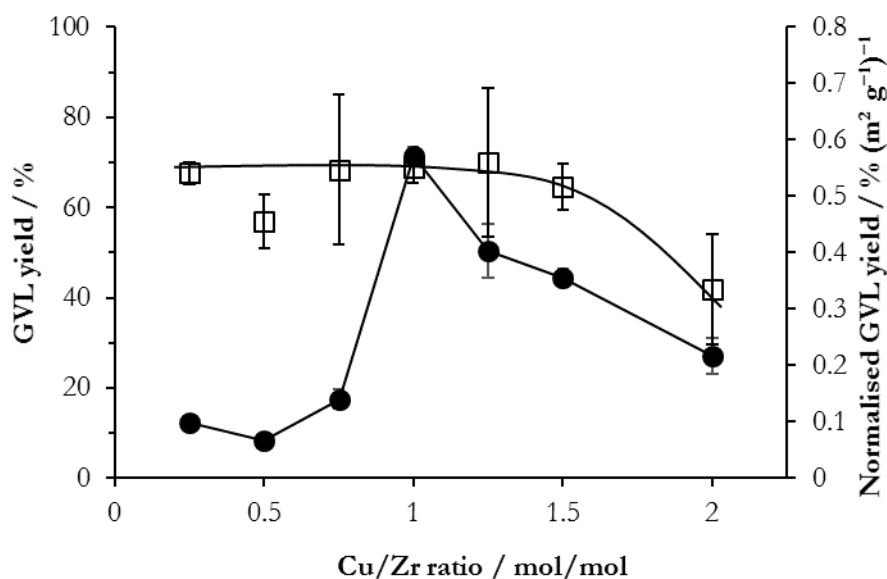


Figure 5.1. Effect of the variation of Cu/Zr ratio on GVL yield. ●: GVL yield; ×: GVL yield normalised by BET surface area. **Reaction conditions:** 200 °C, 35 bar H₂, 2 h, 5 wt.% LA/H₂O, 0.05 g catalyst.

Table 5.2. BET surface area for the catalysts prepared with different Cu/Zr ratios.

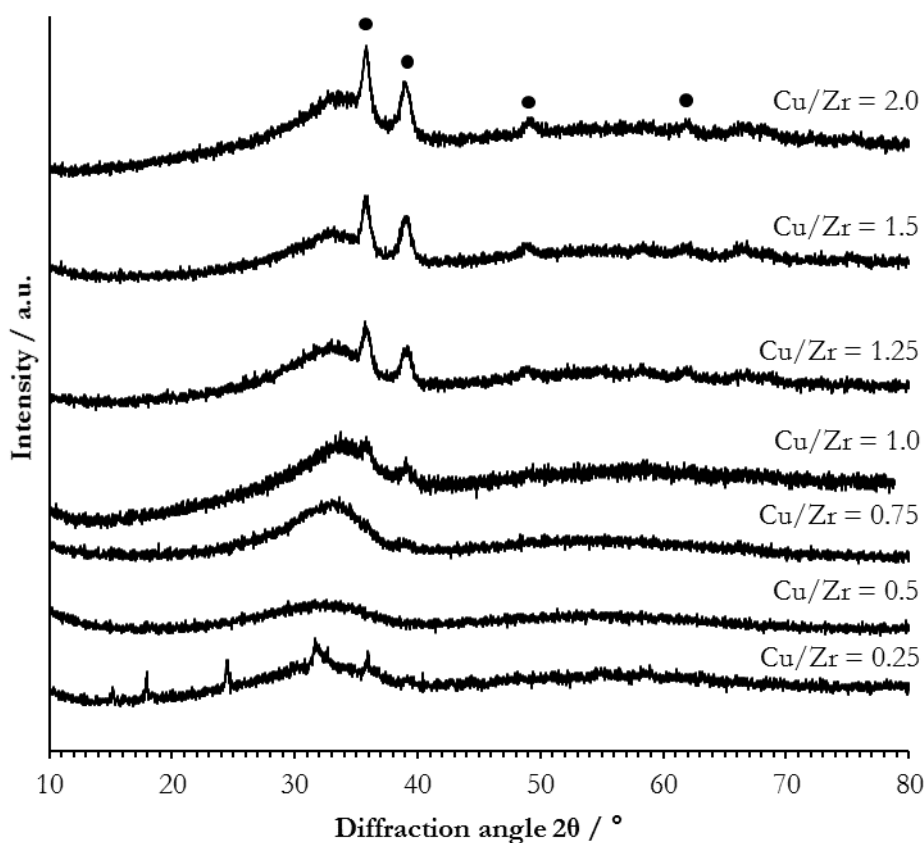
Cu/Zr / mol/mol	BET surface area / m ² g ⁻¹
0.25	23
0.50	18
0.75	32
1.00	149
1.25	90
1.50	86
2.00	81
ZrO ₂	7

A correlation was also observed between the Cu surface area and the catalytic activity with this series of catalysts. Three of the catalysts representing low, middling, and high Cu/Zr ratios were selected for N₂O titration analysis (Table 5.3) and it was found that the catalyst that showed the highest GVL yield also had the highest Cu surface area (4.1 m² g⁻¹). Cu/Zr = 0.75 had much lower Cu surface area (0.5 m² g⁻¹). It might have been expected that a low loading of Cu might be highly dispersed across the surface, but as discussed above, Cu can be incorporated into the support lattice, where it would not be available to undergo oxidation during N₂O analysis. This also suggests that only the Cu present on the surface was catalytically active.

Table 5.3. Cu surface area of a selection of catalysts prepared with different Cu/Zr ratios.

Cu/Zr /mol/mol	Cu surface area / m ² g ⁻¹
0.75	0.5
1.0	4.1
2.0	1.0

XRD analysis was performed on all the catalysts prepared by the variation of Cu/Zr ratio and the resulting patterns are shown in Figure 5.2. Catalysts with Cu/Zr < 1 were found to be completely amorphous, with no assignable reflections in the XRD. For Cu/Zr = 1, reflections appearing at $2\theta = 35^\circ$ and 39° were observed corresponding to CuO (ICDD = 00-041-0254). Increasing the Cu/Zr ratio resulted in an increase in intensity of both of these reflections. Additional CuO reflections were observed at $2\theta = 49^\circ$ and 62° (ICDD = 00-041-0254) in catalysts with Cu/Zr ≥ 1.25 .

**Figure 5.2.** XRD patterns for catalysts prepared with varying Cu/Zr ratio. ●: CuO.

The most intense reflection at $2\theta = 35^\circ$ (CuO[111]) was used to estimate the CuO particle size using the Scherrer equation (Table 5.4). Catalysts with Cu/Zr < 1 that were amorphous in the XRD were considered to have CuO particles sizes below 5 nm. The most active catalyst (Cu/Zr = 1) had the lowest metal ratio at which a CuO phase was observed in the XRD. This catalyst also had the highest surface

area of all the catalysts synthesised. Though a margin of error is to be expected in the particle size estimations due to the small size of the reflections^{12,13}, the high BET surface area implies that the CuO particles are highly dispersed across the surface, which may have enhanced the catalytic activity. The increasing Cu/Zr ratio can be correlated with an increase in the intensity of XRD reflection and a corresponding CuO particle size but there was also a loose relationship between the intensity of the CuO reflections and the BET surface area. Where there were intense reflections present – indicative of larger CuO particles – the BET surface area was quite low. This suggests that the larger CuO particles were not dispersed well on the surface and resulted in poor catalytic activity. Conversely, the BET surface area was higher when there were no discernible phases in the XRD pattern. The activity of these catalysts was high. These observations suggest that the CuO particle size in the as prepared material is important for the catalytic activity. Of course, these CuO particles are precursors to the active catalytic species. Under reaction conditions, it is expected that these oxide particles were reduced to metallic Cu⁹.

Table 5.4. Particle sizes of catalysts prepared with different Cu/Zr ratio using the Scherrer equation.

Cu/Zr / mol/mol	CuO particle size ^a / nm
0.25	Unable to acceptably estimate particle size using the Scherrer equation
0.50	
0.75	
1.00	11.0
1.25	8.3
1.50	20.0

^a hkl = [111]

XPS analysis confirmed the presence of CuO in all catalysts, with a Cu(2p_{3/2}) signal at 933.2 eV and the satellite structure and Cu LMM Auger peaks characteristic of CuO at 933.2 eV (binding energy) and 917.7 eV (kinetic energy) respectively. These spectra are presented in Figure 5.3. After preparation and calcination Cu was present solely as Cu(II) as determined by XPS – there was no indication of a Cu₂O signal indicating that Cu(I) was not formed.

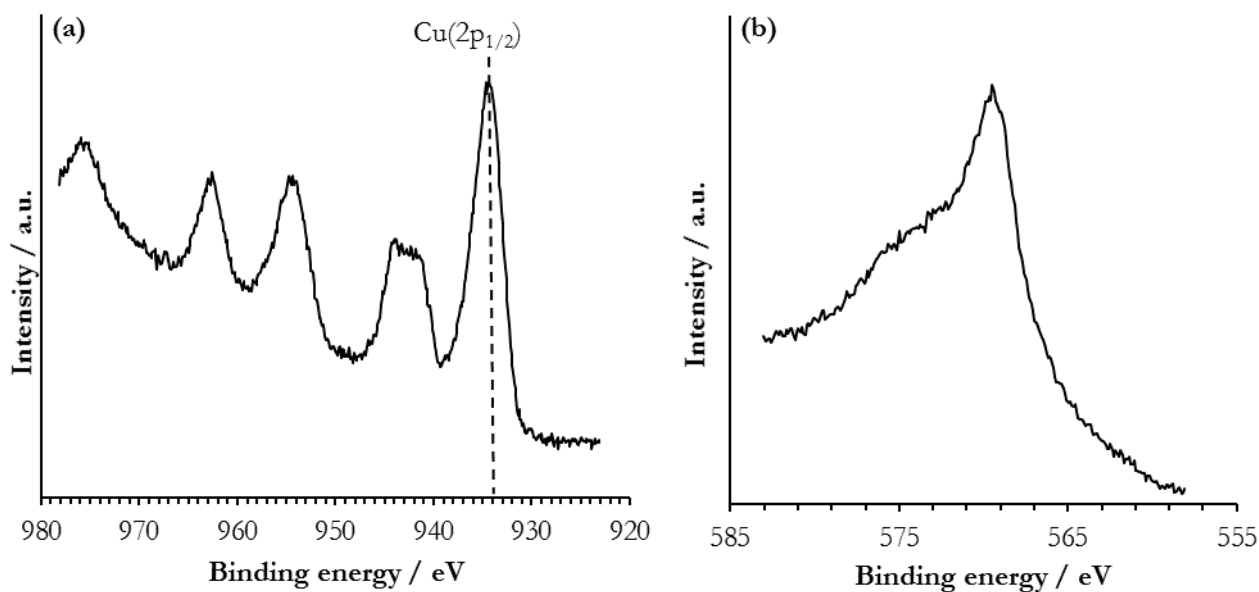


Figure 5.3. (a) A typical XPS profile and (b) Auger peak of Cu-ZrO₂ catalysts.

TPR analysis was carried out on all catalysts and the resulting reduction profiles are shown in Figure 5.4. There are no reduction signals observed in the catalysts prepared with $\text{Cu/Zr} \leq 0.75$, though ICP-AES confirmed that Cu was indeed present in quantities matching the calculated ratios from the preparation procedure, XPS also indicated the presence of CuO. The absence of any reduction signals in these catalysts suggests that Cu was only present in the bulk matrix of ZrO₂ lattice, and not as separate oxides. These observations are in agreement with the low surface areas discussion above. The surface area of the catalyst prepared with $\text{Cu/Zr} = 0.75$ was low compared to the other catalysts because there was only a small amount of Cu present, which was likely incorporated into the lattice rather than dispersed across the surface. The TPR signal was consequently weak because most of the Cu was not accessible for reduction. Figure 5.1 shows that the catalysts with $\text{Cu/Zr} \leq 0.75$ gave less than 20 % yield of GVL. This indicates that CuO (likely Cu(0) under reaction conditions given the TPR data) was present in the catalyst, but only in the lattice where it is inaccessible to the substrate. The catalyst prepared with $\text{Cu/Zr} = 0.75$ showed a broad, low intensity reduction signal starting around 170 °C and centred at 240 °C. There is a significant change in the reduction profiles in catalysts with $\text{Cu/Zr} \geq 1$, with two reduction events observed in the range of 150–225 °C. Multiple steps for the reduction of CuO to metallic Cu have been observed in previous literature, and are attributed to varying degrees of interaction of Cu nanoparticles with their supports^{9,14,15}. Lower temperature TPR features indicate smaller CuO particles that have a relatively strong interaction with their support that enhances the reducibility of CuO, as shown by Huang *et al.*¹⁶ Recent work by Zhou *et al.* demonstrated using TPD, IR and Raman techniques that there are synergistic interactions between Cu and Zr in catalysts prepared by CP, with Zr not only serving as a support but also as an activator of metallic Cu nanoparticles¹⁷. The catalyst prepared with $\text{Cu/Zr} = 1$,

which was most active, showed two sharp reduction signals at 155 °C and 181 °C. These two features were observed in the catalysts prepared with $\text{Cu/Zr} > 1$, though with some variation in the position of the higher temperature signal. For $\text{Cu/Zr} = 1$, the intensity of each signal is roughly equal, whereas the other catalysts showed a reduction signal at higher temperature that was significantly more intense than the one at lower temperature. TPR analysis of ZrO_2 was performed, but no reduction signal was observed between 50–450 °C, indicating unreduced ZrO_2 was present in all catalysts.

The more intense lower temperature signal in the most active catalyst ($\text{Cu/Zr} = 1$) indicates greater reducibility of CuO in this catalyst compared with the others. The small CuO particles that are highly dispersed across the surface as suggested by particle size estimate and BET surface area can interact strongly with the ZrO_2 support, making them more reducible¹¹. The reduction peak at a higher temperature is indicative of larger CuO particles that interact weakly with ZrO_2 . Comparison of this TPR data with the activity data presented in Figure 5.1 indicates that the reducibility of CuO is an important factor in preparing a catalyst that is highly active. Better reducibility of the catalyst represented by a more intense lower temperature reduction signal was always a feature of the more active catalysts. The XRD data show that large CuO particles are present in catalysts with $\text{Cu/Zr} \geq 1.25$. The presence of an intense reduction signal at a higher temperature in the TPR also suggests large CuO particles. Given that these species were largely in a reduced state at the reaction temperature of 200 °C, it can be concluded that the large particles that were present were not active as hydrogenation catalysts.

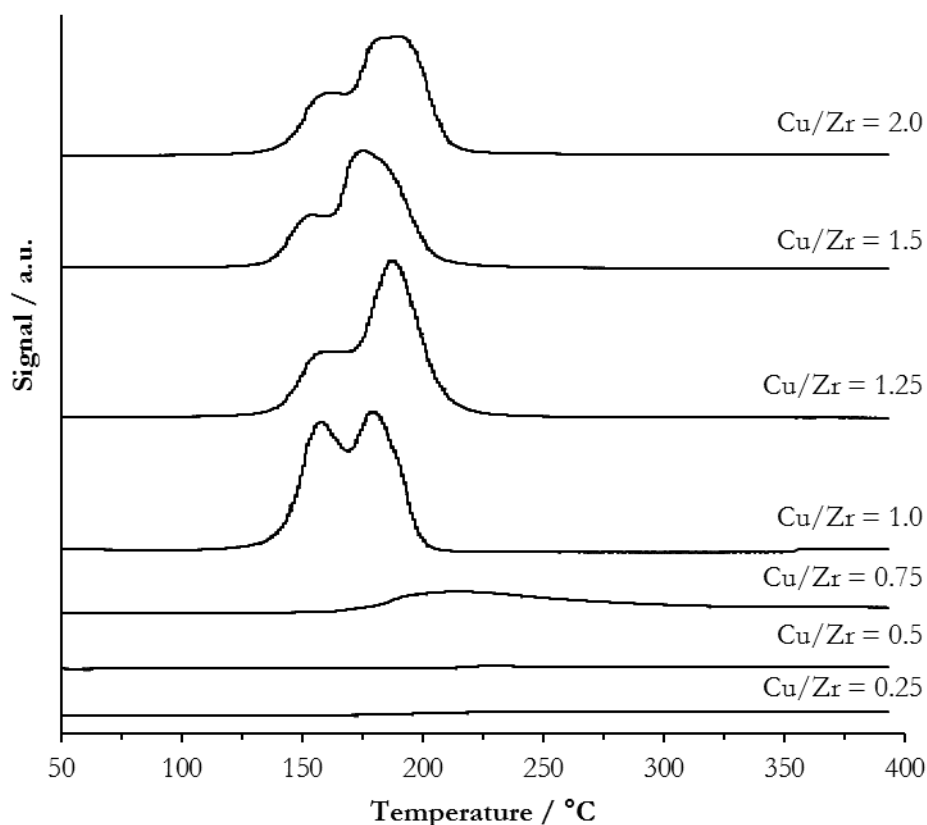


Figure 5.4. TPR profiles of the catalysts prepared with varying Cu/Zr ratios.

It can be concluded from the catalytic data that the catalyst prepared with Cu/Zr = 1 was the most optimum ratio for active catalysts. Both XRD and XPS analyses showed the presence of small CuO particles on an amorphous ZrO₂ support. TPR data showed that CuO particles in all catalysts with Cu/Zr \geq 1 were reduced up to 200 °C and therefore under reaction conditions employed (200 °C, 35 bar H₂, 2 h). However, small Cu crystallites that are highly reducible due to strong interactions with the ZrO₂ support were required to achieve a higher activity. Small Cu clusters are known to exhibit catalytically relevant Lewis acidity^{18,19}, which in turn is known to be a requirement for LA hydrogenation^{20,21}. It is logical to say that the catalyst with an abundance of small Cu clusters will have more Lewis acidity, which will be beneficial to the catalytic activity. Further to this, we performed variation of calcination temperature and the catalyst with Cu/Zr ratio of unity was chosen for this purpose. The next section is devoted to the discussion of data achieved by varying the calcination temperature.

5.2.2. The effect of calcination temperature

The effect of calcination temperature was studied by calcining a catalyst prepared with $\text{Cu/Zr} = 1$ at temperatures between 300–800 °C in static air for 4 hours. The catalysts calcined at different temperatures were tested for LA hydrogenation and the results are presented in Figure 5.5. GVL yield increased when the catalyst was calcined at 400 °C compared with 300 °C, but above 400 °C there was a significant decline in GVL yield with an increase in calcination temperature. The BET surface area was determined for each catalyst calcined at various temperatures (Table 5.5). These BET surface area values were used to normalise the GVL yield data in Figure 5.5. With increasing calcination temperature, the BET surface area steadily declined and the normalised GVL yield followed the same trend. The catalyst calcined at 400 °C showed higher normalised activity than the catalysts calcined at 300, 500, and 600 °C. This suggests that the surface area was not the determining feature in the catalyst activity in this set of experiments. The data suggests that there was a greater number of active sites present on the surface of the catalyst calcined at 400 °C than the catalysts calcined at temperatures lower and higher than 400 °C.

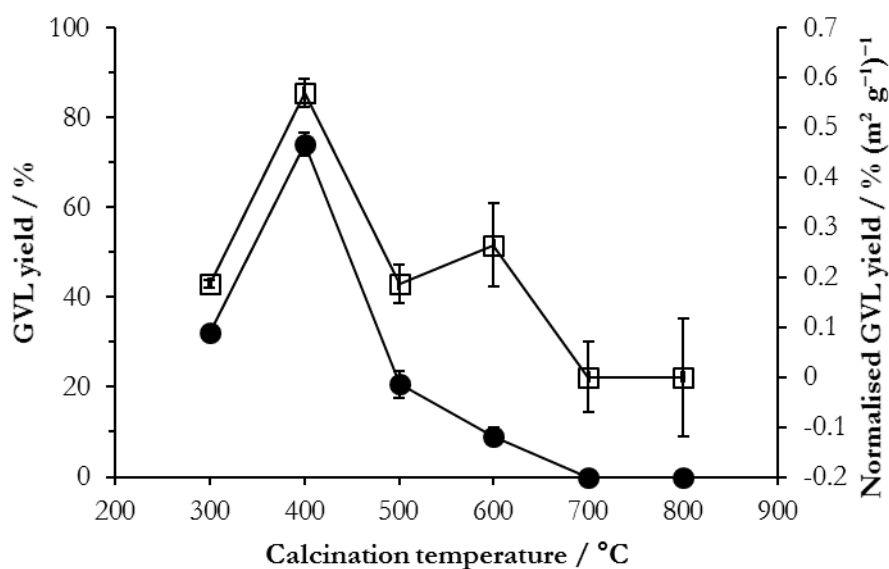


Figure 5.5. Effect of catalyst calcination temperature on GVL. ●: GVL yield; ×: GVL yield normalised by BET surface area. *Reaction conditions:* 200 °C, 35 bar H₂, 2 h, 5 wt.% LA/H₂O, 0.05 g catalyst.

Table 5.5. BET surface area for the catalysts calcined at different temperatures.

Calcination temperature / °C	BET surface area / m ² g ⁻¹
300	171
400	149
500	111
600	34
700	10
800	6

Cu surface area was measured by N₂O titration and the data for Cu metal surface area are presented in Table 5.6. The most active catalyst calcined at 400 °C and one of the least active catalysts calcined at 600 °C had the same Cu surface area (4.2 m² g⁻¹). There was no trend observed that could be related to the catalytic activity. This data implies that there was not an even distribution of Cu throughout any of the catalysts (or else an increase in Cu surface area would be expected to result in an increase of GVL yield), but also the earlier observation that the majority of Cu present on the surface was not part of the catalytically active site.

Table 5.6. Cu surface area of Cu-ZrO₂ catalysts calcined at different temperatures.

Calcination temperature / °C	Cu surface area / m ² g ⁻¹
300	1.7
400	4.1
500	0.7
600	4.1
700	1.0
800	0.3

The reaction data would imply that there is change in catalyst behaviour due to a structural or compositional change during calcination treatment between 300–800 °C. The XRD patterns presented in Figure 5.7 showed a marked change in crystalline phases with an increase in calcination temperature. The catalyst calcined at 300 °C was found to be mostly amorphous (am-ZrO₂), with only two small reflections assignable to CuO at $2\theta = 35^\circ$ and 39° (ICDD-00-041-0254). These reflections increased in intensity with increasing calcination temperature. Additional CuO reflections were observed for the catalysts calcined at 600 °C at $2\theta = 49^\circ$ and 62° . Also, this catalyst showed new reflections with a significant intensity assigned to tetragonal-(t)-ZrO₂ at $2\theta = 31.5^\circ$, 51° , and 61° (ICDD-01-070-8758). There was a shift observed in the ZrO₂ reflection at $2\theta = 31.5^\circ$ to a lower diffraction angle of 30.2° from the catalyst calcined at 600 °C to the catalyst calcined at 700 °C, suggesting the incorporation of Cu into

the ZrO_2 matrix¹. Further increasing the calcination temperature from 700 °C to 800 °C resulted in another phase transition from t- ZrO_2 to monoclinic-(m)- ZrO_2 with intense reflections at $2\theta = 28^\circ, 31^\circ, 34^\circ,$ and 41° (ICDD-00-007-0343). Such phase changes are known for Cu/ ZrO_2 materials and occur at the same calcination temperatures as ZrO_2 itself^{22,23}, which implies that the incorporation of Cu into ZrO_2 does not have a marked effect on the phase transition temperatures of ZrO_2 . The most active catalyst calcined at 400 °C had relatively small particles supported on am- ZrO_2 . The formation of t- ZrO_2 resulted in a decreased yield of GVL for the catalyst calcined at 600 °C. The formation of large CuO particles and the m- ZrO_2 phase in the catalysts calcined at 700 °C and 800 °C resulted in a total loss of catalytic activity. Once again, the CuO particle size was calculated using the Scherrer equation and the data are presented in Table 5.7. An increase in particle size was observed in line with the increasing reflection intensity on increasing calcination temperature.

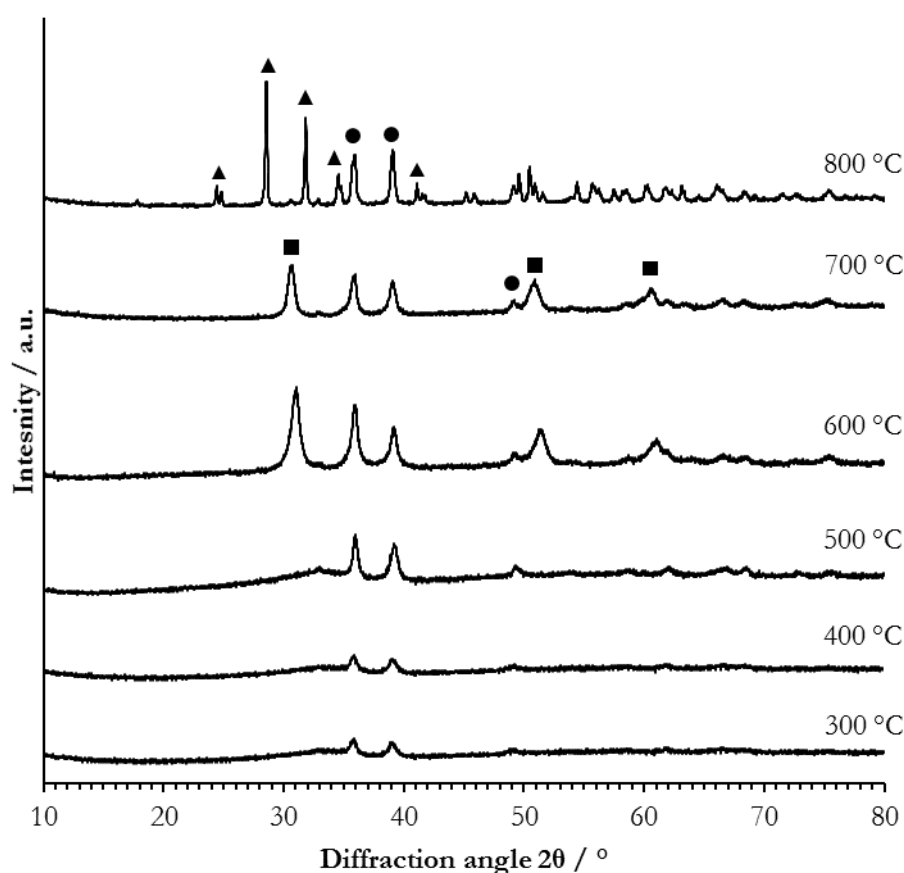


Figure 5.6. XRD patterns for catalysts calcined at different temperatures. ●: CuO; ■: t- ZrO_2 ; ▲: m- ZrO_2 .

Table 5.7. CuO particles sizes of catalysts calcined at different temperatures.

Calcination temperature / °C	CuO particle size ^a / nm
300	4.0
400	5.4
500	8.3
600	12.2
700	17.9
800	23.4

^a hkl = [111]

XPS analysis was performed on all the catalysts calcined at different temperatures and the data are shown in Table 5.8. Catalysts calcined at 400 °C showed the best dispersion of Cu, suggesting smaller particles. There was no correlation between the surface Cu/Zr ratio determined by XPS and GVL yield, which suggests once again that the majority of Cu present is not present in a catalytically active state. The presence of carbon in the samples was considerable and there was a higher concentration of oxygen than expected. This could indicate the retention of carbonate from the K₂CO₃ used as the precipitant during the preparation despite the washing step.

Table 5.8. XPS analysis for catalysts calcined at different temperatures.

Calcination temperature / °C	Surface Elemental Concentration at.%				Surface Cu/Zr ratio
	Cu 2p	O 1s	C 1s	Zr 3d	
Uncalcined	5.74	26.28	62.96	5.01	1.15
300	4.94	15.56	77.33	2.18	2.27
400	3.92	22.75	68.29	5.03	0.78
500	8.35	25.23	61.07	5.36	1.56
600	8.39	28.05	56.94	6.62	1.27
700	9.62	34.98	45.71	9.69	0.99

TPR analysis was performed on the catalysts calcined at different temperatures and the data are presented in Figure 5.7. The most active catalyst calcined at 400 °C was the only catalyst that showed a complete reduction below the reaction temperature of 200 °C. Two reduction signals were observed in all of these catalysts as previously discussed in section 5.2.1. The catalysts calcined at 300 °C and above 400 °C showed reduction signals above the reaction temperature. The increasing shift to higher reduction temperatures in catalysts calcined above 400 °C correlates with the particle sizes shown in Table 5.5. The increasing breadth of the reduction signal suggests that bulk-like CuO was formed at higher calcination temperatures, particularly when calcined at 800 °C. This observation, when combined with the XRD

data, could suggest that the segregation of CuO particles occurs at higher calcination temperatures, also suggested by Wang *et al.* in their investigation into Cu/ZrO₂ catalysts¹. The catalyst calcined at 300 °C however did not have a large particle size, yet exhibits the same reduction behaviour as the catalyst calcined at 800 °C and shows poor catalytic activity. This suggests that 300 °C was not a high enough temperature to enable the strong interactions of the CuO with the ZrO₂ support as discussed in section 5.2.1.

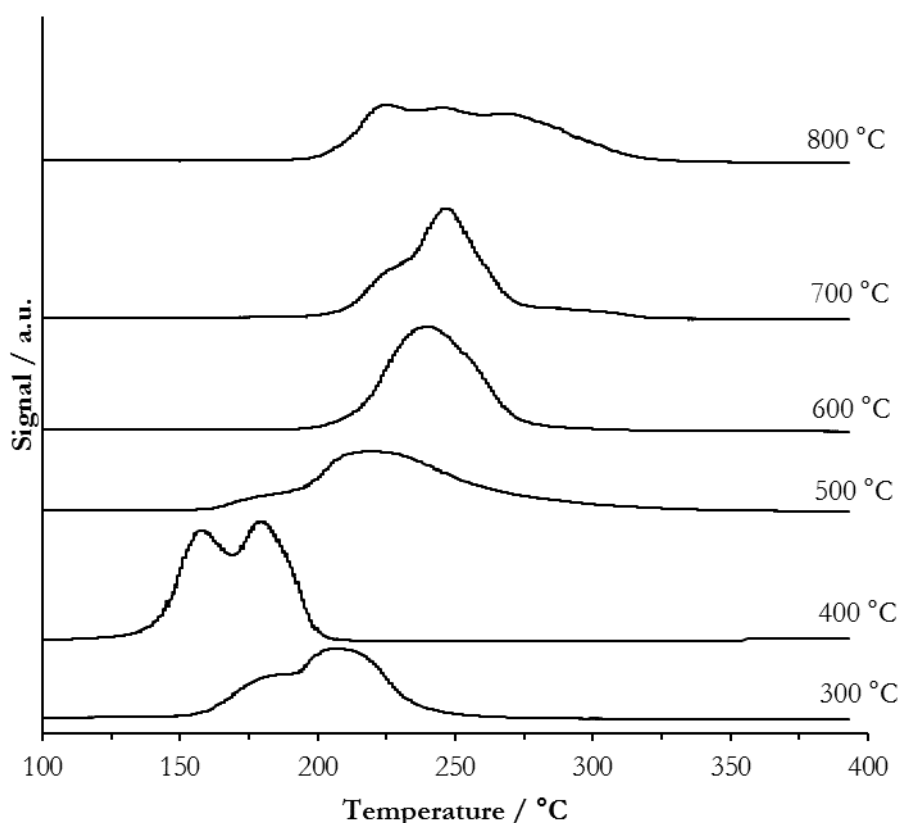


Figure 5.7. TPR profiles of catalysts calcined at different temperatures.

So far, it can be concluded that 400 °C is the optimum calcination temperature for the Cu-ZrO₂ catalyst prepared by keeping the Cu/Zr ratio of 1 because it produced the highest yield of GVL in LA hydrogenation. The catalyst calcined at 400 °C showed am-ZrO₂ pattern and was more active than catalysts in which t-ZrO₂ and m-ZrO₂ were prominent. Though the catalyst calcined at 300 °C had a smaller CuO particle size and higher BET surface area, the catalyst calcined at 400 °C was more reducible because of stronger CuO interactions with the ZrO₂ support. In the next step of catalyst preparation matrix program, variation of ageing time of the precipitates during CP was performed.

5.2.3. The effect of precipitate ageing time

Using the optimal unity Cu/Zr ratio, the precipitates were aged for times between 0 and 24 h before filtration. The preparation method is detailed in Chapter 2, section 2.2 and all the catalysts were calcined at 400 °C. Catalysts prepared with varying the precipitate ageing times were tested for LA hydrogenation and the corresponding GVL yield are presented in Figure 5.8a. The catalyst prepared with an unaged precipitate showed a lower activity. GVL yield increased with an increase in precipitate ageing time from 1 h up to 6 h. Further increasing the precipitate ageing time resulted in a steady decline in GVL production. Interestingly, the activity of the unaged catalyst and the catalyst aged for 24 hours showed an identical GVL yield which can be linked with the dissolution of precipitates when left in mother liquor between 16–24 h²⁴. BET surface area analysis was performed on the catalysts prepared by variation of ageing time and the data are presented in Table 5.8 and was used to normalize GVL yield presented in Figure 5.8b. BET surface area analysis presented in Table 5.9 showed that there was an increase in total surface area with an increase in ageing time up to 6 h. Catalysts prepared with a precipitate aged for longer than 6 h showed a decrease in surface area. This data trend could suggest the increasing dispersion of CuO particles between 0–6 h, with reformation of larger particles occurring at longer ageing times. Once again, the Cu surface area data for a selection of catalysts from this series representing short, middling, and long ageing times (Table 5.10) showed no trend that could be related with catalytic activity.

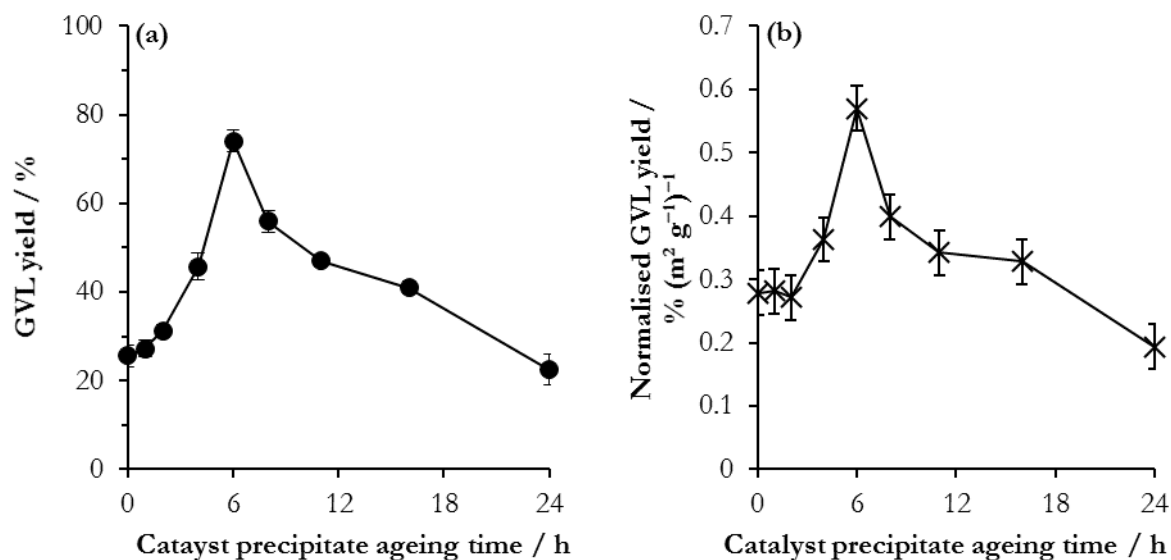


Figure 5.8. Effect of precipitate ageing time on GVL yield. (a) GVL yield; (b) GVL yield normalised by BET surface area. *Reaction conditions:* 200 °C, 35 bar H₂, 2 h, 5 wt.% LA/H₂O, 0.05 g catalyst.

Table 5.9. BET surface area for the catalysts prepared with different precipitate ageing times.

Precipitates ageing time / h	BET surface area / $\text{m}^2 \text{g}^{-1}$
0	92
1	97
2	115
4	126
6	149
8	140
11	137
16	121
24	116

Table 5.10. Cu surface area for a selection of catalysts prepared with different precipitate ageing times.

Precipitate ageing time / h	Cu surface area / $\text{m}^2 \text{g}^{-1}$
0	2.6
6	4.1
8	2.1
16	3.4

XRD analysis was performed on all the catalysts prepared by the variation of ageing time and the resulting patterns are provided in Figure 5.9. Typical reflections corresponding to CuO[111] were observed at $2\theta = 35^\circ$, 39° , 49° , and 62° (ICDD-00-041-0254) for the catalyst prepared without ageing. The reflections at $2\theta = 49^\circ$ and 62° were not observed with an increase in ageing times between 1–16 h but were observed once again in the catalyst aged for 24 h. The similarity in phase composition of unaged catalyst and the ones aged for 24 hours can be linked with the similar catalytic activity presented in Figure 5.8. The reflections at $2\theta = 35^\circ$ and 39° were present in all XRD patterns except for the catalyst with a precipitate aged for 16 h, which was completely amorphous in the XRD, following the trend of increasingly amorphous morphology in the catalysts aged from 0–16 h. These reflections broadened and decreased in intensity in the catalysts which were aged between 4–8 h. This is indicative of a decrease in CuO particle size with increasing ageing time.

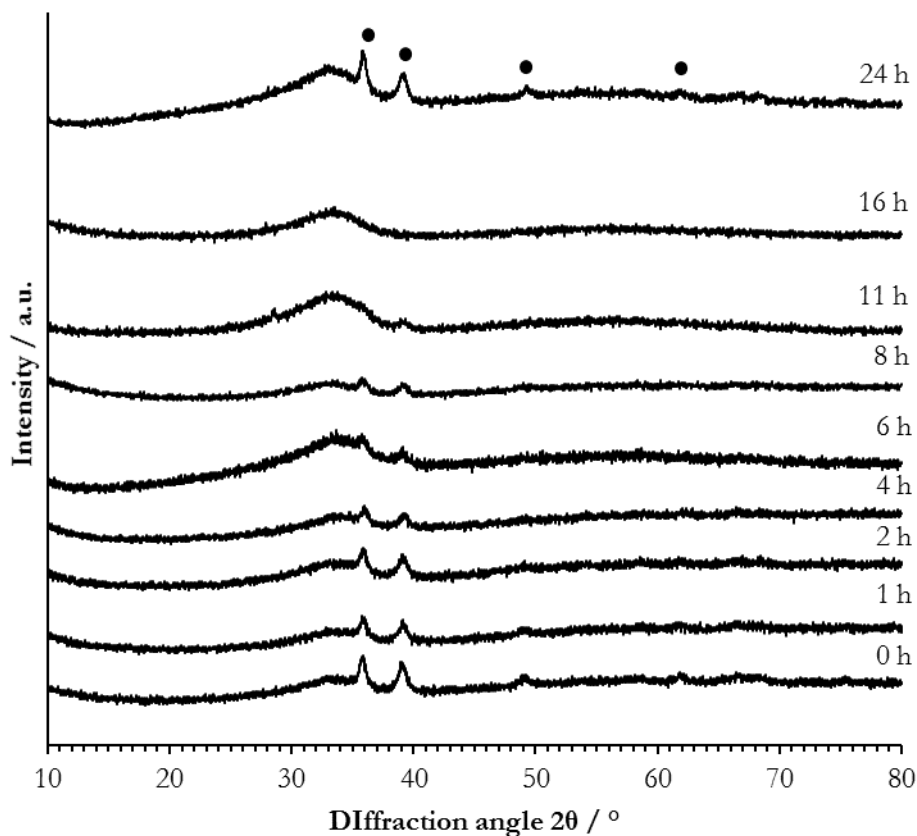


Figure 5.9. XRD patterns for Cu-ZrO₂ catalysts prepared with different precipitate ageing times. ●: CuO.

The CuO particles sizes were estimated by the Scherrer equation where this was possible and are presented in Table 5.11. There is a decrease in CuO particle size with an increase in ageing time up to 16 h. XRD patterns showed a less crystalline morphology between 8–16 h, therefore the particle size for these catalysts was considered to be <4 nm. The CuO particle size then increased when the precipitate was aged for 24 hours. The dissolution and reformation of CuO and MnO nanoparticle phases have been previously observed in CuMn catalysts prepared by CP with increased crystallinity observed at longer ageing times^{24,25}.

Table 5.11. Particle sizes of CuO in the catalysts prepared with different precipitate ageing times.

Precipitate ageing time / h	CuO particle size ^a / nm
0	10.2
1	8.4
2	5.7
4	6.3
6	5.4
8	5.0
11	Unable to acceptably estimate particle size using the Scherrer equation
16	
24	12.9

^a hkl = [111]

Figure 5.10 shows the TPR profiles of catalysts prepared with different precipitate ageing times. All catalysts showed reduction signals at $T = 155\text{ }^{\circ}\text{C}$ and $180\text{ }^{\circ}\text{C}$. There was a gradual increase in the contribution of the lower temperature signal to the overall reduction profile, with a corresponding decrease in the contribution of the higher temperature reduction signal with the catalysts aged up to 6 h. At an ageing time of 6 hours, both signals had equal contributions to the overall reduction profile. Further increase in precipitate ageing time above 6 h resulted in a reversal of this trend. A decrease in lower temperature peak intensity and increase in higher temperature peak intensity was observed with an ageing time up to 24 h. As previously discussed, the contribution of the lower temperature peak was the result of small, easily reducible CuO particle strongly interacting with the ZrO_2 support. The intensity of this signal correlates well with the trend in GVL yield. In addition, the catalysts prepared with unaged precipitate and a precipitate aged for 24 h have similar TPR profiles, supporting the data given by the XRD, and produced similar yields of GVL (25.5 % and 22.5% respectively). This also supports the dissolution and reformation of phases with an extended ageing time.

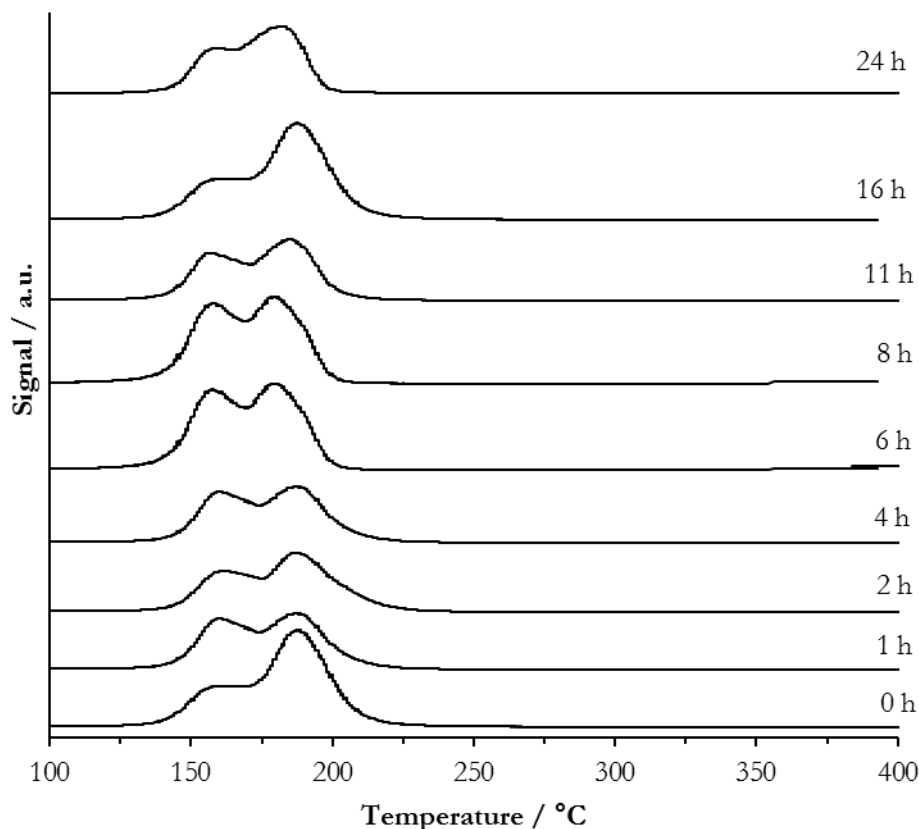


Figure 5.10. TPR profiles of catalysts prepared with different precipitate ageing times.

It can be concluded from these data that 6 h is the optimal precipitate ageing time when preparing these catalysts. Ageing of the precipitates for 6 hours is beneficial for the dispersion of small CuO nanoparticles across the catalyst surface, which may have reduced to Cu metal under reaction conditions. Once again, it can be concluded that small surface Cu particles with strong interactions with the support are required for their high activity.

5.2.4. Time-on-line and catalyst reuse

The most active catalyst – prepared with Cu/Zr = 1, aged for 6 h, and calcined at 400 °C – was subjected to an extended reaction time. The time-on-line data shown in Figure 5.11 did not show an induction period as was observed with Ru/C catalysts discussed in Chapters 3 and 4. The reaction profile is a standard batch reaction profile, with no deactivation observed up to 5 h. GVL is the only product observed during the reaction and the mass balance was 100 % within experimental error. This data showed that sampling at 2 h was a good measure of catalyst activity. It also shows that the 100 % yield of GVL can be achieved after 3 h. Given the linearity of the reaction profile up to 2 h, the rate of reaction was estimated to be $8.90 \times 10^{-5} \text{ mol dm}^{-3} \text{ s}^{-1}$, which is comparable to a RuSn/C catalyst reported by Dumesic and co-workers²⁶. There was no induction period observed with Cu-ZrO₂, in contrast to the

Ru/C catalysts presented in Chapter 4. Rejection of water from the hydrophobic surface was postulated as a cause of the induction period in those cases. The lack of it in this case is reasonable because Cu-ZrO₂ is less hydrophobic than carbon therefore preparation of the surface by rejecting water and adsorbing the organic material would not occur in the same manner.

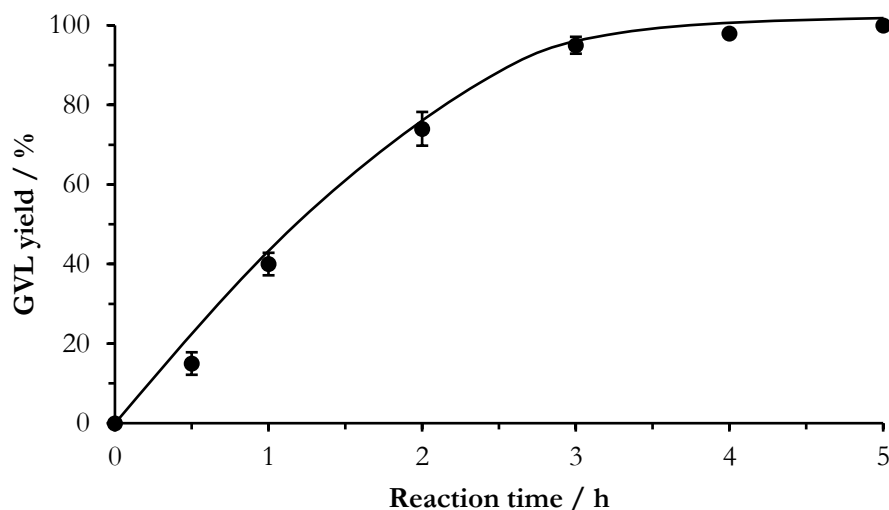


Figure 5.11. Time-on-line profile for the most active Cu-ZrO₂ catalyst. Catalyst preparation parameters: Cu/Zr = 1; precipitate ageing time = 6 h; calcination temperature = 400 °C. **Reaction conditions:** 200 °C, 35 bar H₂, 5 wt.% LA/H₂O, 0.05 g catalyst.

The catalyst was subjected to reuse tests as described in Section 2.3. Figure 5.12 shows the catalyst stability and clearly a decrease in activity was observed after the first use. MP-AES analysis showed only minimal leaching of Cu from the catalyst, thereby eliminating it as a cause of deactivation. XRD analysis shown in Figure 5.13 on the used catalyst showed that Cu metal was formed with a large particle size of 38 nm (Figure 5.13). This is a significant increase from the 5.4 nm CuO nanoparticles observed prior to catalyst testing. It can be concluded that Cu sintering caused by the high temperature and hydrogen pressure could be the cause of the loss in catalytic activity.

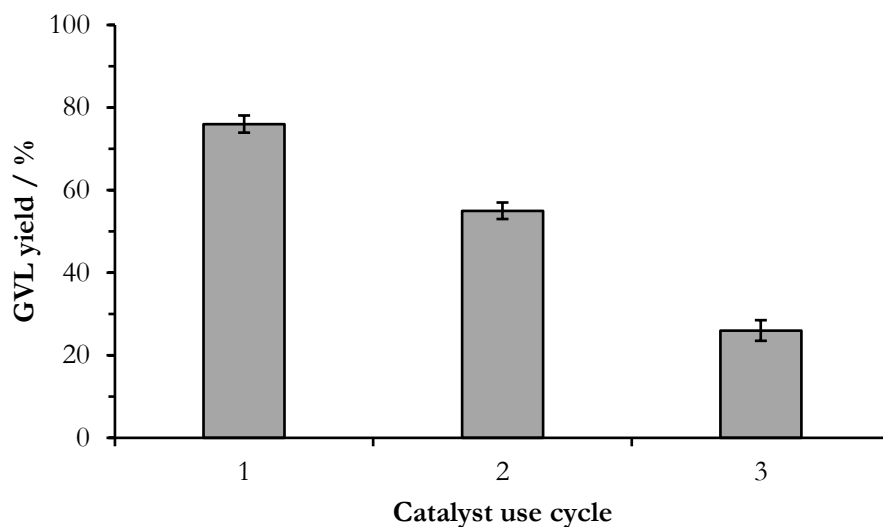


Figure 5.12. The catalytic activity of Cu-ZrO₂ with successive reuse. *Reaction conditions:* 200 °C, 35 bar H₂, 2 h, 5 wt.% LA/H₂O, 0.05 g catalyst.

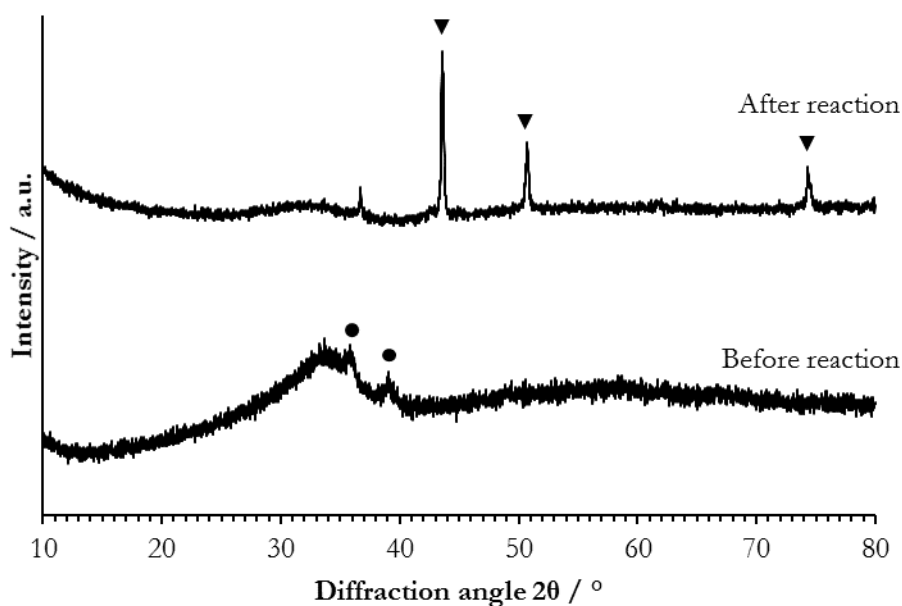


Figure 5.13. XRD patterns the most active Cu-ZrO₂ catalyst before and after use. ●: CuO; ▼: Cu.

5.3. Conclusions

Cu-ZrO₂ prepared by CP is a cheap and abundant catalyst that is active and selective for the hydrogenation of LA to GVL. The catalyst prepared with a Cu/Zr ratio of 1 gave a GVL yield of around 80 % after a reaction time of 2 h at 200 °C. The effective rate of the reaction was $8.90 \times 10^{-5} \text{ mol dm}^{-3} \text{ s}^{-1}$. Characterisation of the catalysts showed that much of the Cu deposited during the CP procedure was present as a spectator species that was not catalytically active. This excess of Cu was present either as part

of the Zr lattice, or as large CuO particles. Although most of the CuO was reduced under the reaction conditions of 200 °C and 35 bar H₂, it appears to be inactive for LA hydrogenation. The small particles present were the active form, likely increasing the Lewis acidity required for the reaction to proceed. It follows that it should be possible to synthesise a catalyst with a low Cu content that is active for LA hydrogenation.

The study of precipitate ageing time and catalyst calcination temperature showed that ageing of the precipitate for 6 h, followed by calcination at 400 °C resulted in the catalyst with the highest yield of GVL. Lower calcination temperatures produced a material with a high surface area, but lower activity.

Cu has emerged as promising choice for the replacement of Ru for LA hydrogenation catalysts, but little effort has been expended on the *design* of these catalysts. The investigation of the different CP preparation parameters presented in this chapter has resulted in the identification of the active features of the catalyst and where is scope for further development. Small, well-dispersed, and highly-reducible Cu particles have been shown to contribute to the catalytic activity of the catalyst, but the observation of a catalytically inactive spectator species resulting from excess Cu highlights the inefficiency of this method of catalyst preparation. For base metal catalysts to be a viable alternative to precious metals such as Ru, costs must be kept as low as possible, meaning that efficient use of materials to attain maximum catalytic activity per mole of Cu used and reduce waste is essential. The results presented in this chapter identify that the key features of the catalyst that should be enhanced and features that should be avoided, providing the ideal design of a Cu-ZrO₂ catalyst for LA hydrogenation.

5.4. References

- 1 L.-C. Wang, Q. Liu, M. Chen, Y.-M. Liu, Y. Cao, H.-Y. He and K.-N. Fan, *J. Phys. Chem. C*, 2007, **111**, 16549–16557.
- 2 Y. Ma, Q. Sun, D. Wu, W.-H. Fan, Y.-L. Zhang and J.-F. Deng, *Appl. Catal. A Gen.*, 1998, **171**, 45–55.
- 3 L. Yu, X.-L. Du, J. Yuan, Y.-M. Liu, Y. Cao, H.-Y. He and K.-N. Fan, *ChemSusChem*, 2013, **6**, 42–46.
- 4 X.-R. Zhang, L.-C. Wang, C.-Z. Yao, Y. Cao, W.-L. Dai, H.-Y. He and K.-N. Fan, *Catal. Letters*, 2005, **102**, 183–190.
- 5 J. Yuan, S.-S. Li, L. Yu, Y.-M. Liu, Y. Cao, H.-Y. He and K.-N. Fan, *Energy Environ. Sci.*, 2013, **6**, 3308–3313.
- 6 P. Balla, V. Perupogu, P. K. Vanama and V. R. C. Komandur, *J. Chem. Technol. Biotechnol.*, 2016, **91**, 769–776.

- 7 A. M. Hengne and C. V Rode, *Green Chem.*, 2012, **14**, 1064–1072.
- 8 G. Águila, J. Jiménez, S. Guerrero, F. Gracia, B. Chornik, S. Quinteros and P. Araya, *Appl. Catal. A Gen.*, 2009, **360**, 98–105.
- 9 J. Sloczynski, R. Grabowski, A. Kozłowska, P. K. Olszewski and J. Stoch, *Phys. Chem. Chem. Phys.*, 2003, **5**, 4631–4640.
- 10 G. Águila, F. Gracia, J. Cortés and P. Araya, *Appl. Catal. B Environ.*, 2008, **77**, 325–338.
- 11 Z. Liu, W. Ji, L. Dong and Y. Chen, *J. Catal.*, 1997, **172**, 243–246.
- 12 A. K. Singh and I. Defence, Metallurgical Research Laboratory (Hyderabad), *Advanced X-ray Techniques in Research and Industry*, IOS Press, 2005.
- 13 A. Monshi, M. R. Foroughi and M. R. Monshi, *World J. Nanosci. Eng.*, 2012, **2**, 154–160.
- 14 S. Sitthisa, W. An and D. E. Resasco, *J. Catal.*, 2011, **284**, 90–101.
- 15 M. Shimokawabe, H. Asakawa and N. Takezawa, *Appl. Catal.*, 1990, **59**, 45–58.
- 16 G. Huang, B.-J. Liaw, C.-J. Jhang and Y.-Z. Chen, *Appl. Catal. A Gen.*, 2009, **358**, 7–12.
- 17 J. Zhou, Y. Zhang, G. Wu, D. Mao and G. Lu, *RSC Adv.*, 2016, **6**, 30176–30183.
- 18 N. Scotti, M. Dangat, A. Gervasini, C. Evangelisti, N. Ravasio and F. Zaccheria, *ACS Catal.*, 2014, **4**, 2818–2826.
- 19 M. Mariani, F. Zaccheria, R. Psaro and N. Ravasio, *Catal. Commun.*, 2014, **44**, 19–23.
- 20 Y. Román-Leshkov and M. E. Davis, *ACS Catal.*, 2011, **1**, 1566–1580.
- 21 L. Bui, H. Luo, W. R. Gunther and Y. Román-Leshkov, *Angew. Chemie*, 2013, **125**, 8180–8183.
- 22 S. Xie, E. Iglesia and A. T. Bell, *Chem. Mater.*, 2000, **12**, 2442–2447.
- 23 C. Li and M. Li, *J. Raman Spectrosc.*, 2002, **33**, 301–308.
- 24 G. J. Hutchings, A. A. Mirzaei, R. W. Joyner, M. R. H. Siddiqui and S. H. Taylor, *Appl. Catal. A Gen.*, 1998, **166**, 143–152.
- 25 D. M. Whittle, A. A. Mirzaei, J. S. J. Hargreaves, R. W. Joyner, C. J. Kiely, S. H. Taylor and G. J. Hutchings, *Phys. Chem. Chem. Phys.*, 2002, **4**, 5915–5920.
- 26 S. G. Wettstein, J. Q. Bond, D. M. Alonso, H. N. Pham, A. K. Datye and J. A. Dumesic, *Appl. Catal. B Environ.*, 2012, **117–118**, 321–329.

Chapter 6

Cu-ZrO₂, Ni-Cu-ZrO₂, and Ni-ZrO₂ catalysts for the hydrogenation of levulinic acid

6.1. Introduction

In Chapter 5, it was demonstrated that Cu-ZrO₂ prepared by CP is an active catalyst for LA hydrogenation to GVL. It was also discussed in Chapter 1 that Ni is one of the active catalysts for LA hydrogenation. Ni based catalysts have been reported. Hengst *et al.*¹ synthesized a Ni/Al₂O catalyst that yielded 92 % GVL in 6 h, at 150 °C and 10 bar H₂; Mohan *et al.*^{2,3} investigated Ni on a variety of different supports; and Shimizu *et al.*⁴ demonstrated that MoO_x could be incorporated into a Ni/C catalyst to improve its activity.

Ni has also been incorporated into Cu-based catalysts and studied for GVL production from LA. Cu-based catalysts have been shown to be susceptible to sintering and deactivation in gas phase LA hydrogenation^{5,6}. Upare *et al.* showed that the addition of Ni to a Cu-SiO₂ system could help alleviate previously reported problems with the stability of the catalyst⁷. The same catalyst was in fact stable for 100 h on stream when LA hydrogenation was carried out using formic acid as a source of H₂⁷. Arias and co-workers investigated Cu and Ni based catalysts for LA hydrogenation to 2-MTHF and found that while Ni-based catalysts were more active, Cu-based catalysts were more selective for MTHF⁸. An optimum ratio of Cu/Ni yielded 55 % yield of 2-MTHF, the highest recorded yet for a base metal catalyst. In this chapter, an investigation of Cu-, Ni-, and Ni-Cu-ZrO₂ catalysts for LA hydrogenation will be presented.

6.2. Results and discussion

6.2.1. The effect of Ni-Cu content in Ni-Cu-ZrO₂ catalysts

6.2.1.1. Catalytic data

Cu-ZrO₂, Ni-Cu-ZrO₂ of various compositions, and Ni-ZrO₂ catalysts were prepared by the OG methodology detailed in Chapter 2, section 2.2.4. These catalysts were subjected to reduction treatment using 5% H₂/Ar (after calcination at 550 °C) at different temperatures. Each catalyst was then tested for its activity for the conversion of LA into GVL, and the results are presented in Figure 6.1. Each catalyst showed 100 % selectivity to GVL under the reaction conditions used and no by-products were detected. The 50Cu-ZrO₂ catalyst reduced at 300 °C was the most active of the 50Cu-ZrO₂ catalysts and produced a GVL yield of 50 % after 30 minutes. 50Ni-ZrO₂ was generally a poorer catalyst, regardless of the reduction temperature, and produced a GVL yield between 28–30 % suggesting it was relatively unaffected by reduction treatment. Of the Ni-Cu-ZrO₂ catalysts, the Ni-rich catalysts were more active than the Cu-rich catalysts. The Cu-rich catalysts were less active than 50Cu-ZrO₂. The most active Ni-Cu-ZrO₂ catalyst was 45Ni-5Cu-ZrO₂ reduced at 400 °C, which produced a GVL yield of 76 % after 30 minutes of reaction. The addition of small amounts of Cu into Ni-ZrO₂ resulted in a much more active catalyst. This effect has been observed by Reshетенko *et al.* in Ni-Cu-Al₂O₃ catalysts for methane conversion. They showed that a small amount of Cu doped into the catalyst gave far superior activity than a 1:1 Ni:Cu catalyst⁹.

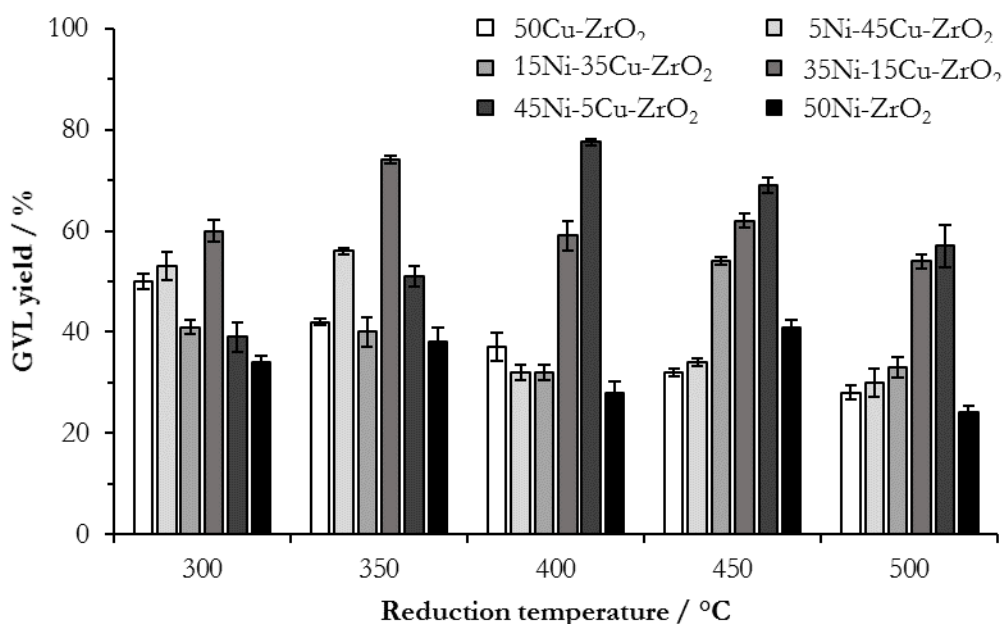


Figure 6.1. Catalytic activity of Ni-Cu-ZrO₂ catalysts prepared with different Ni-Cu compositions and reduction temperatures. **Reaction conditions:** 200 °C, 35 bar H₂, 30 minutes, 5 wt.% LA/H₂O, 0.05 g catalyst.

The Cu-ZrO₂, Ni-ZrO₂, and Ni-Cu-ZrO₂ catalysts prepared and reduced at 400 °C were investigated further because the most active catalyst was contained within this group, and the group showed the clearest difference in activity between the catalysts with a high Ni content (35Ni-15Cu-ZrO₂ and 45Ni-5Cu-ZrO₂) and low Ni contents (5Ni-45Cu-ZrO₂ and 15Ni-35Cu-ZrO₂). The reaction profiles of each of these catalysts over a reaction time between 0 and 90 minutes is shown in Figure 6.2. 50Cu-ZrO₂, 35Ni-15Cu-ZrO₂, and 45Ni-5Cu-ZrO₂ achieved 100 % GVL yield after 90, 75, and 55 minutes respectively. The other catalysts – 50Ni-ZrO₂, 15Ni-35Cu-ZrO₂, and 5Ni-45Cu-ZrO₂ – started to show decreased activity after 40 minutes and did not proceed to completion within a reaction time of 90 minutes. Because the reaction profiles were initially linear up to 30 minutes, the turnover number (TON) up to 30 minutes was calculated for each of these catalysts and presented in Table 6.1. The values reported in Table 1 are comparable to the values previously reported by Wettstein *et al.* for RuSn/C catalysts¹⁰, and Cu-ZrO₂ catalysts presented in Chapter 5¹¹.

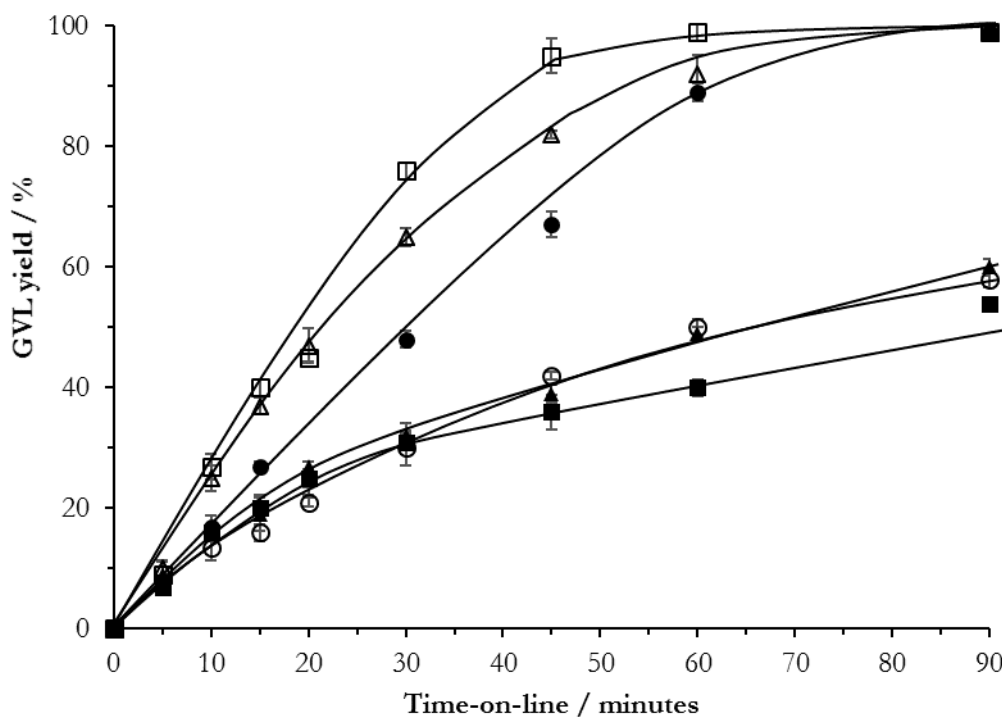


Figure 6.2. Time-on-line data for Ni-Cu-ZrO₂ prepared with different Ni-Cu compositions reduced at 400 °C. **Reaction conditions:** 200 °C, 35 bar H₂, 5 wt.% LA/H₂O, 0.05 g of catalyst. ●: 50Cu (reduced at 300 °C); ■: 5Ni-45Cu; ▲: 15Ni-35Cu; △: 35Ni-15Cu; □: 45Ni-5 Cu; ○: 50Ni.

Table 6.1. The initial rates and TONs for Cu-ZrO₂, Ni-ZrO₂, and Ni-Cu-ZrO₂ catalysts.

Catalyst	Initial rate of reaction / mol dm ⁻³ s ⁻¹	TON up to 30 minutes / g _{GVL} g _{cat} ⁻¹
50Cu-ZrO ₂	8.26×10^{-5}	1.71×10^{-3}
5Ni-45Cu-ZrO ₂	6.43×10^{-5}	1.14×10^{-3}
15Ni-35Cu-ZrO ₂	6.43×10^{-5}	1.14×10^{-3}
35Ni-15Cu-ZrO ₂	1.21×10^{-4}	2.31×10^{-3}
45Ni-5Cu-ZrO ₂	1.32×10^{-4}	2.70×10^{-3}
50Ni-ZrO ₂	5.56×10^{-5}	1.06×10^{-3}

Reaction conditions: 200 °C, 35 bar H₂, 30 minutes, 5 wt.% LA/H₂O, 0.05 g of catalyst.

Kinetic measurements were carried out using the most active catalyst – 45Ni-5Cu-ZrO₂ reduced at 400 °C. The orders of reaction were determined for both reactants (LA and H₂) and are shown in Figure 6.3. The reaction was found to be zero order with respect to LA. This matches with previous reports of zero order behaviour in organic substrates (including LA) and suggests that LA is in excess at the catalyst surface. The rate determining step is likely the dissociation of H₂¹² as discussed previously in Chapter 4. The order of reaction with respect to H₂ was initially first order, but tended to a zero order plot with an increase in H₂ pressure. This indicates that at higher pressures the surface became saturated with H₂ and the rate was no longer affected by increasing the H₂ pressure. This behaviour with respect to H₂ has been observed in previous studies utilising high H₂ pressures and Ru catalysts for LA hydrogenation^{13,14}.

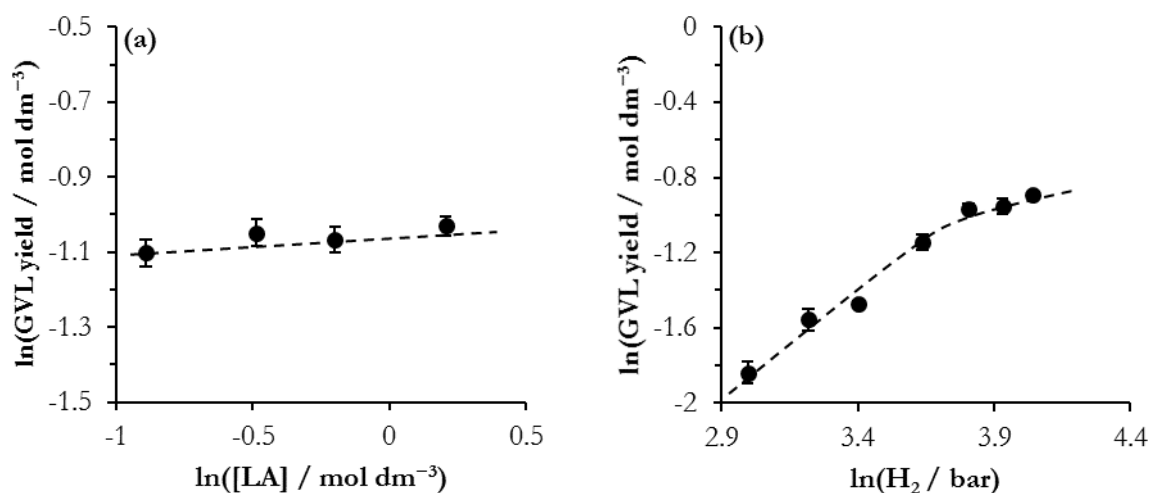


Figure 6.3. Reaction order with respect to (a) LA, and (b) H₂. **Reaction conditions:** 200 °C, 0.05 g of catalyst, 5 wt.% LA/H₂O.

6.2.1.2. Characterisation

XRD patterns were obtained for all of the catalysts prepared by varying the Cu:Ni ratio and reduction temperature (Figure 6.4). The most prominent reflections belonged to t-ZrO₂ (ICDD: 01-080-2155) at $2\theta = 30.6^\circ$, 51.4° , 61.0° and 74.5° , observed in 50Cu-ZrO₂, 35Ni-15Cu-ZrO₂, 45Ni-5Cu-ZrO₂, and 50Ni-ZrO₂ catalysts. These reflections were of lower intensity ($2\theta = 30.6^\circ$ and 74.5°) or missing entirely ($2\theta = 51.4^\circ$ and 61.0°) in 5Ni-45Cu-ZrO₂ and 15Ni-35Cu-ZrO₂. The catalysts with lower Ni-content were the least active of all the catalysts in Figure 6.1. The reflections at $2\theta = 35^\circ$, 37° and 63° correspond to NiO (ICDD: 01-089-7101) in the catalysts with higher amount of Ni (35Ni-15Cu-ZrO₂, 45Ni-5Cu-ZrO₂ and 50Ni-ZrO₂). In 50Ni there were two reflections at $2\theta = 43.6^\circ$ and 44.2° the former corresponding to NiO and the latter corresponding to Ni metal (ICDD: 03-065-0360). There was a change in the XRD patterns between $2\theta = 43^\circ$ – 46° in the bimetallic catalysts. A reflection corresponding to Cu metal that was observed at 43.3° in the 50Cu-ZrO₂ catalyst shifted to a higher diffraction angle (43.7°) on addition of Ni into Cu-ZrO₂ catalyst. This shift gradually increased from 43.5° to 44.2° from 5Ni-45Cu-ZrO₂ to 45Ni-5Cu-ZrO₂ respectively. There were no other peak shifts observed in the bimetallic catalyst relating any other phases, which confirmed that this peak shift was real. This shift implies that an alloy of Cu and Ni (ICDD: 01-071-7847) was formed in all bimetallic catalysts, with the presence of Ni shifting the reflection in all bimetallic catalysts to values between $2\theta = 43.3^\circ$ (Cu metal: 50Cu-ZrO₂) to $2\theta = 44.2^\circ$ (Ni metal: 50Ni-ZrO₂). With an increase in Ni-content, the intensity of the alloy reflection decreases to the point where it was barely observed in 45Ni-5Cu-ZrO₂.

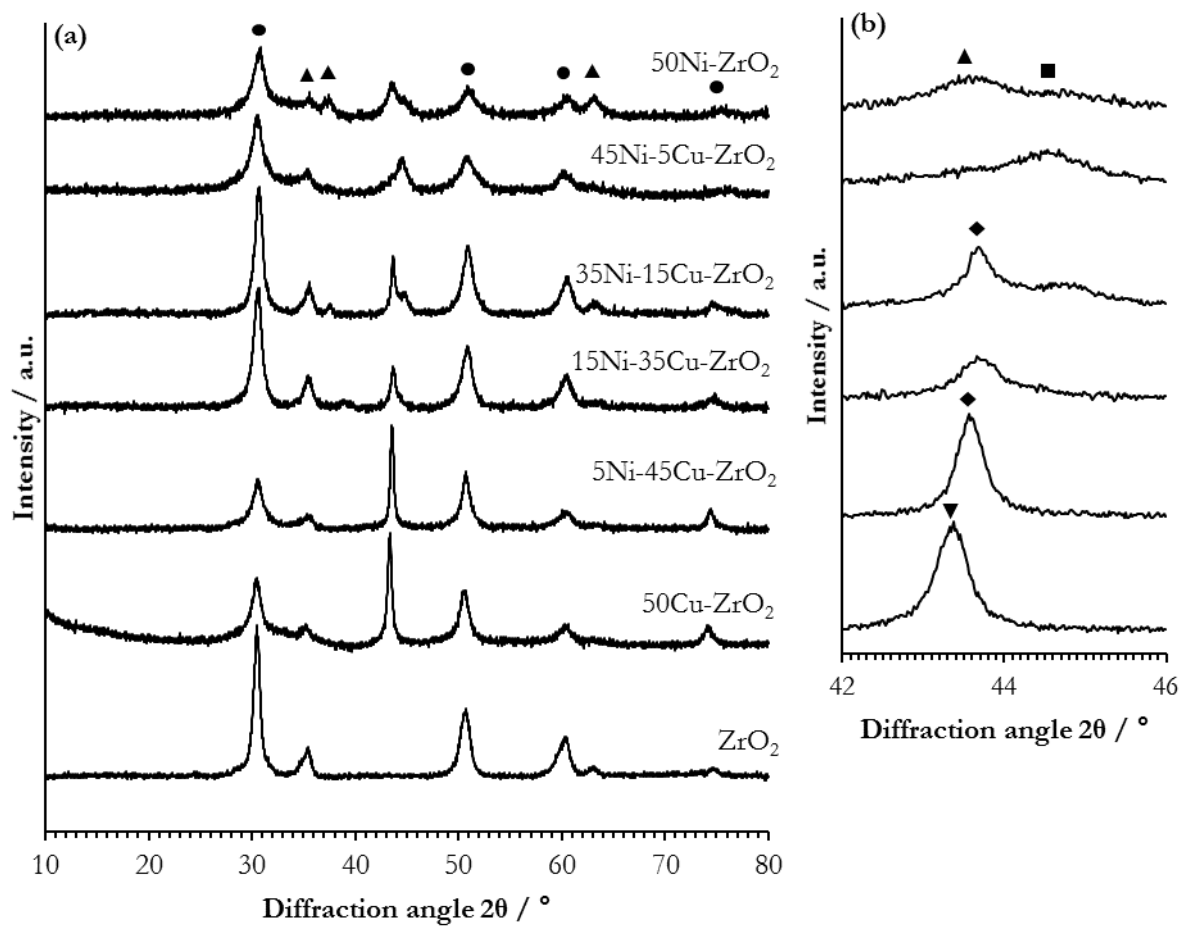


Figure 6.4. XRD patterns of Cu-Ni-ZrO₂ catalysts with increasing Cu-Ni contents, reduced at 400 °C. (a): Full diffraction pattern; (b): diffraction pattern zoomed between $2\theta = 42\text{--}46^\circ$. ●: ZrO₂; ▲: NiO; ■: Ni; ▼: Cu; ◆: Cu-Ni.

There was a decrease in reflection intensity of the alloy phase observed. The Scherrer Equation was used to calculate the particle size (Table 6.2). The data shows that there was a decrease in alloy particle size with an increase in Ni-content. 35Ni-15Cu-ZrO₂ and 45Ni-5Cu-ZrO₂ were more active Ni-Cu-ZrO₂ catalysts and both had small alloy particle sizes as implied by XRD. This suggests that a small particle size was required in order to achieve high catalytic activity, and the synthesis of small metal particle sizes was achieved by increasing the Ni-content in the catalyst.

Table 6.2. Average particle sizes of the Cu-Ni alloy species calculated using the Scherer equation at $2\theta = 42\text{--}46^\circ$.

Catalyst	Alloy peak particle size / nm
50Cu-ZrO ₂	--
5Ni-45Cu-ZrO ₂	19.7
15Ni-35Cu-ZrO ₂	14.8
35Ni-15Cu-ZrO ₂	8.5
45Ni-5Cu-ZrO ₂	6.8
50Ni-ZrO ₂	--

BET and N₂O titration for the determination of total surface area and metal surface area respectively were carried out for each of the above catalysts. Because both Cu and Ni can undergo oxidation by N₂O, the surface area cannot be accurately assigned to a particular element, therefore the total N₂O adsorption is reported (Table 6.3). The data show that both the BET surface area and metal surface area were affected by varying the Cu-Ni composition of the catalyst. The Cu-ZrO₂ catalyst with lower Ni-content (5Ni-45Cu-ZrO₂ and 15Ni-35Cu-ZrO₂) had comparable BET surface areas of between 50–65 m² g⁻¹. The catalysts with a higher Ni-content (35Ni-15Cu-ZrO₂ and 45Ni-5Cu-ZrO₂) showed BET surface areas of 90–100 m² g⁻¹. The same general trend was observed in the N₂O adsorption, with a gradual increase in specific adsorption of N₂O with an increase in Ni content. The exception in both cases was 50Ni-ZrO₂ which showed a lower BET surface area and lower specific adsorption of N₂O. The results can be related with the catalytic activity shown in Figure 6.1. The most active catalyst (45Ni-5Cu-ZrO₂) had the highest BET surface area and the highest specific adsorption of N₂O, whereas the least active catalyst of the series (5Ni-45Cu-ZrO₂) showed the lowest BET surface area and lowest specific adsorption of N₂O. These results show that surface area is an important parameter in the activity of catalysts for LA hydrogenation, a feature highlighted in Chapter 5¹¹. The increase in BET surface area is likely to be due to the naturally higher surface area of Ni compared with Cu^{15–17}.

Table 6.3. BET surface area and N₂O adsorption data of catalysts prepared with different Cu-Ni content.

Catalyst	BET surface area / m ² g ⁻¹	Specific adsorption of N ₂ O / μL g ⁻¹
50Cu-ZrO ₂	60	582
5Ni-45Cu-ZrO ₂	50	674
15Ni-35Cu-ZrO ₂	65	1441
35Ni-15Cu-ZrO ₂	90	1582
45Ni-5Cu-ZrO ₂	110	3156
50Ni-ZrO ₂	80	383

TPR analysis was carried out on all catalysts after calcination at 550 °C before reduction in 5 % H₂/Ar at 400 °C and the resulting profiles are shown in Figure 6.5. Only Cu and Ni species were reduced under the TPR conditions employed; there was no reduction signal observed for ZrO₂ only. From the 50Cu-ZrO₂ profile it can be seen that Cu oxide showed a reduction signal between 140–210 °C. This is in agreement with the Cu-ZrO₂ TPR data discussed in Chapter 5. 50Ni-ZrO₂ showed a reduction signal between 325–500 °C with the reduction temperature of approximately 450 °C. This indicates that a proportion of Ni oxide present was not fully reduced. This was confirmed by the presence of NiO peaks observed in the XRD patterns (Figure 6.4). The presence of NiO in the catalyst explains why low N₂O adsorption was observed for 50Ni-ZrO₂ (Table 6.3). N₂O cannot be adsorbed on NiO – metallic Ni is required. With an increase in Ni content and a corresponding change in Cu content, there was a decrease in Cu reduction signal intensity. There was no observable signal corresponding to Ni reduction in 5Ni-45Cu-ZrO₂, presumably due to the small amount of Ni present. In addition to signals corresponding to CuO reduction at 150 °C and 200 °C, 15Ni-35Cu-ZrO₂ showed a low intensity reduction signal corresponding to NiO at a temperature of 480 °C. The catalysts with higher Ni-content (35Ni-15Cu-ZrO₂ and 45Ni-5Cu-ZrO₂) showed a much different reduction profile to the lower Ni-content catalysts (5Ni-45Cu-ZrO₂ and 15Ni-35Cu-ZrO₂). Extra reduction signals between 200–250 °C were observed in both 35Ni-15Cu-ZrO₂ and 45Ni-5Cu-ZrO₂ which likely correspond to the lower temperature reduction of NiO facilitated by the presence of Cu^{8,18}. The facile reduction of NiO due to interaction of Cu is well documented. Arias and co-workers⁸ and Miranda *et al.*¹⁸ both reported that the addition of Cu resulted in a decrease in NiO reduction temperature in their catalysts for LA hydrogenation and glycerol conversion respectively. It is also possible that the reduction signal signals between 200–250 °C was due to the Cu-Ni alloy suggested by the XRD data.

The Cu-rich catalysts were the more reducible – this is due to the Cu species reducing at a much lower temperature compared with Ni. Catalysts with high Cu-content contained more total reduced metal (at the reduction temperature of 400 °C) than the Ni-rich catalysts. However, the activity of the Ni-rich catalysts was higher than the activity of the Cu-rich catalysts despite the relatively lower reducibility. This suggests that the reducibility of the catalyst was less important than the formation of an alloy species/solid solution that could exhibit superior catalytic activity

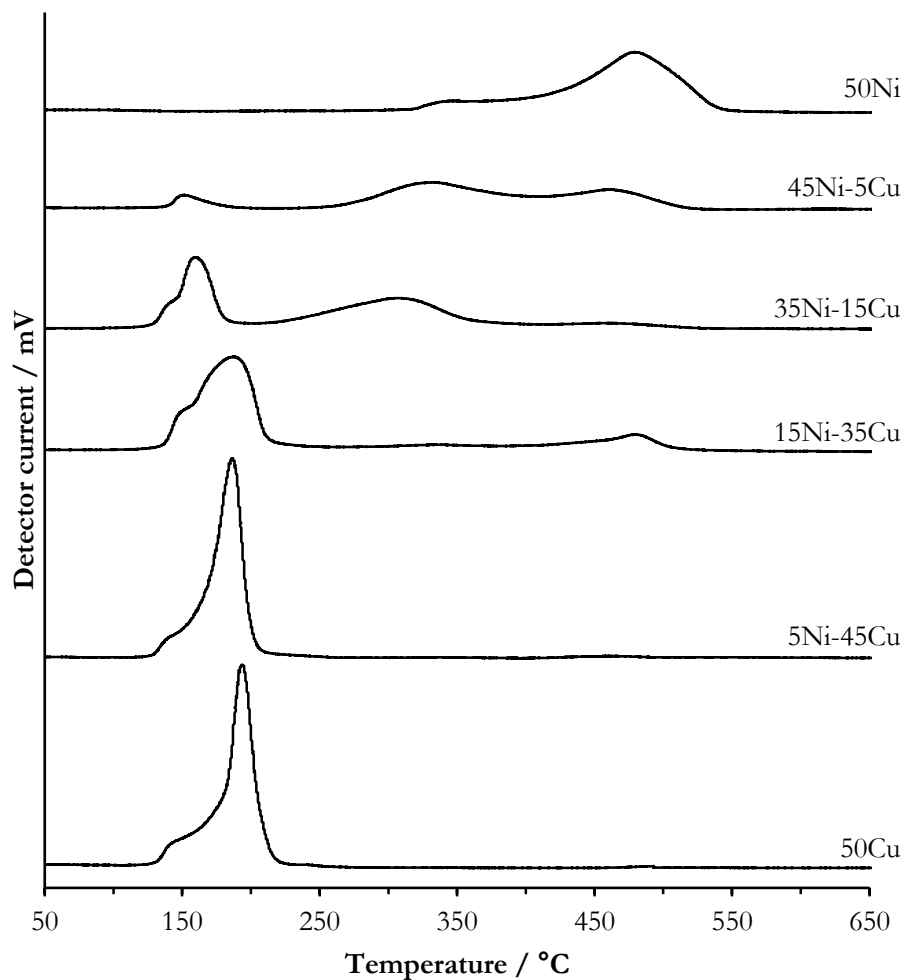


Figure 6.5. TPR profiles of Cu-ZrO₂, Ni-Cu-ZrO₂, and Ni-ZrO₂ catalysts.

SEM/EDX analysis was carried out on the Ni-Cu-ZrO₂ in order to investigate the surface composition of the catalysts. Firstly, the quantification of surface species was carried out by EDX and is presented in Table 6.4. The actual compositions of the Ni-Cu catalysts were shown to be similar to the theoretical compositions.

Table 6.4. Surface metal ratios obtained by EDX analysis.

Catalyst	Surface concentration / at.%		
	Ni	Cu	Zr
5Ni-45Cu-ZrO ₂	3	45	50
15Ni-35Cu-ZrO ₂	16	33	51
35Ni-15Cu-ZrO ₂	33	14	49
45Ni-5Cu-ZrO ₂	47	3	48

Figures 6.6–6.10 show the SEM images of the 5Ni-45Cu-ZrO₂, 15Ni-35Cu-ZrO₂, 35Ni-15Cu-ZrO₂, and 45Ni-5Cu-ZrO₂ catalyst surfaces. The elemental maps suggest that Cu and Ni were homogeneously dispersed across the surface (Figures 6.6b–6.9b). However, a closer look at one of the images of 45Ni-5Cu-ZrO₂ (Figure 6.10) reveals that was not necessarily the case. Figure 6.10(b) clearly shows an area that is rich in Cu, and Figure 6.10(c) clearly shows that the content of Ni was depleted in the same area. When the XRD and TPR data are considered, it is likely that the Ni and Cu alloyed but only to a small degree. This observation is in line with findings presented by Bian *et al.*¹⁹, Lortie *et al.*²⁰, and Studt *et al.*²¹ who all concluded that only a small fraction of the Cu and Ni they deposited on their catalysts alloyed. Despite this, all of them reported that the small fraction that alloyed caused an appreciable increase in catalytic activity. These findings show that even though there were very few alloy sites, they were particularly active. It could be suggested that if a method to synthesise and deposit small alloy particles exclusively could be developed, fewer of these sites would be required than separate Cu and Ni sites, meaning less material would need to be used in the synthesis, thus making a NCM catalyst cheaper still.

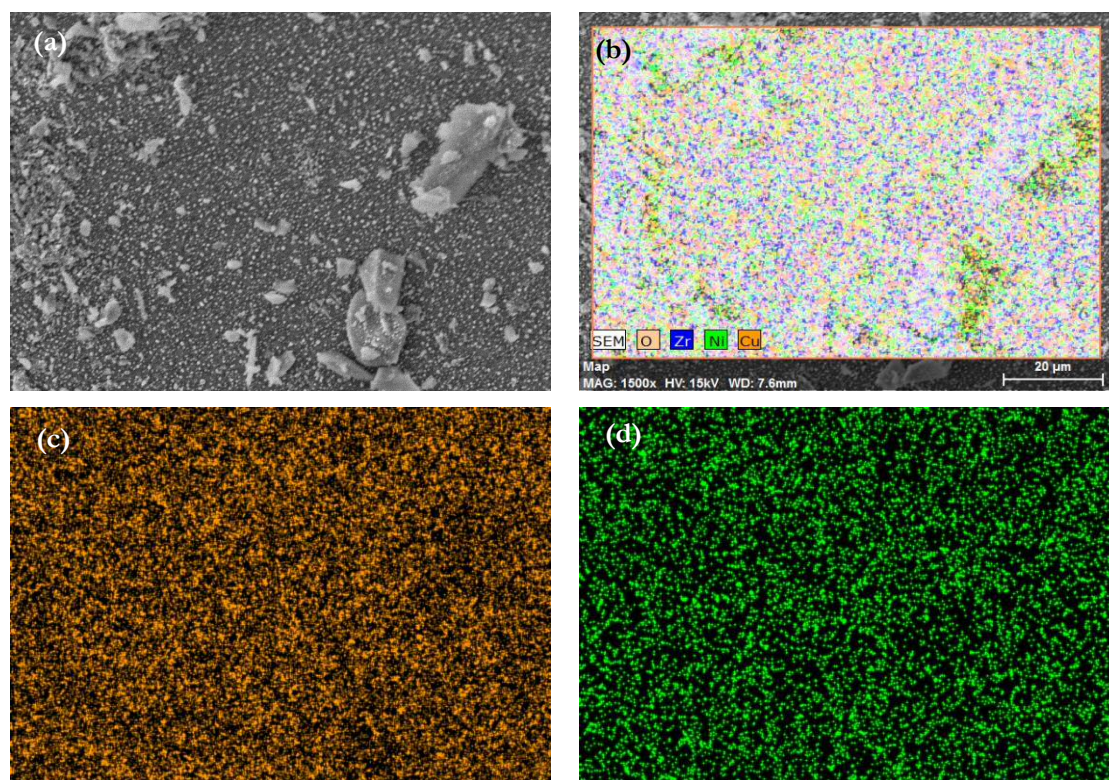


Figure 6.6. SEM/EDX images of 5Ni-45Cu-ZrO₂. (a): SEM image; (b): mixed EDX analysis showing Cu, Ni, and Zr; (c): EDX image showing Cu only; (d) EDX image showing Ni only.

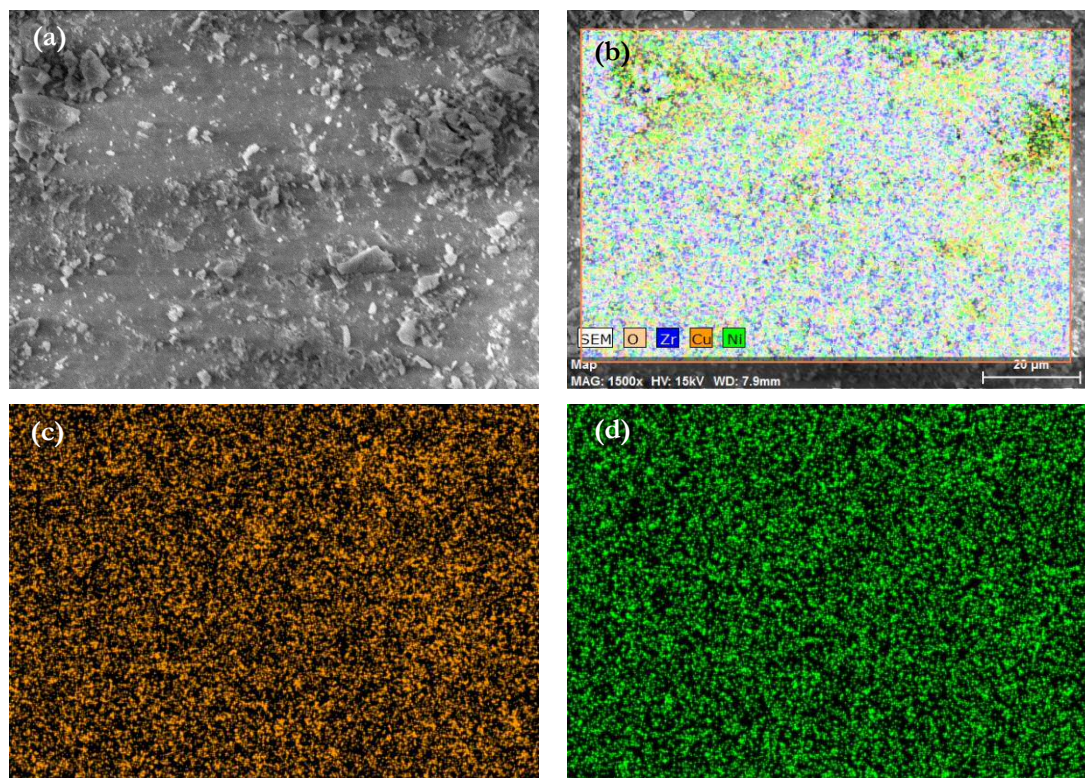


Figure 6.7. SEM/EDX images of 15Ni-35Cu-ZrO₂. (a): SEM image; (b): mixed EDX analysis showing Cu, Ni, and Zr; (c): EDX image showing Cu only; (d) EDX image showing Ni only.

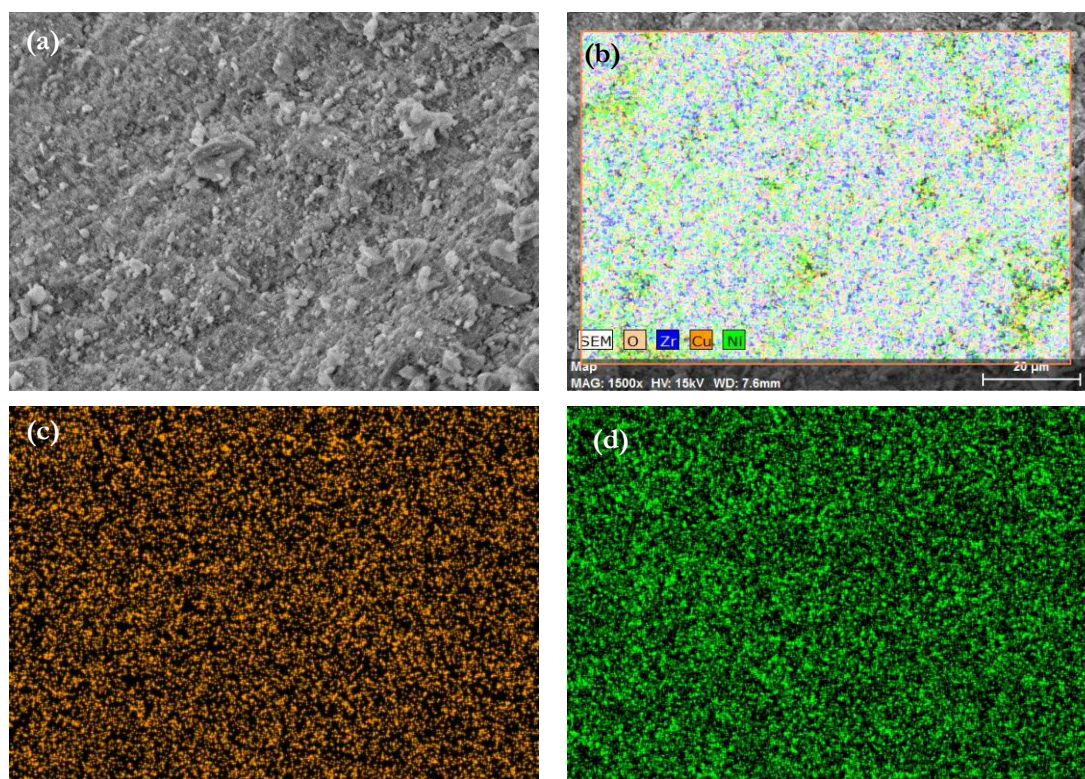


Figure 6.8. SEM/EDX images of 35Ni-15Cu-ZrO₂. (a): SEM image; (b): mixed EDX analysis showing Cu, Ni, and Zr; (c): EDX image showing Cu only; (d) EDX image showing Ni only.

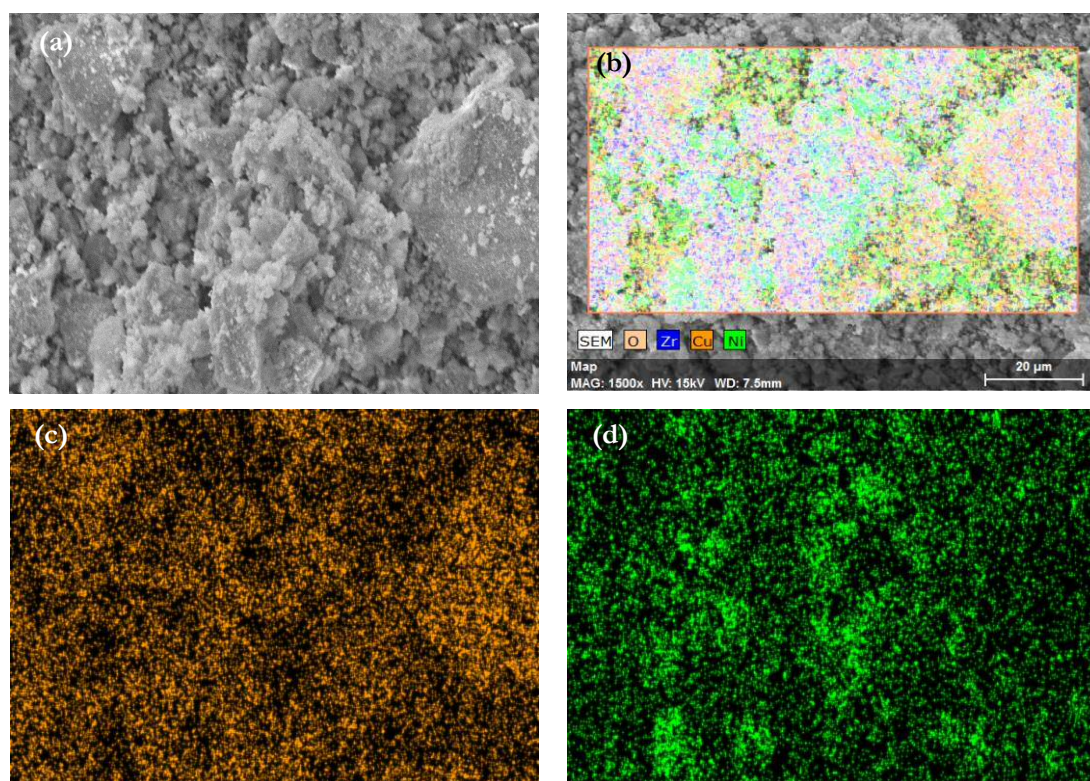


Figure 6.9. SEM/EDX images of 45Ni-5Cu-ZrO₂. (a): SEM image; (b): mixed EDX analysis showing Cu, Ni, and Zr; (c): EDX image showing Cu only; (d) EDX image showing Ni only.

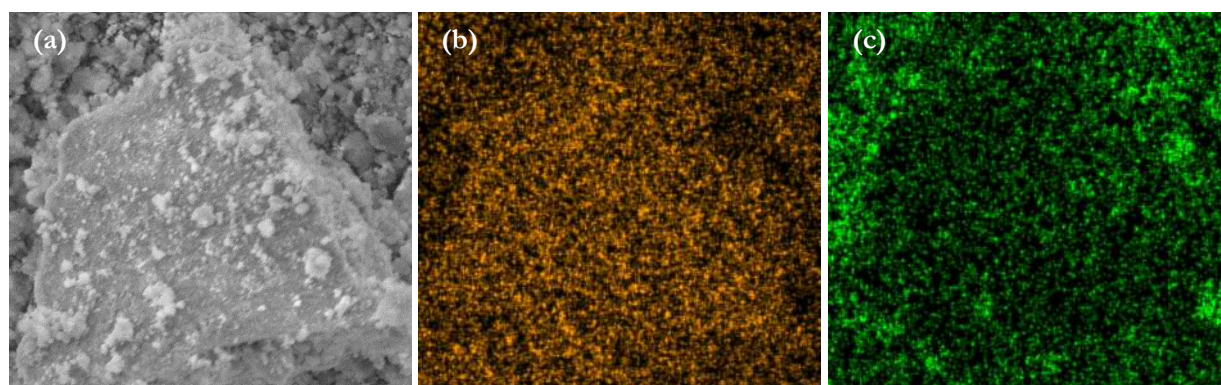


Figure 6.10. SEM/EDX images of 35Ni-15Cu-ZrO₂. (a): SEM image; (b): EDX image showing Cu only; (c) EDX image showing Ni only.

XPS analysis was carried out on all catalysts and the corresponding data are presented in Figure 6.11. The binding energies of the Cu(2p_{3/2}) species of 50Cu-ZrO₂ and Ni(2p_{3/2}) species of 50Ni-ZrO₂ were 932.9 eV and 854.8 eV respectively. The Zr(3d_{5/2}) binding energy was found to be 182.1 eV in all catalysts, which is consistent with Zr(IV) present as ZrO₂ as previously reported by Morant *et al.*²² The Cu(2p_{3/2}) binding energy decreased with a decrease in the amount of Cu in the catalyst. This phenomenon was observed in Cu-doped Ni/Al₂O₃ catalysts by Naghash *et al.* where they reported a gradual decrease in binding energy of Cu with a decrease in the amount of Cu doped onto the catalyst²³. The difference between the Naghash study and the work presented here is the choice of “support” (ZrO₂ *vs.* Al₂O₃) and

catalyst preparation method (OG *vs.* impregnation). This seems to suggest that bimetallic catalysts of this type broadly behave in the same manner.

This shift in Cu($2p_{3/2}$) binding energy can be attributed to the formation of less “bulk-like” Cu²⁴. The Ni($2p_{3/2}$) binding energy increased to 855 eV in bimetallic catalysts, but was relatively unaffected by the amount of Cu present. The higher Ni($2p_{3/2}$) binding energy in the presence of Cu is indicative of a charge transfer interaction from Cu to Ni as previously reported by Naghash *et al.*^{23,25}. Charge transfer to Ni from a secondary metal such as Co has been known to facilitate the reduction of NiO at lower temperatures^{26,27}, as observed in TPR profiles of 35Ni-15Cu-ZrO₂ and 45Ni-5Cu-ZrO₂ (Figure 6.5). XPS therefore seems to support the idea that an alloy or solid solution was formed on the catalyst to some extent.

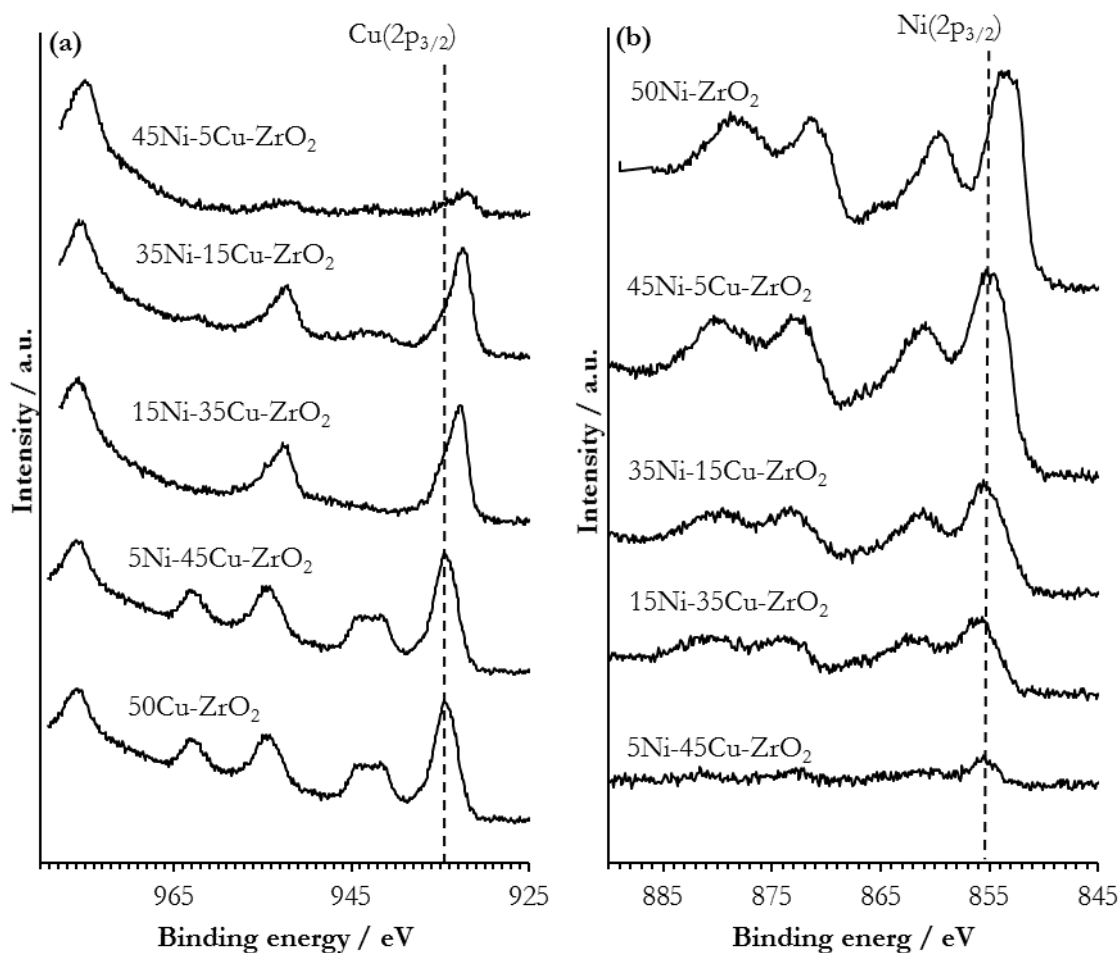


Figure 6.11. XPS analysis of Ni-Cu-ZrO₂ catalysts. (a) Cu($2p_{3/2}$); (b) Ni($2p_{3/2}$).

The surface atomic concentrations of Cu, Ni, and Zr were determined from the XPS spectra and the data are shown in Table 6.5. A (Ni+Cu)/Zr ratio of 1 would indicate that there was a homogeneous dispersion of Ni+Cu and Zr on the surface. The (Ni+Cu)/Zr ratio of all catalysts except 50Ni-ZrO₂

were all below 0.5, indicating more Zr was present at the surface than Cu+Ni. This suggests most of the metals were present in the bulk matrix of the material rather than at the surface. 50Ni-ZrO₂ had a (Ni+Cu)/Zr ratio of 0.845, which indicated there was much less Ni present in the bulk matrix than the other catalysts. The Ni/Cu ratio increased with an increase in Ni content. However, the surface Cu concentration of 15Ni-35Cu-ZrO₂ and 35Ni-15Cu-ZrO₂ were very similar with values of 12.12 % and 11.51 % respectively, while the surface Ni concentration increased from 4.85 % to 8.49 %. These values indicate there was an enrichment of Cu at the surface of these catalysts. Surface enrichment of Cu has previously been observed by Miranda *et al.* in Ni-Cu-Al₂O₃ catalysts prepared with varying contents of Ni and Cu¹⁸. It is known that Cu has a lower surface free energy than Ni, leading to it preferentially occupying the surface sites of bimetallic particles²⁸.

Table 6.5. Surface atomic concentrations of Ni, Cu, and Zr in all Ni-Cu-ZrO₂ catalysts determined by XPS.

Sample	Concentration / at.%			Ni/Cu	(Ni+Cu)/Zr
	Ni(2p _{3/2})	Cu(2p _{3/2})	Zr(3d _{5/2})		
50Cu-ZrO ₂	n/a	29.49	70.51	n/a	0.418
5Ni-45Cu-ZrO ₂	1.78	28.03	70.19	0.064	0.425
15Ni-35Cu-ZrO ₂	4.85	12.12	83.03	0.400	0.204
35Ni-15Cu-ZrO ₂	8.49	11.51	80.00	0.738	0.250
45Ni-5Cu-ZrO ₂	11.97	2.02	86.01	5.936	0.136
50Ni-ZrO ₂	45.81	n/a	54.19	n/a	0.845

6.2.2. Catalyst reuse and stability

As stressed in previous chapters, the ability of a catalyst to maintain its activity on re-use is extremely important. Therefore, the most active Ni-Cu catalyst (45Ni-5Cu-ZrO₂) was tested for its activity on reuse. These reusability reactions were carried out according to the procedure outlined in Chapter 2, Section 2.3.1.1. Figure 6.12 shows that there was a decline in GVL yield from 76 % to 50 % after the 1st reaction. Characterisation of the catalyst after the reaction was carried out to ascertain the reason for the decrease in catalytic activity.

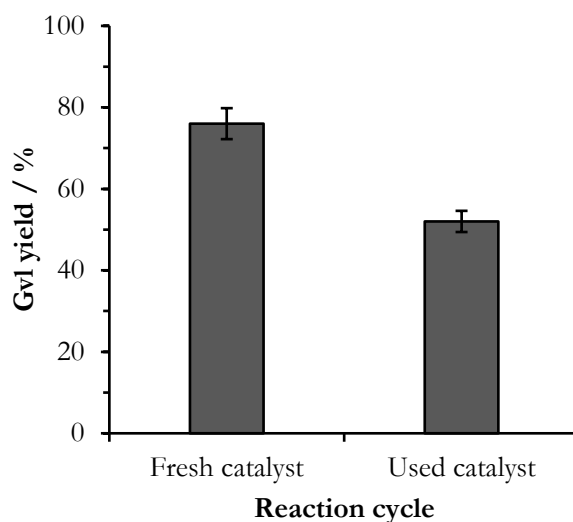


Figure 6.12. Activity of the 45Ni-5Cu-ZrO₂ catalyst on successive reactions. *Reaction conditions:* 200 °C, 35 bar H₂, 30 minutes, 5 wt.% LA/H₂O, 0.05 g of catalyst.

XRD patterns were obtained for the fresh catalyst and the used catalyst (Figure 6.13). There was a decrease in the intensity of the reflection at $2\theta = 42^\circ$ corresponding to the alloy peak, and an increase in the intensity of the reflection at $2\theta = 44.5^\circ$ corresponding to metallic Ni in the used catalyst. This change in peak intensity suggests a segregation of Ni from the alloy particles during the first reaction cycle, which then formed large metallic particles. From the Scherer equation, the Ni metal particle size was estimated to increase from 6 nm prior to the reaction to 17 nm after the reaction. Due to the poorly defined alloy peak, the change in particle size for the alloy could not be obtained. This particle size increase coincided with a decrease in BET surface area from 110 m² g⁻¹ for the fresh catalyst to 80 m² g⁻¹ for the used catalyst. It has been established that high surface area is important for high activity in Cu-ZrO₂, Cu-Ni-ZrO₂, and Ni-ZrO₂ catalysts. Segregation of the alloy, sintering of Ni particles, and decrease in surface area are all possible causes of catalyst deactivation, which could explain why a lower GVL yield was obtained when the catalyst was reused.

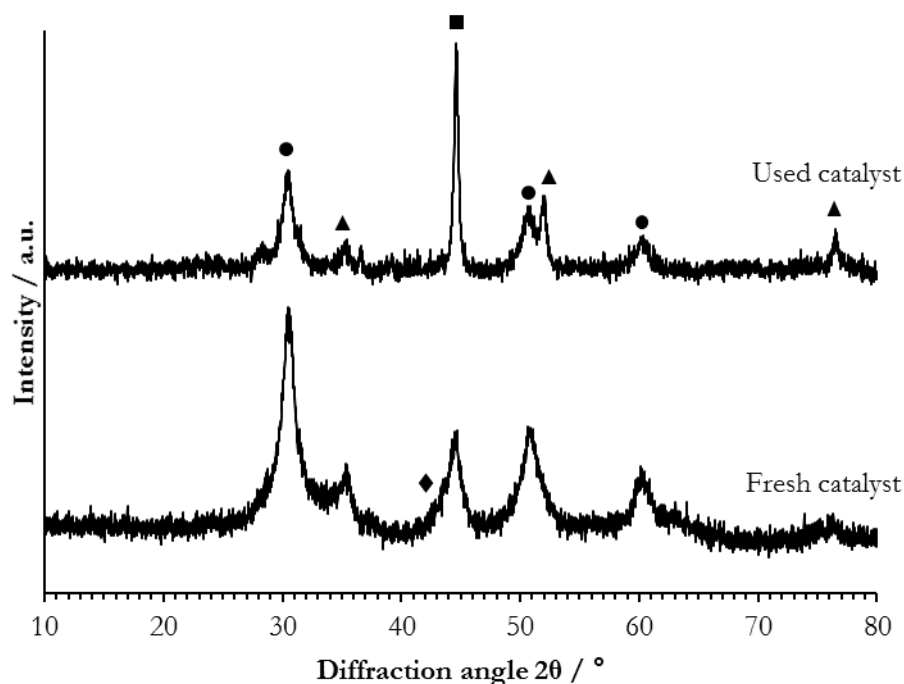


Figure 6.13. XRD patterns of 45Ni-5Cu-ZrO₂ before and after reaction. ●: ZrO₂; ▲: NiO; ■: Ni; ▼: Cu; ◆: Cu-Ni.

MP-AES analysis was carried out on the post-reaction solutions to determine whether loss of metal was partially responsible for the deactivation of the catalyst. The extent of metal leaching from all Ni-Cu-ZrO₂ catalysts is displayed in Table 6.6. There was minimal leaching of Cu from the catalyst observed during the reaction. However, there was a large amount of Ni leaching observed.

Table 6.6. Metal leaching from the catalyst in the post-reaction solution obtained by MP-AES.

Sample	Cu leaching / ppm	Ni leaching / ppm
50Cu-ZrO ₂	0.205	–
5Ni-45Cu-ZrO ₂	0.26	25.19
15Ni-35Cu-ZrO ₂	0.215	36.36
35Ni-15Cu-ZrO ₂	1.455	24.865
45Ni-5Cu-ZrO ₂	0.15	42.94
50Ni-ZrO ₂	–	39.37

In order to determine whether the leached Ni contributed to catalytic activity, the catalyst was filtered after regular reaction of 30 minutes, and the reaction resumed for a further 30 minutes without a catalyst present. 45Ni-5Cu-ZrO₂ was chosen because it was the most active catalyst and showed the largest amount of leached Ni. The result of this experiment is shown in Figure 6.14. The yield of the GVL after 30 minutes in the presence of 45Ni-5Cu-ZrO₂ was around 75 %. The yield of GVL remained

unchanged after removal of the catalyst and further reaction for 30 minutes. This indicates that the reaction was entirely heterogeneous and the leached metal did not play any role in the reaction.

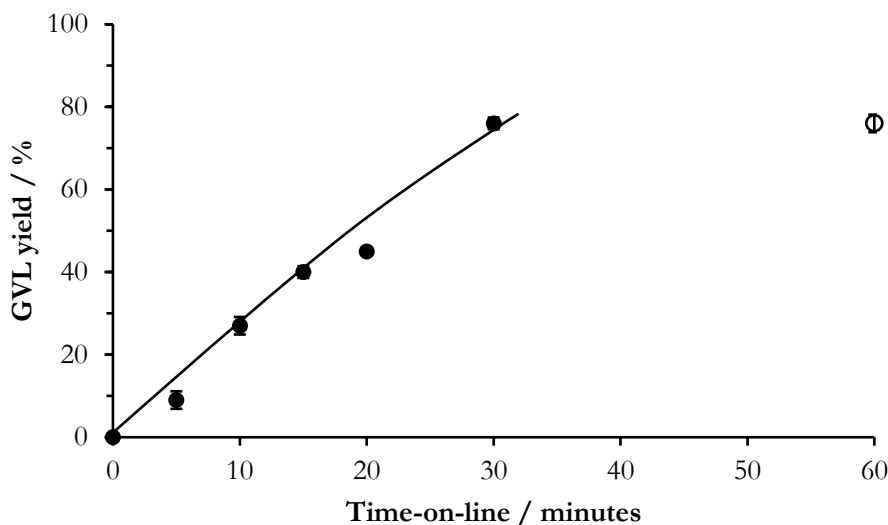


Figure 6.14. The effect of leached metal on GVL yield. ●: 45Ni-5Cu-ZrO₂ catalyst present; ○: 45Ni-5Cu-ZrO₂ removed after 30 minutes. **Reaction conditions:** 200 °C, 35 bar H₂, 5 wt.% LA/H₂O, 0.05 g of catalyst.

To determine the cause of the leaching by reaction intermediates or product, LA, GVL, and model compounds 2-pentanone and pentanoic acid were selected as substrates for a reaction using 45Ni-5Cu-ZrO₂ as a catalyst. 2-Pentanone and pentanoic acid were selected because both represent the two functionalities present in LA i.e. ketone and carboxylic acid. The reaction mixtures underwent MP-AES analysis to determine the metal content (Table 6.7). In all cases, there was minimal Cu leaching observed. However, there was a variation in Ni leaching. LA caused more Ni leaching than GVL. This indicates that there was more Ni leaching in the presence of a large amount of reactant. The use of model compounds can help determine which functionality of the LA was responsible for Ni leaching. Pentanoic acid caused more Ni leaching than 2-pentanone, which shows that the carboxylic acid functionality of LA was more prone to causing the observed metal leaching than the ketone group.

Table 6.7. Metal leaching from 45Ni-5Cu-ZrO₂ after reaction with model substrates.

Substrate	Cu leaching / ppm	Ni leaching / ppm
Levulinic acid	0.15	42.94
GVL	0.04	9.7
Valeric acid	0.15	16.23
2-Pentanone	0.10	2.97

This experiment also suggests that the pH of the system might be important. An experiment should be performed using a mineral acid such as HCl rather than levulinic or valeric acid in order to ascertain whether leaching occurred due to the pH of the system, or due to the presence of the C₅ acids specifically.

6.2.3. Ball milling (BM) and physical mixing (PM)

50Cu-ZrO₂, 45Ni-5Cu-ZrO₂, and 50Ni-ZrO₂ catalysts were prepared using the ball-milling (BM) and physical mixing (PM) methods outlined in Sections 2.2.4.1 and 2.2.4.2 respectively. The catalysts were reduced in a flow of 5 % H₂/Ar at 300 °C (50Cu-ZrO₂) or 400 °C (45Ni-5Cu-ZrO₂ and 50Ni-ZrO₂ catalysts) in accordance with the results discussed in Section 6.2.1. The catalysts were then tested for LA hydrogenation and the data are presented in Figure 6.14. A significantly increased yield of GVL was achieved using the BM catalysts, with both 50Cu-ZrO₂ and 45Ni-5Cu-ZrO₂ yielding 100 % GVL after 30 minutes compared with the catalysts which were not prepared with a BM step. 50Ni-ZrO₂ also showed a modest increase in activity when prepared with the BM step. A 50 % yield of GVL was obtained compared with a 30 % yield for 50Ni-ZrO₂ catalyst prepared without a ball milling step.

The catalysts prepared by the PM method were all much less active than the catalysts prepared by the original OG method without a BM step (Figure 6.15). This is likely due to an absence of strong bonding interactions between the Cu/Cu-Ni/Ni with ZrO₂, effectively making the material a crude mix of bulk materials.

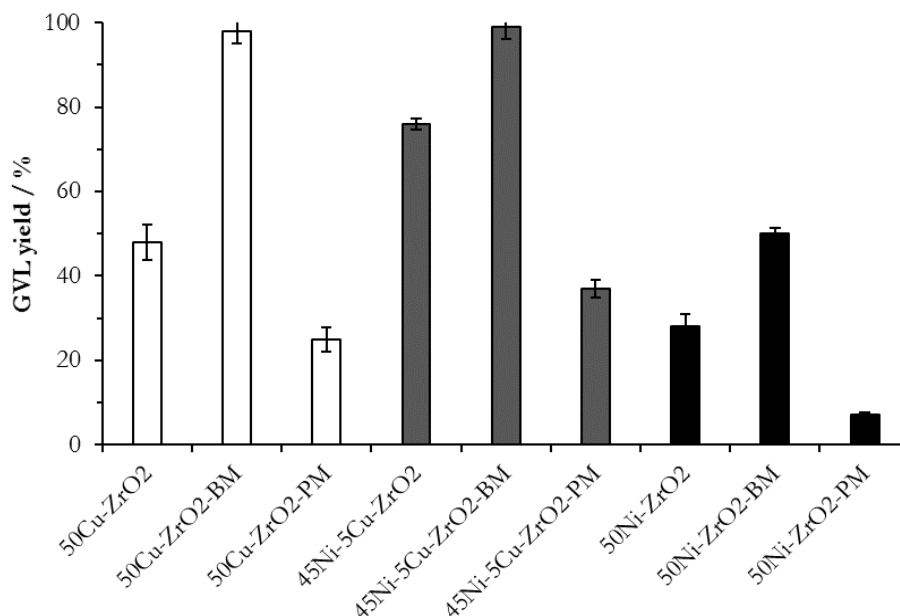


Figure 6.15. The effect of BM and PM methods on catalytic activity. **Reaction conditions:** 200 °C, 35 bar H₂, 30 minutes, 5 wt.% LA/H₂O, 0.05 g of catalyst.

Time-on-line data was obtained in order to determine the initial rates of reaction of 50Cu-ZrO₂-BM and 45Ni-5Cu-ZrO₂-BM (Figure 6.16). Given the linearity of the data, the rate of reaction was effectively estimated from the data obtained up to 30 minutes. The initial rates of reaction for 50Cu-ZrO₂-BM and 45Ni-5Cu-ZrO₂-BM had initial rates of 2.10×10^{-4} and 3.13×10^{-4} mol dm⁻³ s⁻¹. This represents a two-to-threefold increase from initial rates of 8.26×10^{-5} and 1.32×10^{-4} mol dm⁻³ s⁻¹ for 50Cu-ZrO₂ and 45Ni-5Cu-ZrO₂ prepared without a BM step.

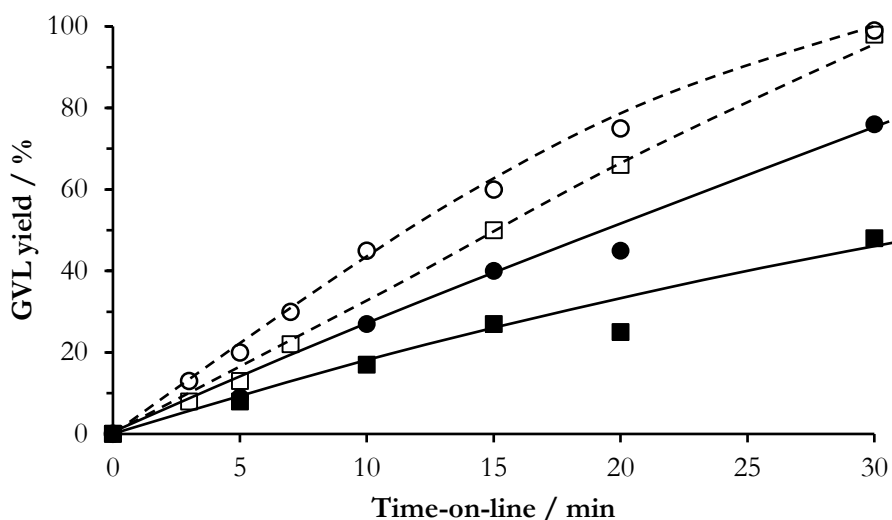


Figure 6.16. Time-on-line data for catalysts prepared with a BM step. ■ 50Cu-ZrO₂; ● 45Ni-5Cu-ZrO₂; □ 50Cu-ZrO₂-BM; ○ 45Ni-5Cu-ZrO₂-BM. **Reaction conditions:** 200 °C, 35 bar H₂, 5 wt.% LA/H₂O, 0.05 g of catalyst.

Characterisation of the OG catalysts prepared with a BM step and the catalysts prepared by PM was carried out. XRD patterns of all of these catalysts are shown in Figures 6.17–6.19. There was little difference observed between the XRD patterns of the catalysts prepared with a BM step and the catalysts prepared without a BM step both in terms of their phase composition and intensity. However, there were significant differences observed between untreated catalysts and the catalysts, which went through BM and PM treatment. The reflection corresponding to t-ZrO₂ ($2\theta = 30^\circ$) was more intense for the PM catalysts than the untreated catalyst and the catalysts treated by a BM step. The reflections corresponding to metallic Cu in 50Cu-ZrO₂ ($2\theta = 43^\circ$, Figure 6.17), the alloy species ($2\theta = 43.3^\circ$, Figure 4.18), and NiO ($2\theta = 44.5^\circ$, Figure 6.19) were also much more intense than they were in the untreated catalyst and the catalysts treated by BM. The particle sizes are shown in Table 6.8. In the case of 50Ni-ZrO₂-PM (Figure 6.19), there were also differences in the Ni species present compared with the catalysts prepared with and without a BM step. 50Ni-ZrO₂ prepared with and without a BM step did not show the prominent reflection at $2\theta = 44.1^\circ$ that is indicative of Ni metal, which is present in the pattern where PM was used.

This is likely because there was no Ni present in the ZrO_2 lattice allowing more of it to become reduced at 400 °C, thus resulting in a more intense reflection. The low activity of all the catalysts prepared by PM can be attributed to the large metal particle sizes (Table 6.8) and poor interaction between the “metal” component and the ZrO_2 “support”.

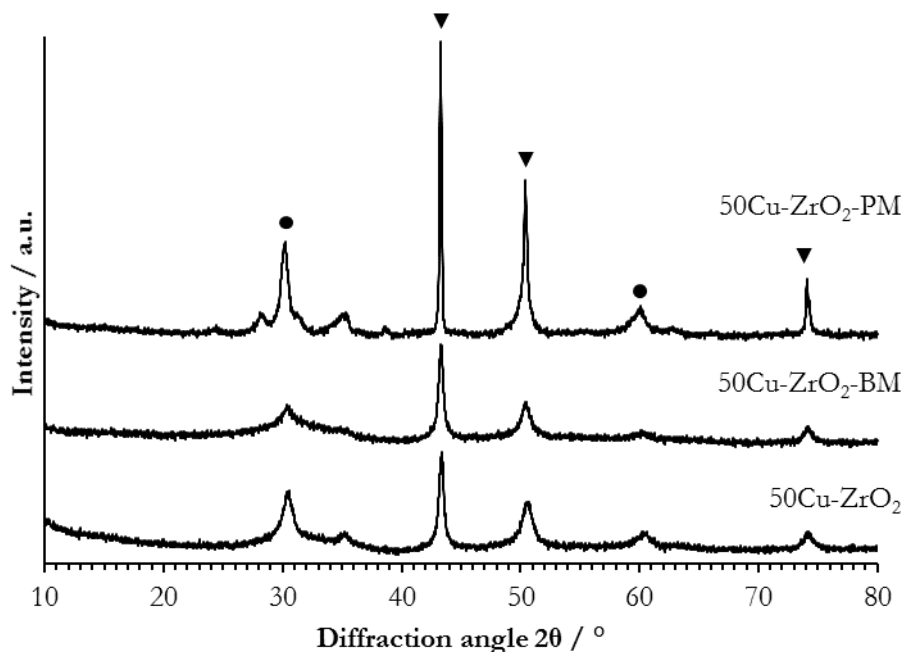


Figure 6.17. XRD patterns for Cu-ZrO_2 catalysts prepared with varying methods. ●: ZrO_2 ; ▼: Cu.

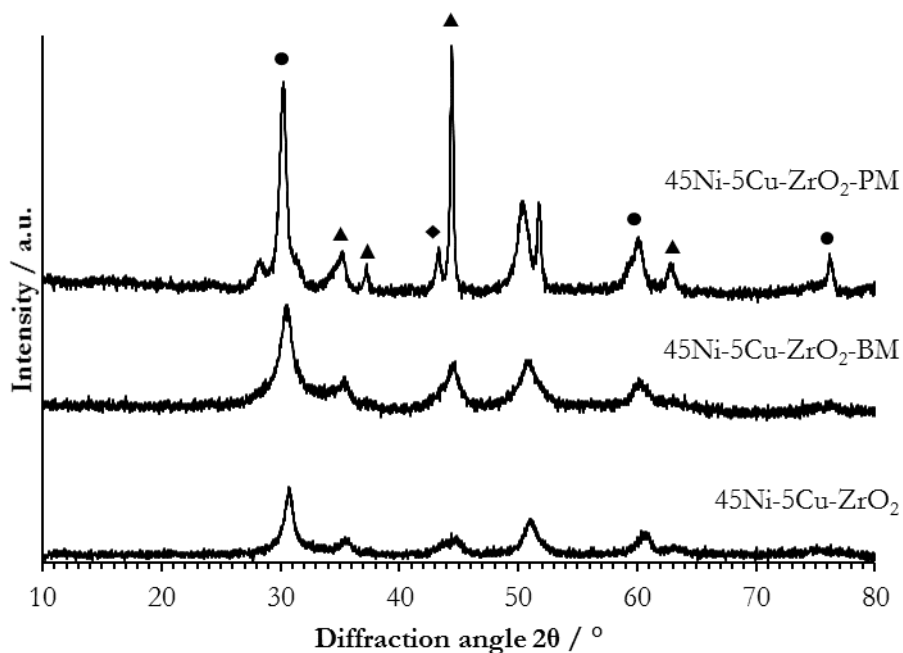


Figure 6.18. XRD patterns of 45Ni-5Cu-ZrO_2 catalysts prepared with varying methods. ●: ZrO_2 ; ▲: NiO ; ◆: Cu-Ni .

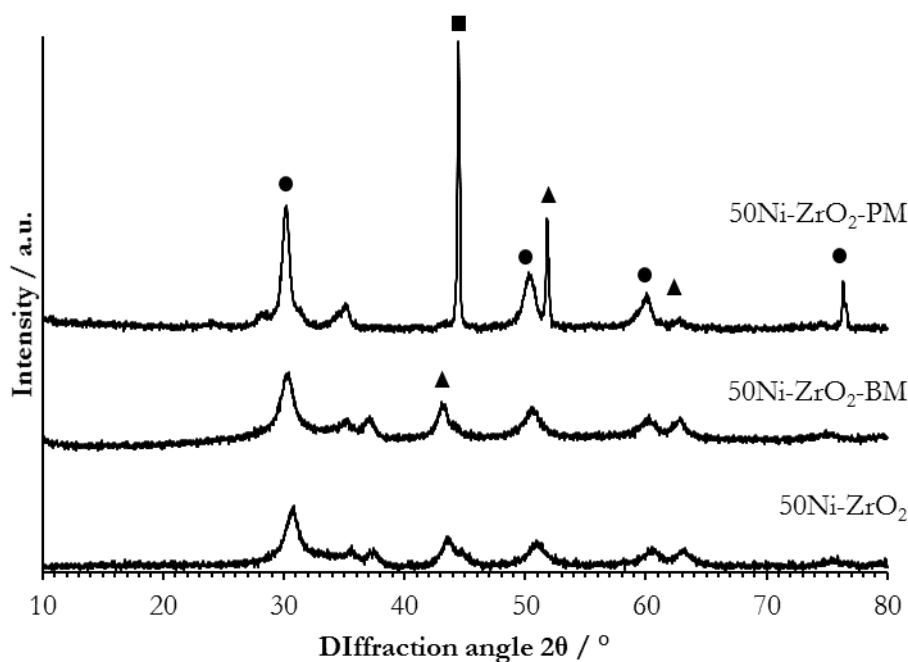


Figure 6.19. XRD patterns of Ni-ZrO₂ catalysts prepared with varying methods. ●: ZrO₂; ▲: NiO; ■: Ni.

Table 6.8. Particle sizes for BM and PM catalysts calculated by the Scherer equation.

Sample	Particle sizes / nm *			
	Cu metal	Ni-Cu alloy	Ni metal	NiO
50Cu-ZrO ₂	15.0	—	—	—
50Cu-ZrO ₂ -BM	13.0	—	—	—
50Cu-ZrO ₂ -PM	24.1	—	—	—
45Ni-5Cu-ZrO ₂	—	6.8	—	10.1
45Ni-5Cu-ZrO ₂ -BM	—	5.9	—	11.2
45Ni-5Cu-ZrO ₂ -PM	—	9.0	—	21.0
50Ni-ZrO ₂	—	—	—	8.4
50Ni-ZrO ₂ -BM	—	—	—	8.1
50Ni-ZrO ₂ -PM	—	—	19.3	—

* hkl [111]

BET surface area analysis was carried out on all of the catalysts prepared by PM and BM and comparative data are shown in Table 6.9. From this data, the BM catalysts had an increased surface area when compared to the catalyst prepared without the BM step; for example, the surface area of 50Cu-ZrO₂ increased from 61 m² g⁻¹ of OG catalyst prepared without a BM step, to 110 m² g⁻¹ after a BM step was incorporated. Similar increases were observed for 45Ni-5Cu-ZrO₂ and 50Ni-ZrO₂ (OG *vs.* BM). When the catalytic activity is normalised by the BET surface area, it can be seen that there were no

differences between the catalysts with and without BM steps. It is clear that the increase in activity is due to the increase in surface area caused by BM step. The normalised activities for the PM catalysts did not relate to the normalised activities for the catalysts prepared with and without a BM step. While the normalised activity for 45Ni-5Cu-ZrO₂-PM was similar to the normalised activity of 45Ni-5Cu-ZrO₂ and 45Ni-5Cu-ZrO₂-BM (0.717, 0.825, and 0.822 % (m² g⁻¹)⁻¹ respectively), there were significant differences between the normalised activities of each of the monometallic catalysts prepared by PM compared to those prepared with and without a BM step. This suggests that the BET surface area of the PM catalysts was not the reason for their low activity.

Table 6.9. BET surface areas of Cu-, Cu-Ni-, and Ni-ZrO₂ catalysts related to their activity.

Catalyst	GVL yield / %	BET surface area / m ² g ⁻¹	Normalised activity / % (m ² g ⁻¹) ⁻¹
50Cu-ZrO ₂	48	61	0.876
50Cu-ZrO ₂ -BM	98	110	0.890
50Cu-ZrO ₂ -PM	25	24	1.042
45Ni-5Cu-ZrO ₂	76	106	0.717
45Ni-5Cu-ZrO ₂ -BM	99	120	0.825
45Ni-5Cu-ZrO ₂ -PM	37	45	0.822
50Ni-ZrO ₂	28	78	0.359
50Ni-ZrO ₂ -BM	50	110	0.450
50Ni-ZrO ₂ -PM	7	37	0.189

6.2.4. Solvent screening

It was noted in section 6.2.2. that 45Ni-5Cu-ZrO₂ was not particularly reusable, with sintering being proposed as the reason. Solvent screening was carried out in order to determine whether the choice of solvent would have an effect on the catalytic activity and stability of the catalyst. 50Cu-ZrO₂ and 45Ni-5Cu-ZrO₂ (note that these catalysts were *not subjected to BM treatment*) were both tested for their activity for LA hydrogenation in MeOH, so chosen because of its similar dipole moment to water. The data for LA hydrogenation are presented in Figure 6.20. When the reaction was performed in MeOH, methyl levulinate (ML) was formed along with GVL, thereby indicating that LA was first esterified before the lactonisation mechanism took place. In the case of 50Cu-ZrO₂, the conversion of LA increased from 50 % when water was used to 100 % when MeOH was used, however, there was only a modest increase in GVL yield to 60 %. 45Ni-5Cu-ZrO₂ performed worse in MeOH than in water, converting 59 % LA compared with 76 % in water, and yielding just 47 % GVL.

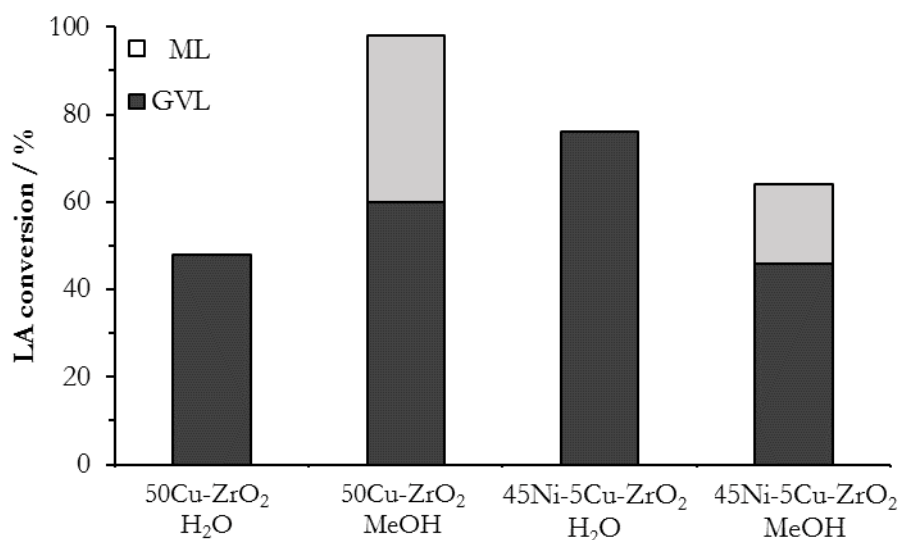


Figure 6.20. The effect of solvent on the catalytic activity of 50Cu-ZrO₂ and 45Ni-5Cu-ZrO₂. **Reaction conditions:** 200 °C, 35 bar H₂, 30 minutes, 5 wt.% LA/H₂O, 0.05 g of catalyst.

In order to determine whether 50Cu-ZrO₂ deactivated in the presence of MeOH, the catalyst was used with increasing loadings of LA and increasing reaction times. The results of these tests are presented in Figure 6.21. Using this method, continuous catalyst use could be simulated under batch conditions. The turnover number (TON) was calculated as a measure of activity. Figure 6.21 shows that all LA was converted in MeOH in the presence of 50Cu-ZrO₂ at loadings up to 15 wt.% LA in MeOH. An increase in TON was observed with an increase in LA loading, and a maximum turnover number of 2227 g_{LA}/g_{cat} was calculated after 1.5 h. Increasing the reaction time from 1.5 h to 16 h at 15 wt.% LA/MeOH resulted in a greater yield of GVL being produced, indicating that the catalyst continued to be active for the conversion of ML to GVL. However, increasing the reaction time further from 16 h to 24 h did not result in an increased yield of GVL, which indicates the catalyst deactivated at some point between 16–24 h. These results show that 50Cu-ZrO₂ is relatively stable when continuously used in MeOH. This is a promising observation when considered against the reuse data shown in Figure 6.12 and the poor reusability shown by the Cu-ZrO₂ catalysts presented in Chapter 5 (Figure 5.12). Research should turn towards understanding the deactivation of these catalysts and investigating whether the implementation of a continuous flow reaction system could improve the longevity of the catalyst.

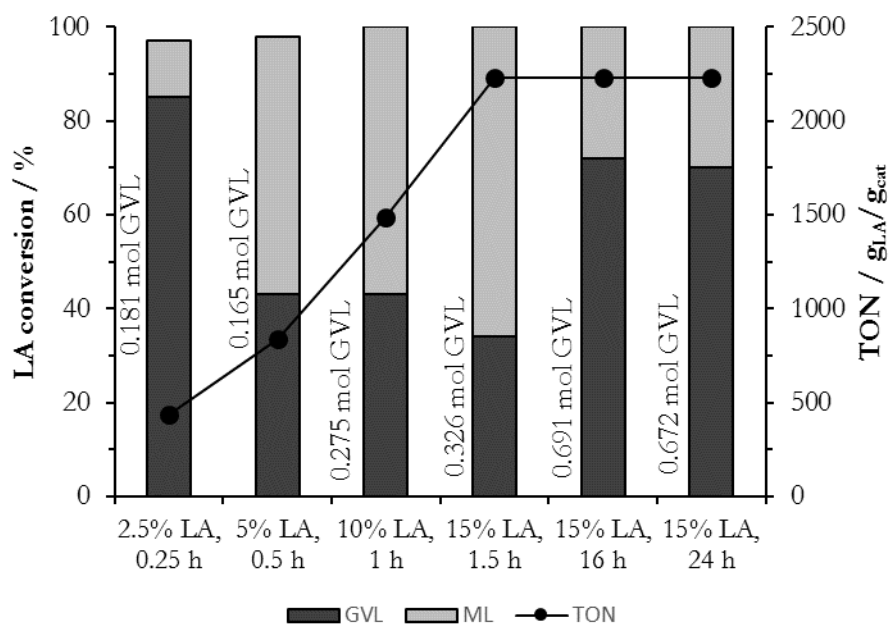


Figure 6.21. Activity of 50Cu-ZrO₂ at increasing loadings of LA in MeOH and increasing reaction times. **Reaction conditions:** 200 °C, 35 bar H₂, 0.05 g of catalyst.

6.3. Conclusions

A series of Cu-, Ni-, and Ni-Cu-ZrO₂ catalysts with varying Ni-Cu contents were prepared by an OG method and were found to be active for LA hydrogenation, with 45Ni-5Cu-ZrO₂ producing a GVL yield of 76 % in 30 minutes. Formation of a Ni-Cu alloy species was observed with an increase in Ni content. It was found that Ni-rich catalysts were more active than Cu-rich catalysts. This was attributed to the small particle size of the alloy species as observed by XRD, the large BET area, and large number of exposed metallic sites shown by adsorption of a large amount of N₂O. TPR analysis showed that the reduction temperature of NiO was decreased by the presence of Cu, which indicated that a greater proportion of reduced metal was present under reaction conditions. XPS suggested there was a charge transfer interaction from the Cu to the Ni, indicating that an alloy or solid solution was formed to some extent. Although the formation of an alloy was observed by XRD and suggested by TPR and XPS, SEM/EDX analysis showed that most of the Cu and Ni did not alloy, indicating that there was an excess of Cu and Ni present in the catalyst. This was confirmed by MP-AES analysis, which showed that a significant leaching of Ni occurred during the reaction (though only minimal leaching of Cu).

Reusability tests were conducted for the 45Ni-5Cu-ZrO₂ catalyst. It was found that the catalyst activity declined after one use from 76 % to 50 %. The deactivation was attributed to a decrease in surface area and the segregation and growth of NiO particles from the alloy species.

Furthermore, a BM step was added into the 45Ni-5Cu-ZrO₂ catalyst and a superior activity was observed due to an increase in surface area. The effect of solvent was also touched upon, and 50Cu-ZrO₂ was shown to be stable for the production of GVL for up to 16 h.

The catalysts presented here show great promise for replacing precious metal catalysts for LA hydrogenation. Work should now be dedicated to preparing catalysts that use less metal while attaining comparable activity. This study gives some clues as to the design of catalyst required for high activity, paving the way for novel syntheses to be developed.

6.4. References

- 1 K. Hengst, M. Schubert, H. W. P. Carvalho, C. Lu, W. Kleist and J.-D. Grunwaldt, *Appl. Catal. A Gen.*, 2015, **502**, 18–26.
- 2 V. Mohan, V. Venkateshwarlu, C. V. Pramod, B. D. Raju and K. S. R. Rao, *Catal. Sci. Technol.*, 2014, **4**, 1253–1259.
- 3 V. Mohan, C. Raghavendra, C. V. Pramod, B. D. Raju and K. S. Rama Rao, *RSC Adv.*, 2014, **4**, 9660–9668.
- 4 K. Shimizu, S. Kanno and K. Kon, *Green Chem.*, 2014, **16**, 3899–3903.
- 5 D. W. Hwang, P. Kashinathan, J. M. Lee, J. H. Lee, U. Lee, J.-S. Hwang, Y. K. Hwang and J.-S. Chang, *Green Chem.*, 2011, **13**, 1672–1675.
- 6 C. I. Meyer, A. J. Marchi, A. Monzon and T. F. Garetto, *Appl. Catal. A Gen.*, 2009, **367**, 122–129.
- 7 P. P. Upare, Y. K. Hwang, J.-M. Lee, D. W. Hwang and J.-S. Chang, *ChemSusChem*, 2015, **8**, 2345–2357.
- 8 I. Obregón, I. Gandarias, N. Miletić, A. Ocio and P. L. Arias, *ChemSusChem*, 2015, **8**, 3483–3488.
- 9 T. V Reshetenko, L. B. Avdeeva, Z. R. Ismagilov, A. L. Chuvilin and V. A. Ushakov, *Appl. Catal. A Gen.*, 2003, **247**, 51–63.
- 10 S. G. Wettstein, J. Q. Bond, D. M. Alonso, H. N. Pham, A. K. Datye and J. A. Dumesic, *Appl. Catal. B Environ.*, 2012, **117–118**, 321–329.
- 11 D. R. Jones, S. Iqbal, S. Ishikawa, C. Reece, L. M. Thomas, P. J. Miedziak, D. J. Morgan, J. K. Edwards, J. K. Bartley, D. J. Willock and G. J. Hutchings, *Catal. Sci. Technol.*, 2016, **6**, 6022–6030.
- 12 O. A. Abdelrahman, A. Heyden and J. Q. Bond, *ACS Catal.*, 2014, **4**, 1171–1181.
- 13 M. Chalid, A. A. Broekhuis and H. J. Heeres, *J. Mol. Catal. A Chem.*, 2011, **341**, 14–21.

- 14 S.-I. Fujita, Y. Sano, B. M. Bhanage and M. Arai, *J. Chem. Eng. JAPAN*, 2003, **36**, 155–160.
- 15 J. Ahmed, K. V Ramanujachary, S. E. Lofland, A. Furiato, G. Gupta, S. M. Shivaprasad and A. K. Ganguli, *Colloids Surfaces A Physicochem. Eng. Asp.*, 2008, **331**, 206–212.
- 16 Z. Wei, P. Yan, W. Feng, J. Dai, Q. Wang and T. Xia, *Mater. Charact.*, 2006, **57**, 176–181.
- 17 Z. Wei, T. Xia, W. Feng, J. Dal, Q. Wang, W. Li and P. Yan, *Rare Met.*, 2006, **25**, 172–176.
- 18 B. C. Miranda, R. J. Chimentão, J. Szanyi, A. H. Braga, J. B. O. Santos, F. Gispert-Guirado, J. Llorca and F. Medina, *Appl. Catal. B Environ.*, 2015, **166–167**, 166–180.
- 19 J. Bian, M. Xiao, S. Wang, X. Wang, Y. Lu and Y. Meng, *Chem. Eng. J.*, 2009, **147**, 287–296.
- 20 M. Lortie, R. Isaifan, Y. Liu and S. Mommers, *Int. J. Chem. Eng.*, 2015, **2015**, 9 pages.
- 21 F. Studt, F. Abild-Pedersen, Q. Wu, A. D. Jensen, B. Temel, J.-D. Grunwaldt and J. K. Nørskov, *J. Catal.*, 2012, **293**, 51–60.
- 22 C. Morant, J. M. Sanz, L. Galán, L. Soriano and F. Rueda, *Surf. Sci.*, 1989, **218**, 331–345.
- 23 A. R. Naghash, T. H. Etsell and S. Xu, *Chem. Mater.*, 2006, **18**, 2480–2488.
- 24 J. Ashok, M. Subrahmanyam and A. Venugopal, *Int. J. Hydrogen Energy*, 2008, **33**, 2704–2713.
- 25 A. R. Naghash, Z. Xu and T. H. Etsell, *Chem. Mater.*, 2005, **17**, 815–821.
- 26 J. Zhang, H. Wang and A. K. Dalai, *J. Catal.*, 2007, **249**, 300–310.
- 27 K. Takanabe, K. Nagaoka, K. Nariai and K. Aika, *J. Catal.*, 2005, **232**, 268–275.
- 28 A. Kitla, O. V Safonova and K. Föttinger, *Catal. Letters*, 2013, **143**, 517–530.

Chapter 7

Conclusions and future work

7.1. Conclusions

The world's increasing energy demands have led to a significant increase in research related with the conversion of biomass into chemicals that can be utilised by the fuel and chemical industries. The conversion of LA into GVL has been extensively studied because of the vast potential of GVL to be used as a fuel. However, many catalysts utilise relatively expensive precious metals in order to facilitate this conversion. While there are some examples of cheap and abundant metal catalysts being used for LA hydrogenation there needs to be a greater focus on catalyst design and identifying the active features of these catalysts.

This thesis has attempted to investigate some preparation strategies for both precious metal catalysts and NCM catalysts for LA conversion, and identify the features of the catalyst that make them active, thereby informing the design of future catalysts. A survey of the state of the art was presented in Chapter 1, encompassing both precious metal and NCM catalysts. It was clear that an understanding of the effect of catalyst preparation methods is lacking, therefore investigation into catalyst preparation methods both for precious metal (Ru) and NCM (Cu, Ni) catalysts are presented in Chapter 3–6.

The first half of the discussion was dedicated to the study of Ru/C catalysts. An investigation into the use of 5 wt.% Ru/C catalysts for the conversion of lactic acid to PDO was presented in Chapter 3 as a model reaction for LA hydrogenation. A comparison was made between a 5 wt.% Ru/C catalyst prepared by the SI method and a commercially available 5 wt.% Ru/C catalyst. This was first time a Ru/C catalyst prepared by SI was reported. The catalyst prepared by SI was found to be initially more active than the commercial catalyst, however it deactivated at longer reaction times and on reuse. The commercial catalyst did not show a high activity initially compared with SI catalyst, but became more

active as the reaction progressed over time and showed an increase in activity on reuse. Characterisation of both of these catalysts showed that the SI catalyst had the features of an active catalyst prior to use, i.e. a high dispersion of discrete metallic Ru nanoparticles, whereas the commercial catalyst achieved the desired characteristics after exposure to reaction conditions. The deactivation of the SI catalyst over time was attributed to the formation of lactide species on the catalytic active sites.

Further, 1 wt.% Ru/C catalysts were investigated for LA conversion to GVL in Chapter 4. The choice of carbon support, Ru precursor, and catalyst preparation method were investigated. XC72R was found to be superior to G60 as a catalyst support, and for the first time it was demonstrated that a low metal content catalyst prepared by SI from RuCl_3 was able to produce a 90 % yield of GVL under mild reaction conditions (100 °C, 5 bar H_2 , and a reaction time of 1 h). The effects of the ratios of PVA/Ru and $\text{NaBH}_4/\text{RuCl}_3$ were investigated in order to elucidate the reason for the observed activity of the catalysts. It was found that a low PVA/Ru ratio of 0.1 was required for high activity. PVA had the effect of controlling the size of the Ru nanoparticles to some extent, but the use of excess PVA caused blockage of the active sites and consequently a decrease in GVL yield was observed. The variation of $\text{NaBH}_4/\text{RuCl}_3$ ratio was found to result in a volcano type plot with an optimum ratio of 2.5. $\text{NaBH}_4/\text{RuCl}_3$ ratios below 2.5 did not sufficiently reduce the Ru precursor, resulting in the presence of chloride and a lower GVL yield from LA hydrogenation. $\text{NaBH}_4/\text{RuCl}_3$ ratios above 2.5 resulted in the formation of larger Ru particles. XPS analysis showed that the RuO_x was present on the surface of all 1 wt.% Ru/C catalysts prepared by SI. The role of NaBH_4 is therefore primarily for dictating the rate of nanoparticle formation and not permanently reducing the Ru to its metallic state. When the rate of nanoparticle formation is high, large nanoparticles are formed. A decrease in GVL yield on reuse of the SI catalysts was attributed to a decrease in BET surface area, likely from coking and/or particle sintering.

The second half of discussion reported an investigation into utilizing NCM catalysts for LA conversion. In Chapter 5, an investigation into Cu-ZrO₂ catalysts prepared by the CP method is presented. The preparation parameters, i.e. the Cu/Zr ratio, precipitate ageing time, and calcination temperature were varied and the resulting materials were characterised and tested. It was found that Cu-ZrO₂ was a highly active catalyst for LA conversion, yielding 80 % GVL after a reaction time of 2 h at 200 °C. A Cu/Zr ratio of 1, precipitate ageing time of 6 h, and calcination temperature of 400 °C were found to be the optimum preparation parameters for synthesising a catalyst with easily reducible Cu particles that were ultimately active for catalytic hydrogenation. A high BET surface area was also found to be an important factor of the catalytic activity. However, it was also found that most of the Cu deposited during the CP procedure was present as spectator species that was not catalytically active, either as part of the ZrO₂ lattice or as large CuO particles. The catalyst also showed a decline in activity on reuse, which was attributed to the sintering of Cu at high temperature and pressure.

Furthermore, Ni metal was incorporated into Cu-ZrO₂ catalysts using the OG method and a detailed investigation of their activity is reported in Chapter 6. The Ni-Cu content and the reduction temperature of the catalysts were varied during catalyst preparation and it was discovered that 45Ni-5Cu-ZrO₂ reduced at 400 °C was more active compared with Cu-ZrO₂ catalyst with a GVL yield of 76 % produced in 30 minutes at 200 °C. The increased activity on incorporation of Ni into Cu catalysts was attributed to the formation of a Ni-Cu alloy species. Characterisation of the catalyst revealed that a charge transfer interaction from the Cu to the Ni caused the Ni to become more easily reducible and hence more active for hydrogenation. The BET surface area and the number of exposed metal sites (as determined by N₂O titration) were also found to be superior for 45Ni-5Cu-ZrO₂ compared to the other catalysts (monometallic Cu and the catalysts prepared with various ratios of Cu-Ni). The OG method was further modified to include a ball milling step, and a comparison was made with a catalyst prepared by physical mixing. The catalysts prepared with ball mill treatment achieved a 100 % yield of GVL within 30 minutes. An increase in the surface area was directly relatable to the enhanced catalytic activity. The catalyst prepared by physically mixing the oxide species showed low activity because there was little interaction between the Ni-Cu and ZrO₂ components, effectively rendering the catalysts a crude mixture of bulk materials. Unfortunately, Cu-Ni catalyst also showed a loss in activity (similar to Cu-ZrO₂ and Ru/C catalysts) on reuse. Sintering of Ni was found to be a cause of deactivation. Also, an excess of metal was found to be present on the surface which was leached during the reaction but was not found to be catalytically active.

One of the main objectives of this thesis was to investigate the viability of the NCM catalysts as a possible replacement for precious metal catalysts such as Ru/C. Ru/C catalysts are highly active hydrogenation catalysts under relatively mild reaction conditions (100 °C, 5–35 bar H₂, 1 h). But for NCM catalysts to be active, much harsher reaction conditions need to be employed (200 °C, ≥ 35 bar H₂). While a comparable activity could be achieved, a lot more metal was required in the NCM catalysts compared to Ru/C, and a higher catalyst/substrate ratio was required.

7.2. Future work

The conclusions presented in section 7.1 open up many avenues for further research. A recurring issue with the catalysts presented throughout this thesis was their activities on re-use. More research needs to be carried out on Ru/C catalysts in order to prepare stable catalysts.

Similar to Ru/C catalysts preparation methodologies for Cu-Ni-ZrO₂ catalysts need to be developed that can stabilise the active sites from sintering. One factor in the sintering of the active sites in these catalysts is the harshness of the operating conditions required. NCM catalysts required a higher energy input compared with Ru catalysts, therefore the development of NCM catalysts that can show a good catalytic performance at lower temperatures would be beneficial both from the point of view that

it would minimise the requirement for high energy input and could lead to less sintering during the reaction. A technological and economic analysis of the process would be required to determine whether the use of NCM catalysts could offset the requirement for harsher operating conditions and make scaling up the process viable.

It was also highlighted that the Cu-ZrO₂ and Ni-Cu-ZrO₂ catalysts presented in this thesis used an excess of metal. In order for a process to be truly sustainable, the catalyst used should also be sustainable. However, the use of a significantly larger amount of a NCM as a catalyst compared to a small amount of a precious metal would also not be sustainable long term. Therefore, variation of the preparation methodologies that utilise a lesser amount of metal while maintaining comparable activity. There are still challenges to overcome with the use of NCM catalysts for the hydrogenation reaction listed in this thesis, but the study presented here shows that these are promising alternatives to precious metals if the challenges can be overcome.